Sofia Magalhães Cunha

Dinâmica de pacote de onda e propriedades eletrônicas e de transporte em materiais 2D

————

Wave-packet dynamics and electronic transport properties in 2D materials

————

Golfpakketdynamica en elektrontransport in 2D materialen

Fortaleza

2022

Sofia Magalhães Cunha

Dinâmica de pacote de onda e propriedades eletrônicas e de transporte em materiais 2D

——

Wave-packet dynamics and electronic transport properties in 2D materials

——

Golfpakketdynamica en elektrontransport in 2D materialen

Tese apresentada ao Curso de Pós-graduação em Física da Universidade Federal do Ceará como parte dos requisitos necessários para a obtenção do título de Doutor em Física.

Orientador:
Prof. Dr. João Milton Pereira Junior

Co-orientador:
Prof. Dr. Diego Rabelo da Costa
Prof. Dr. François M. Peeters

DOUTORADO EM FÍSICA
DEPARTAMENTO DE FÍSICA
PROGRAMA DE PÓS-GRADUAÇÃO EM FÍSICA
CENTRO DE CIÊNCIAS
UNIVERSIDADE FEDERAL DO CEARÁ

Fortaleza - CE
11 de Janeiro de 2022

SOFIA MAGALHÃES CUNHA

Dinâmica de pacote de onda e propriedades eletrônicas e de transporte em materiais 2D

——

Wave-packet dynamics and electronic transport properties in 2D materials

——

Golfpakketdynamica en elektrontransport in 2D materialen

Tese de doutorado apresentada ao Curso de Pós-graduação em Física da Universidade Federal do Ceará como parte dos requisitos necessários para a obtenção do título de Doutor em Física.

Aprovada em: 11/01/2022.

BANCA EXAMINADORA

———————————————————
Prof. Dr. João Milton Pereira Junior (Orientador)
Departamento de Física – UFC

———————————————————
Prof. Dr. François Maria Leopold Peeters (Co-orientador)
Department of Physics - University of Antwerp
Belgium

———————————————————
Prof. Dr. Diego Rabelo da Costa (Co-orientador)
Departamento de Física – UFC

———————————————————
Dr. Ben Van Duppen
Department of Physics - University of Antwerp
Belgium

———————————————————
Prof. Dr. Raimundo Nogueira da Costa Filho
Departamento de Física – UFC

To God,
to my family,
and to my friends who help me during all
my steps along this way.

Acknowledgments

I first thank God because until now He has supported me with His infinite mercy, always putting wonderful people in my life and comforting me in times of difficulty.

I am immensely grateful to my parents Joana Lúcia and Almir for all their support throughout my personal and professional education. For always believing and supporting my dreams since I was a child. To my brother Matheus for the moments of relaxation. Thanks to my little dog Laika for always keeping me company as I worked and studied since my graduation (and even for barking on all my video calls to discuss work).

I am especially grateful to my family, my dear aunts Terezinha and Regina Célia for always being present at every moment of my life, following my every step since I was a child and always interested in my well-being.

I am especially grateful to Professor Raimundo Nogueira da Costa Filho for all his emotional support, friendship, good advice and for believing in me professionally and personally, and for your support even by distance in all moments of my life. God always put incredible people in my life and you are one of them. Thank you for everything!

To my best friend Kercia Ferreira, for our good conversations and confidentiality since school days. Even from a distance, we were always in contact, helping me to endure moments of solitude while away from everyone I love.

Thanks to Professor Diego Rabelo da Costa for his patience and guidance during my Masters and Doctorate. To Professor João Milton for his guidance, to Professor François Peeters for his attention, availability to help, patience, guidance and financial support. Thanks to Ben Van Duppen for helping me gain more scientific independence, guidance, and for our long and always very scientifically productive conversations.

I thank my great friends at the Federal University of Ceará: Janaína Sobreira, Michel Andrade, Nathan, Lucas Miranda, Sérgio Levy and Sabrina Sá.

Thanks to the special people brought to my life during my sandwich doctorate in Antwerp: Rob Proost (for his presence during my last two months in Antwerp even now, despite the distance), Jovana, Ablenya Barros, Cecília, Michal Wyszyński and Sara Conti.

I thank all the Professors of the Department of Physics who contributed to my aca-

demic development.

Finally, I would like to thank CAPES, CNPq and University of Antwerp for the financial support, which made the development of this work possible.

"When pride comes, there comes shame, but wisdom is with the quiet in spirit."

Proverbs 11:2

Resumo

Este trabalho se divide em duas partes. Na primeira, a evolução temporal dos pacotes de ondas em sistemas 2D é analisada pela técnica *Split-Operator* em três cenários diferentes: em multicamadas de fósforo negro, as oscilações transientes dependente do tempo nos valores médios de posição e momento foram observadas devido a o efeito *zitterbewegung* e o pacote de ondas se propagam de maneira não uniforme ao longo do espaço, deformando-se em uma forma elíptica. Esses resultados foram corroborados pelo formalismo da função de Green, exceto para maiores valores de momento e após intervalos maiores de tempo. Em fios quânticos semicondutores 2D com massas efetivas anisotrópicas e diferentes orientações de ângulo em relação ao eixo anisotrópico, mostramos que quanto maior este ângulo, menor é o espaçamento dos níveis de energia, implicando em um aumento dos estados eletrônicos acessíveis. Além disso, para o campo magnético não-nulo, os estados quânticos de *Hall edge states* são significativamente afetados pela orientação das bordas. No caso anisotrópico, oscilações amortecidas nos valores médios de velocidade nas direções x e y foram obtidas. Essas oscilações são originadas pela geometria do fio quântico, mas também de subpacotes de onda com diferentes orientações de momento, enquanto que para fios quanticos isotrópicos o pacote de onda se dispersa sem se dividir; no terceiro cenário, a técnica *split-operator* foi usada para estudar os níveis de Landau, as trajetórias do pacote de ondas e as velocidades dos elétrons no grafeno em regime de baixa energia descrito por uma equação de Dirac modificada onde o operador momentum é escrito em uma forma generalizada como resultado da aplicação do formalismo do operador de tradução dependente da posição.

Na segunda parte desta tese, as propriedades eletrônicas e de tunelamento das redes $\alpha - T_3$ foram estudadas. Os elétrons nessas redes se comportam de forma análoga aos férmions de Dirac de spin inteiro. A presença de um terceiro sítio atômico na célula unitária leva a uma banda plana no espectro de energia, fornecendo propriedades eletrônicas e de tunelamento únicas. A presença de um potencial superperiódico e a inclusão de termos de quebra de simetria resultam em desvios da equivalência atômica entre os sítios atômicos que afetam os pontos de Dirac e o *band-gap* no espectro de energia. Pequenos desvios na equivalência entre os sítios atômicos e o número de barreiras alteram as propriedades de transmissão nessas redes. Além disso, novas regiões de tunelamento são possíveis ajustando a simetria entre os sítios atômicos e afetando a transmissão total omnidirecional chamada super-tunelamento de Klein observada nessas redes. Comparamos esses resultados com as probabilidades de tunelamento por meio de regiões onde o espectro de energia muda de linear com uma banda plana do meio para uma dispersão hiperbólica.

Abstract

This piece of work is twofold. First, the time evolution of wave-packets in 2D systems is analyzed by the *Split-Operator* technique in three different scenarios: In multilayer phosphorene, the transient oscillations in the time-dependent average of position and momentum were observed due to the *zitterbewegung* effect, and the wave packet propagates non-uniformly along the space deforming itself into an elliptical shape. These results were corroborated by the Green's function formalism except for large values of the wave-vector and long times; In 2D semiconductor quantum wires (QWs) with anisotropic effective masses and different angle orientations with respect to the anisotropic axis. We have shown that the greater this angle, the smaller is the energy levels spacing implying in an increase of the accessible electronic states. Additionally, for non-null magnetic field, the quantum Hall edge states are significantly affected by the edge orientation. In the anisotropic case damped oscillations in the average values of velocity in both x and y directions where obtained. Theses oscillations are originated by the QW geometry but also from subwavepackets with different momentum orientations, whereas for isotropic QWs the wavepacket disperses without splitting; in the third scenario the *split-operator* technique was used to study the Landau levels, the wave packet trajectories and velocities of electrons in graphene at low-energy regime described by a modified Dirac equation where the momentum-operator is written in a generalized form as result of applying the position-dependent translation operator formalism (PDTO).

In the second part of this thesis, the electronic and tunneling properties of $\alpha - T_3$ lattices were studied. Electrons in these lattices behave analogous to integer-spin Dirac Fermions. The presence of a third atomic site in the unit cell leads to a flat band in the energy spectrum, providing unique electronic and tunneling properties. The presence of a super-periodic potential and the inclusion of symmetry-breaking terms results in deviations of the atomic equivalence between the atomic sites affecting the Dirac points and the band-gap. Small deviations in the equivalence between the atomic sites and the number of barriers change the transmission properties in these lattices. Additionally, new tunneling regions are possible by adjusting the symmetry between the atomic sites and affect the omnidirectional total transmission called super-Klein tunneling observed in these lattices. We compare those results to the tunneling probabilities through regions where the energy spectrum changes from linear with a middle flat band to a hyperbolic dispersion.

Abstract

Dit werkstuk is tweeledig. Eerst wordt de tijdsevolutie van golfpakketten in 2D-systemen geanalyseerd door de *Split-Operator*-techniek in drie verschillende scenario's: In meerlaags fosforeen werden de tijdelijke oscillaties in het tijdsafhankelijke gemiddelde van positie en momentum waargenomen als gevolg van het zitterbewegung-effect (ZBW), en het golfpakket plant zich niet-uniform voort langs de ruimte en vervormt zichzelf tot een elliptische vorm. Deze resultaten werden bevestigd door het functie formalisme van Green, behalve voor grote waarden van de golfvector en lange tijden; In 2D halfgeleider kwantumdraden (QW's) met anisotrope effectieve massa's en verschillende hoekoriëntaties ten opzichte van de anisotrope as. We hebben aangetoond dat hoe groter deze hoek, hoe kleiner de energieniveaus zijn, wat een toename van de toegankelijke elektronische toestanden impliceert. Bovendien worden voor niet-nul magnetische velden de quantum Hall-randtoestanden aanzienlijk beïnvloed door de randoriëntatie. In het anisotrope geval werden gedempte oscillaties in de gemiddelde waarden van snelheid in zowel x als y richtingen verkregen. Deze oscillaties worden veroorzaakt door de QW-geometrie, maar ook door subgolfpakketten met verschillende impulsoriëntaties, terwijl voor isotrope QW's het golfpakket zich verspreidt zonder te splitsen; in het derde scenario werd de *split-operator*-techniek gebruikt om de Landau-niveaus, de golfpakkettrajecten en snelheden van elektronen in grafeen bij een laag energieregime te bestuderen, beschreven door een gewijzigde Dirac-vergelijking waarbij de momentum-operator is geschreven in een gegeneraliseerde vorm als resultaat van het toepassen van het positieafhankelijke vertaaloperatorformalisme (PDTO).

In het tweede deel van dit proefschrift werden de elektronische en tunnel eigenschappen van $\alpha - T_3$ roosters bestudeerd. Elektronen in deze roosters gedragen zich analoog aan integer-spin Dirac Fermions. De aanwezigheid van een derde atomaire plaats in de eenheidscel leidt tot een vlakke band in het energiespectrum, wat zorgt voor unieke elektronische en tunnel eigenschappen. De aanwezigheid van een superperiodieke potentiaal en de opname van symmetriebreking termen resulteert in afwijkingen van de atomaire equivalentie tussen de atomaire locaties die de Dirac-punten en de bandgap beïnvloeden. Kleine afwijkingen in de equivalentie tussen de atomaire locaties en het aantal barrières veranderen de transmissie-eigenschappen in deze roosters. Bovendien zijn nieuwe tunnel gebieden mogelijk door de symmetrie tussen de atomaire locaties aan te passen en de omnidirectionele totale transmissie genaamd super-Klein-tunneling (SKT) te beïnvloeden die in deze roosters wordt waargenomen. We vergelijken die resultaten met de tunnelkansen door regio's waar het energiespectrum verandert van lineair met een middelste platte band naar een hyperbolische dispersie.

Contents

List of Figures

List of Tables

List of abbreviations

$2D$	Two-dimensional
KT	*Klein-tunneling*
ZBW	*Zitterbewegung*
BP	black-phosphorus
GGA	generalized gradient approximation
GW	gradient wave
HCL	honeycomb lattice
SKT	*Super Klein-tunneling*
QWs	quantum wires
TB	*Tight-binding*
SOT	*Split-operator* technique
PDTO	position-dependent translation operator
h-BN	Hexagonal boron nitride
DOS	Density of states

List of Nomenclatures

v_F	Fermi velocity
$t,\ \alpha$	Hopping parameters
Ψ_A	The probability of finding the electron on sublattice A
Ψ_B	The probability of finding the electron on sublattice B
Ψ_C	The probability of finding the electron on sublattice C
e	Elementary electron charge
$\vec{A}$	Vector potential
$\vec{B}$	Magnetic field
l_B	Magnetic length
ϕ_0	Magnetic quantum flux
$\vec{k}$	wave-vector
$\mathbb{1}$	Identity matrix
M	Mass-term matrix
Δ	Mass potential
$\hat{S}$	Time evolution operator
S	spin number
T	Kinetic operator
V	Potential operator
$\vec{a}_i$	Real lattice vector i
$\vec{b}_i$	Reciprocal lattice vector i
H	Hamiltonian
H_K	Dirac Hamiltonian
$\mathbf{a}_i^\dagger$	Creation operator of electrons on the site i of the subllatice A
$\mathbf{a}_i$	Annihilation operator of electrons on the site i of the subllatice A
$\mathbf{b}_i^\dagger$	Creation operator of electrons on the site i of the subllatice B
$\mathbf{b}_i$	Annihilation operator of electrons on the site i of the subllatice B

$f(\vec{k})$	Structure factor of the crystal
$\hbar$	Plank constant
K	Dirac cone K
K'	Dirac cone K'
ϵ_i	Self-energy on site i
d	Width of initial gaussian wave packet
W_w	Width of well
W_b	Width of barrier
L	Width of cell in a superlattice
k	The modulus of the wave vector
θ_w	Incident angle
Γ	Gamma point, center of first Brillouin zone
$\vec{\sigma}_i$	Pauli matrix i
g	Metric dimensionless parameter
a	Lattice parameter
E	Energy
E_g	Gap energy

1

Introduction

1.1 Graphene: 'CERN on one's desk'

In 2004, researchers at the Manchester University were able to isolate films consisting of just a few layers of graphite and even a single carbon layer, named graphene, which boosted the search for new materials. This material, unlike theoretically expected [1, 2], exhibits high quality and stability even under ambient conditions [3, 4]. Since graphene has been proving to have very peculiar and interesting properties that could possibly generate new carbon-based electronic devices, this material has received a lot of attention from researchers. As a consequence of this "boom" in two-dimensional (2D) (two-dimensional) materials related research, Andre Geim and Konstantin Novoselov were awarded with the nobel prize in physics for groundbreaking experiments regarding this special two-dimensional material.

Graphene is a 2D crystal of carbon atoms arranged in a honeycomb lattice (HCL) formed by the combination of two trigonal lattices shifted from each other. The atoms have sp^2 hybridization and each one of them is bounded to the other three, by means of strong σ bonds. Perpendicular to the plane of atoms there is the pure half-filled p_z orbitals left out of the hybridization making weak delocalized π bonds with the neighbors atoms. Since the p_z orbital of a given carbon atom is not bound to a specific neighbor, p_z orbital constantly changes the direction of the superposition around the three neighbors, which gives rise to the delocalized π bonds. Therefore, unpaired electrons in the p_z orbitals could hop from atom to atom as the π bonds are formed, making these π electrons the main responsible for the transport properties of graphene [5, 6].

A striking feature of graphene is that its charge carriers are governed by an equation analogous to the Dirac equation that is used to describe spin 1/2 particles in quantum electrodynamics [7]. Due to that, electrons in graphene behave like zero-mass relativistic particles that travel with a Fermi velocity that is equivalent to the speed of light $v_\text{F} = 10^6 m/s$ (for more details see Chapter 2), exhibiting a gapless conical spectrum at low energies ($E < 1eV$). As a result, some relativistic effects such as *Klein-tunneling* (KT) and the phenomenon known as *zitterbewegung* (ZBW) can be observed in graphene.

The KT effect emerges when one tries to confine the graphene electrons by means of electrostatic potentials. However, these electrons can not be trapped by such electrostatic potentials and they can be totally transmitted through any electrostatic barrier [8]. This effect is usually called *Klein-paradox* or KT in graphene, in analogy to the so called *Klein-paradox* in quantum electrodynamics. We are going to discuss this effect in detail in Chapter 2.

Another effect that can be observed in graphene is the trembling motion of its propagating wave-function, this effect is called *zitterbewegung* [9, 10, 11] (ZBW). ZBW was theoretically predicted for the first time in 1930 by Schrödinger [12] and, in recent years, interest in this topic has been renewed. Previous theoretical work has suggested some ways to observe ZBW experimentally, for example in quantum wells formed by III-V zinc-blende semiconductors with spin-orbit coupling [13] and, more recently, in monolayers [14] and bilayers [15] of graphene. One experimental simulation of ZBW for relativistic free electrons in vacuum was made by Gerritsma et al. [16] using trapped ions. This phenomenon, which has been attributed to an interference between the positive and negative energy states in the wave-packet, was also analyzed numerically and analytically in Refs. [16, 17].

Because graphene provides the possibility of mimicking relativistic effects in laboratory, and from a technological point of view it is a very stable material, perfectly 2D, which also brings two new degrees of freedom that can be manipulated for electronics: the valleys [18] and the pseudo-spin. There are many other properties not included here that can generate new technologies by exploring the physics of graphene.

1.2 Phosphorene: an anisotropic semiconductor

More recently, in 2014, a group of researchers from the University of North Carolina managed to obtain monolayers of black phosphorus (BP), also known as phosphorene using the micromechanical cleavage technique [19], the same technique used to obtain graphene. Unlike graphene, BP has a direct gap and its energy value is adjustable with the number of layers [19], in addition it has anisotropy [20] and high electronic mobility [20, 21], as we discuss further.

Phosphorus is a non-metallic element that is highly reactive and oxidizes quickly when in contact with oxygen in the atmosphere. This chemical element is not found freely in nature. Phosphorus has many allotropes being BP the most stable one first obtained in 1914 from white phosphorus under high pressure and high temperature [22, 23]. Similar to graphite, its a structure is arranged in rough layers bound by van der Waals interactions [24]. Previous studies showed that this material exhibits a structural phase transition [25, 26], and is superconducting at high pressures and temperatures above $10K$ [27, 28]. At low temperatures the conductivity is dominated by holes [23, 25, 29].

Just like graphene, that is an isolated single layer obtained from graphite, phosphorene is a monolayer of BP [30, 31]. In this structure, the phosphorus atoms are covalently

bonded to the three neighboring atoms and have sp^3 hybridization, unlike graphene where the C atoms are bound by sp^2 hybridization, which explains the rough surface of the material, as shown in Fig. 1.1. Moreover its *bulk* form is a semiconductor, whose energy gap value is about 0.31-0.35 eV, and monolayer BP has a direct energy gap of 1.60 eV [23, 25, 32]. Experimentally it was observed that the energy gap value increases with the number of layers of the material [31], which was later confirmed by theoretical works [19, 33, 34, 35, 21].
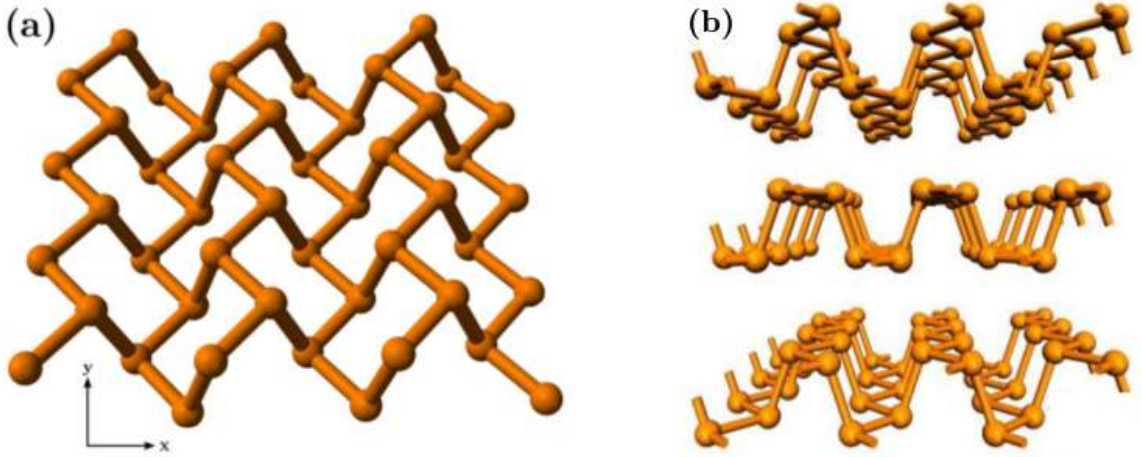
Figure 1.1: Representation of (a) monolayer phosphorene (top view), (b) side view of phosphorene layers exhibiting its buckled structure [36].

BP also has particularities in its electronic properties. An interesting characteristic of this material is the difference between the energy gap value between the valence and conduction bands of its *bulk* form, which is around 0.33 eV which increased to around 1.01 eV for bilayer [37]. This difference in the energy gap values of bulk and bilayer is larger than values observed in any other thin film. For graphene, *bulk* properties are observed in samples with at least 20 layers [38], while for BP we observe *bulk* characteristics in samples with at least 10 layers [39].

Figure 1.2 shows the band structures of BP in its *bulk* form using first-principles calculations for two types of functionals: GGA (generalized gradient approximation) and GW (gradient wave). We can see from Fig. 1.2 that there is a small energy gap between the valence and the conduction bands in the region close to the Fermi level (Γ point) when calculation is done within the GW approximation. Although none of these techniques provide a result of energy gap values consistent with the experimental values, which are approximately 0.31-0.35eV, the GW technique is the most suitable as it presents qualitative results similar to the experimental results of the material.

Furthermore, as the number of layers increases, the valence band undergoes a split close to the Fermi level, which causes a reduction in the energy value of its gap [40] as noticed in Fig. 1.3. This occurs due to the presence of negative hopping values, called repulsion hoppings, between layers and between close neighbors both within a layer and
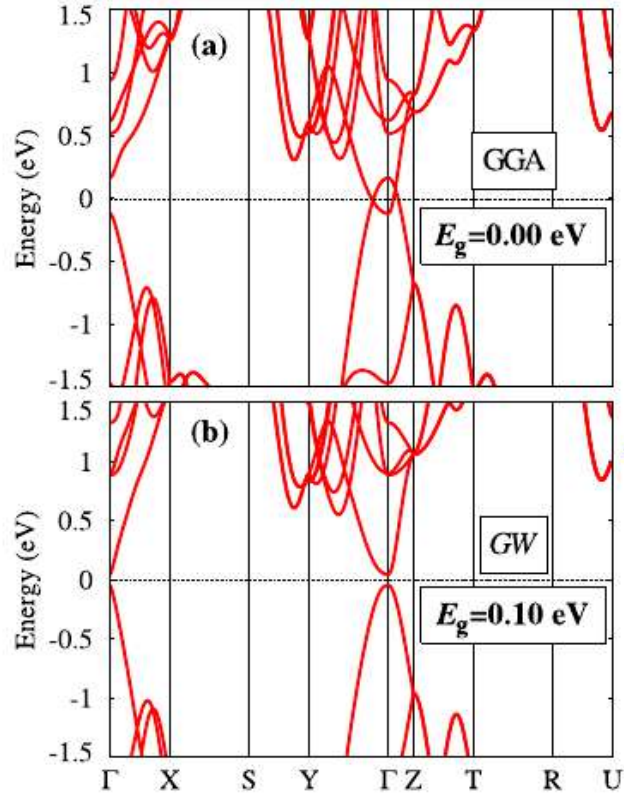
Figure 1.2: Band structure for bulk BP calculated using (a) *DFT-GGA* (generalized gradient approximation) [40, 41], and (b) *DFT-GW.* [42, 43].

between the sites of one layer and another [40], this interaction being due to the buckled structure of the material. The dependence of energy gap on the number of layers is more evident by analyzing the charge mobility in this material [21, 20], which is greater in the x direction indicating therefore an anisotropy (direction-dependent physical properties) in BP [20].

Due to some peculiar properties of BP described in this section, this material is very remarkable for technological applications, such as optical and electronic devices, presenting excellent performance in batteries [44, 45] and arousing a lot of interest in the development of transistors [44, 46, 47, 48, 49]. A major drawback is that this material is not stable in air.

1.3 Introducing $\alpha - T_3$ lattices: transition from honeycomb lattice to dice

An analogous lattice to graphene, the T_3 or dice lattice, is shown on the right hand side of Fig. 1.4. The dice lattice is described by the same Dirac Hamiltonian as graphene, but with an enlarged pseudospin $S = 1$. In the dice lattice case, the geometry of the
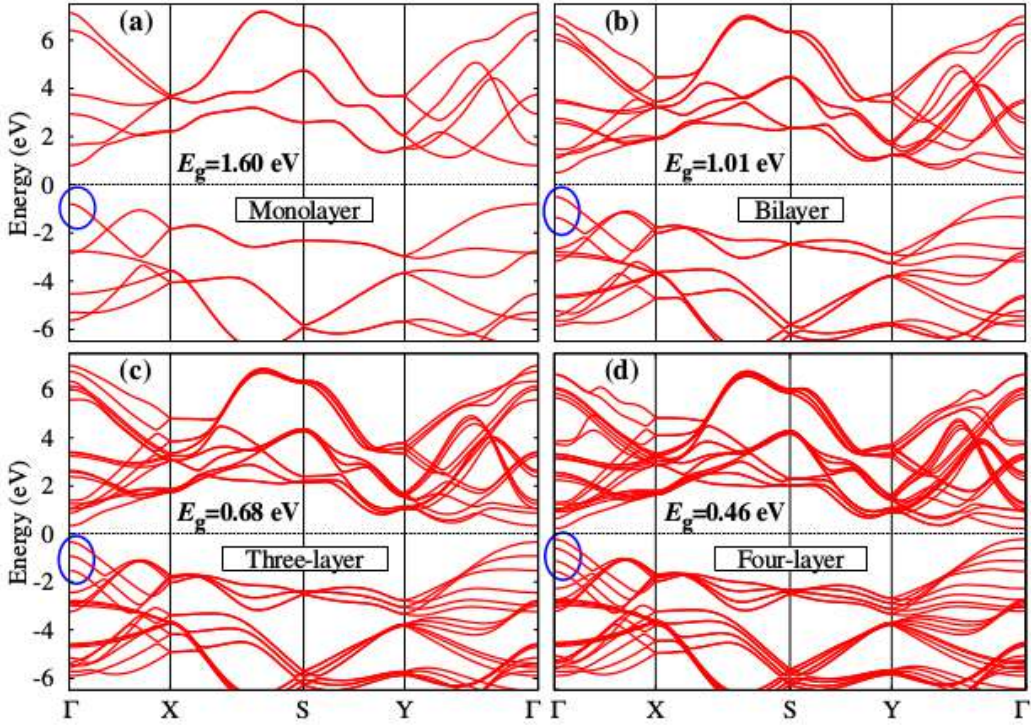
Figure 1.3: Band structures calculated using *DFT-GW* for different numbers of layers: (a) monolayer, (b) bilayer, (c) trilayer, (d) tetralayer of BP [40].

HCL is altered by an additional atom located at the center of each hexagon coupled only to one of the two topologically nonequivalent atomic sites of the HCL. The dice lattice can be naturally obtained by growing a trilayer structure of cubic lattices in the (111) direction [50] (for example $SrTiO_3$ /$SrIrO_3$ /$SrTiO_3$) or by confining cold atoms to an optical lattice [51]. The properties of general pseudospin S lattices arising from the generalized Dirac Hamiltonian have been explored recently [52, 53, 54], providing insight into the understanding of lattices with pseudospin equal or greater than $S = 1/2$.

From the $\alpha - T_3$ model [56] the HCL and dice (or T_3) lattice can be obtained by a continuous evolution of the parameter α, which is proportional to the strength of the coupling with the additional atom at the center of the HCL, as observed in Fig. 1.4 where the limiting cases, the HCL ($\alpha = 0$) and dice lattice ($\alpha = 1$) are represented.

The $\alpha - T_3$ model was initially proposed in 2014 paper [56] to investigate cold atom systems highlighting the diamagnetic [57] ($\alpha = 0$) to paramagnetic [58, 59] ($\alpha = 1$) transition in the orbital magnetic response of the lattice. This behaviour has recently been linked to the evolution of the Berry phase in this system, which ranges continuously from π to zero as it evolves from HCL to dice, respectively. Additionally, in the 2D limit, at critical doping and considering $\alpha = \sqrt{1/3}$ three-dimensional $Hg_{1x}Cd_xTe$ maps onto the $\alpha - T_3$ model in the intermediate regime between the dice and HCL [60]. The $\alpha - T_3$ model has also been extended to include additional terms and variations [61] in its Hamiltonian.
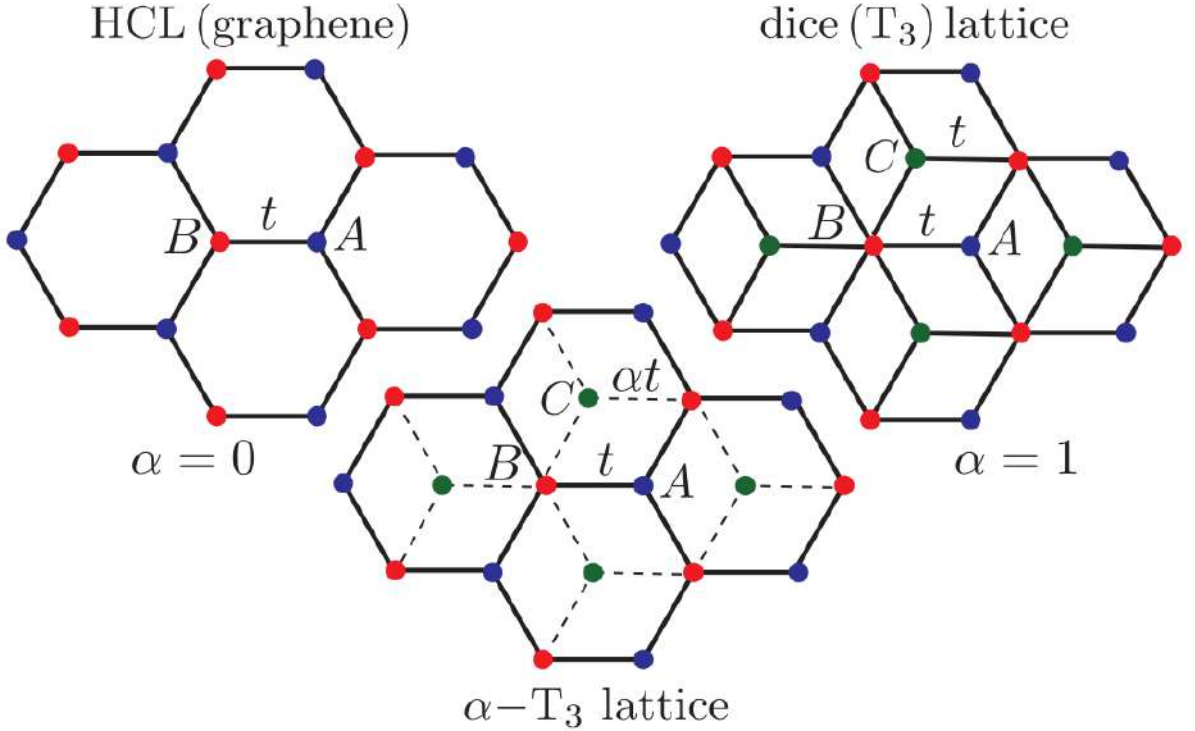
Figure 1.4: Some lattices obtained from the $\alpha - T_3$ model assuming $\alpha = 0$ representing HCL, on the left. For $\alpha = 1$ (dice) there is an additional site at the center of each hexagon, as shown on the right. The general $\alpha - T_3$ lattice is in the bottom [55].

1.4 Outline and goals of this thesis

This thesis has two main objectives: the first one is to develop efficient methods to solve the time-dependent Schrödinger and Dirac equations, and then apply them to the study of the transport properties of nanoscale structures in graphene into the PDTO approach and to anisotropic semiconductors. The second one is to investigate the electronic and tunneling properties in $\alpha - T_3$ superlattices focusing on the explanation of the appearance of new Dirac points, band-gap formation and how the omniderectional tunneling is altered by the inclusion of small deviations in the symmetry of the atomic sites.

First, in order to obtain the Dirac equation which describes charge carriers in graphene and to understand the main electronic and transport properties of this material, in Chapter 2 we present the *tight-binding* model applied to graphene and perform the continuum limit approximation in order to obtain an effective Hamiltonian valid for a low density of carriers, which allows the analogy with quantum electrodynamics. We also discuss the electronic and tunneling properties of graphene in the presence of square potential barriers and superlattices highlighting the appearance of KT and the emergence of new Dirac points in the energy spectrum.

In Chapter 3 we summarize the electronic properties of phosphorene, from *tight-binding* model to effective mass model, discussing the anisotropy of this material.

The Dirac equation for enlarged pseudospin S which describes the $\alpha - T_3$ lattices and the discussion of the consequences of it in the tunneling transport are performed in Chapter 4 where the SKT is presented.

In Chapter 5 we show how to solve the time-dependent Schrödinger and Dirac equations numerically using the *split-operator* method, giving details about this method, highlighting its efficiency in the analysis of wave packet propagation. In Chapter 6 we calculate the time evolution in BP multilayers and develop the numerical method described in Chapter 5 for BP multilayers, something not yet reported in the literature, enabling the investigation of wave packet evolution in this material as well as the understanding of the relationship between the material's anisotropy and the aforementioned ZBW effect.

In Chapter 7 we investigate theoretically the electronic properties of 2D semiconductor quantum wires (QWs) with anisotropic effective masses and different orientations with respect to the anisotropic axis in the absence of magnetic field and non-null magnetic field. Moreover we apply the *split-operator* method to analyze the wave-packet dynamic in these systems.

In Chapter 8 we apply the method described in Chapter 5 to the modified Dirac equation of graphene, when the momentum operator is rewritten in a generalized form. Moreover we obtain analytical expressions for the eigenstates and Landau levels spectrum in graphene under the presence of a perpendicularly applied magnetic field.

The second objective of this thesis is to analyze the electronic and tunneling properties of $\alpha - T_3$ superlattices to understand how the inclusion of symmetry-breaking terms could affect the band-gap morphing and supress the SKT. In Chapter 9 we investigate the dependency of superlattice mini-bands on the parameter α accounting for different symmetry-breaking terms and show how it affects band gap formation. In Chapter 10 we show that small deviations in the equivalence between the atomic sites, as well as the number of barriers can strongly change the transmission properties in these lattices. Conclusions and perspectives can be found in Chapter 11.

2

Physical properties of graphene

In this chapter we discussed the electronic properties of graphene. We derived the tight-binding approximation followed by the low-energy Hamiltonian obtained from the continuum model. We also discuss the electronic properties of charge carriers in the presence of single- or multiple barriers, where we present the striking effect called KT and the emergence of new Dirac points when a superlattice is considered in graphene.

2.1 Tight-binding approximation
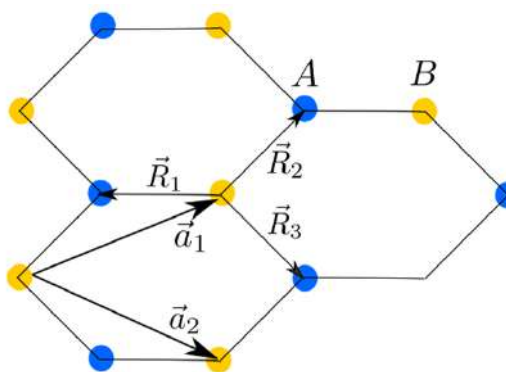
Figure 2.1: The structure of graphene crystal showing two sublattices A (blue dots) and B (yellow dots). The primitive vectors that span the lattice are $\vec{a}_1$ and $\vec{a}_2$, while R_i (with $i = 1, 2, 3$) localizes the nearest neighbors [62].

Initially, we need to define the crystallographic structure of graphene: a crystal structure composed by carbon atoms arranged in a 2D-honeycomb lattice. This graphene structure contains two-sites per unit cell, as shown in Fig. 2.1 This unit cell consists of a superposition of two triangular sublattices denoted by A and B [63]. The crystal structure is formed from the primitive vectors $\vec{a}_1$ and $\vec{a}_2$ given by

$$\vec{a}_1 = \left(\frac{3a}{2}, \frac{a\sqrt{3}}{2} \right) \quad , \quad \vec{a}_2 = \left(\frac{3a}{2}, \frac{-a\sqrt{3}}{2} \right), \tag{2.1}$$

where $a \approx 1.42$Å corresponds to the distance between the carbon sites. From Eqs. (2.1) it is possible to get the vectors of reciprocal space $\vec{b}_1$ and $\vec{b}_2$:

$$\vec{b}_1 = \left(\frac{2\pi}{3a}, \frac{2\pi\sqrt{3}}{3a} \right) \quad , \quad \vec{b}_2 = \left(\frac{2\pi}{3a}, \frac{-2\pi\sqrt{3}}{3a} \right). \tag{2.2}$$

Now we have described the crystallographic structure of graphene and we are able to derive the tight-binding model. In this model it is assumed that wave-functions describing electrons is peaked at the site, indicating electrons are tightly bound to the atom. We are going to consider that electrons just hop between the nearest neighbors. Moreover, we consider π orbitals since the electronic properties of graphene for low-energy excitation are determined by these π bands.

The tight-binding Hamiltonian that describes electrons in graphene considering only the hopping between the nearest-neighbors in second quantization formalism is:

$$H = - \sum_{i,j} \gamma_0 \left(\mathbf{a_i^\dagger b_j} + \mathbf{b_j^\dagger a_i} \right), \tag{2.3}$$

where $\gamma_0 = 2.8$ eV is the hopping parameter [62]. The operator $\mathbf{a_i^\dagger}$ ($\mathbf{a_i}$) creates (annihilates) electrons on the site i of sublattice A. Similarly, $\mathbf{b_j^\dagger}$ ($\mathbf{b_j}$) acts on the j-sites of sublattice B.

Considering an infinity lattice, we define the Fourier transformation of the creation and annihilation operators. In order to do that, we assume:

$$\mathbf{a_i} = \frac{1}{\sqrt{N}} \sum_{k} e^{i\vec{k}\cdot\vec{r}_i} \mathbf{a_k} \quad , \quad \mathbf{a_i^\dagger} = \frac{1}{\sqrt{N}} \sum_{k} e^{-i\vec{k}\cdot\vec{r}_i} \mathbf{a_k^\dagger}, \tag{2.4a}$$

$$\mathbf{b_j} = \frac{1}{\sqrt{N}} \sum_{k'} e^{i\vec{k'}\cdot\vec{r}_j} \mathbf{b_{k'}} \quad , \quad \mathbf{b_j^\dagger} = \frac{1}{\sqrt{N}} \sum_{k}{}' e^{-i\vec{k'}\cdot\vec{r}_j} \mathbf{b_{k'}^\dagger}. \tag{2.4b}$$

Substituting Eqs. (2.4) into Eq. (2.3) the Hamiltonian is rewritten as:

$$H = - \sum_{i,j} \frac{\gamma_0}{N} \left[\sum_{k,k'} e^{-i\vec{k}\cdot\vec{r}_i} e^{-i\vec{k'}\cdot\vec{r}_j} \mathbf{a_k^\dagger b_{k'}} + \sum_{k,k'} e^{-i\vec{k'}\cdot\vec{r}_j} e^{i\vec{k}\cdot\vec{r}_i} \mathbf{a_k b_{k'}^\dagger} \right], \tag{2.5}$$

which takes the form of:

$$H = -\frac{\gamma_0}{N} \sum_{i,j} \sum_{k,k'} \left[e^{-i(\vec{k}-\vec{k'})\cdot\vec{r}_i} e^{-i\vec{k'}\cdot(\vec{r}_j-\vec{r}_i)} \mathbf{a_k^\dagger b_{k'}} + e^{-i(\vec{k'}-\vec{k})\cdot\vec{r}_i} e^{-i\vec{k'}\cdot(\vec{r}_j-\vec{r}_i)} \mathbf{b_{k'}^\dagger a_k} \right]. \tag{2.6}$$

Considering $\vec{r}_j - \vec{r}_i$ the vectors that localize the three nearest neighbors in relation to site A with index i (see Fig. 2.1) as $\vec{R}_1 = (-a, 0)$, $\vec{R}_2 = (a/2, a\sqrt{3}/2)$ and $\vec{R}_3 = (a/2, -a\sqrt{3}/2)$ we have

$$H = -\frac{\gamma_0}{N} \sum_{i} \sum_{k,k'} \left[e^{-i(\vec{k}-\vec{k'})\cdot\vec{r}_i} \mathbf{a_k^\dagger b_{k'}} \left(e^{-ik'_x a} + e^{-ik'_x a/2} e^{-ik'_y \sqrt{3}a/2} + e^{ik'_x a/2} e^{-ik'_y \sqrt{3}a/2} \right) \right.$$
$$\left. + e^{-i(\vec{k'}-\vec{k})\cdot\vec{r}_i} \mathbf{b_{k'}^\dagger a_k} \left(e^{-ik'_x a} + e^{-ik'_x a/2} e^{-ik'_y \sqrt{3}a/2} + e^{-ik'_x a/2} e^{ik'_y \sqrt{3}a/2} \right) \right], \tag{2.7}$$

which is reduced to

$$H = -\gamma_0 \sum_k \left[f(\vec{k}) \mathbf{a_k^\dagger b_k} + f^*(\vec{k}) \mathbf{b_k^\dagger a_k} \right], \tag{2.8}$$

where $f(\vec{k})$ consists of the structure factor of the crystal. Since $|\Psi_k\rangle = (\mathbf{a_k} \quad \mathbf{b_k})^T$ is the electronic state for a given $\vec{k}$, Eq. (2.8) can be written as $H = \langle \Psi_k | H_k | \Psi_k \rangle$, where H_k is a 2×2 matrix representing the Hamiltonian for that $\vec{k}$:

$$H_k = \begin{pmatrix} 0 & -\gamma_0 f(\vec{k}) \\ -\gamma_0 f^*(\vec{k}) & 0 \end{pmatrix}. \tag{2.9}$$

We obtain the eigenvalues of H_k as

$$E_{\pm k} = \pm \gamma_0 |f(\vec{k})| = \pm \gamma_0 \sqrt{3 + g(\vec{k})}, \tag{2.10}$$

with $g(\vec{k}) = 4\cos(3k_x a/2)\cos(k_y a\sqrt{3}/2) + 2\cos(k_y a\sqrt{3})$, and $+ \, (-)$ representing the conduction (valence) band. The electronic band structure found from Eq. (2.10) is depicted in Fig. 2.2(a). We can see that the conduction and valence bands touch at six points where $E(k_x, k_y) = 0$ and the bands are symmetric in relation to this value of energy, which means that there is electron-hole symmetry. These six points are called Dirac points, and their coordinates can be found setting $E(k_x, k_y) = 0 \to f(\vec{k}) = 0$. So,

$$Re[f(k_x, k_y)] = \cos(k_x a) + 2\cos(k_y a\sqrt{3}/2)\cos(k_x a/2) = 0, \tag{2.11a}$$

$$Im[f(k_x, k_y)] = \sin(k_x a) - 2\cos(k_y a\sqrt{3}/2)\sin(k_x a/2) = 0, \tag{2.11b}$$

which leading to

$$\vec{k}_1 = \left(0, \frac{4\pi}{3\sqrt{3}a}\right) \quad , \quad \vec{k}_2 = \left(\frac{2\pi}{3a}, \frac{2\pi}{3\sqrt{3}a}\right) \quad , \quad \vec{k}_3 = \left(\frac{2\pi}{3a}, \frac{-2\pi}{3\sqrt{3}a}\right), \tag{2.12a}$$

$$\vec{k}_4 = \left(0, \frac{-4\pi}{3\sqrt{3}a}\right) \quad , \quad \vec{k}_5 = \left(\frac{-2\pi}{3a}, \frac{-2\pi}{3\sqrt{3}a}\right) \quad , \quad \vec{k}_6 = \left(\frac{-2\pi}{3a}, \frac{2\pi}{3\sqrt{3}a}\right). \tag{2.12b}$$

These points are located at the crystallographic points K and K' in the corner of the first Brillouin zone, as shown in Fig. 2.2(b). Therefore, since the points $\vec{k}_1$, $\vec{k}_2$ and $\vec{k}_6$ ($\vec{k}_3$, $\vec{k}_4$ and $\vec{k}_5$) are associated to the K (K') points connected by the reciprocal lattice, these points are equivalents[1].

2.2 Continuum model

Expanding the Hamiltonian in Eq. (2.9), i.e. $f(k_x, k_y)$ around one of the Dirac points, for example $\vec{k}_3$, and retaining just the first order terms in k_x and k_y we have

$$f(\delta\vec{k}) \approx f(\vec{k}_3) + \frac{\partial f}{\partial k_x}\bigg|_{\vec{k}=\vec{k}_3} (k_x - k_{3x}) + \frac{\partial f}{\partial k_y}\bigg|_{\vec{k}=\vec{k}_3} (k_y - k_{3y}) + \mathcal{O}(\delta k^2). \tag{2.13}$$

---

[1]Due to that, from now on we restrict in this thesis to H_K.
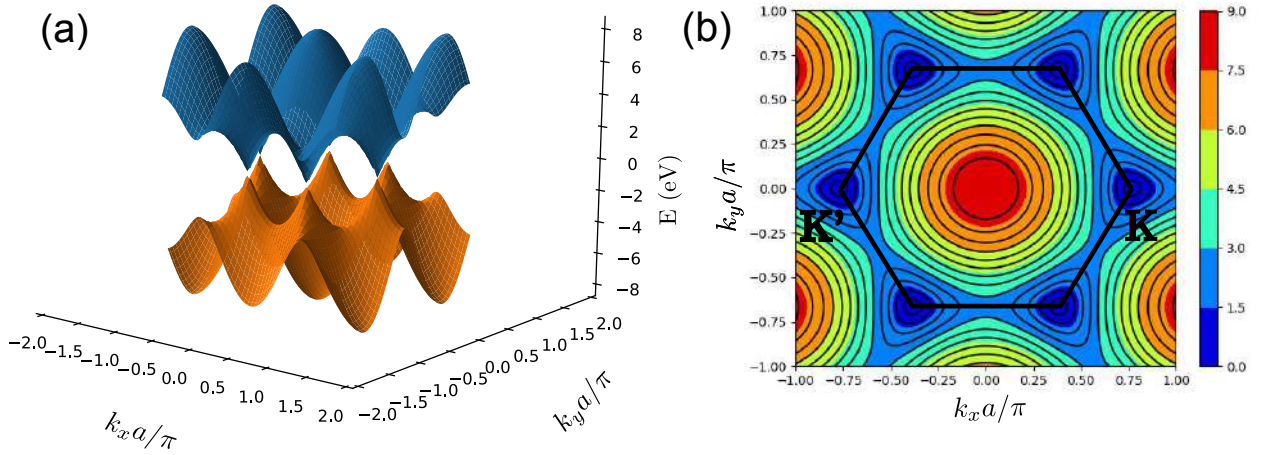
Figure 2.2: (a) The electronic bands of graphene obtained by the *tight-binding* approximation, (b) the contour plot of the conduction band indicating the Dirac points K and K'.

After evaluating Eq. (2.13) we obtain:

$$f(\delta \vec{k}) \approx \frac{3a}{2}(k_x - ik_y)e^{-i5\pi/6}, \tag{2.14}$$

where the complex exponential can be incorporated as a phase into the wave functions, since its norm is one. Thus, the effective Hamiltonian near the point $\vec{k}_3(K)$ is

$$H_K = \begin{pmatrix} 0 & \hbar v_{\mathrm{F}}(k_x - ik_y) \\ \hbar v_{\mathrm{F}}(k_x + ik_y) & 0 \end{pmatrix}, \tag{2.15}$$

with $\hbar v_{\mathrm{F}} = 3a\gamma_0/2$. Note that the Hamiltonian in Eq. (2.15) has the same form as the Dirac Hamiltonian that describes relativistic particles with a zero mass, but in this case the light velocity c is replaced by the Fermi velocity $v_{\mathrm{F}} \approx 10^6$ m/s [64]. The similarity between ultra-relativistic particles and electrons in graphene makes it a promising material to investigate relativistic effects such as KT which will be considered in the next session. The Hamiltonian in Eq. (2.15) can be rewritten in a succinct way as:

$$H_K = v_{\mathrm{F}}\boldsymbol{\sigma} \cdot \mathbf{p}, \tag{2.16}$$

where $\boldsymbol{\sigma}$ are the Pauli matrices given by:

$$\sigma_x = \begin{pmatrix} 0 & 1 \\ 1 & 0 \end{pmatrix}, \quad \sigma_y = \begin{pmatrix} 0 & -i \\ i & 0 \end{pmatrix}, \quad \sigma_z = \begin{pmatrix} 1 & 0 \\ 0 & 1 \end{pmatrix}. \tag{2.17}$$

In the Dirac approach, which describes relativistic particles without mass, the Pauli matrices are related to the spin degree of freedom [64]. However, in this case the Pauli matrices arise as a consequence of the crystallographic structure of graphene. This is the reason why $\boldsymbol{\sigma}$ is called *pseudospin*, and the eigenstate of Eq. (2.15) given by $|\Psi_K\rangle = (\psi_A, \psi_B)$ is

called *pseudospinor* and consists of the components describing the distribution of electrons in sublattices A and B, so that *pseudospin* "up"("down") means sublattice $A(B)$. By diagonalizing the Hamiltonian in Eq. (2.15) we find a linear energy spectrum $E = \pm \hbar v_{\mathrm{F}} k$ and the eigenstates are

$$\left| \Psi_K^{\pm} \right\rangle = \frac{1}{\sqrt{2}} \begin{pmatrix} 1 \\ \pm e^{i\theta} \end{pmatrix}, \tag{2.18}$$

with $\theta = \tan^{-1}(k_y/k_x)$.

Performing the same approximation of Eq. (2.13) but around the $K'(\vec{k}_6)$ point we find

$$H_{k'} = v_{\mathrm{F}} \boldsymbol{\sigma}^* \cdot \mathbf{p}, \tag{2.19}$$

with the eigenstates

$$\left| \Psi_{K'}^{\pm} \right\rangle = \frac{1}{\sqrt{2}} \begin{pmatrix} 1 \\ \pm e^{-i\theta} \end{pmatrix}. \tag{2.20}$$

Thus, the Hamiltonian that describes the low-energy electronic excitation in graphene, i.e around the points K and K' is given by a 2×2 block matrix:

$$H_{K,K'} = \begin{pmatrix} v_{\mathrm{F}} \boldsymbol{\sigma} \cdot \mathbf{p} & 0 \\ 0 & v_{\mathrm{F}} \boldsymbol{\sigma}^* \cdot \mathbf{p} \end{pmatrix}, \tag{2.21}$$

with eigenvalues $E = \pm \hbar v_{\mathrm{F}} k$ and eigenstates $|\Psi\rangle = (\Psi_K, \Psi_{K'}) = (\psi_A, \psi_B, \psi_C, \psi_D)^T$. For the case of ideal graphene the off-diagonal terms scatter electrons from K to K' and viceversa, which are called valleys, are decoupled and they are said to be *valley degenerate*.

In summary, we have just demonstrated that, when considering low-energy electrons, the problem of an electron under the influence of the carbon atoms in an infinite lattice that make up graphene becomes equivalent to the problem of a massless free quasi-particle obeying the Dirac equation, and as mentioned previously this results in peculiar effects such as KT.

2.3 Dirac fermions in graphene and Klein-tunneling

The existence of transmission of a quantum particle even with a tiny probability through a classically forbidden region is usually obtained from the Schrödinger equation [65, 66, 64] and known as quantum tunneling. Unlike expected from the point of view of classical particles dynamics, particles could create a "tunnel" such they could traverse a potential barrier that is higher than their kinetic energy. In this case, the tunneling of a particle can be said to arise due to the coupling of the propagating solutions of Schrödinger equation at either side of the potential barrier with decaying solutions in the barrier region, leading to non-zero transmission probability.

Nonetheless, the advent of a covariant relativist version of quantum mechanics developed by Dirac in 1928 [67] led to several important discoveries such as the prediction

of particles with negative energies. One consequence of this theory was recognized by Klein [68], which predicted that regardless of the height and the width of the barrier, for a certain range of energies, the transmission probability for a single square barrier could reach 1. This effect has been know as *Klein-paradox* or KT and it is due to the overlap between positive and negative energy states outside and inside the barriers [69].

Multiple experiments were made in order to detect KT but since very large fields are required to detect the tunneling of relativistic particles, many difficulties were faced. However the development and fabrication of monolayer graphene [70, 71], where a similar effect, though for 2D massless Dirac electrons, has been predicted [8, 72, 73] and evidences of its observation were reported [74, 75, 76, 77].

It is important to highlight that the KT observed in graphene, which we will discuss now, is not a tunnel effect in the usual quantum mechanical sense and there is no paradox in this case. Indeed we will demonstrate that the unusual tunneling behaviour of massless Dirac particles in graphene is a consequence of pseudospin conservation [8, 78, 79].

2.3.1 Conservation of pseudospin and the absence of backscattering

We now demonstrate that the absence of backscattering of massless Dirac fermions normally incident on a potential $V(x)\hat{I}$, where $\hat{I}$ is the unit matrix, is a consequence of the conservation of their pseudospin σ_x along the x direction.

Including an external translational invariant potential $V(x) = V_0$ in the y direction in the Hamiltonian, Eq.(2.15), it reads

$$\hat{H} = k_x \sigma_x + k_y \sigma_y + V(x)\hat{I}. \tag{2.22}$$

The velocity operator along the x direction according to Heisenberg equation is

$$\hat{v}_x = -i\hbar[x, \hat{H}] = \begin{pmatrix} 0 & 1 \\ 1 & 0 \end{pmatrix} = \sigma_x, \tag{2.23}$$

where we assume $\hbar = 1$. So, the time evolution of $\hat{v}_x$ is

$$\dot{\hat{v}}_x = -i[\hat{v}_x, \hat{H}] = -i[\sigma_x, \hat{H}]. \tag{2.24}$$

Eq. (2.24) can be written as

$$\dot{\hat{v}}_x = -i \begin{pmatrix} 2ik_y & 0 \\ 0 & -2ik_y \end{pmatrix} = 2\sigma_z k_y. \tag{2.25}$$

Since we consider the translational invariance along the y direction, $\dot{k}_y = -i[k_y, \hat{H}] = 0$, so $k_y(t) = k_y(0)$. If the initial state of the electron $|\psi(0)\rangle$ is an eigenstate of zero momentum in the y direction $k_y(0)|\psi(0)\rangle = 0$, i.e. the electron is initially perpendicular to the potential interface, then at time $t > 0$ we have

$$\langle\psi(t)|\dot{\hat{v}}_x|\psi(t)\rangle = 2\langle\psi(t)|\sigma_z k_y|\psi(t)\rangle = 2\langle\psi(0)|\sigma_z k_y|\psi(0)\rangle = 0, \tag{2.26}$$

which means that $\hat{v}_x$ is a constant of the motion. Therefore, the electron normally incident on a translational invariant potential is perfectly transmitted and its motion is exactly the same as in the absence of the potential. This has important physical consequences on the transport properties of massless Dirac electrons, such as the perfect transmission of charge carriers through barriers at normal incidence [78], as we are going to demonstrate now.

Let us consider a square potential barrier $V(x, y) = V(x)$ as depicted in Fig. 2.3. This system consists of three regions: region I: $x < 0$ ($V(x) = 0$), region II: $0 < x < d$ ($V(x) = V_0$) and region III: $x > 0$ ($V(x) = 0$). The waves-function for each region are determined using Eq. (2.18), and they are

$$\psi_I = e^{ik_y y} \left[e^{ik_x x} \begin{pmatrix} 1 \\ e^{i\theta_w} \end{pmatrix} + r e^{-ik_x x} \begin{pmatrix} 1 \\ -e^{-i\theta_w} \end{pmatrix} \right], \tag{2.27a}$$

$$\psi_{II} = e^{ik_y y} \left[A e^{iq_x x} \begin{pmatrix} 1 \\ -e^{i\theta_b} \end{pmatrix} + B e^{-iq_x x} \begin{pmatrix} 1 \\ -e^{-i\theta_b} \end{pmatrix} \right], \tag{2.27b}$$

$$\psi_{III} = t e^{ik_y y} e^{ik_x x} \begin{pmatrix} 1 \\ e^{i\theta_w} \end{pmatrix}, \tag{2.27c}$$
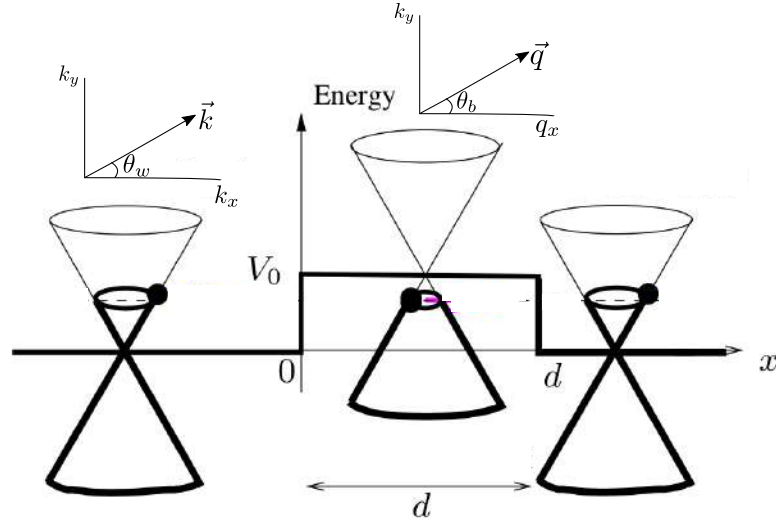
Figure 2.3: Band structure across a square potential barrier with width d and height of potential $V(x) = V_0$. The wave-vectors inside and outside of the barrier are denoted by $\vec{k}$ and $\vec{q}$. Dirac cones are superposed on the potential barrier.

where A and B are determinedby continuity of the wave-function at the potential edges, the transmission T and reflection R probabilities are obtained from $T = |t|^2$ and $R = |r|^2$ respectively. The angles $\theta_w = \tan^{-1}(k_y/k_w)$ ($\theta_b = \tan^{-1}(k_y/k_w)$) correspond to the angle between the wave vector $\vec{k} = (k_x, k_y)$ outside ($\vec{q} = (q_x, k_y)$ inside) of barrier and the x axis (see Fig. 2.3). Moreover, the wave vectors in the x direction outside and inside of potential are $k_x = E/\hbar v_F - k_y^2$ and $q_x = \sqrt{(E - V_0)^2/\hbar^2 v_F^2 - k_y^2}$.

The continuity of wave function is used in $x = 0$ and $x = d$ leading to the following system of equations:

$$1 + r = A + B, \tag{2.28a}$$

$$e^{i\theta_w} - re^{-i\theta_w} = -Ae^{i\theta_b} + Be^{-i\theta_b}, \tag{2.28b}$$

$$Ae^{iq_xd} + Be^{-iq_xd} = te^{ik_xd}, \tag{2.28c}$$

$$-Ae^{iq_xd}e^{i\theta_b} + Be^{-iq_xd}e^{-i\theta_b} = te^{ik_xd}e^{i\theta_w}. \tag{2.28d}$$

Solving this system by substitution, we get the transmission probability T as [8]:

$$T = \frac{\cos^2\theta_w \cos^2\theta_b}{\cos^2\theta_w \cos^2\theta_b \cos^2(q_xd) + \sin^2(q_xd)[1 + \sin\theta_b \sin\theta_w]^2}, \tag{2.29}$$

where $q_xd = 2\pi L\sqrt{1 - 2\varepsilon + \varepsilon^2\cos^2\theta_w}$ with the dimensionless barrier width $L = V_0d/2\pi\hbar v_\mathrm{F}$ and dimensionless energy $\varepsilon = E/V_0$. In the limit of high barriers $|V_0| >> E$, the expression for T can be simplified to

$$T = \frac{\cos^2\theta_w}{1 - \cos^2(q_xd)\sin^2\theta_w}. \tag{2.30}$$

Examples of the angular dependence of transmission probability using Eq. (2.29) is shown in Fig. 2.4. We note that if the incident angle is zero, the barrier is fully transparent and the transmission is total. This perfect transmission at normal incidence known as KT, as discussed previously, is due to the conservation of the pseudospin leading to the absence of backscattering. Furthermore, for oblique incidences ($\theta_w \neq 0$) and low energies, the incoming waves might interfere itself between the two interfaces $x = 0$ and $x = d$ originating multiples resonances in the transmission, as observed in Fig. 2.4 [8, 78][2].

2.4 Superlattices in graphene and the emergence of new Dirac points

Another interesting system to consider is the application of a periodic potential to graphene, i.e. a superlattice, which under certain conditions leads to the appearance of extra points where the conduction and valence bands touch each other (zero modes or Dirac points) in the energy spectrum [80, 81, 82, 83, 84]. Additionally, Ref. [80] discusses

---

[2]These multiples resonances in the transmission of Dirac fermions in graphene through square barriers are called *Fabry-Pérot resonances*, an effect analogous to the optical system Fabry-Pérot interferometer, where inside of it oscillating waves are able to interfere between them resulting in resonances.
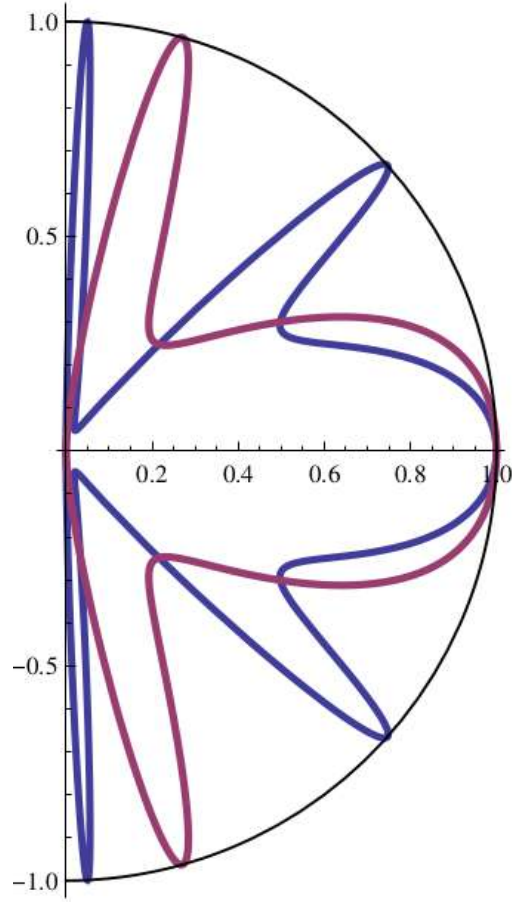
Figure 2.4: Polar plot of the transmission coefficient T for the square barrier potential at fixed energy $\varepsilon = 0.41519$ and width $L = 4.85$ (blue line), and $\varepsilon = 0.291038$, $L = 6.91$ (purple line). The petal structure is clearly seen and correspond to Fabry-Pérot resonances [78].

which conditions lead to the emergence of extra Dirac points and the renormalization of group velocity around them.

In this section we are going to discuss the electronic properties of charge carriers in superlattices of graphene from the dispersion relation for an infinite series of square barriers.

Let us start by considering an infinite number of periodically spaced barriers, as shown in Fig. 2.5, with the width of unit cell $L = W_b + W_w$, where W_w and W_b are the width of well ($V(x) = -V_0/2$) and barrier ($V(x) = V_0/2$) region, respectively. Since the potential is applied along the x direction, the Hamiltonian that describes the Dirac fermions in this system is given by Eq. (2.22). The wave-functions $\Psi(x, y) = \psi_j(x)e^{ik_y y}$ where $j = w(b)$ used to denote the wave-function outside (inside) of the barrier are

$$\psi_j(x) = A_j \begin{pmatrix} 1 \\ e^{i\theta_j} \end{pmatrix} e^{ik_j x} + B_j \begin{pmatrix} 1 \\ -e^{-i\theta_j} \end{pmatrix} e^{-ik_j x}, \tag{2.31}$$

with the wave-vectors $k_j = k_w$ and $k_j = k_b$ representing the wave-vectors in the well and barrier, respectively. The angle between them and the x direction are $\theta_w = \tan^{-1}(k_y/k_w)$,

and $\theta_b = \tan^{-1}(k_y/k_b)$.
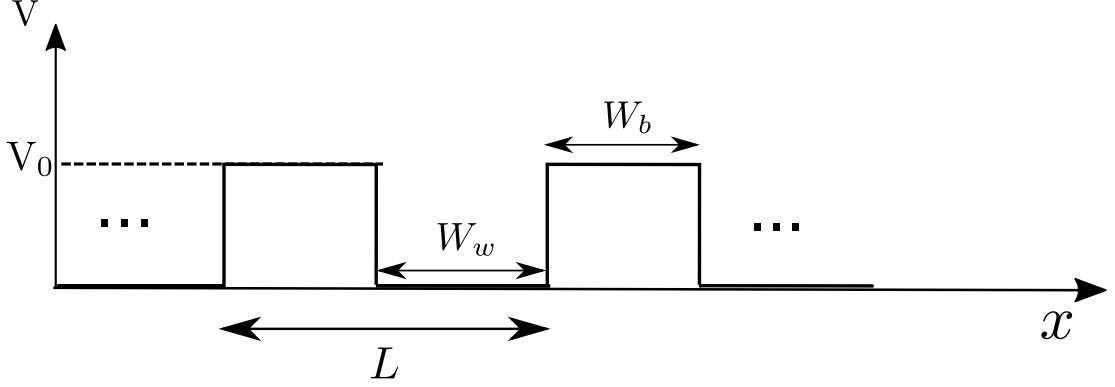
Figure 2.5: Schematics of the superlattice potential $V(x) = V_0$ consisting of square barriers with width W_b and wells with width W_w.

The wave-function of this periodic system is a Bloch function and the transfer matrix T leads an expression for the dispersion relation. The transfer matrix can be written as [85]

$$T = \Omega_{k_w}(L)\Omega_{k_w}^{-1}(W_b)\Omega_{k_b}(W_b)\Omega_{k_b}^{-1}(0), \tag{2.32}$$

where the terms $\Omega_{k_j}(x)$ are obtained from the continuity of wave-function in the interface between well and barrier:

$$\Omega_j(x) = \begin{pmatrix} e^{ik_j x} & e^{-ik_j x} \\ \lambda_j e^{ik_j x} & -\lambda_j^* e^{ik_j x} \end{pmatrix}, \tag{2.33}$$

with $\lambda_j = (k_j + ik_y)\hbar v_{\mathrm{F}}/E_j$, where $E_j = E_w$ or $E_j = E_b$:

$$E_w = E + V_0/2 \qquad , \qquad E_b = E - V_0/2. \tag{2.34}$$

For simplicity, we introduce the dimensionless variables: $\epsilon = EL/\hbar v_{\mathrm{F}}$, $u(x) = u = V_0/L\hbar v_{\mathrm{F}}$, $W_b \to W_b L$, $W_w \to 1 - W_b/L$, $k_w \to k_w L$, $k_b \to k_b L$, $k_y \to k_y L$, $K_x \to K_x L$, where K_x is related to the periodicity of the system. So, the energies in Eq. (2.34) become:

$$\epsilon_w = \epsilon + uW_b \qquad , \qquad E = \epsilon - uW_w. \tag{2.35}$$

Developing the transfer matrix in Eq. (2.32) and using Bloch's theorem $\cos(K_x) = T_{11} + T_{22}/2$, we obtain the equation that determines the dispersion relation for the super-lattice in graphene as:

$$\cos(K_x) = \cos(k_w W_w)\cos(k_b W_b) + G\sin(k_w W_w)\sin(k_b W_b), \tag{2.36}$$

where

$$G = (\epsilon_w \epsilon_b - k_y^2)/k_w k_b, \tag{2.37}$$

with $k_w = \sqrt{\epsilon_w^2 - k_y^2}$ and $k_b = \sqrt{\epsilon_b^2 - k_y^2}$.

The location of Dirac points when $W_w = W_b = 1/2$ (symmetric case) in the energy spectrum could be determined assuming $\epsilon = 0$ ($k_w = k_b$) at $K_x = 0$ in Eq. (2.36), leading to:

$$\cos^2 k_w/2 + \left[\frac{u^2/4 + k_y^2}{u^2/4 - k_y^2}\right] \sin^2 k_w/2 = 1. \tag{2.38}$$

Note that Eq. (2.38) has real solution when $(u^2/4 + k_y^2)/(u^2/4 - k_y^2) = 1$, and therefore when $k_y = 0$, corresponding to the usual Dirac point. The other possibility for a real solution is when $\sin^2 k_w/2 = 0$, corresponding to the condition of the emergence of extra Dirac points, which are located along the k_y axis following the relation:

$$k_{y,m} = \sqrt{\frac{u^2}{4} - 4\pi^2 m^2}. \tag{2.39}$$
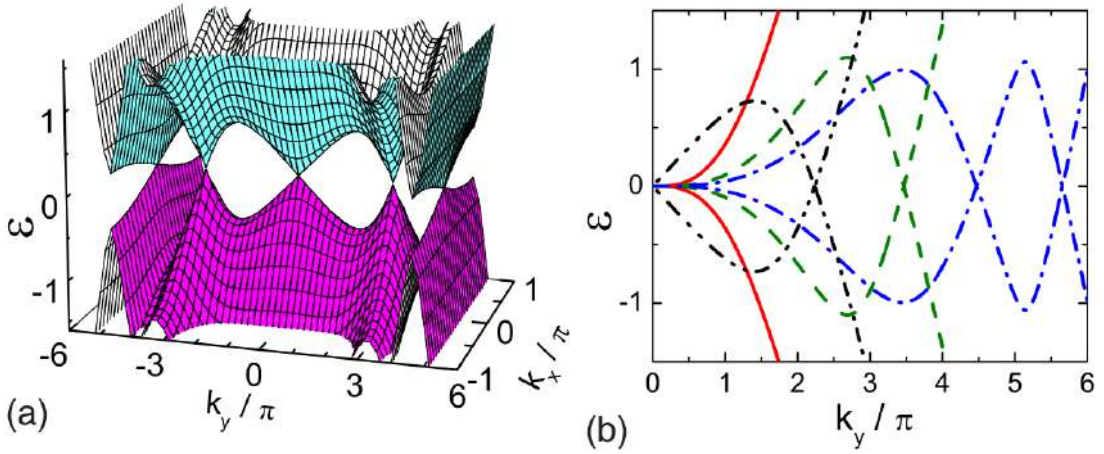
Figure 2.6: (a) Valence and conduction bands of the spectrum of a superlattice assuming square barriers of width $W_b = 1/2$ and height $u = 10\pi$. (b) Slices of the superlattice spectrum along k_y for fixed $W_b = 0.5$ and $K_x = 0$. The solid red, dot-dot-dashed black, dashed green, and dash-dotted blue curves are for different values of the barrier height such that $u/2 = 2\pi, 3\pi, 4\pi$, and 6π, respectively [80].

The energy spectra of a superlattice in graphene at $K_x = 0$ along k_y axis assuming $W_b = W_w = 0.5$ and different values of potential $u(x) = u = 4\pi, 6\pi, 8\pi, 12\pi$ are shown in Fig. 2.6(a). We can observe that for values of the potential u proportional to 4π new Dirac points are generated and the dispersion relation around them becomes almost flat along k_y direction, indicating the collimation of electrons [80, 86, 87, 88]. Moreover, unlike the usual Dirac point at $k_y = 0$, the extra Dirac cones are no longer symmetric and the slope is renormalized [80], as depicted in Fig. 2.6(b), where we show the conduction and valence bands of the superlattice when $W_b = W_w = 0.5$ and $u = 6\pi$.

Therefore, the emergence of new Dirac points can be controlled by adjusting the hight and width of the potential [80, 83, 89, 84]. The presence of extra Dirac points

in graphene leads to strong consequences in the transport properties in this material like enhancement of the conductivity [83]. Nonetheless, the appearance of these new zero modes are robust against the structural disorder in the crystal structure [84]. They were recent experimentally detected by using the technique of dielectric patterning [90], where the transport response was measured when a current was applied both parallel and perpendicular to the superlattice [91]. The appearance of extra Dirac points using this techinique is represented in Fig. 2.7.
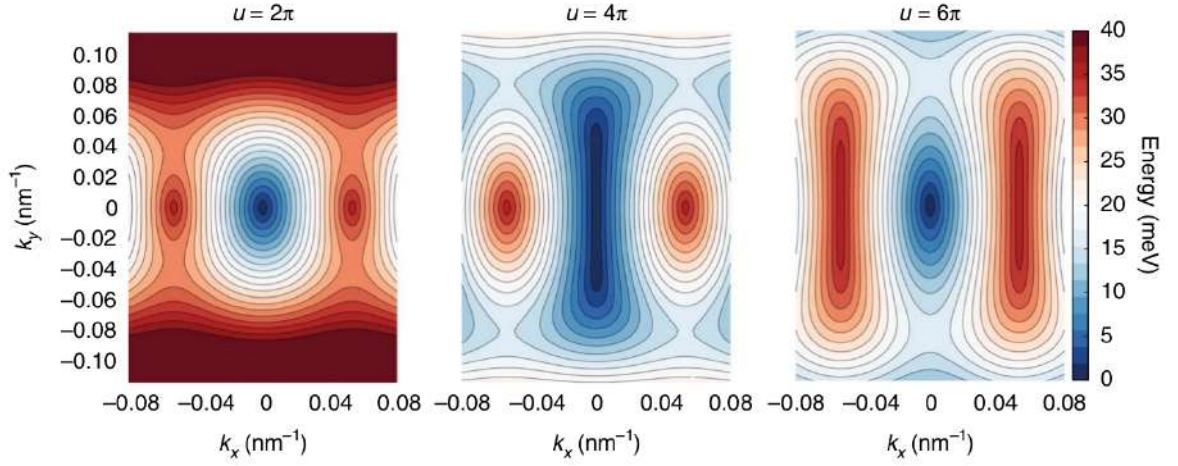
Figure 2.7: Contour plots of the first conduction band showing the main DP ($k_x = 0$) and the first extra Dirac points ($k_x \neq 0$) for $u = 2\pi, 4\pi$, and 6π [91].

Physical properties of phosphorene

In this chapter we obtained the energy spectrum of phosphorene using the *tight-binding* approximation, and we found an energy spectrum with four energy bands. We develop the continuum approximation for the two energy bands closest to the Fermi level (Γ region), which we verify to be anisotropic around the Γ region by means of the effective mass approximation.

3.1   Tight-binding approximation

The Hamiltonian which describes particles in a monolayer phosphorene was proposed in Ref. [40], and given by

$$H = \sum_i \epsilon_i n_i + \sum_{i \neq j} t_{ij} c_i^\dagger c_j, \tag{3.1}$$

where ϵ_i is the energy of the site i, n_i is the number operator, t_{ij} is the integral of *hopping* between the sites i and j and the electron state creation and annihilation operators are respectively represented by $c^\dagger$ and c. Phosphorene, unlike graphene, has four sublattices denoted by A, B, C and D. Taking the sublattice A as the origin of the system and developing the *hopping* terms in Eq. (3.1), we have

$$H = \sum_i \epsilon_i n_i + \sum_{i \neq j} \left(t_{ij}^b b_i^\dagger a_j + t_{ij}^c c_i^\dagger a_j + t_{ij}^d d_i^\dagger a_j \right) + h \cdot c. \tag{3.2}$$

The terms $b^\dagger, c^\dagger$ and $d^\dagger$ are, respectively, the creation operators in the sublattices B, C and D, a_j the destruction operator in the sublattice A and the conjugate terms represented by the product $h \cdot c$. The terms $b_i^\dagger a_j, c_i^\dagger a_j, d_i^\dagger a_j$ indicate which electron states are being respectively annihilated in A and created in B, C and D. In Fig. 3.1 are indicated the five *hopping* parameters that are used in the *tight-binding* approximation.

Assuming that the crystal lattice is periodic and infinite, we can rewrite the creation and annihilation terms of each site as Fourier transforms

$$a_i = \frac{1}{\sqrt{N}} \sum_k e^{i\mathbf{K} \cdot \mathbf{r_i}} a_k, \qquad b_i^\dagger = \frac{1}{\sqrt{N}} \sum_{k'} e^{i\mathbf{K'} \cdot \mathbf{r_i}} b_{k'}^\dagger, \tag{3.3a}$$
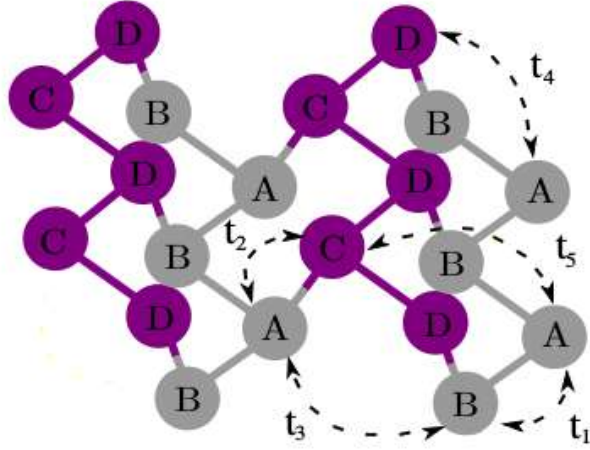
Figure 3.1: Schematic figure of the crystal structure of phosphorene with the five *hopping* parameters [92].

$$c_i^\dagger = \frac{1}{\sqrt{N}} \sum_k e^{-i\mathbf{K}''\cdot\mathbf{r_i}} c_{k''}^\dagger, \qquad d_i^\dagger = \frac{1}{\sqrt{N}} \sum_{k'''} e^{-i\mathbf{K}'''\cdot\mathbf{r_i}} d_{k'''}^\dagger. \tag{3.3b}$$

Denoting the second sum in the Hamiltonian of Eq. (3.2) as H' and using the Fourier transforms indicated in Eq. (3.3), the term H' is rewritten as

$$H' = \frac{1}{N} \sum_{kk'} \sum_{i,j} t_{ij}^b e^{-i(\mathbf{k}-\mathbf{k}')\cdot\mathbf{r_j}} e^{i\mathbf{k}'\cdot\delta_{\mathbf{ji}}} b_{k'}^\dagger a_k + \frac{1}{N} \sum_{kk''} \sum_{i,j} t_{ij}^c e^{-i(\mathbf{k}-\mathbf{k}'')\cdot\mathbf{r_j}} e^{i\mathbf{k}''\cdot\delta_{\mathbf{ji}}} c_{k'}^\dagger a_k$$
$$+ \frac{1}{N} \sum_{kk'''} \sum_{i,j} t_{ij}^d e^{-i(\mathbf{k}-\mathbf{k}''')\cdot\mathbf{r_j}} e^{i\mathbf{k}'''\cdot\delta_{\mathbf{ji}}} d_{k'''}^\dagger a_k. \tag{3.4}$$

Using the following definitions to eliminate the sum in j of Eq. (3.4):

$$\delta(k - k') = \frac{1}{N} \sum_j e^{-i(\mathbf{k}-\mathbf{k}')\cdot\mathbf{r_j}}, \tag{3.5a}$$

$$\delta(k - k'') = \frac{1}{N} \sum_j e^{-i(\mathbf{k}-\mathbf{k}'')\cdot\mathbf{r_j}}, \tag{3.5b}$$

$$\delta(k - k''') = \frac{1}{N} \sum_j e^{-i(\mathbf{k}-\mathbf{k}''')\cdot\mathbf{r_j}}, \tag{3.5c}$$

we obtain the final expression for H' in terms of the five *hopping* parameters after replacing Eq. (3.5) into Eq. (3.4)

$$H' = \sum_k \sum_i \left(t_i^b e^{i\mathbf{k}\cdot\delta_{\mathbf{i}}^{\mathbf{b}}} b_k^\dagger a_k + t_i^c e^{i\mathbf{k}\cdot\delta_{\mathbf{i}}^{\mathbf{c}}} c_k^\dagger a_k + t_i^d e^{i\mathbf{k}\cdot\delta_{\mathbf{i}}^{\mathbf{d}}} d_k^\dagger a_k \right). \tag{3.6}$$

Figure 3.2 shows the distance and angles between the first neighbors of the A site. From these parameters we can find expressions for t_1 and t_3 represented, respectively by

δ_1^b, δ_2^b and δ_3^b, δ_4^b , which consist of the positions from sublattice B, where electrons are created, in relation to the sublattice A, where electrons are annihilated. Similarly, the parameters t_2 and t_5 are represented by δ_1^c and δ_2^c which are the positions of sublattice C, where electrons are created, in relation to the sublattice A. Moreover, t_5 is represented by $\delta_1^d, \delta_2^d, \delta_3^d, \delta_4^d$ corresponding to the position of sublattice D in relation to sublattice A. Taking into account the considerations made above and based on Fig. 3.2, then we have
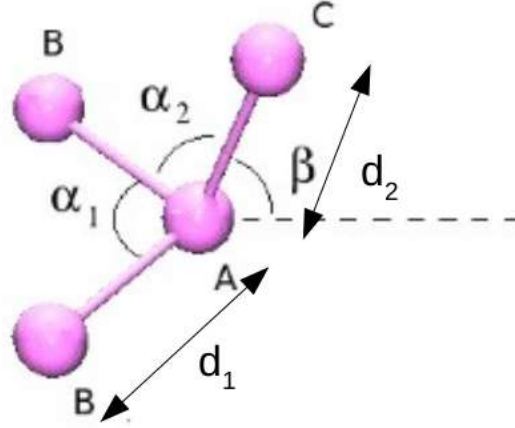
Figure 3.2: Representation of the first neighbors in the crystal lattice of phosphorene with their respective position vectors with respect to atomic site A [93].

$$
\begin{align}
\delta_1^b &= d_1 \sin\left(\alpha_1/2\right)\hat{x} - d_1 \cos\left(\alpha_1/2\right)\hat{y}, \tag{3.7a}\\
\delta_2^b &= -d_1 \sin\left(\alpha_1/2\right)\hat{x} - d_1 \cos\left(\alpha_1/2\right)\hat{y}, \tag{3.7b}\\
\delta_3^b &= d_1 \sin\left(\alpha_1/2\right)\hat{x} + \left(2d_2 \cos\beta + d_1 \cos\left(\alpha_1/2\right)\right)\hat{y}, \tag{3.7c}\\
\delta_4^b &= -d_1 \sin\left(\alpha_1/2\right)\hat{x} + \left(2d_2 \cos\beta + d_1 \cos(\alpha_1/2)\right)\hat{y}, \tag{3.7d}\\
\delta_1^c &= d_2 \cos\beta\hat{y} + d_2 \sin\beta\hat{z}, \tag{3.7e}\\
\delta_2^c &= -\left[d_1 \cos\left(\alpha_1/2\right) + d_2 \cos\beta\right]\hat{y} + d_2 \sin\beta\hat{z}, \tag{3.7f}\\
\delta_1^d &= d_1 \sin\left(\alpha_1/2\right)\hat{x} + \left(d_1 \cos\left(\alpha_1/2\right) + d_2 \cos\beta\right)\hat{y} + d_2 \sin\beta\hat{z}, \tag{3.7g}\\
\delta_2^d &= -d_1 \sin\left(\alpha_1/2\right)\hat{x} + \left(d_1 \cos\left(\alpha_1/2\right) + d_2 \cos\beta\right)\hat{y} + d_2 \sin\beta\hat{z}, \tag{3.7h}\\
\delta_3^d &= d_1 \sin\left(\alpha_1/2\right)\hat{x} - \left(d_1 \cos\left(\alpha_1/2\right) + d_2 \cos\beta\right)\hat{y} + d_2 \sin\beta\hat{z}, \tag{3.7i}\\
\delta_4^d &= -d_1 \sin\left(\alpha_1/2\right)\hat{x} - \left(d_1 \cos\left(\alpha_1/2\right) + d_2 \cos\beta\right)\hat{y} + d_2 \sin\beta\hat{z}. \tag{3.7j}
\end{align}
$$

Since each term of the integral of *hopping* are associated to the distances as follow:

$$
\begin{cases}
t_1 \rightarrow \delta_1^b; \delta_2^b;\\
t_2 \rightarrow \delta_1^c;\\
t_3 \rightarrow \delta_3^b; \delta_4^b;\\
t_4 \rightarrow \delta_1^d; \delta_2^d; \delta_3^d, \delta_4^d;\\
t_5 \rightarrow \delta_2^c,
\end{cases} \tag{3.8}
$$

we can replace the relations given by Eq. (3.8) into Eq. (3.6), which leads to

$$\sum_i t_i^b e^{i\mathbf{k}\cdot\delta_\mathbf{i}^\mathbf{b}} = t_1\left(e^{i\mathbf{k}\cdot\delta_\mathbf{1}^\mathbf{b}} + e^{i\mathbf{k}\cdot\delta_\mathbf{2}^\mathbf{b}}\right) + t_3\left(e^{i\mathbf{k}\cdot\delta_\mathbf{3}^\mathbf{b}} + e^{i\mathbf{k}\cdot\delta_\mathbf{4}^\mathbf{b}}\right) = \mathcal{U}_{AB}, \quad (3.9a)$$

$$\sum_i t_i^c e^{i\mathbf{k}\cdot\delta_\mathbf{i}^\mathbf{c}} = t_2 e^{i\mathbf{k}\cdot\delta_\mathbf{1}^\mathbf{c}} + t_5 e^{i\mathbf{k}\cdot\delta_\mathbf{2}^\mathbf{c}} = \mathcal{U}_{AC}, \quad (3.9b)$$

$$\sum_i t_i^d e^{i\mathbf{k}\cdot\delta_\mathbf{i}^\mathbf{d}} = t_4\left(e^{i\mathbf{k}\cdot\delta_\mathbf{1}^\mathbf{d}} + e^{i\mathbf{k}\cdot\delta_\mathbf{2}^\mathbf{d}} + e^{i\mathbf{k}\cdot\delta_\mathbf{3}^\mathbf{d}} + e^{i\mathbf{k}\cdot\delta_\mathbf{4}^\mathbf{d}}\right) = \mathcal{U}_{AD}. \quad (3.9c)$$

Using Eqs. (3.7) in Eqs. (3.9), the terms δ_i^j in the z direction cancel each other, due to the product with $\vec{k} = (k_x, k_y)$. Making these same procedures but considering the sublattices C and D as origin of the system[1], the Hamiltonian in Eq. (3.2) takes the matrix form

$$H = \begin{pmatrix} \epsilon_A & \mathcal{U}_{AB} & \mathcal{U}_{AC} & \mathcal{U}_{AD} \\ \mathcal{U}_{AB}^* & \epsilon_B & \mathcal{U}_{AC}^* & \mathcal{U}_{AD}^* \\ \mathcal{U}_{AD} & \mathcal{U}_{AC} & \epsilon_D & \mathcal{U}_{AB} \\ \mathcal{U}_{AC}^* & \mathcal{U}_{AD} & \mathcal{U}_{AB}^* & \epsilon_C \end{pmatrix}, \quad (3.10)$$

where the terms $\mathcal{U}_{AB}, \mathcal{U}_{AC}$ and $\mathcal{U}_{AD}$ are

$$\mathcal{U}_{AB} = \cos\left(k_x d_1 \sin\left(\alpha_1/2\right)\right)\left[2t_1 e^{-ik_y d_1 \cos(\alpha_1/2)} + 2t_3 e^{ik_y(2d_2\cos\beta + d_1\cos(\alpha_1/2))}\right] (3.11a)$$

$$\mathcal{U}_{AC} = t_2 e^{ik_y d_2 \cos\beta} + t_5 e^{-ik_y(2d_1\cos(\alpha_1/2)+d_2\cos\beta)}, \quad (3.11b)$$

$$\mathcal{U}_{AD} = 4t_4 \cos\left(k_x d_1 \sin\left(\alpha_1/2\right)\right)\left[\cos k_y\left(d_1\cos\left(\alpha_1/2\right) + d_2\cos\beta\right)\right]. \quad (3.11c)$$

Since all atoms of the crystal are atoms of phosphorus we consider $\sum_i \epsilon_i = \epsilon$, and we obtain the following matrix of *tight-binding* approximation for phosphorene

$$H = \begin{pmatrix} \epsilon & \mathcal{U}_{AB} & \mathcal{U}_{AC} & \mathcal{U}_{AD} \\ \mathcal{U}_{AB}^* & \epsilon & \mathcal{U}_{AC}^* & \mathcal{U}_{AD}^* \\ \mathcal{U}_{AD} & \mathcal{U}_{AC} & \epsilon & \mathcal{U}_{AB} \\ \mathcal{U}_{AC}^* & \mathcal{U}_{AD} & \mathcal{U}_{AB}^* & \epsilon \end{pmatrix}. \quad (3.12)$$

In order to obtain the eigenenergies of Eq. (3.12), we reduce the matrix (3.12) into two 2×2 matrices since the sublattices A and D are symmetric, as depicted in Figure 3.3, where each term of these two sub-matrices provide a pair of energy bands. To do that, we start by considering that the eigenstate for the matrix in Eq. (3.12) has the general form $\psi = (\phi_A, \phi_B, \phi_D, \phi_C)$, and the eigenvalue equation is given by

$$\begin{pmatrix} \epsilon & \mathcal{U}_{AB} & \mathcal{U}_{AC} & \mathcal{U}_{AD} \\ \mathcal{U}_{AB}^* & \epsilon & \mathcal{U}_{AC}^* & \mathcal{U}_{AD}^* \\ \mathcal{U}_{AD} & \mathcal{U}_{AC} & \epsilon & \mathcal{U}_{AB} \\ \mathcal{U}_{AC}^* & \mathcal{U}_{AD} & \mathcal{U}_{AB}^* & \epsilon \end{pmatrix} \begin{pmatrix} \phi_A \\ \phi_B \\ \phi_D \\ \phi_C \end{pmatrix} = E \begin{pmatrix} \phi_A \\ \phi_B \\ \phi_D \\ \phi_C \end{pmatrix}, \quad (3.13)$$

---

[1]These calculations can be checked in Ref. [93].
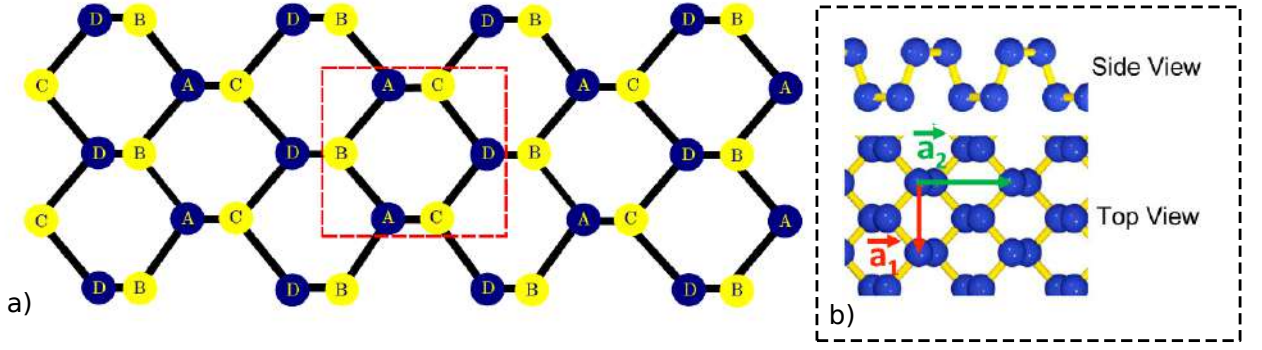
Figure 3.3: Representation of crystal structure of phosphorene with the four atomic sites A, B, C and D. (a) Top view, and (b) lateral view indicating the lattice parameters $\vec{a}_1$ and $\vec{a}_2$ and showing the roughness of the crystal structure [36, 19].

leading to the following system of equations:

$$\epsilon\phi_A + \mathcal{U}_{AB}\phi_B + \mathcal{U}_{AD}\phi_D + \mathcal{U}_{AC}\phi_C = E\phi_A, \tag{3.14a}$$

$$\mathcal{U}_{AB}^*\phi_A + \epsilon\phi_B + \mathcal{U}_{AC}^*\phi_D + \mathcal{U}_{AD}\phi_C = E\phi_B, \tag{3.14b}$$

$$\mathcal{U}_{AD}\phi_A + \mathcal{U}_{AC}\phi_B + \epsilon\phi_D + \mathcal{U}_{AB}\phi_C = E\phi_D, \tag{3.14c}$$

$$\mathcal{U}_{AC}^*\phi_A + \mathcal{U}_{AD}\phi_B + \mathcal{U}_{AB}^*\phi_D + \epsilon\phi_C = E\phi_C. \tag{3.14d}$$

Adding Eqs. (3.14a) to (3.14c), and Eqs. (3.14b) to (3.14d) we obtain respectively

$$(\epsilon + \mathcal{U}_{AD})(\phi_A + \phi_D) + (\mathcal{U}_{AB} + \mathcal{U}_{AC})(\phi_B + \phi_C) = E(\phi_A + \phi_D), \tag{3.15a}$$

$$(\mathcal{U}_{AB}^* + \mathcal{U}_{AC}^*)(\phi_A + \phi_D) + (\epsilon + \mathcal{U}_{AD})(\phi_B + \phi_C) = E(\phi_B + \phi_C), \tag{3.15b}$$

and subtracting Eqs. (3.14a) and (3.14c), and Eqs. (3.14b) and (3.14d) we have

$$(\epsilon - \mathcal{U}_{AD})(\phi_A - \phi_D) + (\mathcal{U}_{AB} - \mathcal{U}_{AC})(\phi_B - \phi_C) = E(\phi_A - \phi_D), \tag{3.16a}$$

$$(\mathcal{U}_{AB}^* - \mathcal{U}_{AC}^*)(\phi_A - \phi_D) + (\epsilon - \mathcal{U}_{AD})(\phi_B - \phi_C) = E(\phi_B - \phi_C). \tag{3.16b}$$

Using Eqs. (3.15) and (3.16) we obtain the eigenvalues equation as a matrix system

$$\begin{pmatrix} \epsilon + \mathcal{U}_{AD} & \mathcal{U}_{AB} + \mathcal{U}_{AC} & 0 & 0 \\ \mathcal{U}_{AB}^* + \mathcal{U}_{AC}^* & \epsilon + \mathcal{U}_{AD} & 0 & 0 \\ 0 & 0 & \epsilon - \mathcal{U}_{AD} & \mathcal{U}_{AB} - \mathcal{U}_{AC} \\ 0 & 0 & \mathcal{U}_{AB}^* - \mathcal{U}_{AC}^* & \epsilon - \mathcal{U}_{AD} \end{pmatrix} \begin{pmatrix} \phi_A + \phi_D \\ \phi_B + \phi_C \\ \phi_A - \phi_C \\ \phi_B + \phi_C \end{pmatrix} = E \begin{pmatrix} \phi_A + \phi_D \\ \phi_B + \phi_C \\ \phi_A - \phi_C \\ \phi_B + \phi_C \end{pmatrix}. \tag{3.17}$$

From Eq. (3.12) we obtain four energy bands. Two of them are closer to the Fermi level and given by the upper matrix of Eq. (3.12), in that case the eigenvalue equation is given by

$$\begin{pmatrix} \epsilon + \mathcal{U}_{AD} & \mathcal{U}_{AB} + \mathcal{U}_{AC} \\ \mathcal{U}_{AB}^* + \mathcal{U}_{AC}^* & \epsilon + \mathcal{U}_{AD} \end{pmatrix} \begin{pmatrix} \phi_A + \phi_D \\ \phi_B + \phi_C \end{pmatrix} = E \begin{pmatrix} \phi_A + \phi_D \\ \phi_B + \phi_C \end{pmatrix}. \tag{3.18}$$

On the other hand, the eigenvalue equation concerning energy bands further from the Fermi level is given by the lower matrix of Eq. (3.12)

$$\begin{pmatrix} \epsilon - \mathcal{U}_{AD} & \mathcal{U}_{AB} - \mathcal{U}_{AC} \\ \mathcal{U}_{AB}^* - \mathcal{U}_{AC}^* & \epsilon - \mathcal{U}_{AD} \end{pmatrix} \begin{pmatrix} \phi_A + \phi_D \\ \phi_B + \phi_C \end{pmatrix} = E \begin{pmatrix} \phi_A - \phi_C \\ \phi_B + \phi_C \end{pmatrix}. \tag{3.19}$$

From Eqs. (3.18) and (3.19) we determine the expressions of the four energy bands

$$E(k_x, k_y) = 2\epsilon + 8t_4 \cos(k_x a_1) \cos(k_y a_2) \pm [4(z_1 + z_2) \cos(k_x a_1) + 4z_3 \cos(k_y a_2)]^{1/2}, \tag{3.20a}$$

$$E(k_x, k_y) = 2\epsilon + 8t_4 \cos(k_x a_1) \cos(k_y a_2) \pm \{4(z_1 - z_2) \cos(k_x a_1) - 4z_3 \cos(k_y a_2)\}^{1/2}, \tag{3.20b}$$

where

$$z_1 = \left[t_1^2 + t_3^2 + 2t_1 t_3 \cos(2k_y a_2) \right], \tag{3.21a}$$

$$z_2 = t_3 \left[t_2 \cos(k_y a_2) + t_5 \cos(3k_y a_2) \right], \tag{3.21b}$$

$$z_3 = t_1 \left[t_2 + t_5 \right] \cos(k_x a_1), \tag{3.21c}$$

$$a_1 = d_1 \sin(\alpha_1/2), \tag{3.21d}$$

$$a_2 = d_1 \cos(\alpha_1/2) + d_2 \cos\beta, \tag{3.21e}$$

and +(-) before the square root in Eq. (3.20a) corresponds to the conduction (valence) band. The four energy bands obtained from Eqs (3.20a) and (3.20b) are depicted in Fig. 3.4.

3.2   Continuum model

Similar as in the graphene case, where we developed a model which describes the electrons around K and K' points, it is interesting to develop an approximation to the energy spectrum from the *tight-binding* model of phosphorene around the point where there is a band-gap and the electronic and transport properties take place. In that case, we approximate the terms of the upper matrix in Eq. (3.17), which leads to the energy
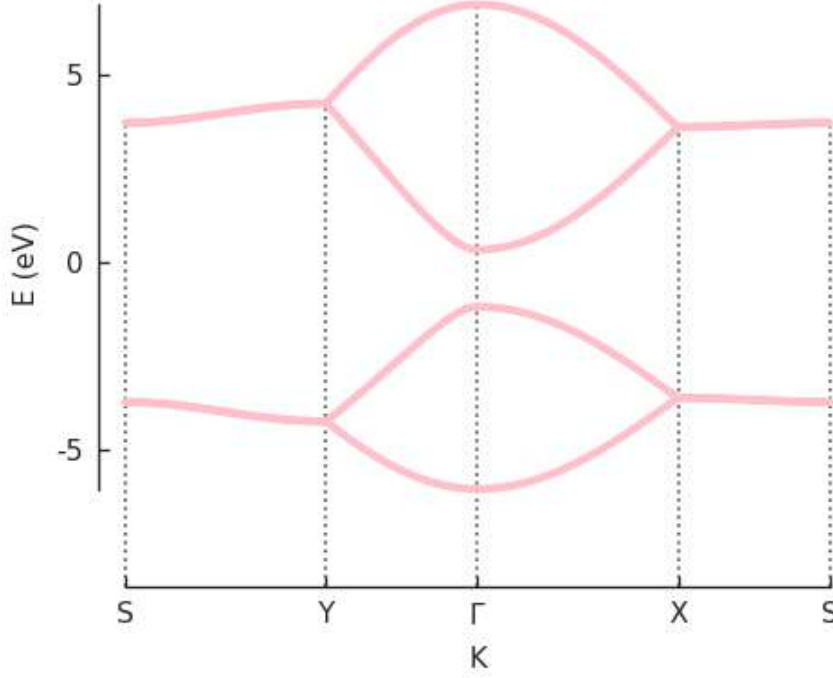
Figure 3.4: Energy spectrum of phosphorene obtained using the *tight-binding* model.

spectrum closer to the Fermi level, around the point Γ ($k_x = k_y = 0$), thus obtaining the continuum model for the electrons in phosphorene. Developing this approximation in terms of the matrix in Eq. (3.18) we find

$$\mathcal{U}_{AD} \approx 4t_4 - 2t_4 \left[d_1 \sin\left(\alpha_1/2\right) \right]^2 k_x^2 - 4t_4 d_1 \left[\sin\left(\alpha_1/2\right) + d_2 \sin\beta \right]^2 k_y^2, \quad (3.22a)$$

$$\begin{aligned} \mathcal{U}_{AB} \approx \ & 2\left(t_1 + t_3\right) - \left(t_1 + t_3\right)\left[d_1 \sin\left(\alpha_1/2\right)\right]^2 k_x^2 \\ & - \left\{ t_1 \left[d_1 \cos\left(\alpha_1/2\right)\right]^2 + t_3 \left[d_1 \cos\left(\alpha_1/2\right) + 2d_2 \cos\beta\right]^2 \right\} k_y^2 \\ & + i\left[-2t_1 \cos\left(\alpha_1/2\right) + 2t_3 \left(d_1 \cos\left(\alpha_1/2\right) + 2d_2 \cos\beta \right) \right] k_y, \end{aligned} \quad (3.22b)$$

$$\begin{aligned} \mathcal{U}_{AC} \approx \ & \left(t_2 + t_5\right) - \left\{ t_2 \left[d_2 \cos\beta\right]^2 / 2 + t_5 \left[2d_1 \cos\left(\alpha_1/2\right) + 2d_2 \cos\beta\right]^2 / 2 \right\} k_y^2 \\ & + i\left\{ t_2 d_2 \cos\beta - t_5 \left[2d_1 \cos\left(\alpha_1/2\right) + 2d_2 \cos\beta\right] \right\} k_y. \end{aligned} \quad (3.22c)$$

Replacing the expressions given by Eqs. (3.22) in the matrix of (3.18) and setting $\epsilon = 0$, we obtain the matrix of the Hamiltonian in the continuum model

$$H = \begin{pmatrix} u_o + \eta_x k_x^2 + \eta_y k_y^2 & \delta + \gamma_x k_x^2 + \gamma_y k_y^2 + i\chi k_y \\ \delta + \gamma_x k_x^2 + \gamma_y k_y^2 - i\chi k_y & u_o + \eta_x k_x^2 + \eta_y k_y^2 \end{pmatrix}, \quad (3.23)$$

where

$$
\begin{aligned}
u_o &= 4t_4; \\
\delta &= 2\left(t_1 + t_3\right) + t_2 + t_5; \\
\gamma_x &= -\left(t_1 + t_3\right)\left(d_1 \sin\left(\alpha_1/2\right)\right)^2; \\
\gamma_y &= -t_1\left(d_1 \cos\left(\alpha_1/2\right)\right)^2 - t_2\left(d_2 \cos\beta\right)^2/2 - t_3\left(d_1 \cos\left(\alpha_1/2\right) + 2d_2 \cos\beta\right)^2 \\
&\quad - t_5\left(2d_1 \cos\left(\alpha_1/2\right) + d_2 \cos\beta\right)^2/2; \\
\chi &= -2t_1 d_1 \cos\left(\alpha_1/2\right) + t_2 d_2 \cos\beta + 2t_3\left(d_1 \cos\left(\alpha_1/2\right) + 2d_2 \cos\beta\right) \\
&\quad - t_5\left(2d_1 \cos\left(\alpha_1/2\right) + d_2 \cos\beta\right); \\
\eta_x &= -2t_4\left(d_1 \sin\left(\alpha_1/2\right)\right)^2; \\
\eta_y &= -2t_4\left(d_1 \cos\left(\alpha_1/2\right) + d_2 \cos\beta\right).
\end{aligned}
$$

By diagonalizing Eq. (3.23) we obtain the eigenvalues of the continuum model

$$
E = u_0 + \eta_x k_x^2 + \eta_y k_y^2 \pm \sqrt{\left(\delta + \gamma_x k_x^2 + \gamma_y k_y^2\right)^2 + \chi^2 k_y^2}; \tag{3.24}
$$

where $+(-)$ corresponds to the conduction (valence) bands. The *hopping* parameters, lattice and continuum parameters and their values are listed in Table 3.2. Using those values in Eq. (3.24) we plot the energy spectrum shown in Fig. (3.5).

Hoppings	Continuum parameters	Lattice parameters
$t_1 = -1.220$	$u_0 = -0.42$ eV	$\alpha_1 = 96.5°$
$t_2 = 3.665$	$\eta_x = 0.58$ eV.^{2}	$\alpha_2 = 101.9°$
$t_3 = -0.205$	$\eta_y = 1.01$eV.^{2}	$d_1 = 2.22$
$t_4 = -0.105$	$\delta = 0.76$ eV.	$d_2 = 2.24$
$t_5 = -0.055$	$\chi = 5.25$ eV.^{2}	$\cos\beta = -\cos\left(\alpha_2\right)/\cos\left(\alpha_1\right)$
	$\gamma_x = 3.93$ eV.^{2}	
	$\gamma_y = 3.788$ eV.^{2}	

Table 3.1: *Hoppings*, continuum parameters, and lattice parameters of phosphorene [93].

From Fig. 3.5 we note that the continuum model agrees very well with the *tight-binding* in the range of energy values between -2.0eV to 1.5 eV, this being exactly the region close to the band-gap of energy, indicating that the electronic and transport properties of phosphorene can be investigated efficiently within this continuum approach. It is important to highlight that the anisotropy in the energy spectrum around the Γ point. This anisotropy results in interesting electronic and transport properties in phosphorene. One of the effects of this anisotropy in the energy spectrum on the transport properties of this material can be observed when analyzing the wave packet dynamics in black phosphorus multilayers, as we are going to discuss in the Chapter 5.
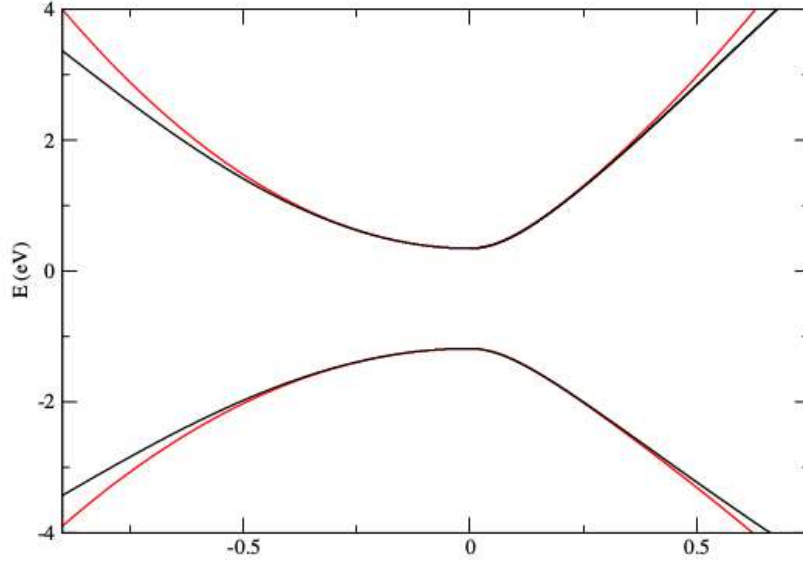
Figure 3.5: Comparison between the phosphorene energy spectra obtained from the *tight-binding* model close to Γ point (black line) and the continuum model (red line)[93].

To determine the eigenstates of the Hamiltonian in Eq. (3.23), the wave-function can be written as

$$\Psi = \begin{pmatrix} \phi_1 \\ \phi_2 \end{pmatrix}, \tag{3.25}$$

where ϕ_1 and ϕ_2 are superpositions of the wave functions in the four sublattices and given by $(\phi_A + \phi_D)/2$ and $(\phi_B + \phi_C)/2$, respectively. Therefore, the eigenstate equation is

$$\begin{pmatrix} u_o + \eta_x k_x^2 + \eta_y k_y^2 & \delta + \gamma_x k_x^2 + \gamma_y k_y^2 + i\chi k_y \\ \delta + \gamma_x k_x^2 + \gamma_y k_y^2 - i\chi k_y & u_o + \eta_x k_x^2 + \eta_y k_y^2 \end{pmatrix} \begin{pmatrix} \phi_1 \\ \phi_2 \end{pmatrix} = E \begin{pmatrix} \phi_1 \\ \phi_2 \end{pmatrix}. \tag{3.26}$$

Rewriting the terms of the off main-diagonal, we get

$$\delta + \gamma_x k_x^2 + \gamma_y k_y^2 \pm i\chi k_y = \sqrt{\left(\delta + \gamma_x k_x^2 + \gamma_y k_y^2\right)^2 + (\chi k_y)^2} e^{\pm i\theta_k},$$

$$\theta_k = \arctan\left[\frac{2\chi k_y}{f_+ - f_-}\right], \tag{3.27}$$

where f_+ e f_- are given by

$$f_\pm = (u_o \pm \delta) + (\eta_x \pm \gamma_x) k_x^2 + (\eta_y \pm \gamma_y) k_y^2. \tag{3.28}$$

We can rewrite the Hamiltonian in Eq. (3.23) in terms of f_+ and f_-

$$H = \begin{pmatrix} \varepsilon_1 & \varepsilon_2 e^{i\theta_k} \\ \varepsilon_2 e^{-i\theta_k} & \varepsilon_1 \end{pmatrix}, \tag{3.29}$$

where

$$\varepsilon_1 = \frac{f_+ + f_-}{2} \quad , \varepsilon_2 = \sqrt{\left(\frac{f_- - f_+}{2}\right)^2 + (\chi k_y)^2}. \tag{3.30}$$

Applying (3.29) to (3.25) we determine the eigenstates of the continuum model Hamiltonian

$$\Psi_\lambda = \frac{1}{\sqrt{2}} \begin{pmatrix} 1 \\ \lambda e^{i\theta_k} \end{pmatrix}, \tag{3.31}$$

with $\lambda = 1(-1)$ for electrons (holes) and θ represents the phase angle of the wave functions, unlike graphene case where the parameter θ represents the angle that the wave-vector makes with the x axis in the momentum space and gives the propagation direction of the electron.

3.3 Effective-mass model

Due to the presence of band-gap and non-zero group velocity around the Γ point in the phosphorene energy spectrum, we can obtain an even simpler model for the electrons around the point where the anisotropy of the energy bands of phosphorene appears more directly in the so-called effective mass model.

The effective mass model assumes that the electrons in a crystal lattice under the action of an external force (an electric field, for example) behaves like a free electron with a mass given by m^* which is inversely proportional to the second derivative of energy with respect to the wave-vector $\vec{k}$ [94]

$$\vec{m}^* = \frac{\hbar^2}{\partial^2 E / \partial \vec{k}^2}, \tag{3.32}$$

from (3.24) we obtain the derivative of second order of the energy in the x direction of the wave-vector

$$\frac{\partial^2 E_{e(h)}}{\partial k_x^2} = 2\eta_x \pm \left(\frac{2\gamma_x \left(\delta + 3\gamma_x k_x^2 + \gamma_y k_y^2 \right) k_x}{\sqrt{\left(\delta + \gamma_x k_x^2 + \gamma_y k_y^2 \right)^2 + \chi^2 k_y^2}} + \cdots \right), \tag{3.33}$$

Since we are analyzing the region around the Γ point we have that for small values of k_x and k_y the effective mass in the x direction is given by

$$m_x^{e(h)} = \frac{\hbar^2}{2 \left(\eta_x \pm \gamma_x \right)}, \tag{3.34}$$

where the positive and negative signs represent the effective mass for electrons and holes, respectively.

On the other hand, making the same procedure but now for the y direction we obtain

$$m_y^{e(h)} = \frac{\hbar^2}{2 \left(\eta_x \pm \gamma_x \pm \chi^2/2\delta \right)}, \tag{3.35}$$

where, again, the positive and negative signs correspond to the values for electrons and holes respectively. Rewriting the energy expression given in (3.24) in terms of the effective

masses in the direction x and y given by Eqs. (3.34) and (3.35) we get the following expression for the energy spectrum

$$E = (u_o \pm \delta) + \frac{\hbar^2}{2m_x^{e(h)}}k_x^2 + \frac{\hbar^2}{2m_y^{e(h)}}k_y^2. \tag{3.36}$$

From (3.36) we can see that the energy levels in moments space are ellipses with their semi-axes given by the effective masses in the directions x and y. Thus, charge carriers in phosphorene have direction-dependent electronic properties, as discussed in Chapter 7.

The $\alpha - T_3$ lattice

In this chapter we discuss the electronic properties of $\alpha - T_3$ lattices introduced in Chapter 1 by starting from the *Tight-binding* approximation and further considering the low-energy regime where we are going to demonstrate that the charge carriers in these lattices are described by an equation analogous to the Dirac equation, similar to graphene but with a enlarged pseudospin though, which provides interesting effects such as super-Klein tunneling that we are also going to discuss in the last section of this chapter.

4.1 Tight-binding approximation

The $\alpha - T_3$ lattice is depicted in Fig. 4.1(a). The unit cell is formed by three triangular lattices with three atoms at sites A, B and C where the additional atom at site C placed at the center of the unit cell and coupled only to the atomic sites B through the parameter α. The value of the coupling parameter α can be adjusted to obtain a honeycomb lattice (HCL) analogous to the crystal structure of graphene but with an additional site. The Bravais lattice vectors for the lattice are shown in Fig. 4.1(b). They can be written as

$$\vec{a_1} = \left(\frac{-a\sqrt{3}}{2}, \frac{3a}{2} \right) \quad , \quad \vec{a_2} = \left(\frac{a\sqrt{3}}{2}, \frac{3a}{2} \right), \tag{4.1}$$

where a is the atom-atom distance, as indicated in Fig. 4.1(b). In graphene, the carbon-carbon distance is approximately $a = 1.42\text{Å}$. To determine the reciprocal vectors that describe the first Brillouin zone we use the following relations

$$\vec{b_1} = 2\pi \frac{\vec{a_2} \times \vec{a_3}}{\vec{a_1} \cdot (\vec{a_2} \times \vec{a_3})} \quad , \quad \vec{b_2} = 2\pi \frac{\vec{a_3} \times \vec{a_1}}{\vec{a_1} \cdot (\vec{a_2} \times \vec{a_3})}. \tag{4.2}$$

Since we are considering a 2D structure, we take $\vec{a_3} = (0, 0, 1)$, so the reciprocal vectors are

$$\vec{b_1} = \left(-\frac{2\pi}{a\sqrt{3}}, \frac{2\pi}{3a} \right) \quad , \quad \vec{b_2} = \left(\frac{2\pi}{a\sqrt{3}}, \frac{2\pi}{3a} \right), \tag{4.3}$$
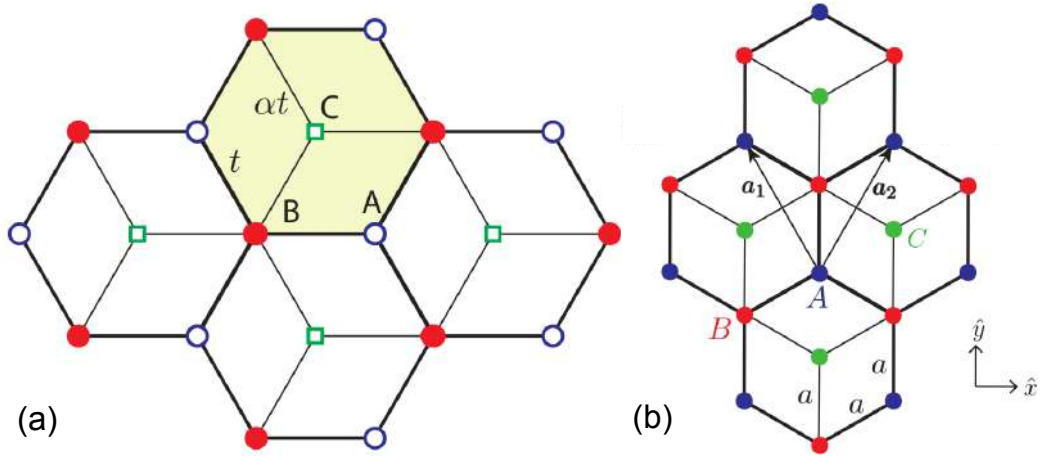
Figure 4.1: (a) Representation of the $\alpha - T_3$ model lattice with hopping t between the atoms in the HCL and hopping αt between the atomic sites B (red dots) and C (green squares). (b) The lattice showing the primitive vectors a_1 and a_2 and the inter-atomic distance $a = 1.42\text{Å}$ [55]

if we consider the site B at the origin of the coordinate system that describes the infinite lattice in real space, we can get the binding vectors between sites A-B and B-C. Similar to graphene lattice, the site B has three nearest neighbors sites A with its vectors of position in relation to site B denoted by $\vec{\delta_1^A}, \vec{\delta_2^A}, \vec{\delta_3^A}$, and given by

$$\vec{\delta_1^A} = (0, -a), \tag{4.4a}$$

$$\vec{\delta_2^A} = \left(\frac{a\sqrt{3}}{2}, \frac{a}{2} \right), \tag{4.4b}$$

$$\vec{\delta_3^A} = \left(\frac{-a\sqrt{3}}{2}, \frac{a}{2} \right). \tag{4.4c}$$

Since in the case of the $\alpha - T_3$ lattice there is an additional site C placed at the center of each hexagon which is only coupled to site B, this site has three nearest neighbors sites C with the position vectors $\vec{\delta_1^C}, \vec{\delta_2^C}, \vec{\delta_3^C}$ and given by

$$\vec{\delta_1^C} = (0, a) = -\vec{\delta_1^A}, \tag{4.5a}$$

$$\vec{\delta_2^C} = \left(\frac{-a\sqrt{3}}{2}, \frac{-a}{2} \right) = -\vec{\delta_2^A}, \tag{4.5b}$$

$$\vec{\delta_3^C} = \left(\frac{a\sqrt{3}}{2}, -\frac{a}{2} \right) = -\vec{\delta_3^A}. \tag{4.5c}$$

After discussing the crystallographic properties of the $\alpha - T_3$ lattices we are going to derive the *tight-binding* model for these lattices. For the $\alpha - T_3$ lattice, the *hopping* parameter between the atomic sites A and B is denoted by t, while between B and C sites the hopping parameter is denoted by αt. The coupling variable α is unitless, and can be varied between 0 and 1. For the case $\alpha = 0$, the atomic site C is uncoupled from the atomic site B, and we obtain a lattice analogous to the HCL of graphene with an inert C-sublattice. Assuming $\alpha = 1$ the hopping parameter between the atomic sites A and B is identical to the one between the B and C sites, and the dice lattice is recovered.

The Hamiltonian of the $\alpha - T_3$ lattice in the *tight-binding* model using the first quantization formalism is defined as

$$H_{ij} = \langle \Phi_i | H | \Phi_j \rangle, \tag{4.6}$$

where $\Phi_i(\Phi_j)$ corresponds to the orbital Bloch wave-functions to site $i(j)$ in the crystal lattice, so for the $\alpha - T_3$ lattice we have three orbital Bloch wave-functions

$$\Phi_A(\vec{k}, \vec{r}) = \frac{1}{\sqrt{N}} \sum_{R_A} e^{i\vec{k}\cdot\vec{R_A}} \varphi_A(\vec{r} - \vec{R_A}), \tag{4.7a}$$

$$\Phi_B(\vec{k}, \vec{r}) = \frac{1}{\sqrt{N}} \sum_{R_B} e^{i\vec{k}\cdot\vec{R_B}} \varphi_B(\vec{r} - \vec{R_B}), \tag{4.7b}$$

$$\Phi_C(\vec{k}, \vec{r}) = \frac{1}{\sqrt{N}} \sum_{R_C} e^{i\vec{k}\cdot\vec{R_C}} \varphi_C(\vec{r} - \vec{R_C}), \tag{4.7c}$$

where $\vec{R_A}, \vec{R_B}$ and $\vec{R_C}$ corresponds to the position of sites A, B and C in the infinite crystal lattice respectively.

The next step is to define the terms of the matrix H_{ij} in Eq. (4.6). First, consider the terms related to site A:

$$H_{AB} = \frac{1}{N} \sum_{R_A, R_B} e^{-i\vec{k}\cdot\vec{R_A}} . e^{i\vec{k}\cdot\vec{R_B}} \left\langle \varphi_A(\vec{r} - \vec{R_A}) | H | \varphi_B(\vec{r} - \vec{R_B}) \right\rangle, \tag{4.8a}$$

$$H_{AC} = \frac{1}{N} \sum_{R_A, R_C} e^{-i\vec{k}\cdot\vec{R_A}} . e^{i\vec{k}\cdot\vec{R_C}} \left\langle \varphi_A(\vec{r} - \vec{R_C}) | H | \varphi_B(\vec{r} - \vec{R_C}) \right\rangle, \tag{4.8b}$$

$$H_{AA} = \frac{1}{N} \sum_{R_A, R_A} e^{-i\vec{k}\cdot\vec{R_A}} . e^{i\vec{k}\cdot\vec{R_A}} \left\langle \varphi_A(\vec{r} - \vec{R_A}) | H | \varphi_B(\vec{r} - \vec{R_A}) \right\rangle. \tag{4.8c}$$

Since the site C is only coupled to site B and we are taking into account only the nearest-neighbour, we have $H_{AC} = 0$ and $H_{AA} = 0$. Therefore, for the term H_{AB} we have

$$H_{AB} = \frac{1}{N} \sum_{R_{AB}} e^{-i\vec{k}\cdot(\vec{R_A} - \vec{R_B})} \left\langle \varphi_A(\vec{r} - \vec{R_A}) | H | \varphi_B(\vec{r} - \vec{R_B}) \right\rangle. \tag{4.9}$$

The expression $\left\langle \varphi_i(\vec{r} - \vec{R_i})|H|\varphi_j(\vec{r} - \vec{R_j})\right\rangle$ is associated to the *hopping* parameter of the crystal lattice, which is related to the interaction energy between the sites of the unit cell. Since in the $\alpha - T_3$ lattices the *hopping* parameter between the sites A and B is given by t. So, the term H_{AB} becomes

$$
\begin{aligned}
H_{AB} &= -t\left(e^{-i\vec{k}\cdot\vec{\delta_1^A}} + e^{-i\vec{k}\cdot\vec{\delta_2^A}} + e^{-i\vec{k}\cdot\vec{\delta_3^A}}\right), \\
H_{AB} &= -t\left(e^{ik_y a} + 2e^{-ik_y a/2}\cos(k_x a\sqrt{3}/2)\right), & (4.10) \\
H_{AB} &= f(\vec{k}). & (4.11)
\end{aligned}
$$

For the atomic site B we have

$$H_{BB} = 0, \tag{4.12a}$$

$$H_{BA} = -t\sum_{R_{BA}} e^{-i\vec{k}\cdot(\vec{R_B} - \vec{R_A})} = H_{AB}^* = f^*(\vec{k}), \tag{4.12b}$$

$$H_{BC} = \frac{1}{N}\sum_{R_{BC}} e^{-i\vec{k}\cdot(\vec{R_B} - \vec{R_C})}\left\langle \varphi_B(\vec{r} - \vec{R_B})|H|\varphi_C(\vec{r} - \vec{R_C})\right\rangle. \tag{4.12c}$$

Since the *hopping* parameter between the atomic sites B and C is given by αt, for the the term H_{BC} we have

$$
\begin{aligned}
H_{BC} &= -\alpha t\left(e^{i\vec{k}\cdot\vec{\delta_1^C}} + e^{i\vec{k}\cdot\vec{\delta_2^C}} + e^{i\vec{k}\cdot\vec{\delta_3^C}}\right), & (4.13) \\
H_{BC} &= -\alpha t\left(e^{-i\vec{k}\cdot\vec{\delta_1^A}} + e^{-i\vec{k}\cdot\vec{\delta_2^A}} + e^{-i\vec{k}\cdot\vec{\delta_3^A}}\right), \\
H_{BC} &= \alpha f(\vec{k}). & (4.14)
\end{aligned}
$$

Similarly, the terms concerning the atomic site C are given by

$$H_{CA} = 0, \tag{4.15a}$$

$$H_{CC} = 0, \tag{4.15b}$$

$$H_{CB} = -\alpha t\sum_{R_{CB}} e^{-i\vec{k}\cdot(\vec{R_C} - \vec{R_B})} = H_{BC}^* = \alpha f^*(\vec{k}). \tag{4.15c}$$

Thus, we finally obtain the matrix that corresponds to the *tight-binding* Hamiltonian for the $\alpha - T_3$ lattices

$$
H_{TB} = \begin{pmatrix} 0 & f(\vec{k}) & 0 \\ f^*(\vec{k}) & 0 & f(\vec{k})\tan\theta \\ 0 & f^*(\vec{k})\tan\theta & 0 \end{pmatrix}, \tag{4.16}
$$

where we have parametrized $\alpha = \tan^{-1}\theta$. Rescaling the hamiltonian by $\cos\theta$ gives us the matrix hamiltonian that was originally utilized to introduce the $\alpha - T_3$ model

$$H_{TB} = \begin{pmatrix} 0 & f(\vec{k})\cos\theta & 0 \\ f^*(\vec{k})\cos\theta & 0 & f(\vec{k})\sin\theta \\ 0 & f^*(\vec{k})\sin\theta & 0 \end{pmatrix}. \tag{4.17}$$

We calculate the eigenvalues of the hamiltonian in order to obtain the energy dispersion for the $\alpha - T_3$ lattice:

$$\begin{vmatrix} -E & f(\vec{k})\cos\theta & 0 \\ f^*(\vec{k})\cos\theta & -E & f(\vec{k})\sin\theta \\ 0 & f^*(\vec{k})\sin\theta & -E \end{vmatrix} = 0, \tag{4.18}$$

$$E\left(E^2 - f(\vec{k})f^*(\vec{k})\right) = 0,$$

$$E = 0 \quad , \quad E = \pm\left|f(\vec{k})\right|. \tag{4.19}$$
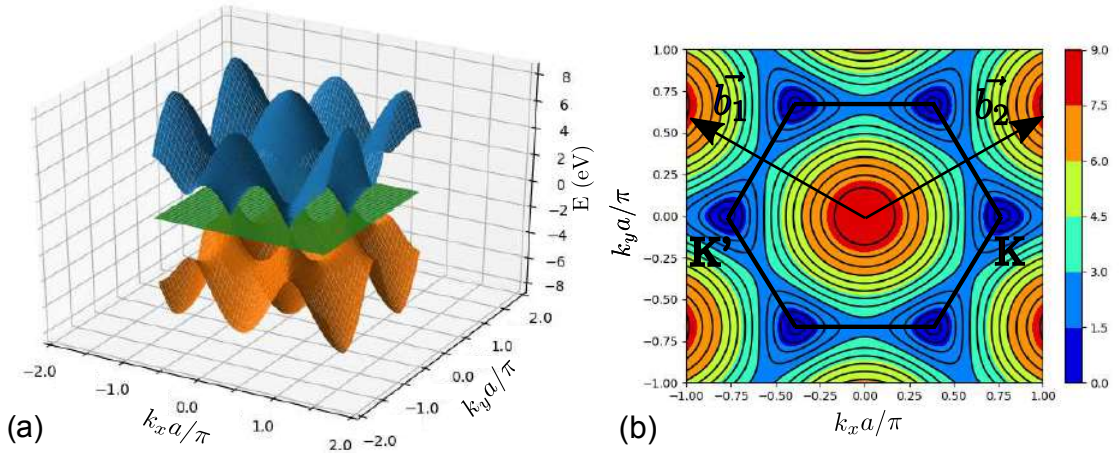
Figure 4.2: (a) Electronic band structures of $\alpha - T_3$ model obtained by *tight-binding* approximation, and (b) the contour plot of the conduction and valence bands indicating the Dirac points K and K' and vectors of reciprocal space $\vec{b}_1$ and $\vec{b}_2$.

In the terms of the primitive vectors of the unit cell, $\left|f(\vec{k})\right|$ is given by

$$\left|f(\vec{k})\right| = t\sqrt{3 + 2\cos(k_x a\sqrt{3}) + 4\cos(k_x a\sqrt{3})\cos(3k_y a/2)}. \tag{4.20}$$

The above energy dispersion is identical to the energy dispersion of the conduction and valence bands of graphene with the addition of a dispersionless flat band that cuts through the Dirac points. A schematic of the three bands of the $\alpha - T_3$ lattices can be found in Fig. 4.2(a). All three bands are present for the full range of α.

4.2   Continuum model

As is typically done in graphene, we can do a low-energy expansion around the Dirac point located at K and K' valleys shown in Fig. 4.2(b). Using Taylor's series we can expand the term $f(\vec{k})$ around the K and K' points restricting to only the terms of first order. For K and K' points we have

$$f(\delta\vec{k}) = f(\vec{K}) + \left.\frac{\partial f}{\partial k_x}\right|_{\vec{k}=\vec{K}} (k_x - K_x) + \left.\frac{\partial f}{\partial k_y}\right|_{\vec{k}=\vec{K}} (k_y - K_y), \tag{4.21a}$$

$$f(\delta\vec{k}) = f(\vec{K'}) + \left.\frac{\partial f}{\partial k_x}\right|_{\vec{k}=\vec{K'}} \left(k_x - K'_x\right) + \left.\frac{\partial f}{\partial k_y}\right|_{\vec{k}=\vec{K'}} \left(k_y - K'_y\right), \tag{4.21b}$$

which can be written in a shorter way as

$$f(\vec{k}) \approx \frac{3at}{2} (\xi k_x - ik_y), \tag{4.22}$$

where $\xi = +1(-1)$ corresponds to valley K (K'). The constant $\frac{3at}{2}$ has the unit of Planck's constant multiplied by the velocity, so we can write Eq. (4.22) as

$$f(\vec{k}) \approx \hbar v_c (\xi k_x - ik_y). \tag{4.23}$$

Replacing Eq. (4.23) into the hamiltonian given by Eq. (4.17) we obtain

$$H_D = \hbar v_c \begin{pmatrix} 0 & (\xi k_x - ik_y)\cos\theta & 0 \\ (\xi k_x + ik_y)\cos\theta & 0 & (\xi k_x - ik_y)\sin\theta \\ 0 & (\xi k_x + ik_y)\sin\theta & 0 \end{pmatrix}. \tag{4.24}$$

By diagonalizing the matrix in Eq. (4.24) we get the energy dispersion for $\alpha - T_3$ lattices in the low-energy regime

$$E = 0 \quad , \quad E = \pm\hbar v_c |\vec{k}|. \tag{4.25}$$

Notice that there are three bands: a flat band with energy zero for all momenta, and two linear bands with energy $E = s\hbar v_c k$, with $s = \pm 1$ for the conduction and valence band, respectively. The linear spectrum implies that electrons move at speed $v_c = v_f$ in analogy to relativistic massless particles, where v_f is substituted for the speed of light. In graphene, the Fermi velocity is approximately 10^6 m/s, so from now we are going to consider $v_c = v_f$, similar as done in Chapter 2.

The low-energy hamiltonian given by Eq. (4.24) can be written as

$$H_D = \hbar k_x \left[\xi \begin{pmatrix} 0 & \cos\theta & 0 \\ \cos\theta & 0 & \sin\theta \\ 0 & \sin\theta & 0 \end{pmatrix} - ik_y \begin{pmatrix} 0 & \cos\theta & 0 \\ -\cos\theta & 0 & \sin\theta \\ 0 & -\sin\theta & 0 \end{pmatrix} \right]. \tag{4.26}$$

When $\alpha = 0 \rightarrow \theta = 0$, we recover the same Eq. (2.15) for graphene in the low-energy regime

$$H_{graphene}^{K,K'} = \hbar v_f \begin{pmatrix} 0 & (\xi k_x - i k_y) \\ (\xi k_x + i k_y) & 0 \end{pmatrix}. \tag{4.27}$$

More generally the Dirac-Weyl hamiltonian for general pseudospin S can be written as:

$$H_{DW} = \hbar v_f \vec{S} \cdot \vec{k}. \tag{4.28}$$

So, for graphene case, Eq. (4.27) can be written using the general form of Eq. (4.28) as

$$H_{graphene}^{K} = \hbar v_f \vec{\sigma} \cdot \vec{k}, \tag{4.29a}$$

$$H_{graphene}^{K'} = \hbar v_f \vec{\sigma}^* \cdot \vec{k}, \tag{4.29b}$$

where $\vec{\sigma}$ corresponds to the Pauli's matrices. So, the hamiltonian of graphene is a special case represented of Eq. (4.28) with pseudospin $S = 1/2$. Now, when we consider the case of $\alpha = 1 \rightarrow \theta = \pi/4$ we recover the hamiltonian for the dice lattice, and Eq (4.26) becomes

$$H_{dice} = \hbar k_x \left[\xi \frac{1}{\sqrt{2}} \begin{pmatrix} 0 & 1 & 0 \\ 1 & 0 & 1 \\ 0 & 1 & 0 \end{pmatrix} + k_y \frac{1}{\sqrt{2}} \begin{pmatrix} 0 & -i & 0 \\ i & 0 & -i \\ 0 & i & 0 \end{pmatrix} \right]. \tag{4.30}$$

Note that Eq. (4.30) can be written in terms of the pseudospin matrices given by

$$S_x = \frac{1}{\sqrt{2}} \begin{pmatrix} 0 & 1 & 0 \\ 1 & 0 & 1 \\ 0 & 1 & 0 \end{pmatrix} \quad , \quad S_y = \frac{1}{\sqrt{2}} \begin{pmatrix} 0 & -i & 0 \\ i & 0 & -i \\ 0 & i & 0 \end{pmatrix}. \tag{4.31}$$

So, the hamiltonian for the dice lattice in the low-energy regime around the Dirac points located at the K and K' valleys are

$$H_{dice}^{K} = \hbar v_f \vec{S} \cdot \vec{k}, \tag{4.32a}$$

$$H_{dice}^{K'} = \hbar v_f \vec{S}^* \cdot \vec{k}. \tag{4.32b}$$

where in this case $S = 1$. Since the conduction and valence bands are linear in the energy spectrum, the particles behave like massless Dirac Fermions, however the hamiltonian which describes the charge carriers due to the presence of an additional atomic site as in the dice lattice has wave-functions represented by an enlarged and integer pseudospin.

4.2.1 Wavefunctions of the $\alpha - T_3$ lattices

We obtain the eigenvectors of the low-energy Hamiltonian given by Eq. (4.26) associated with each of the three eigenvalues. For the linear bands we obtain

$$|\Psi_s\rangle = \begin{pmatrix} e^{i\theta_k}\cos\theta \\ s \\ e^{-i\theta_k}\sin\theta \end{pmatrix}. \tag{4.33}$$

For the flat band we find

$$|\Psi_0\rangle = \begin{pmatrix} e^{i\theta_k}\sin\theta \\ 0 \\ e^{-i\theta_k}\cos\theta \end{pmatrix}, \tag{4.34}$$

where $s = \pm 1$ for the conduction and valence band, respectively. Here, θ_k is the angle associated with momentum $\vec{k}$ and given by $\theta_k = \tan^{-1}(k_y/k_x)$. In the next session we are going to use these wave-functions to investigate the unique tunneling properties of $\alpha - T_3$ lattices as a consequence of the enlarged pseudospin of these lattices.

4.3 Klein tunneling in $\alpha - T_3$ lattice

As discussed in Chapter 2, electrons in graphene at low-energy regime are well-described by the two-dimensional massless Dirac equation with pseudospin $S = 1/2$, which makes it a promising material for directly testing ideas of relativistic physics. The novel materials such as the dice lattice, and the $\alpha - T_3$ lattice provide similar opportunities.

The *Klein tunnelling* (KT) for both of the two limiting cases of the $\alpha - T_3$ model, graphene ($\alpha = 0$) [8, 95, 78]and the dice ($\alpha = 1$) lattice [96, 97], as well for intermediate regimes of α [98] has been investigated in the literature. For the dice lattice, the effect is known as SKT which consists in an all-angle transmission across electrostatic barriers and was reported for particular values of the incident electron energy [96, 97]. Additionally, KT into the flat band across a potential step for generalized pseudospin has been discussed in [52]. In this section we summarize the results discussed in Ref. [55] concerning the transmission properties across a potential barrier in the $\alpha - T_3$ lattice considering some values of α, highlighting omnidirectional transmission (SKT) for incident electrons with energy equal to half the height of the potential barrier for the dice lattice [96, 97]. In Chapter 10 the problem of electrons tunneling through potential barriers and their tunneling properties in the presence of small deviations in the atomic equivalence in the $\alpha - T_3$ lattices are discussed, which has not been reported in the literature.

The low-energy Hamiltonian for the $\alpha - T_3$ around the K point in the presence of an electrostatic potential is

$$\hat{H} = \hat{H}_{kin} + V(x)\hat{I}, \tag{4.35}$$

where $\hat{H}_{kin}$ is given by Eq. (4.24) with $\xi = +1$, $V(x)$ corresponds to the potential barrier and $\hat{I}$ is the identity matrix.

We are going to consider potential barriers that are smooth on the atomic scale, but sharp on the length scale of the Fermi wavelength [95, 78, 96]. Consequently, we need to define the matching conditions required for the wave-functions across such interfaces. To do that we use the Peierls substitution $(\vec{k} \rightarrow \vec{p})$ and integrate the eigenvalue equation $\hat{H}\Psi = E\Psi$ over a small interval $x = [\epsilon, \epsilon]$ [52, 96] and allow the interval to approach zero. So, by assuming the wave-function written in a general form $\Psi(x) = [\psi_A(x), \psi_B(x), \psi_C(x)]$ we obtain $\hbar v_{\mathrm{F}}(\frac{d}{dx} - i\frac{d}{dy})\cos\theta\psi_B = E\psi_A$. Integrating both sides and letting $\epsilon \rightarrow 0$ leads to $\psi_B(-\epsilon) - \psi_B(\epsilon) = 0$, giving one of the three matching conditions. The complete set of matching conditions is

$$\psi_B(-\epsilon) = \psi_B(\epsilon), \tag{4.36a}$$

$$\cos\theta\psi_A(-\epsilon) + \sin\theta\psi_C(-\epsilon) = \cos\theta\psi_A(\epsilon) + \sin\theta\psi_C(\epsilon). \tag{4.36b}$$

Note that these matching conditions differ from those when pseudospin $S = 1/2$ graphene ($\alpha = 0$) and pseudospin $S = 1$ dice lattice ($\alpha = 1$). For graphene, the matching conditions require the continuity of each component of the two-component wave-function. On the other hand, the matching conditions of the dice lattice [96] include a sum of the first and last component of the wave-function indicated in Eq. (4.36b) setting $\sin\theta = \cos\theta = 1/2$. For the other cases of $\alpha - T_3$ lattices, the matching conditions are of the same form as those of the dice lattice, but generalized to account for a variable α.

Consider a square potential barrier $V(x)$ in Eq. (4.35) with width d in a system formed by three zones: $x < 0$ $(V(x) = 0)$, $0 < x < d$ $(V(x) = V_0)$ and $x > 0$ $(V(x) = 0)$, as depicted in Fig. 2.3. The wave-functions in each zone are

$$|\Psi_I\rangle = \frac{1}{\sqrt{2}}\begin{pmatrix} e^{i\theta_k}\cos\theta \\ s \\ e^{-i\theta_k}\sin\theta \end{pmatrix} e^{ik_y y}e^{ik_x x} + \frac{r}{\sqrt{2}}\begin{pmatrix} -e^{-i\theta_k}\cos\theta \\ s \\ -e^{i\theta_k}\sin\theta \end{pmatrix} e^{ik_y y}e^{-ik_x x}, \tag{4.37a}$$

$$|\Psi_{II}\rangle = \frac{a}{\sqrt{2}}\begin{pmatrix} e^{i\theta_q}\cos\theta \\ s' \\ e^{-i\theta_q}\sin\theta \end{pmatrix} e^{ik_y y}e^{iq_x x} + \frac{b}{\sqrt{2}}\begin{pmatrix} -e^{-i\theta_q}\cos\theta \\ s' \\ -e^{i\theta_q}\sin\theta \end{pmatrix} e^{ik_y y}e^{-iq_x x}, \tag{4.37b}$$

$$|\Psi_{III}\rangle = \frac{t}{\sqrt{2}}\begin{pmatrix} e^{i\theta_k}\cos\theta \\ s \\ e^{-i\theta_k}\sin\theta \end{pmatrix} e^{ik_y y}e^{ik_x x}, \tag{4.37c}$$

where $\tan\theta_k = \frac{k_y}{k_x}$, $\tan\theta_q = \frac{k_y}{q_x}$, $R = |r|^2$ and $T = |t|^2$ are the reflection and transmission probabilities of waves, respectively. Using the matching conditions in Eq. (4.36) at $x = 0$

and $x = d$, we obtain the following system of equations for the unknown amplitudes a, b, r, t

$$1 + r = ss'(a + b), \tag{4.38a}$$

$$A(\theta_k) - rB(\theta_k) = A(\theta_q) - rB(\theta_q), \tag{4.38b}$$

$$as'e^{iq_x d} + bs'e^{-iq_x d} = tse^{ik_x d}, \tag{4.38c}$$

$$aA(\theta_q)e^{iq_x d} - bB(\theta_q)e^{-iq_x d} = tA(\theta_k)e^{ik_x d}, \tag{4.38d}$$

with $A(x) = \cos^2\theta e^{ix} + \sin^2\theta e^{-ix}$ and $B(x) = \cos^2\theta e^{-ix} + \sin^2\theta e^{ix}$ for convenience. Assuming that the junction in Fig. 2.3 is a *pnp* junction we consider $ss' = -1$ and after some algebra we find

$$T = \frac{16\cos^2\theta_q \cos^2\theta_k}{g_+^2 + g_-^2 - 2g_+g_- \cos(2q_x d)}, \tag{4.39}$$

where $g_\pm = 2 \pm 2\cos(\theta_q + \theta_k) - \sin^2 2\theta(\sin\theta_q + \sin\theta_k)^2$.

In Fig. 4.3 the transmission probability for some values of E/V_0 ratios considering a range of α values are shown. Note that there is a general enhancement of the transmission as α increases. Moreover the ressonances known as Fabry-Pérot resonances take place when $q_x d$ is multiple of π. As α is increased from 0 to 1, the sharp resonances of graphene become softer and less pronounced, and the broadening of the resonance peaks results in an increased transmission for angles close to the resonance condition, contributing to the enhancement of the transmission as α increases. It is important to highlight the "super" angle transmission, i.e. SKT at $E/V_0 = 0.5$ represented in Fig. 4.3(c), where the sharp resonances of graphene transform to full transmission in the $\alpha = 1$ limit.

The unconventional transparency experienced by electrons across interfaces such as *npn* junctions, which act like negative index interfaces, presents possibilities for electron focusing similar to the focusing of light in optics. Therefore to understand other Dirac-like materials, such $\alpha - T_3$ model could present more possibilities for electron focusing and electron optics.
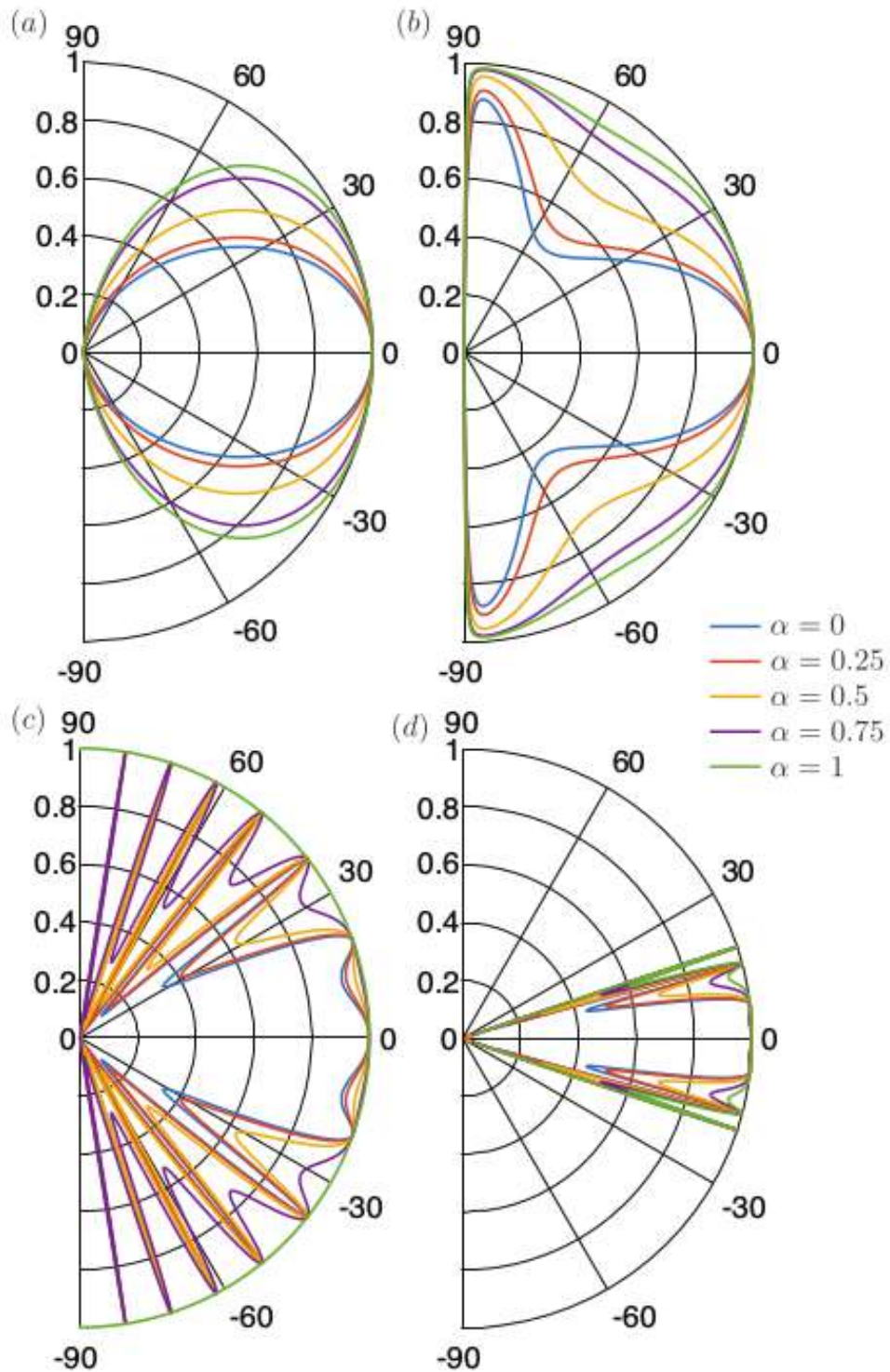
Figure 4.3: Polar plot of the transmission probability for some values of α with (a) $E/V_0 = 0.1$, (b) $E/V_0 = 0.25$, (c) $E/V_0 = 0.5$ and (d) $E/V_0 = 0.75$. The barrier width is $d = 40V_0$, taking $d_0 = \hbar v_F/V_0$ to normalize the barrier width d. [55].

5

Temporal evolution: The split-operator technique

The analysis of wave-packet dynamics in a given system is useful to obtain information about its energy spectrum [99] and electrical conductivity [100], for example.

Many computational techniques for analyzing wave-packet dynamics have been developed. However, to obtain the full description of wave-packet propagation in a system, for most of the numerical techniques it is necessary to write the initial wave function of the system in the basis of all eigenstates and their eigenenergies, which for some systems is infeasible. To work around this problem, some alternative techniques were developed, and one of them being known as *split-operator* [99, 101].

The technique *Split-operator* (SOT) was initially developed by M.D. Feit, J.A. Fleck and A. Steiger [102] and applied to the study of energy levels of triatomic molecules [103]. Wave packet dynamics methods can also be used in the study of the Aharonov-Bohm effect [104], in the conductance analysis of an asymmetric quantum ring [105], in the explanation of the observed effect on Onsanger symmetry breaking in a semiconductor quantum wire coupled to a metal [106] among others.

In the further chapters of this thesis we discuss the wave-packet dynamics in some materials with or without external potential using the SOT. This chapter is devoted to discuss the basic concepts behind this technique that is based on the expansion of the temporal evolution operator and separates this operator in kinetic and potential terms, doing that we avoid to write the momentum operator, as we are going to demonstrate in the next section.

Let us start by considering an initial wave-function $\Psi(\vec{r}, t_0)$ expanded around the time $t = t_0$ and assuming a small time-interval $\Delta t = t - t_0$.

$$\Psi(\vec{r}, t_0 + \Delta t) = \Psi(\vec{r}, t_0) + \sum_{n=1}^{\infty} \frac{1}{n!} \left(\frac{\partial^n \Psi}{\partial t^n} \right)_{t=t_0} \Delta t^n. \tag{5.1}$$

Using the time-dependent Schrödinger's equation given by

$$\frac{\partial \Psi(\vec{r}, t)}{\partial t} = -\frac{i}{\hbar} H \Psi(\vec{r}, t), \tag{5.2}$$

in Eq. (5.1), we obtain the equation to determine the wave-function at an arbitrary posterior time $t_0 + \Delta t$

$$\Psi(\vec{r}, t_0 + \Delta t) = \sum_{n=0}^{\infty} \left[\frac{1}{n!} \left(-\frac{i}{\hbar} H \Delta t \right)^n \right] \Psi(\vec{r}, t_0), \tag{5.3}$$

which after developing the sum is exactly the expression of exponential series. Therefore,

$$\Psi(\vec{r}, t_0 + \Delta t) = \exp \left[-\frac{i}{\hbar} H \Delta t \right] \Psi(\vec{r}, t_0). \tag{5.4}$$

Note that the operator defined in Eq. (5.4) can be identified as the time-evolution operator, which "translate" the initial wave-function from initial time t_0 to arbitrary time $t = t + \Delta t_0$. Therefore, since we know the hamiltonian which describes the system from Eq. (5.4) we obtain the time-evolution of an initial wave-packet. Furthermore, rewriting the wave-function as a spinor and considering the Dirac Hamiltonian, the time-evolution of the wave-packet can also be determined using Eq. (5.4).

Some works in the literature usually use the so-called "Cayley form" to solve Eq. (5.4), which consists of an approximation to the exponential in the evolution operator and is written as

$$\exp \left[-\frac{i}{\hbar} H \Delta t \right] \Psi(\vec{r}, t) \simeq \frac{1 - \frac{i}{2\hbar} H \Delta t}{1 + \frac{i}{2\hbar} H \Delta t} \Psi(\vec{r}, t) = \Psi(\vec{r}, t + \Delta t),$$

$$\left(1 + \frac{i}{2\hbar} H \Delta t \right) \Psi(\vec{r}, t + \Delta t) = \left(1 - \frac{i}{2\hbar} H \Delta t \right) \Psi(\vec{r}, t). \tag{5.5}$$

To solve Eq. (5.5), the space and functions that describe the potentials are discretized, and the wave-function at an instant-time t is also discretized into points $i = 1, 2, ... N$, resulting in a column matrix; the right-hand operation in Eq. (5.5) is done, resulting in a new column matrix. The operation on the left side is rewritten as a matrix equation, where the variables to be determined are Ψ_i at time $t + \Delta t$. Solving this matrix equation at successive times, we obtain the wave-function at each instant. The solution of the above equation for the one-dimensional case can be done easily, but for problems with more dimensions this technique presents several difficulties. Therefore, it is necessary to use a technique that overcomes this problem. In this context, the SOT presents itself as an alternative and facilitating method, since through it we can transform an operator with any number of variables into a sequence of one-dimensional operators and solving Eq. (5.5) is reduced to solve a matrix system of equations.

In order to avoid writing derivatives, we rewrite the time-evolution operator such that the kinetic and potential terms in the Hamiltonian are separated, however we cannot just assume $\exp(T + V) = \exp(T) . \exp(V)$, because T (kinetic energy) and V (potential energy) are non-commuting operators. To solve this problem Masuo Suzuki proposed an approximate solution to this problem [107]:

$$\exp \left[\varepsilon \sum_{j=1}^{q} \hat{A} \right] = f_m \left(\hat{A}_1, \hat{A}_2, \cdots, \hat{A}_q \right) + \mathcal{O}(\varepsilon^{m+1}), \tag{5.6}$$

where $f_m\left(\hat{A}_1, \hat{A}_2, \cdots, \hat{A}_q\right)$ is an approximation term and $\mathcal{O}(\varepsilon^{m+1)})$ is an error of the order of (ε^{m+1}). We will use the expressions for $f_m\left(\hat{A}_1, \hat{A}_2\right)$ and $m = 2$ in order to ensure a maximum error of the order of Δt^3. Approximations are given by

$$f_2(\hat{A}_1, \hat{A}_2) = \exp\left[\frac{\varepsilon}{2}\hat{A}_1\right] \exp[\varepsilon\hat{A}_2] \exp\left[\frac{\varepsilon}{2}\hat{A}_1\right]. \tag{5.7}$$

The demonstration of terms with other values of m can be seen in Ref. [108]. After this approximation we can separate the time-evolution operator as follows

$$\exp\left[-\frac{i}{\hbar}H\Delta t\right] = \exp\left[-\frac{i}{2\hbar}V\Delta t\right] \exp\left[-\frac{i}{\hbar}T\Delta t\right] \exp\left[-\frac{i}{2\hbar}V\Delta t\right] + \mathcal{O}(\Delta t^3), \tag{5.8}$$

where the terms higher than Δt^3 can be neglected if we consider a small time interval Δt.

Now we are going to consider an arbitrary wave function $\Psi(\vec{r}, t)$ and apply to it the time-evolution operator given by the approximation of (5.8), so we have

$$\Psi(\vec{r}, t + \Delta t) = \exp\left[-\frac{i}{2\hbar}V\Delta t\right] \exp\left[-\frac{i}{\hbar}T\Delta t\right] \exp\left[-\frac{i}{2\hbar}V\Delta t\right] \Psi(\vec{r}, t). \tag{5.9}$$

5.1 Hamiltonian without spin involved

In order to calculate the wave function at a posterior time $t + \Delta t$ it is necessary to discretize the time, the potential V and the wave-function, so we define ξ as

$$\xi_i = \exp\left[-\frac{i}{2\hbar}V_i\Delta t\right] |\Psi_i\rangle_t, \tag{5.10}$$

where $V_i, \Delta t$, and $|\Psi_i\rangle_t$ consist of the potential, time and wave-function discretized respectively. The next step is to multiply ξ_i in equation (5.10) by the kinetic term, such product being represented by η_i,[1] and to use Cayley's formula. We obtain

$$\eta_i = \left[-\frac{i}{\hbar}T\Delta t\right] \xi_i = \left(\frac{1 - \frac{i}{2\hbar}T\Delta t}{1 + \frac{i}{2\hbar}T\Delta t}\right) \xi_i, \tag{5.11}$$

$$\left(1 + \frac{i}{2\hbar}T\Delta t\right) \eta_i = \left(1 - \frac{i}{2\hbar}T\Delta t\right) \xi_i, \tag{5.12}$$

and the kinetic term in the absence of a magnetic field is

$$T_n = \frac{\hbar^2}{2m}\frac{d^2}{dx_n^2}, \tag{5.13}$$

where m represents the mass of the particle and x_n is an arbitrary spatial variable. Replacing the kinetic term T in Eq. (5.11) and making $\kappa = \frac{i\hbar}{4m}\Delta t$ we obtain a differential equation for the time-evolution operator as follow

$$\eta_i - \kappa\frac{d^2}{dx_n^2}\eta_i = \xi_i + \kappa\frac{d^2}{dx_n^2}\xi_i. \tag{5.14}$$

---

[1]This multiplication can be done by taking the Fourier transform of ξ_i and rewriting it in reciprocal space and taking the exponential of the kinetic term also in reciprocal space. For convenience we avoided Fourier transforms and worked only with real space.

To solve Eq. (5.14) we need to use the finite difference method. We can define the derivative of a continuous function as

$$\frac{df}{dx_n} = \lim_{\Delta x_n \to 0} \frac{f(x_n + \Delta x_n) - f(x_n)}{\Delta x_n}, \tag{5.15}$$

and by discretizing the space we can write the derivative of a function

$$\frac{\partial f}{\partial x_n} \approx \frac{f_{i+1} - f_{i-1}}{\Delta x_n} \quad , \quad \frac{\partial^2 f}{\partial x_n^2} \approx \frac{f_{i+1} - 2f_i + f_{i-1}}{2\Delta x_n^2}. \tag{5.16}$$

Applying in Eq. (5.14) we get

$$\eta_i - \kappa \left(\frac{\kappa_{i+1} - 2\kappa_i + \kappa_{i-1}}{\Delta x_n^2} \right) = \xi_i + \kappa \left(\frac{\xi_{i+1} - 2\xi_i + \xi_{i-1}}{\Delta x_n^2} \right), \tag{5.17}$$

developing the terms above and making $\lambda_{x_n} = \frac{\kappa}{\Delta x_n^2} = \frac{i\hbar \Delta t}{4m\Delta x_n^2}$ we obtain

$$-\lambda_{x_n} \kappa_{i-1} + \kappa_i (1 + 2\lambda_{x_n}) - \lambda_{x_n} \kappa_{i+1} = \lambda_{x_n} \xi_{i-1} + \xi_i (1 - 2\lambda_{x_n}) + \lambda_{x_n} \xi_{i+1}, \tag{5.18}$$

where $\lambda_{x_n} = \left(\frac{\kappa}{\Delta x_n^2} \right) = \frac{i\hbar \Delta t}{4m\Delta x_n^2}$. From above equation we obtain a matrix equation system [108]:

$$\begin{pmatrix} D_1 & D_2 & 0 & 0 & \cdots \\ D_2 & D_1 & D_2 & 0 & \cdots \\ 0 & D_2 & D_1 & D_2 & \cdots \\ 0 & 0 & D_2 & D_1 & \ddots \\ 0 & 0 & 0 & \ddots & \ddots \end{pmatrix} \begin{pmatrix} \vdots \\ \eta_{i-1} \\ \eta_i \\ \eta_{i+1} \\ \vdots \end{pmatrix} = \begin{pmatrix} D_1' & D_2' & 0 & 0 & \cdots \\ D_2' & D_1' & D_2' & 0 & \cdots \\ 0 & D_2' & D_1' & D_2' & \cdots \\ 0 & 0 & D_2' & D_1' & \ddots \\ 0 & 0 & 0 & \ddots & \ddots \end{pmatrix} \begin{pmatrix} \vdots \\ \xi_{i-1} \\ \xi_i \\ \xi_{i+1} \\ \vdots \end{pmatrix}, \tag{5.19}$$

where the matrix terms are

$$D_2 = -\lambda_{x_n} \quad , \quad D_1 = 1 + 2\lambda_{x_n}, \tag{5.20a}$$

$$D_2' = \lambda_{x_n} \quad , \quad D_1' = 1 - 2\lambda_{x_n}. \tag{5.20b}$$

Using the matrix equation in Eq. (5.19) we can determine the values of η_i through computational subroutines, such as TRIDAG [109] since we know the values of ξ_i for all i points of the grid. Finally, we have the wave-packet at arbitrary time $t + \Delta t$ given by

$$|\Psi_i\rangle_{t+\Delta t} = \exp\left[-\frac{i}{2\hbar} V_i \Delta t \right] \eta_i. \tag{5.21}$$

As mentioned previously, if the system has more than one spatial variable, we can repeat the procedure of Eqs. (5.11) to (5.19) for the kinetic energy in each direction, performing only operations with tridiagonal matrices, one for each dimension, instead of having to do a matrix operation with a gigantic matrix that involves discretization in all the spatial variables, which is usually done when the Cayley's form is used without the SOT.

5.2 Hamiltonian depending on the Pauli matrices

There is a special group of Hamiltonians that can be rewritten in terms of the Pauli's matrices and the SOT can easily applied to them. In general, Hamiltonians can be rewritten in terms of Pauli matrices as

$$\vec{\sigma} = \sigma_x \hat{i} + \sigma_y \hat{j} + \sigma_z \hat{k}, \tag{5.22}$$

where

$$\sigma_x = \begin{pmatrix} 0 & 1 \\ 1 & 0 \end{pmatrix} \quad , \quad \sigma_y = \begin{pmatrix} 0 & -i \\ i & 0 \end{pmatrix} \quad , \quad \sigma_z = \begin{pmatrix} 1 & 0 \\ 0 & -1 \end{pmatrix}. \tag{5.23}$$

Some examples of Hamiltonians that can be written in this way are that describes the Zeeman effect and the continuum model of graphene [110].

Let us consider a general Hamiltonian written as

$$H = \vec{\Sigma} \cdot \vec{\sigma}. \tag{5.24}$$

The time-evolution operator is given by

$$\exp\left[-\frac{i}{\hbar}H\Delta t\right] = \exp\left[-\frac{i}{\hbar}\Delta t \vec{\Sigma} \cdot \vec{\sigma}\right] = \exp\left[-i\vec{S} \cdot \vec{\sigma}\right], \tag{5.25}$$

where $\vec{S} = \frac{\Delta t \vec{\Sigma}}{\hbar}$. We can write $\exp\left[-i\vec{S} \cdot \vec{\sigma}\right]$ as

$$\exp[-i\vec{S} \cdot \vec{\sigma}] = \sum_{n=0}^{\infty} \frac{(-i\vec{S} \cdot \vec{\sigma})^n}{n!}. \tag{5.26}$$

For $n = 0$ Eq. (5.26) reduces to 1, for $n = 1$ Eq. (5.26) becomes

$$\exp[-i\vec{S} \cdot \vec{\sigma}] = -i\vec{S} \cdot \vec{\sigma} = -i(S_x\sigma_x + S_y\sigma_y + S_z\sigma_z) = -i\begin{pmatrix} S_z & S_x - iS_y \\ S_x + iS_y & -S_z \end{pmatrix}, \tag{5.27}$$

For $n = 2$

$$\exp[-i\vec{S} \cdot \vec{\sigma}] = -\frac{1}{2!}\left[\begin{pmatrix} S_z & S_x - iS_y \\ S_x + iS_y & -S_z \end{pmatrix}\begin{pmatrix} S_z & S_x - iS_y \\ S_x + iS_y & -S_z \end{pmatrix}\right] = -\frac{1}{2!}S^2 I, \tag{5.28}$$

with I being $I = \begin{pmatrix} 1 & 0 \\ 0 & 1 \end{pmatrix}$. Making the same procedure until $n = 4$, we can rewrite Eq. (5.26) as

$$\sum_{n=0,2,4,...}^{\infty}\left[1 - \frac{1}{2!}S^2 I + \frac{1}{4!}S^4 I + \cdots\right] - i\sum_{n=1,3,5,...}^{\infty}\left[S^0\left(\frac{\vec{S} \cdot \vec{\sigma}}{1}\right) - S^2\frac{\vec{S} \cdot \vec{\sigma}}{3!} + \cdots\right]. \tag{5.29}$$

By assuming $2k = n$, we can arrive at a recurrence formula for the even and odd terms, and the series above can be rewritten

$$
\sum_{k=0}^{\infty} \frac{(\vec{S} \cdot \vec{\sigma})^{2k}}{2k!} - i \sum_{k=0}^{\infty} \frac{(-1)^k (\vec{S} \cdot \vec{\sigma})^{2k+1}}{(2k+1)!}
$$
$$
= \sum_{k=0}^{\infty} \frac{(-1)^k S^{2k} I}{2k!} - i \sum_{k=0}^{\infty} \frac{(-1)^k S^{2k} (\vec{S} \cdot \vec{\sigma})}{(2k+1)!}. \tag{5.30}
$$

From the recurrence formula, Eq. (5.29) can be rewritten in terms of cosine and sine functions

$$
\left[1 - \frac{(S^2 I)}{2!} + \frac{(S^2 I)^2}{4!} + \cdots \right] - i \left[S^0 (\vec{S} \cdot \vec{\sigma}) - \frac{S^2 (\vec{S} \cdot \vec{\sigma})}{3!} + \cdots \right]. \tag{5.31}
$$

So the time-evolution operator for Hamiltonians written in terms of Pauli's matrices can be written as

$$
\exp\left[-i \vec{S} \cdot \vec{\sigma} \right] = \begin{pmatrix} \cos(S) & 0 \\ 0 & \cos(S) \end{pmatrix} - i \frac{\sin(S)}{S} \begin{pmatrix} S_z & S_x - iS_y \\ S_x + iS_y & -S_z \end{pmatrix}, \tag{5.32}
$$

where S_i and S are the terms and the module of the vector $\vec{S}$ as defined previously. Thus, the temporal evolution operation becomes a matrix multiplication. Furthermore, this matrix form is exact for the temporal evolution operator, without any truncation in the expansion, that is, considering all terms.

The time-evolution in Eq. (5.32) will be used in further chapters to investigate the wave-packet dynamics in phosphorene multilayers (Chapter 6), anisotropic semiconductor quantum-wires (Chapter 7) and in graphene using the position-dependent translation operator formalism (Chapter 8).

6

Wave-packet dynamics in multilayer phosphorene

In this chapter we investigate the dynamics of Gaussian wave packets in multilayer black phosphorus (BP). Time-dependent average position and velocity are calculated analytically and numerically by using a continuum model and a method based on the split-operator technique, respectively. By analyzing the wave packet trajectories with non-vanishing initial momentum along armchair direction, we observed transient spatial oscillations due to the effect known as zitterbewegung (ZBW). We demonstrated that the trembling motion along the armchair direction at small times is unavoidable even for null initial momentum. We verified that the ZBW is directly related to the splitting of the wave packet into two parts moving with opposite velocities, similar to graphene, and the linear dependence on momentum in the off-diagonal terms in the Hamiltonian. Unique to BP, the two portions of the propagated wave packets have an asymmetric shape for unbalanced $\left([1,0]^T\right)$ and phased different $\left([1,i]^T\right)$ initial pseudospin components, which also play a determining role in the amplitude, frequency and duration time of the transient oscillations. As a consequence of the anisotropy on the N-layer BP energy bands, the wave packet propagates non-uniformly along the different directions and deforms into an elliptical shape. By comparing our analytical results with those ones obtained by the split-operator technique, we confirmed quantitative agreement between them, except for large values of wave vector and after long time steps.

6.1 Motivation

The well-known zitterbewegung (ZBW) phenomenon, a trembling motion caused by interference between positive and negative energy states, [111, 112] was predicted by Schrödinger in 1930 for the motion of relativistic electrons in vacuum governed by the Dirac equation and has been subject of renewed interest over the past decade in various condensed matter systems. [12, 113] This oscillatory dynamic of the center of a free wave packet is manifested in the time evolution of the expectation values of some physical observable, such as position, velocity, current and spin angular momentum. The characteristic frequency of ZBW motion is determined by the gap between the two states with

positive and negative energies and is of the order of $2m_0c^2/\hbar$, where m_0 is the bare electron mass, c is the speed of light, and $\hbar$ is the Planck constant, whereas the amplitude of oscillations is of the order of the Compton wavelength, i.e. $\hbar/m_0c$. This corresponds to large oscillation frequencies of $\approx 10^{21}$ Hz and small oscillation amplitudes of $\approx 10^{-3}$ Å, making its direct experimental observation a really hard task. [113, 114, 115, 116, 117, 9, 17] Although, the ZBW is in principle a relativistic effect, it may arise even for a nonrelativistic particle moving in crystalline solids if their band structures could be represented by a two-band model reminiscent of the Dirac equation,[118, 119, 120] or for quasiparticles governed by the Bogoliubov-de Gennes equations in superconductors,[121, 122] in which the energy-wavevector dependence is similar to the relativistic relation, or in some semiconductor nanostructures with spin-orbit coupling [121, 13, 123, 124, 125, 126, 127, 128].

Two of the pioneering works investigating the ZBW effect in narrow-gap semiconductors are the theoretical studies of Schliemann [13] and Zawadzki [129] in 2005, which considered the coupling between the positive-negative energy eigenstates of the quantum systems using a two energy bands model. Zawadzki [129] demonstrated that semiconductor electrons experience a ZBW, by arguing the analogy between the band structure of narrow-gap semiconductors and the Dirac equation for relativistic electrons in vacuum. The former exhibits more experimentally favorable frequency and amplitude characteristics than electrons in a vacuum. Schliemann et al.~[13, 123] studied the ZBW of electronic wave packets in III-V zinc-blende semiconductor quantum wells in the presence of spin-orbit coupling of the Rashba and Dresselhaus type, by using the Hamiltonian of spin splitting (the Bychkov-Rashba mechanism), which requires structure inversion asymmetry of the system. These works triggered a strong interest in the theoretical investigations of wave packet dynamics and ZBW oscillations in other physical systems, as for instance: 2D photonic crystal, [130, 131] 2D sonic crystal, [132] trapped ion, [16, 133] hole Luttinger systems, [134, 135] ultra-cold atoms, [136, 137] topological insulators, [138] and electromagnetic pulses propagating through metamaterials presenting an optical analog ZBW effect [139]. Experimental observations of ZB phenomenon have been reported in 2008 for macroscopic sonic crystals, [132] in 2010 for trapped ion systems [16] and for photonic superlattices [131], and in 2013 for spin-orbit-coupled Bose-Einstein condensates [140, 141].

In the last two decades, the production of graphene has led to a significant level of interest on the physics of layered materials. [3, 70, 62, 142] This interest is not only due to its possible future technological applications, but also because it provides the possibility to probe interesting phenomena predicted by quantum field theories not found in conventional semiconductors and metals. One of these exotic properties of low-energy electrons in single and few-layers graphene, described by the zero mass Dirac equation, is the existence of ZBW as reported in Refs. [143, 144, 145, 146, 147, 14, 148, 149, 150, 151, 152] for monolayer and [143, 147, 15] bilayer graphene. Maksimova et al. [144] in 2008 analyzed the detailed description of wave packet evolution in monolayer graphene, using the Green's function representation and the low-energy Dirac equation, and investigated the

influence on the wave packet dynamics of different pseudospin polarizations for the initial wave function and the phenomenon of ZBW of the packet center. Similar investigation was performed numerically by Chaves et al. [110] in 2010 by means the split-operator technique. Rusin and Zawadzki [147] studied the evolution of the wave packet in bilayer graphene and found the analytical expressions for the pseudospin components of wave function and average position operator as well as analytical results for the ZBW oscillations. They demonstrated that the transient character ZBW in bilayer graphene is related to the increasing spatial separation of the sub-packets corresponding to the positive and negative energy states moving in opposite directions, in a similar way to some pseudospin configurations in monolayer graphene, and not only due to the packet's slow spreading which in turn is responsible for the attenuation and decay of ZBW.

Most recently, there is growing interests in Black Phosphorus (BP), also known as phosphorene. [46, 19, 20, 32, 31, 153] It is a semiconductor with puckered structure due to its sp^3 hybridization and displays a tunable band gap [46, 19, 31, 33, 154, 155, 156, 47, 157, 158, 159, 39, 160, 161] ranging of 1.8 eV for single-layer BP to ≈ 0.4 eV for bulk samples, which is very relevant for possible technological applications. [46, 19, 162, 163, 164, 165, 166] BP presents a highly anisotropic band structure and consequently a large anisotropic effective mass. [39] Although previous works have studied wave-packet propagation for standard semiconductors, [111, 112, 13, 123, 127, 128, 129] monolayer [143, 144, 145, 146, 147, 14, 148, 149, 150, 151, 152] and bilayer [143, 147, 15] graphene, silicene, [167] and transition metal dichalcogenide, [168] no similar theoretical investigation on wave-packet propagation in N-layer BP system was reported in the literature, to the best of our knowledge. Owing the linear terms in momentum in the BP Hamiltonian, strong coupling between conduction and valence states, and small band gap, it is expected very pronounced ZBW effects in BP. Therefore, it is also interesting to see whether the results observed in these cited 2D materials differ or are similar for multilayer phosphorene, and if the anisotropic character of electronic properties of multilayer phosphorene implies in any atypical feature in the dynamics of the wave packets.

In this chapter we present the theoretical models used to describe the time evolution of wave packets in multilayer phosphorene systems, based on the continuum approximation [39, 93, 169] for low-energy electrons. We use Green's function formalism and the split-operator technique [110, 170, 171, 79, 99, 172, 173, 174, 175, 176, 177, 178, 179, 180] for the expansion of the time-evolution operator. The analytical expressions for some physical quantities, such as the average values of position operator and the components of wave function, are found for different configuration of initial pseudospin polarization and these results are compared with the numerical split-operator ones in order to check the limit of accuracy of the both models. We also show the probability amplitudes of the wave packet at different time steps ($t > 0$) to understand the origin of transient character of the oscillations on the average positions. An important remark concerning the wave packet dynamics is about the oscillatory behavior of the velocity as a manifestation of
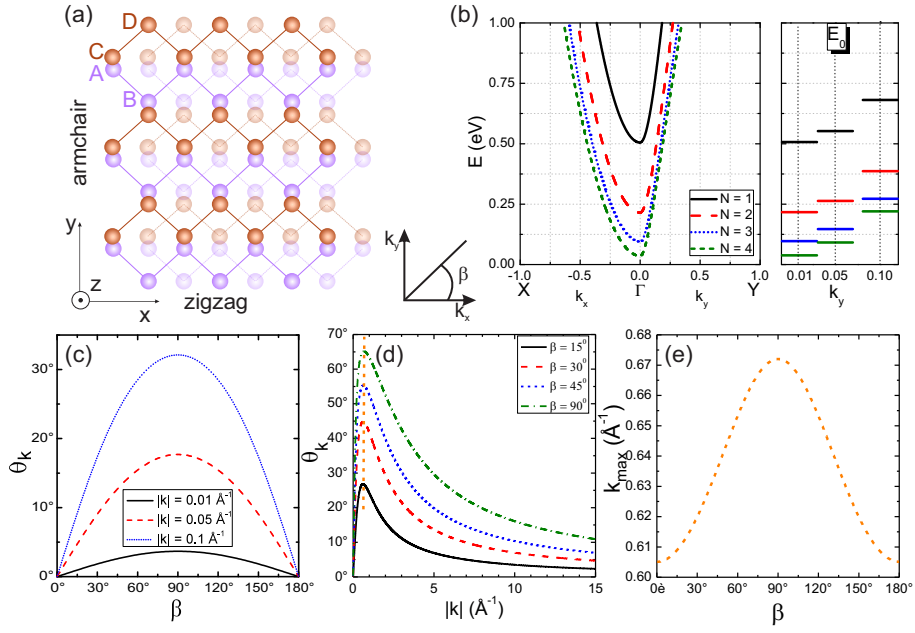
Figure 6.1: (Color online) (a) Top view of lattice structure of AB-stacked N-layer BP system, emphasizing the orientations of the lattice adopted in this work and the four sublattices: A and B at bottom sublayer (purple symbols), and C and D at top sublayer (brown symbols). The x and y coordinates correspond to the zigzag and armchair directions, respectively, and z-direction is the out-of-plane direction. (b) Left: Lowest electronic energy band obtained by diagonalizing the Hamiltonian (7.1) with $n = N$ for monolayer (black solid curve), bilayer (red dashed curve), trilayer (blue dot curve), and tetralayer (green short-dash curve) phosphorene. Right: Initial wave packet energy for the corresponding initial wave vector assumed here in the wave packet simulation. θ_k as a function of (c) the polar angle β for fixed momentum vector and (d) the momentum vector for fixed polar angle β. (e) Momentum value for θ_{max} as a function of the polar angle β, i.e. $|k|$ in which θ_k has a maximum value as emphasized in the orange dashed line in panel (d).

zitterbewegung on the wave packet motion. Additionally, we calculate the velocity operators and their commutators with the continuum Hamiltonian for multilayer phosphorene in order to verify whether v_x and v_y are constants of motion or not, and thus check the consistency of our formalism.

6.2 Continuum approximation for N-layer phosphorene and the polarization angle

Based on the tight-binding model for multilayer phosphorene reported by Rudenko et al. [181] involving ten intralayer and four interlayer hopping parameters and with the layers alignments obeying the AB-stacking (see Fig. 6.1(a)), a simple analytical model was

Table 6.1: d

erived by the expansion of the structure factor coefficients of the tight-binding model for multilayer BP.]Hamiltonian parameters of the effective continuum model [Eq. (7.1)] derived by the expansion of the structure factor coefficients of the tight-binding model for multilayer BP (see Ref. [39]).

Parameter	Value	Parameter	Value
u_0	-0.414 eV	$\delta_{AC'}$	0.712 eV
η_x	1.265 eV·Å^2	$\delta_{AD'}$	-0.132 eV
η_y	-1.384 eV·Å^2	$\eta_{AC'}$	-0.9765 eV·Å^2
δ	0.919 eV	$\eta_{AD'}$	2.699 eV·Å^2
γ_x	2.510 eV·Å^2	$\gamma_{AC'}$	2.443 eV·Å^2
γ_y	2.035 eV·Å^2	$\gamma_{AD'}$	0.364 eV·Å^2
χ	5.896 eV·Å	$\chi_{AC'}$	2.071 eV·Å

recently derived within the long-wavelength approximation to describe low-energy charge carriers in N-layer BP sheet around Γ point. [39] In this continuum approximation, the Hamiltonian for the N-layer BP is composed by N blocks of 2×2 monolayer-type BP Hamiltonians where each one of these effective monolayer Hamiltonians is formed by layer-dependent Hamiltonian coefficients and reads in momentum space as

$$\mathcal{H} = \begin{pmatrix} u_0^n + \eta_x^n k_x^2 + \eta_y^n k_y^2 & \delta^n + \gamma_x^n k_x^2 + \gamma_y^n k_y^2 + i\chi^n k_y \\ \delta^n + \gamma_x^n k_x^2 + \gamma_y^n k_y^2 - i\chi^n k_y & u_0^n + \eta_x^n k_x^2 + \eta_y^n k_y^2 \end{pmatrix}, \tag{6.1}$$

where $u_0^n = u_0 + \lambda_n \delta_{AD'}$, $\eta_x^n = \eta_x + \lambda_n \eta_{AD'}$, $\eta_y^n = \eta_y + \lambda_n \gamma_{AD'}$, $\delta^n = \delta + \lambda_n \delta_{AC'}$, $\gamma_x^n = \gamma_x + \lambda_n \eta_{AC'}$, $\gamma_y^n = \gamma_y + \lambda_n \gamma_{AC'}$, $\chi^n = \chi + \lambda_n \chi_{AC'}$, $\lambda_n = \cos[n\pi/(N+1)]$, N is the number of BP layers and $n \in [1, N]$. The lowest electron-hole energy bands are obtained by assuming $n = N$, being the value we consider here throughout all our analysis (i.e. $n = N = 1, 2, 3, 4$ for monolayer, bilayer, trilayer and tetralayer phosphorene, respectively). The Hamiltonian parameter values are summarized in Table I, being the same ones used in Ref. [39], where they were obtained by expanding the tight-binding structure factors for BP system up to second oder in k. These coefficient values of the Hamiltonian (7.1) include the contribution from the tight-binding hopping energies and the lattice geometry of the BP sheet, incorporating a direct link between the microscopic tight-binding description and the continuum approximation. Refs. [39, 93, 169] have showed that the continuum model for BP system is very suited for describing the physics of large BP systems, yielding very accurate results within its limit of validation, and it is less computationally demanding than microscopic models, as for instance tight-binding model and first-principles calculations.

The eigenstates of $\mathcal{H}$ are two-component spinors given by

$$\Psi = \begin{pmatrix} \phi_1 \\ \phi_2 \end{pmatrix} = \begin{pmatrix} \phi_A + \phi_D \\ \phi_B + \phi_C \end{pmatrix}, \tag{6.2}$$

where $\phi_{A,B,C,D}$ are the probability amplitudes for finding electrons on the atomic sites
A, B, C, and D, respectively, which are related to the four phosphorus atoms that are
contained in the unit cell of a single layer of BP, as shown in Fig. 6.1(a). The Hamiltonian
(7.1) was obtained by taking into account the sublattice symmetry between atomic sites
A/D and B/C in each monolayer BP, due to the D_{2h} group invariance of the BP lattice[39,
93] and, as a consequence, the two-component wave function (6.2) is composed by the
combination of these sublattices in pairs. Rewriting $\mathcal{H}$ in a more compact form in polar
notation, in order to highlight the angular dependence, we find

$$\mathcal{H} = \begin{pmatrix} \varepsilon_1 & \varepsilon_2 e^{i\theta_k} \\ \varepsilon_2 e^{-i\theta_k} & \varepsilon_1 \end{pmatrix}, \tag{6.3}$$

with

$$\varepsilon_1(\vec{p}) = \frac{f_c + f_v}{2}, \tag{6.4a}$$

$$\varepsilon_2(\vec{p}) = \sqrt{\left(\frac{f_c - f_v}{2}\right)^2 + \left(\frac{\chi^n p_y}{\hbar}\right)^2}, \tag{6.4b}$$

$$\theta_k(\vec{p}) = \arctan\left[\frac{2\chi^n p_y}{\hbar(f_c - f_v)}\right], \tag{6.4c}$$

where f_c and f_v are associated with the conduction (c) and valence (v) energy dispersion
terms, respectively, being defined as

$$f_{\substack{c\\v}} = (u_0^n \pm \delta^n) + (\eta_x^n \pm \gamma_x^n)\frac{p_x^2}{\hbar^2} + (\eta_y^n \pm \gamma_y^n)\frac{p_y^2}{\hbar^2}. \tag{6.5}$$

By diagonalizing Eq. (7.1) or equivalently Eq. (6.3), we obtain the dispersion relations for
electrons and holes, given by

$$E_{\vec{p},s} = \varepsilon_1(\vec{p}) + s\varepsilon_2(\vec{p}), \tag{6.6}$$

with $s = +1(-1)$ for electrons (holes), i.e. the plus (minus) sign yields the conduction
(valence) band. Fig. 6.1(b) shows the lowest electronic energy levels for (black solid curve,
$N = 1$) monolayer, (red dashed curve, $N = 2$) bilayer, (blue dot curve, $N = 3$) trilayer,
and (green short-dash curve, $N = 4$) tetralayer phosphorene. In the wave packet dynam-
ics, we choose the initial wave packet energies for electrons standing on these lower bands,
as shown in the right panel of Fig. 6.1(b) for the three assumed initial wave vectors for a
fixed number of layers. Note that, as seen in Fig. 6.1(b): (i) the band gap is tunable by
the number of BP layers, decreasing as N increases, and (ii) phosphorene band structure
is highly anisotropic, exhibiting for small momentum values an approximately parabolic
dispersion along $\Gamma - X$ (zigzag) direction and approximately linear dispersion along $\Gamma - Y$
(armchair) direction, therefore, behaving similarly as Schrödinger and Dirac particles, re-
spectively. As we will discuss further, the linear dependence on k_y in the out-of-diagonal
terms of Eq. (7.1) and this anisotropic feature of the energy levels and, consequently, of
effective masses and group velocities,[39] bring up very interesting consequences in the
wave packet dynamics in phosphorene.

The corresponding eigenstates of Hamiltonian Eq. (6.3) are

$$\Psi_{\vec{p},s} = \frac{1}{\sqrt{2}} \begin{pmatrix} 1 \\ se^{i\theta_k(\vec{p})} \end{pmatrix}. \tag{6.7}$$

Note that this expression is similar to the graphene's eigenstates, [144] but with the fundamental difference that for N-layer phosphorene the phase angle θ_k does not necessarily correspond to the polar angle β associated with the momentum vector:

$$\theta_k(|k|, \beta) = \arctan\left[\frac{\chi^n |k| \sin\beta}{\delta^n + \left(\gamma_x^n \cos^2\beta + \gamma_y^n \sin^2\beta\right)|k|}\right]. \tag{6.8}$$

This can be seen in Fig. 6.1(c), which shows the phase angle θ_k as a function of the polar angle β for three different momentum vectors (whose values are the ones used in the results for the wave packet simulation in Sec. 6.5). It is a very crucial point concerning the initial set up to define the direction of the wave packet propagation. For instance, in the cases of isotropic semiconductors and graphene systems, [144, 110, 170, 171] the phase angle is exactly the same as the polar angle in the momentum space, i.e. $\theta_k = \beta = \arctan(p_y/p_x)$, making the definition of the initial propagation angle value more direct and intuitive. Furthermore, it can be noticed by Fig. 6.1(c) that θ_k exhibits a maximum value at $\beta = \pi/2$ for all momentum values and this critical value $\theta_k(\beta = \pi/2) = \theta_k^{max}$ is energy-momentum-dependent. Figures 6.1(d) and 6.1(e) confirm these statements. From Fig. 6.1(d) it is seen that, as the momentum $|k|$ increases, θ_k approaches a maximum value (emphasized by the orange dashed line) and then decays to zero. The momentum value for θ_k^{max} (i.e. $|k|_{max}$ in which θ_k has a maximum value) is slightly different for different values of the polar angle β, as shown in Fig. 6.1(e). According to Fig. 6.1(e) and also by performing the differentiation of Eq. (6.4c) with respect to $|k|$ at $\beta = \pi/2$, i.e. $(\partial\theta_k/\partial|k|)|_{\beta=\pi/2} = 0$, one can find that $|k|_{max} = 0.67201$ Å^{-1} and the critical phase angle is $\theta_k^{max} = 65.114°$. In summary, the phase angle can assume values in the threshold range between: $-\theta_k^{max} \leq \theta_k \leq \theta_k^{max}$, unlike the polar angle β that can assume any value.

6.3 Green's function formalism for N-layer phosphorene

We now shall follow a similar procedure as reported by Maksimova *et al.* in Ref. [144], based on the Green's function formalism. According to Eq. (7.9a), the time-dependent eigenfunctions of Hamiltonian Eq. (6.3) are given by

$$\varphi_{\vec{p},s}(\vec{r}, t) = \frac{1}{2\sqrt{2\pi}} \exp\left[i\frac{\vec{p}\cdot\vec{r}}{\hbar} - i\frac{E_{\vec{p},s}t}{\hbar}\right] \begin{pmatrix} 1 \\ se^{i\theta_k(\vec{p})} \end{pmatrix}, \tag{6.9}$$

with $E_{\vec{p},s}$ being the energy eigenvalues given in Eq. (6.6). The initial wave packet $\Psi(\vec{r}, 0)$, at $t > 0$ acquires a form that can be calculated as

$$\Psi_\mu(\vec{r}, t) = \int G_{\mu,\nu}(\vec{r}, \vec{r'}, t)\Psi_\nu(\vec{r'}, 0)\, d\vec{r'}, \tag{6.10}$$

where $G(\vec{r}, \vec{r'}, t)$ is the 2×2 Green's function matrix and the matrix indices $(\mu, \nu = 1, 2)$ correspond to the two components of the pseudospin eigenfunctions. The matrix elements of Green's functions are defined as

$$G_{\mu,\nu}(\vec{r}, \vec{r'}, t) = \sum_{s=\pm 1} \int d\vec{p}\, \varphi_{\vec{p},s,\mu}(\vec{r}, t) \varphi^*_{\vec{p},s,\nu}(\vec{r'}, 0). \tag{6.11}$$

Replacing Eq. (7.9b) into Eq. (6.11) and after some straightforward algebra, one finds the components of Green's function matrix, such as

$$G_{11}(\vec{r}, \vec{r'}, t) = G_{22}(\vec{r}, \vec{r'}, t) = \frac{1}{(2\pi\hbar)^2} \int \exp\left[\frac{i\vec{p}\cdot(\vec{r}-\vec{r'})}{\hbar}\right] \exp\left[\frac{-i\varepsilon_1(\vec{p})t}{\hbar}\right] \cos\left[\frac{\varepsilon_2(\vec{p})t}{\hbar}\right] d\vec{p},$$
$$\tag{6.12a}$$

$$G_{12}(\vec{r}, \vec{r'}, t) = \frac{-i}{(2\pi\hbar)^2} \int e^{-i\theta_k(\vec{p})} \exp\left[\frac{i\vec{p}\cdot(\vec{r}-\vec{r'})}{\hbar}\right] \exp\left[\frac{-i\varepsilon_1(\vec{p})t}{\hbar}\right] \sin\left[\frac{\varepsilon_2(\vec{p})t}{\hbar}\right] d\vec{p},$$
$$\tag{6.12b}$$

$$G_{21}(\vec{r}, \vec{r'}, t) = \frac{-i}{(2\pi\hbar)^2} \int e^{i\theta_k(\vec{p})} \exp\left[\frac{i\vec{p}\cdot(\vec{r}-\vec{r'})}{\hbar}\right] \exp\left[\frac{-i\varepsilon_1(\vec{p})t}{\hbar}\right] \sin\left[\frac{\varepsilon_2(\vec{p})t}{\hbar}\right] d\vec{p}. \tag{6.12c}$$

To describe the time evolution of an arbitrary state, we choose the initial wave function to be a Gaussian wave packet, for three main reasons: (i) Gaussian wave packets describe roughly localized quantum states for which the product of the uncertainties in position and momentum is minimal; (ii) by setting the initial state as Gaussian wave packet, this situation covers most cases of practical interest, because any wave packet can be approximated by a superposition of a finite number of Gaussian states; (iii) since the ZBW is, by nature, not a stationary state but a dynamical phenomenon, it is natural to study it with the use of wave packets. [111, 129, 147] The assumed initial Gaussian wave packet, with width d and non-vanishing average momentum along y-direction ($p_{0y} = \hbar k_0$), is given by:

$$\Psi(\vec{r}, t) = \frac{f(\vec{r})}{\sqrt{|c_1|^2 + |c_2|^2}} \begin{pmatrix} c_1 \\ c_2 \end{pmatrix}, \tag{6.13a}$$

$$f(\vec{r}) = \frac{1}{d\sqrt{\pi}} \exp\left[\frac{-r^2}{2d^2} + ik_0 y\right]. \tag{6.13b}$$

where c_1 and c_2 determine the initial pseudospin polarization of the injected wave packet and are related to the two pseudospin components in Eqs. (6.2) and (7.9a). Now inserting Eqs. (6.13a) and (6.13b) into Eq. (6.10) and using the expressions of the components of Green's function matrix (Eqs. (6.12a)-(6.12c)), one obtains the components of the time evolved wave packet $\Psi(\vec{r}, t)$ at a later time t in the following two-component form:

$$\begin{pmatrix} \Psi_1(\vec{r}, t) \\ \Psi_2(\vec{r}, t) \end{pmatrix} = \frac{1}{\sqrt{|c_1|^2 + |c_2|^2}} \begin{pmatrix} c_1\Phi_1(\vec{r}, t) + c_2\Phi_3(\vec{r}, t) \\ c_1\Phi_2(\vec{r}, t) + c_2\Phi_4(\vec{r}, t) \end{pmatrix} \tag{6.14}$$

where

$$\Phi_1(\vec{r}, t) = \int G_{11}(\vec{r}, \vec{r'}, t) f(\vec{r'}) d\vec{r'}$$
$$= \frac{de^{-k_0^2 d^2/2}}{2\hbar^2\sqrt{\pi^3}} \int \exp\left[\frac{i\vec{p}\cdot\vec{r}}{\hbar} - \frac{p^2 d^2}{2\hbar^2} + \frac{p_y k_0 d^2}{\hbar} - \frac{i\varepsilon_1(\vec{p})t}{\hbar}\right] \cos\left(\frac{\varepsilon_2(\vec{p})t}{\hbar}\right) d\vec{p}, \quad (6.15a)$$

$$\Phi_2(\vec{r}, t) = \int G_{21}(\vec{r}, \vec{r'}, t) f(\vec{r'}) d\vec{r'}$$
$$= \frac{-ide^{-k_0^2 d^2/2}}{2\hbar^2\sqrt{\pi^3}} \int e^{i\theta_k(\vec{p})} \exp\left[\frac{i\vec{p}\cdot\vec{r}}{\hbar} - \frac{p^2 d^2}{2\hbar^2} + \frac{p_y k_0 d^2}{\hbar} - \frac{i\varepsilon_1(\vec{p})t}{\hbar}\right] \cos\left(\frac{\varepsilon_2(\vec{p})t}{\hbar}\right) d\vec{p},$$
$$(6.15b)$$

$$\Phi_3(\vec{r}, t) = \int G_{12}(\vec{r}, \vec{r'}, t) f(\vec{r'}) d\vec{r'}$$
$$= \frac{-ide^{-k_0^2 d^2/2}}{2\hbar^2\sqrt{\pi^3}} \int e^{-i\theta_k(\vec{p})} \exp\left[\frac{i\vec{p}\cdot\vec{r}}{\hbar} - \frac{p^2 d^2}{2\hbar^2} + \frac{p_y k_0 d^2}{\hbar} - \frac{i\varepsilon_1(\vec{p})t}{\hbar}\right] \cos\left(\frac{\varepsilon_2(\vec{p})t}{\hbar}\right) d\vec{p},$$
$$(6.15c)$$

and $\Phi_1(\vec{r}, t) = \Phi_4(\vec{r}, t)$, according to Eq. (6.12a).

The time-dependent expectation value of the position operator can be calculated as

$$\langle \vec{r}(t) \rangle = \sum_{j=1}^{2} \int d\vec{p}\, \Psi_j^*(\vec{p}, t) i\hbar \frac{d\Psi_j(\vec{p}, t)}{d\vec{p}}, \quad (6.16)$$

with Ψ in momentum representation. Note that analytical expressions for two components of wave function were found for N-layer BP (Eqs. (6.14) and (6.15a)-(6.15c)), which allows us to investigate the ZBW phenomenon of a Gaussian wave packet for different relations between the initial electron amplitudes on the sublattices, as will be discussed in Sec. 6.5, by means of the analytical calculation of the time dependent expectation values of the position (x, y) of the center of the injected wave packet according to Eq. (6.16).

6.4   Split-operator technique for N-layer phosphorene

In this section, we introduce the split-operator technique for wave packet propagation in N-layer phosphorene, based on the Hamiltonian within the continuum approximation (Eq. (7.1)). This approach is similar to the one developed by A. Chaves et al. [110, 170, 79] for calculating the dynamics of a wave packet in graphene by taking a Dirac-Weyl Hamiltonian. It consists in the solution of time-dependent Schrödinger equation by taking a separation of the time evolution operator in a series of matrices, such that the propagated wave function after a time step Δt can be calculated by applying the expanded exponential time evolution operator on the wave packet at any instant t. [110, 170, 171, 79, 99, 172, 173, 174, 175, 176, 177, 178, 179, 180] The advantage of this technique is due to its flexibility inasmuch as it can be applied for BP systems under arbitrary external potentials and magnetic fields. Besides, it allows to track the center of mass trajectories, which is very important for the understanding of ZBW phenomenon in the current work.

Let us first find the time evolution operator as a series of matrix multiplications for the Hamiltonian Eq. (7.1) and then apply it for the time evolution of the wave packet, following the split-operator method for spin-dependent Hamiltonian as described in Refs. [110, 170, 79]. The long-wavelength Hamiltonian Eq. (7.1) in the presence of a external potential $V(x, y)$ can be written in terms of Pauli matrices $\vec{\sigma} = (\sigma_x, \sigma_y)$ as

$$\mathcal{H} = \mathcal{H}_k + \mathcal{H}_r, \tag{6.17a}$$

$$\mathcal{H}_k = \mathcal{H}_0 1 + \vec{\alpha} \cdot \vec{\sigma} \tag{6.17b}$$

$$\mathcal{H}_r = V(\vec{x}, \vec{y}) 1, \tag{6.17c}$$

where we separated it keeping only the terms which depend on the wave vector in $\mathcal{H}_k$, and on the real-space coordinates in $\mathcal{H}_r$. 1 denotes the 2×2 unit matrix, and

$$\mathcal{H}_0 = u_0^n + \eta_x^n k_x^2 + \eta_y^n k_y^2, \tag{6.18a}$$

$$\vec{\alpha} = (\alpha_x, \alpha_y) = \left(\delta^n + \gamma_x^n k_x^2 + \gamma_y^n k_y^2, -\chi^n k_y \right). \tag{6.18b}$$

Following the split-operator method, the time-evolution operator for the Hamiltonian $\mathcal{H}$ [Eq. (6.17a)] can be approximated as

$$\exp\left[-\frac{i\Delta t}{\hbar}\mathcal{H}\right] \approx \exp\left[-\frac{i\Delta t}{2\hbar}\mathcal{H}_r\right] \exp\left[-\frac{i\Delta t}{\hbar}\mathcal{H}_k\right] \exp\left[-\frac{i\Delta t}{2\hbar}\mathcal{H}_r\right], \tag{6.19}$$

with an error on the order of $\mathcal{O}(\Delta t^3)$, due to the non-commutativity between $\mathcal{H}_k$ e $\mathcal{H}_r$. Since $\mathcal{H}_k$ does not explicitly depend on time and $[\mathcal{H}_0 1, \vec{\alpha} \cdot \vec{\sigma}] = 0$, the momentum-space term of the Hamiltonian, Eq. (6.17b), is given by

$$\exp\left[-\frac{i\Delta t}{\hbar}\mathcal{H}_k\right] = \exp\left[-\frac{i\Delta t}{\hbar}\mathcal{H}_0 1\right] \exp\left[-i\vec{A} \cdot \vec{\sigma}\right], \tag{6.20}$$

where $\vec{A} = \vec{\alpha} \Delta t / \hbar$. Using the properties of the Pauli matrices for the second term in Eq. (6.20), one finds

$$
\begin{aligned}
\mathcal{M}_A &= \exp\left[-i\vec{A} \cdot \vec{\sigma}\right] \\
&= \cos(A) 1 - \frac{i \sin(A)}{A} \begin{pmatrix} 0 & A_x - iA_y \\ A_x + iA_y & 0 \end{pmatrix},
\end{aligned}
\tag{6.21}
$$

where $A = |\vec{A}|$, whereas the first term of Eq. (6.20) is equivalent to

$$\mathcal{M}_{\mathcal{H}_0} = \exp\left[-i\mathcal{H}_0 1 \Delta t / \hbar\right] = 1 \exp\left[-i\mathcal{H}_0 \Delta t \hbar\right]. \tag{6.22}$$

Thus, the time evolution operation is represented by a series of 2×2 matrices multiplications.

The time evolution of $\Psi(\vec{r}, t)$ can be computed by applying the time evolution operator, Eq. (6.19), to obtain the propagated wave function after a time step $t + \Delta t$, such as

$$\Psi(\vec{r}, t + \Delta t) = e^{-i\mathcal{H}\Delta t / \hbar} \Psi(\vec{r}, t) = \mathcal{M}_r \mathcal{M}_k \mathcal{M}_r \Psi(\vec{r}, t), \tag{6.23}$$

with $\mathcal{M}_k = \mathcal{M}_A \mathcal{M}_{H_0}$. Since $\mathcal{M}_{\mathcal{H}_0}$ and $\mathcal{M}_A$ depend on the wave vectors k_x and k_y, the matrix multiplications before (afterwards) of the matrix $\mathcal{M}_k$ are computed in reciprocal space by performing a direct (inverse) Fourier transform on the function, in order to rewrite it in a reciprocal (real) space where the k's are numbers, instead of derivatives. Notice that, in the absence of external fields $V(x, y) = 0$, the separation between the real and reciprocal space-dependent terms in Eqs. (6.17a) and (6.19) is no longer necessary, and the resulting matrix will have an exact representation of the time evolution operator, including all the terms of the expansion of the exponential. In this case, there will be no error induced by the non-commutativity of the involved operators. Although we developed this technique in a more general way for an arbitrary potential, we investigated here the simple case with no external fields.

The initial wave packet is assumed as a circularly symmetric Gaussian distribution, multiplied by the pseudospinor (Eq. (6.2)) that accounts for the probability distributions over the two pairs of coupled sublattices of phosphorene (labeled c_1 for $\phi_A + \phi_D$ and c_2 for $\phi_B + \phi_C$), and by a plane wave with wave vector $\vec{k} = (k_0 \cos \beta, k_0 \sin \beta)$, such as

$$\Psi(\vec{r}, 0) = N \begin{pmatrix} c_1 \\ c_2 \end{pmatrix} \exp \left[-\frac{(x - x_0)^2 + (y - y_0)^2}{d^2} + i(\vec{k} \cdot \vec{r}) \right],$$

(6.24)

where N is a normalization factor, (x_0, y_0) are the coordinates of the center of the Gaussian wave packet in the real space, and d is its width. The pseudospin polarization $[c_1, c_2]^T$ of the wave packet plays an important role in defining the direction of propagation (see Eq. (7.9a)). It is worth to point out that, for phosphorene, the phase angle θ_k does not correspond to the polar angle β associated with the momentum vector (see Eq. (6.8)), such that the characterization of the pseudospin polarization angle and consequently the direction of propagation are not directly related, as it is, for example, in graphene, where we have a wave packet propagating along the $y-$ and $x-$direction in cases of the pseudospin $[1, i]^T$ and $[1, 1]^T$, respectively. [170, 171, 176, 177, 178] Unless otherwise explicitly stated in the text, we consider that the wave packet starts at $(x_0, y_0) = (0, 0)$ Å and its width is $d = 100$ Å. In order to compare the results obtained by the method based on split-operator technique developed in the current section with the ones within the green's function formalism (Sec. 6.3), we assume $k_0^x = 0$ in Eq. (8.19) as in Eq. (6.13b).

6.5 Zitterbewegung of gaussian wave-packet for different pseudospin polarization

Let us now show results for three different Gaussian distributions along the subalttices: (Sec. 6.5.1) $[c_1, c_2]^T = [1, 0]^T$, (Sec. 6.5.2) $[c_1, c_2]^T = [1, 1]^T$, and (Sec. 6.5.3) $[c_1, c_2]^T = [1, i]^T$, where we discuss the presence or absence of ZBW along the x and y directions, manifested by oscillations on the average position and average group velocity of

the Gaussian center of mass of the wave packet, as well as other features of the trembling motion, such as the oscillation amplitude and frequency.

6.5.1 $c_1 = 1$ and $c_2 = 0$

We first consider the simple case where the lower component of the initial electronic wave function (6.13a) is zero, i.e. taking $c_1 = 1$ and $c_2 = 0$. This corresponds to the situation in which the electron probability is initially located only at $\phi_1 = \phi_A + \phi_C$, i.e. at the A and C the sublattices of phosphorene layer. According to Eq. (6.14), the wave function for $t > 0$ in this case is:

$$\Psi(\vec{r}, t) = \begin{pmatrix} \Phi_1(\vec{r}, t) \\ \Phi_2(\vec{r}, t) \end{pmatrix}, \tag{6.25}$$

where $\Phi_{1,2}$ are defined by Eqs. (6.15a) and (6.15b). By using Eq. (6.16) and after some lengthy but straightforward algebra, we calculate the time dependent expectation value of position (x, y) of the wave packet center of mass, given by

$$\langle x(t) \rangle = -\frac{ide^{-a^2}}{\pi} \int_0^\infty \int_{-\pi}^\pi e^{-q^2 + 2aq \sin \beta} \left[\frac{2i\chi^n \gamma_x^n \hbar^4 dq^3 \sin(2\beta) \sin^2 \left(\varepsilon_2(q, \beta) t/\hbar \right)}{\left[\delta^n \hbar^2 d^2 + (\gamma_x^n \cos^2 \beta + \gamma_y^n \sin^2 \beta) q^2 \hbar^2 \right]^2 d^2 (\chi^n)^2 \hbar^4 q^2 \sin^2 \beta} \right.$$
$$\left. + \frac{2it\eta_x^n q^2 \cos \beta}{\hbar d^2} + q^2 \cos \beta \right] d\beta dq, \tag{6.26a}$$

$$\langle y(t) \rangle = -\frac{ide^{-a^2}}{\pi} \int_0^\infty \int_{-\pi}^\pi e^{-q^2 + 2aq \sin \beta} \left[q^2 \sin \beta - aq + \frac{2it\eta_y^n q^2 \sin \beta}{\hbar d^2} \right.$$
$$\left. - \frac{iq\chi^n \hbar^2 d \left(d^2 \delta^n \hbar^2 + \gamma_x^n q^2 \hbar^2 \cos^2 \beta - \gamma_y^n q^2 \hbar^2 \sin^2 \beta \right) \sin^2 \left(\varepsilon_2(q, \beta) t/\hbar \right)}{\left[\delta^n \hbar^2 d^2 + (\gamma_x^n \cos^2 \beta + \gamma_y^n \sin^2 \beta) q^2 \hbar^2 \right]^2 + d^2 (\chi^n)^2 \hbar^4 q^2 \sin^2 \beta} \right] d\beta dq, \tag{6.26b}$$

in which the average values are written explicitly as a function of the polar angle $\beta \in [-\pi, \pi]$ and the dimensionless parameters $q = pd/\hbar$ and $a = k_0 d$, with k_0 corresponding to the initial wave vector. For this, we rewrote ε_1 and ε_2, given by Eqs. (6.4a) and (6.4b), respectively, as functions of q and β.

By performing a numerical integration of Eqs. (6.26a) and (6.26b), we obtain the expectation values as a function of time for different initial central wave vectors and number of BP layers, as shown in Figs. 6.2(a) and 6.2(b), respectively. The average value $\langle x(t) \rangle$ remains constant and does not exhibit any oscillation with time for different k's values and number of BP layers. On the other hand, the expectation value of the y position of the wave packet oscillates, thus indicating the presence of ZBW along the y-direction. The different curves in Fig. 6.2(a) are the results for $k_0 = 0.01$ Å^{-1} (black), $k_0 = 0.05$ Å^{-1} (red) and $k_0 = 0.1$ Å^{-1} (blue). As mentioned in Sec. 6.1, this oscillatory behavior is due to the interference between positive and negative energy-momentum states that makes up the initial Gaussian wave packet and in fact corresponds to the ZBW phenomenon. Note
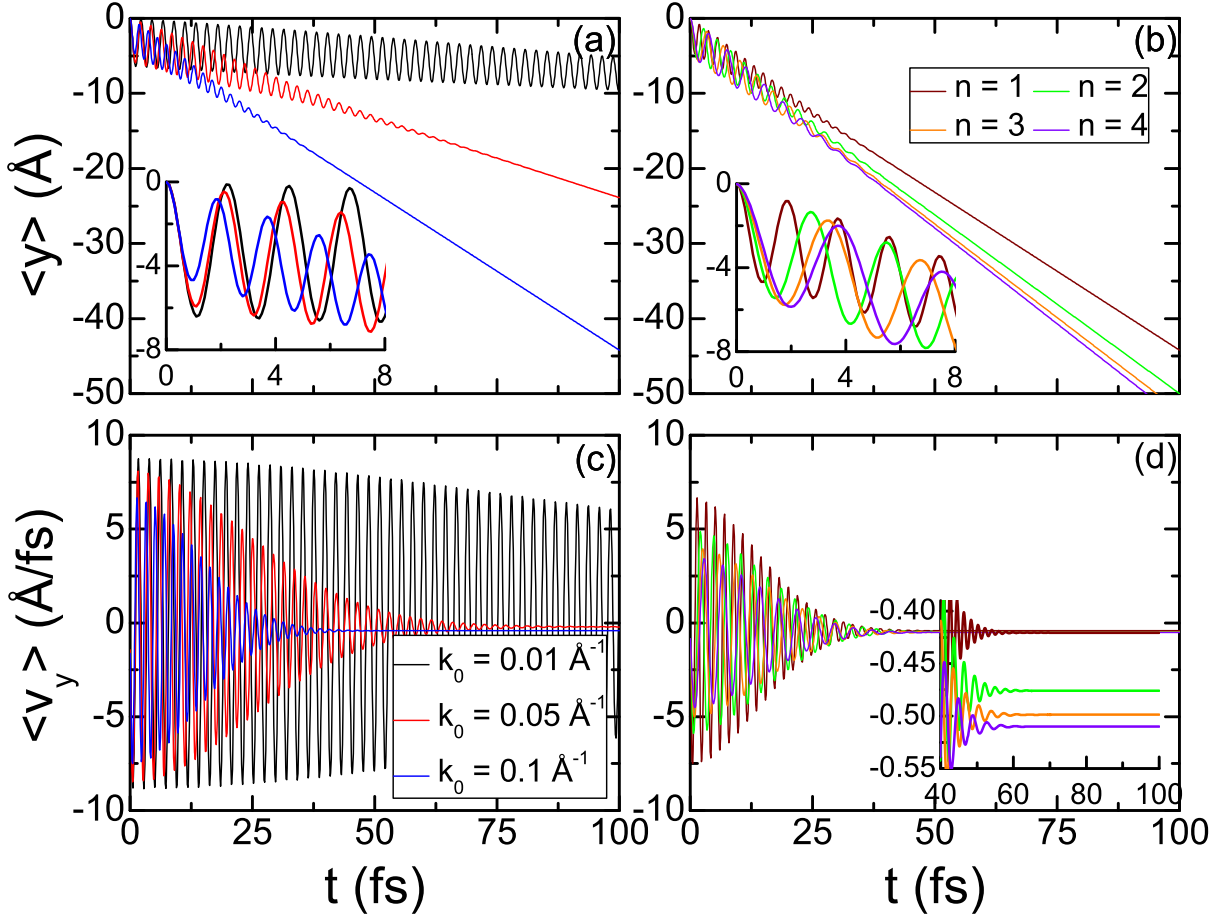
Figure 6.2: (Color online) (a, b) Average position and (c, d) expectation value of the velocity for trajectories of panels (a, b), respectively, of a Gaussian wave packet of width $d = 100$ Å as a function of time for the case $c_1 = 1$ and $c_2 = 0$. (a, c) Wave packet propagating in a monolayer phosphorene sheet ($N = 1$) with different initial central wave vectors: $k_0 = 0.01$ Å^{-1} (black), 0.05 Å^{-1} (red) and 0.1 Å^{-1} (blue). (b, d) Wave packet propagating in multilayer phosphorene ($N = 1, 2, 3, 4$) for fixed wave vector $k_0 = 0.1$ Å^{-1}. The wave packet starts at $(x_0, y_0) = (0, 0)$ Å. The inset shows an enlargement of the physical averages (a, b) for first time steps in order to emphasize the different oscillation amplitudes and oscillation frequencies, and (d) nearby the time steps in which the velocities achieve constant values.

in Fig. 6.2(a) that the ZBW of the wave packet propagating in a monolayer BP have a transient character, i.e. they disappear on a femtosecond time scale. This transient feature of the ZBW presents different amplitude, frequency and duration time for different initial wave vector. One verifies in Fig. 6.2(a) that: (i) the duration time and amplitude of the transient ZBW decays faster as the wave vector increases, and (ii) the larger the initial wave vector, the smaller the oscillation amplitude, as seen in the inset of panel (a). Both features are consequences of the effect of wave packet dispersion.

We also analyze the influence of the number of layers on the wave packet propagation.

Results are shown in Fig. 6.2(b) for $N = 1, 2, 3, 4$, considering a fixed value $k_0 = 0.1$ Å^{-1}.
One observes that increasing the number of layers causes a reduction (increase) of the
frequency (period) of the transient oscillation. This is related to the fact that multilayer
BP with different numbers of BP layers presents slightly different energy band struc-
tures and consequently different effective masses along x and y directions, as discussed
in Sec. 6.2. It is known that the greater the number of layers, the greater (smaller) will
be the effective mass for electrons along the x (y) direction, i.e. along the zigzag (arm-
chair) directions. [39] That in turn affects the mobility of electrons located on the lowest
conduction band, leading to a phase difference in the oscillation of the average position
$\langle y(t) \rangle$ for different number of layers N. By comparing Figs. 6.2(a) and 6.2(b), one verifies
that the oscillatory behavior for multilayer BP is qualitatively similar to monolayer case,
except by this phase difference in the ZBW, as emphasized in the inset of Fig. 6.2(b), due
to the different energy band curvatures as the number of layers BP.

Since the oscillatory behavior of the propagation velocity as a function of time is also a
manifestation of the ZBW effect, we show in Figs. 6.2(c) and 6.2(d) the expectation values
of the velocity v_y for average position y of panels (a) and (b), respectively, calculated by
taking the time derivative of the $\langle y(t) \rangle$ results with respect to time. Note that the average
velocities exhibit clear oscillations that are damped as time evolves, converging to a final
constant value that depends on the initial wave vector k_0 and number of considered BP
layers. The velocity wiggles with shorter period and smaller amplitudes for large values of
k_0 and fixed number N (see Fig. 6.2(c)), as well as for large number of layer and fixed k_0
(see inset in Fig. 6.2(d)). The convergence of the velocities demonstrates that the ZBW
is not a permanent but a transient effect. Notice from the inset in Fig. 6.2(d) that the
converging value of $\langle v_y \rangle$ has slightly larger module for larger N. This is related to the fact
that the lowest energy band along $\Gamma - Y$ direction for multilayer BP has approximately
the same curvatures for different number of layers, and consequently the effective masses
for electrons along y-direction are just slightly different for different layers, as can be
seen by the following values: $m_1^y = 0.19474 m_0$, $m_2^y = 0.18835 m_0$, $m_3^y = 0.17088 m_0$, and
$m_4^y = 0.15648 m_0$, being m_0 the mass of a free electron, and thus leading also to a slight
difference in the electronic mobility and group velocity in y-direction. [39]

Figure 6.3 shows the contour plots of the squared modulus of the propagated wave
functions at (a) $t = 20$ fs, (b) $t = 30$ fs, (c) $t = 40$ fs, and (d) $t = 50$ fs, considering
an initial wave vector $k_0 = 0.05$ Å^{-1} that corresponds the average position of the elec-
tron wave packet motion displayed by the red curve in Fig. 6.2(a). It is seen that the
time evolution of the electronic wave packet for this case is along the armchair (y-) direc-
tion. Starting with a circularly symmetric shape, the wave packet evolves and becomes
distorted into an elliptic shape. This is due to the strong anisotropy in multilayer phos-
phorene, such that the momentum contributions along the (y) armchair and (x) zigzag
directions to the total momentum are different, thus giving rise to elliptic probability
distribution, as shown in Fig. 6.3(a). For a large enough time, the wave packet splits
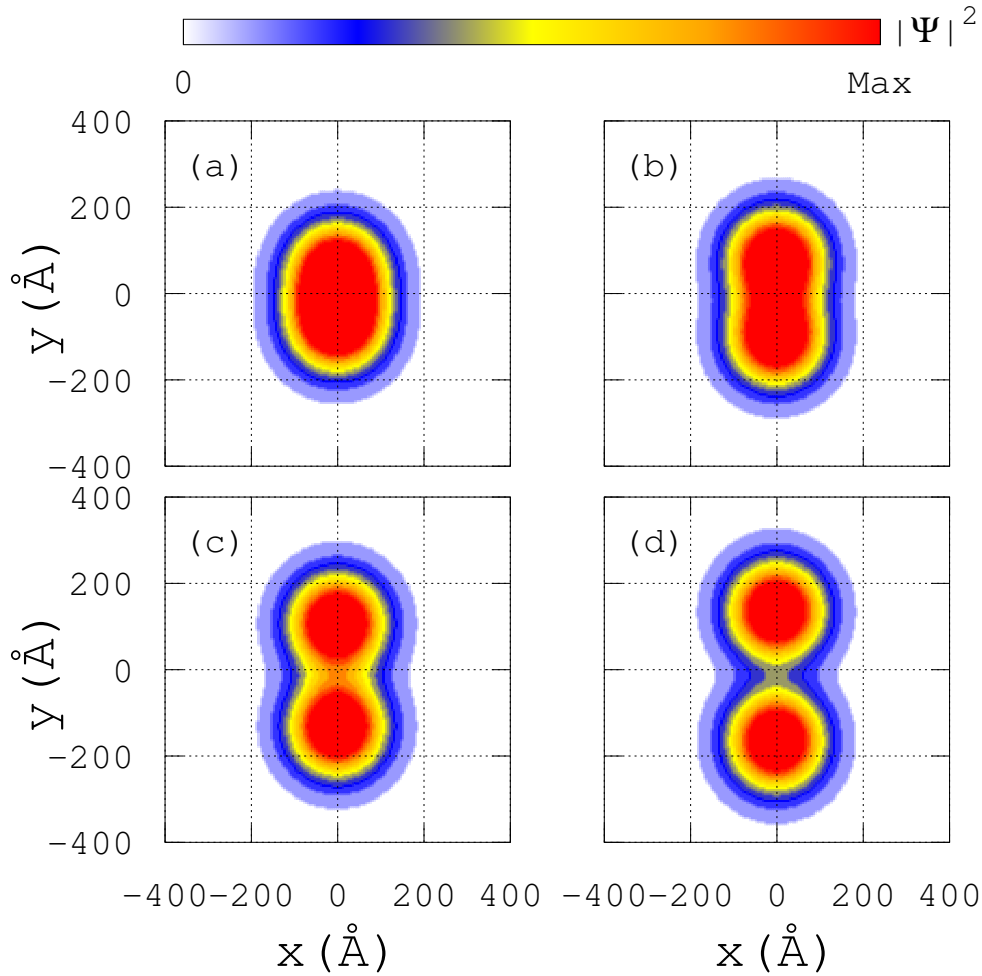
Figure 6.3: (Color online) Time evolution of the electronic wave packet for the case
$[c_1, c_2]^T = [1, 0]^T$ with $|k| = 0.05$ Å^{-1}, corresponding the average position shown by the
red curve in Fig. 6.2(a). Snapshots at (a) $t = 20$ fs, (b) $t = 30$ fs, (c) $t = 40$ fs, and (d)
$t = 50$ fs.

in two parts at $t \approx 50 fs$ (Fig. 6.3(d)) moving along y axis with opposite velocities so
that the electron probability density is almost symmetrical with respect to y at a fixed
time step: $|\Psi(x, y, t)|^2 \approx |\Psi(x, -y, t)|^2$. It should be noticed that the two subpackets
are definitely not completely symmetric, otherwise we would not have a non-null average
position in the y-direction and a total propagation evolving to negative values of y, as
shown in Fig. 6.2(a) and 6.2(b). The two propagating subpackets with approximately
the same probability densities and widths lead to vanishing oscillations in the average
position and expectation values of velocity, as verified by the red curves in Figs. 6.2(a)
and 6.2(c) after $t \approx 85$ fs, which explains the transient behavior of the ZBW and the fact
that the average velocity converges to values close to zero. Although not shown here, it is
easy and intuitive to see that the splitting into two subpackets for the case with greater
wave vector should occur earlier and, therefore, in this situation the average velocity has
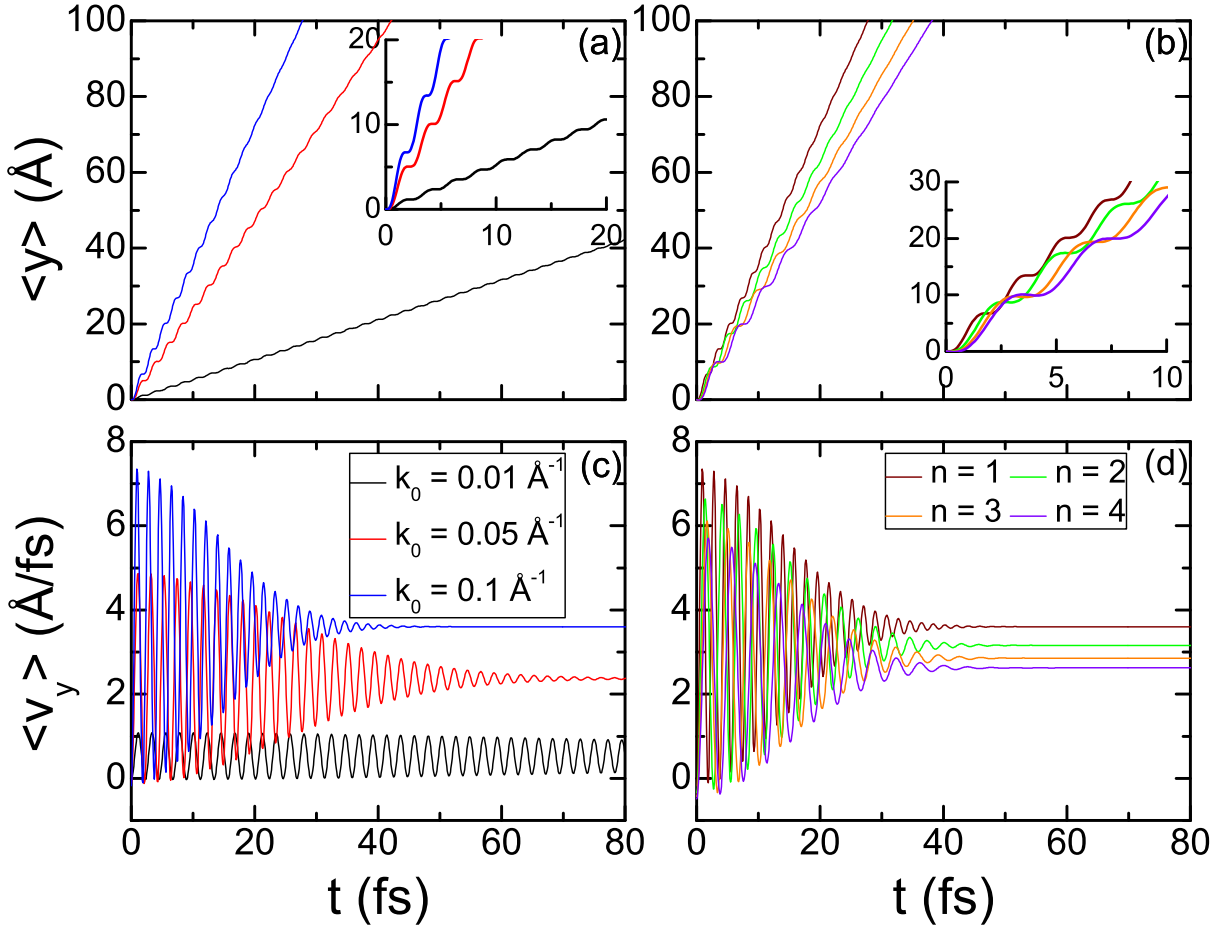
Figure 6.4: (Color online) The same as in Fig. 6.2, but now for the case $c_1 = 1$ and $c_2 = 1$.

a faster decay rate and a shorter transient oscillation time.

In contrast to the results shown in Fig. 6.2 for the given initial polarization $[1, 0]^T$ of wave packet propagating in multilayer BP, the ZBW for monolayer graphene [144, 173] and bilayer graphene [147] occurs in the direction perpendicular to the initial momentum k_0^y, i.e. for initial polarization $[1, 0]^T$ the wave packet propagates along x-direction in which exhibits ZBW effect, whereas $\langle y(t) \rangle$ remains constant. This is counterintuitive, since the initial momentum along x-direction is null as in Eq. (6.13b). However, similar to Fig. 6.3, in graphene the wave function also is found to split in two subpackets along the y-direction.[144] This different direction of propagation between the multilayer BP and those reported for monolayer and bilayer graphene in Refs. [144, 173, 147] can be understood considering the fact that, since the direction of propagation y is the crystallographic direction in the phosphorene in which electrons have greater (lower) kinetic energy (effective mass), then electrons have greater mobility along the y-direction, being its preferred direction of propagation.
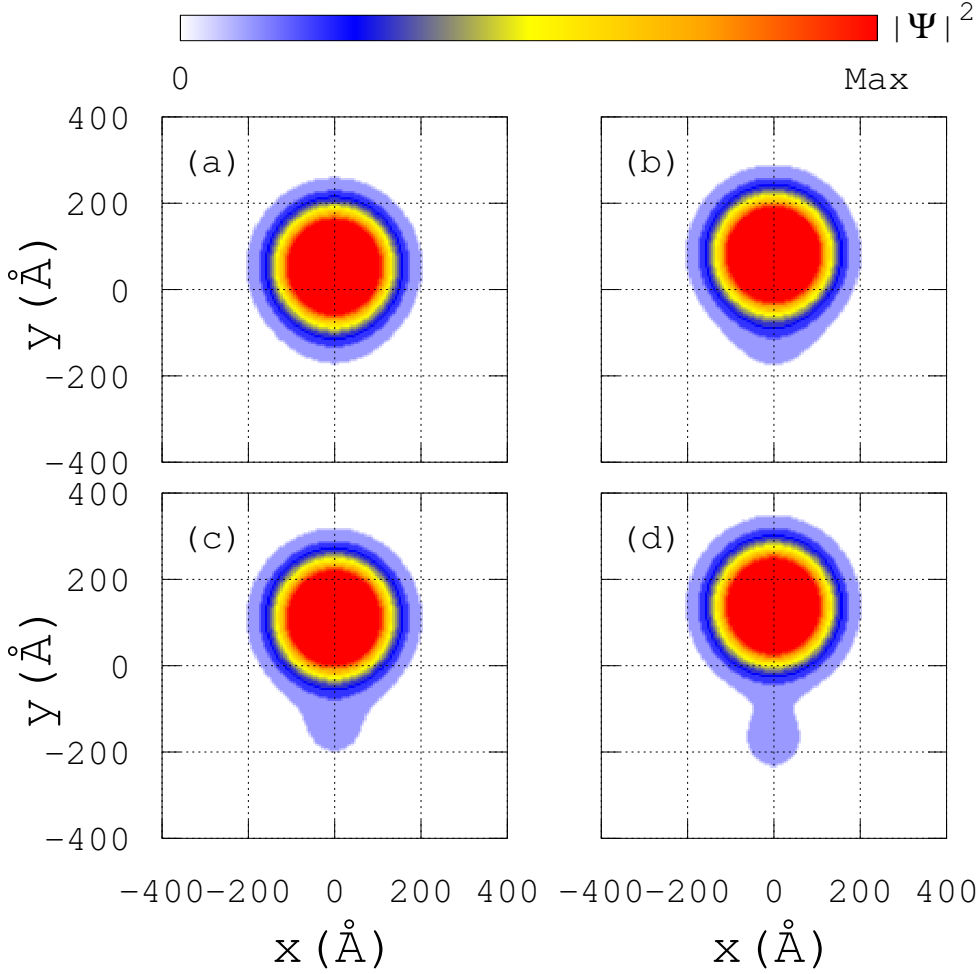
Figure 6.5: (Color online) The same as in Fig. 6.3, but now for the case $c_1 = 1$ and $c_2 = 1$.

6.5.2 $c_1 = 1$ and $c_2 = 1$

We now investigate the case in which the wave function is equally distributed in the
combined sublattices A/C (corresponding to ϕ_1) and B/D (corresponding to ϕ_2), which
is equivalent as choosing $c_1 = 1$ and $c_2 = 1$ in Eq. (6.14), resulting in

$$\Psi(\vec{r}, t) = \frac{1}{\sqrt{2}} \begin{pmatrix} \Phi_1(\vec{r}, t) + \Phi_3(\vec{r}, t) \\ \Phi_1(\vec{r}, t) + \Phi_2(\vec{r}, t) \end{pmatrix}, \tag{6.27}$$

where $\Phi_{1,2,3}$ are defined by Eqs. (6.15a)-(6.15c). Note that an initial wave packet in which
the electron probability density occupies equally all subllatices is more realistic experimen-
tally, as an expected configuration when one creates wave packets by illuminating samples
with short laser pulses [182] and also because for an infinite system the initial wave func-
tion should describe electronic bulk states spread over all sites around the center point of
the Gaussian distribution. On the other hand, the simplistic choice $[1,0]^T$ of the initial
wave packet discussed in previous Sec. 6.5.1 is widely used in the literature, [144, 173, 147]
since it is amenable to analytical treatment and gives valuable insight into the relevant

timescales of the problem. In addition, for the phosphorene case, the initial configuration $[1,0]^T$ can be seen as the representation of quasi-flat edge states in phosphorene nanoribbons with zigzag edges that have non-zero wave function components just in one of the coupled pairs A/D or B/C. [169] Replacing the wave function Eq. (6.27) into Eq. (6.16), we find the following expressions for the average positions in x and y directions:

$$\langle x(t) \rangle = -\frac{ie^{-a^2}}{\pi} \int_0^\infty \int_{-\pi}^\pi e^{-q^2+2aq\sin\beta} \Bigg\{ \frac{i\chi^n\gamma_x^n\hbar^4 d^2 q^3 \sin(2\beta)\sin(2\varepsilon_2(q,\beta)t/\hbar)\sin\theta_k(q,\beta)}{\left[\delta^n\hbar^2 d^2 + (\gamma_x^n\cos^2\beta + \gamma_y^n\sin^2\beta)q^2\hbar^2\right]^2 + d^2(\chi^n)^2\hbar^4 q^2\sin^2\beta}$$

$$+ dq^2\cos\beta + \frac{2it\eta_x^n q^2\cos\beta}{\hbar d} + \left[\sin\left(\frac{2\varepsilon_2(q,\beta)t}{\hbar}\right) - i\cos\theta_k(q,\beta)\cos\left(\frac{2\varepsilon_2(q,\beta)t}{\hbar}\right)\right]$$

$$\times \left[\frac{2t[\delta^n\hbar^2 d^2 + (\gamma_x^n\cos^2\beta + \gamma_y^n\sin^2\beta)q^2\hbar^2]\gamma_x^n q^2\cos\beta}{\hbar^3 d^3\varepsilon_2(q,\beta)}\right] \Bigg\} d\beta dq, \qquad (6.28a)$$

$$\langle y(t) \rangle = -\frac{ie^{-a^2}}{\pi} \int_0^\infty \int_{-\pi}^\pi e^{-q^2+2aq\sin\beta} \Bigg\{ -adq + dq^2\sin\beta + \frac{2it\eta_y^n q^2\sin\beta}{\hbar d} + itq^2\cos\theta_k(q,\beta)$$

$$- \frac{iq\chi^n\hbar^2 d^2\left[\delta^n\hbar^2 d^2 + \left(\gamma_x^n\cos^2\beta - \gamma_y^n\sin^2\beta\right)q^2\hbar^2\right]\sin(2\varepsilon_2(q,\beta)t/\hbar)\sin\theta_k(q,\beta)}{\left[\delta^n\hbar^2 d^2 + (\gamma_x^n\cos^2\beta + \gamma_y^n\sin^2\beta)q^2\hbar^2\right]^2 + d^2(\chi^n)^2\hbar^4 q^2\sin^2\beta}$$

$$\times \left[\frac{2\gamma_x^n\cos\beta[\delta^n\hbar^2 d^2 + (\gamma_x^n\cos^2\beta + \gamma_y^n\sin^2\beta)q^2\hbar^2] + (\chi^n)^2\hbar^2 d^2\sin\beta}{\hbar^3 d^3\varepsilon_2(q,\beta)}\right] \Bigg\} d\beta dq, \qquad (6.28b)$$

with θ_k, $\varepsilon_{1,2}$ written explicitly as a function of the polar angle β and the dimensionless parameters q (see Eq. (6.8)).

Similarly to the previous Sec. 6.5.1 for the pseudospin $[1,0]^T$, in the current case the average value $\langle x(t) \rangle$ is also unchanged with time, whereas the expectation value of the y position oscillates. These results are displayed in Figs. 6.4(a) and 6.4(b) for monolayer BP with different initial wave vectors and for multilayer BP with the fixed value $k_0 = 0.1$ Å^{-1}, respectively. By comparing Figs. 6.4(a, b) with Figs. 6.2(a, b), one can notice that the ZBW for the pseudospin $[1,1]^T$ exhibit a smaller (larger) oscillation frequency (period) than for the case $[1,0]^T$ (see insets in Figs. 6.4(a, b)), with the total average position $\langle y(t) \rangle$ moving faster along the positive y direction than for the case $[1,0]^T$ that moves along the negative y direction. This statement is confirmed by the time derivative $\langle v_y(t) \rangle = \frac{d\langle y(t) \rangle}{dt}$ of the results shown in the panels 6.4(a) and 6.4(b), as demonstrated in Figs. 6.4(c) and 6.4(d), that converges to clearly non-null and larger final values as compared to the ones obtained in Figs. 6.2(c) and 6.2(d). In general, the main features of the ZBW remain the same as the previous case: the dependence of the transient character, as well as the different amplitude, frequency and duration time of the ZBW for different initial wave vector and number of layers. For the expectation values of the velocities (Figs. 6.4(c, d)), note that in contrast to Figs. 6.2(c, d), in the current case, the larger k_0, it leads to large oscillation amplitudes of $\langle v_y(t) \rangle$. Moreover, the oscillatory behavior for multilayer BP (Figs. 6.4(b, d)) remains qualitatively the same as the one observed in Figs. 6.2(b, d) as compared to their monolayer BP results, except for the fact that in the $[1,1]^T$ case,

the difference of the converging final values of $\langle v_y(t) \rangle$ are more pronounced for different numbers of layers.

In order to understand the origin of this weak oscillations and also the fast drift along the y direction for the pseudospin case $[1, 1]^T$, we depict in Fig. 6.5 the spatial time evolution of the initial wave packet by showing snapshots for $t > 0$ of the total probability density. Note that the initial wave packet also splits into two parts propagating along y in opposite directions as in the $[1, 0]^T$ case discussed in Sec. 6.5.1 and shown in Fig. 6.3, but unlike the previous case, the portions of probability amplitudes and widths of the two subpackets are noticeably different, such that the electron probability density is not symmetric with respect to y at a fixed time step: $|\Psi(x, y, t)|^2 \neq |\Psi(x, -y, t)|^2$. This large asymmetry in the probability density explains the less evident ZBW effect in the average y position in Fig. 6.4, so that it becomes clear the reason why $\langle v_y(t) \rangle$ converges to non-zero values, which even increase with k_0, since a greater portion of the wave packet propagates to the positive y direction. Another feature of Fig. 6.5 is that the propagating wave packet does not deform as much as in the previous case, remaining approximately with the same packet width even after the splitting that originates a small subpacket moving in the opposite y direction.

6.5.3 $c_1 = 1$ and $c_2 = i$

The last investigated pseudospin polarization case is composed by the pseudospin components $c_1 = 1$ and $c_2 = i$. That means that all four BP sublattices are filled, but unlike the case $[1, 1]^T$ discussed in the previous Sec. 6.5.2, it has a phase difference between ϕ_1 and ϕ_2 that couples the pairs of sublatices A/D and B/C, respectively (see Eqs. (6.2) and (7.9a)). The reason for the study of this choice of pseudospin polarization is based on the corresponding interest in graphene case, [144, 173] since these two polarizations represent full-filled sublattice states points into perpendicular directions in monolayer graphene: $[1, 1]^T$ is directed along x axis at $t = 0$, whereas $[1, i]^T$ is directed along y axis at $t = 0$. From Eq. (6.14) for $c_1 = 1$ and $c_2 = i$, the wave function is given by

$$\Psi(\vec{r}, t) = \frac{1}{\sqrt{2}} \begin{pmatrix} \Phi_1(\vec{r}, t) + i\Phi_3(\vec{r}, t) \\ i\Phi_1(\vec{r}, t) + \Phi_2(\vec{r}, t) \end{pmatrix}. \tag{6.29}$$

Computing the average values for the position x and y using Eqs. (6.16) and (6.29),
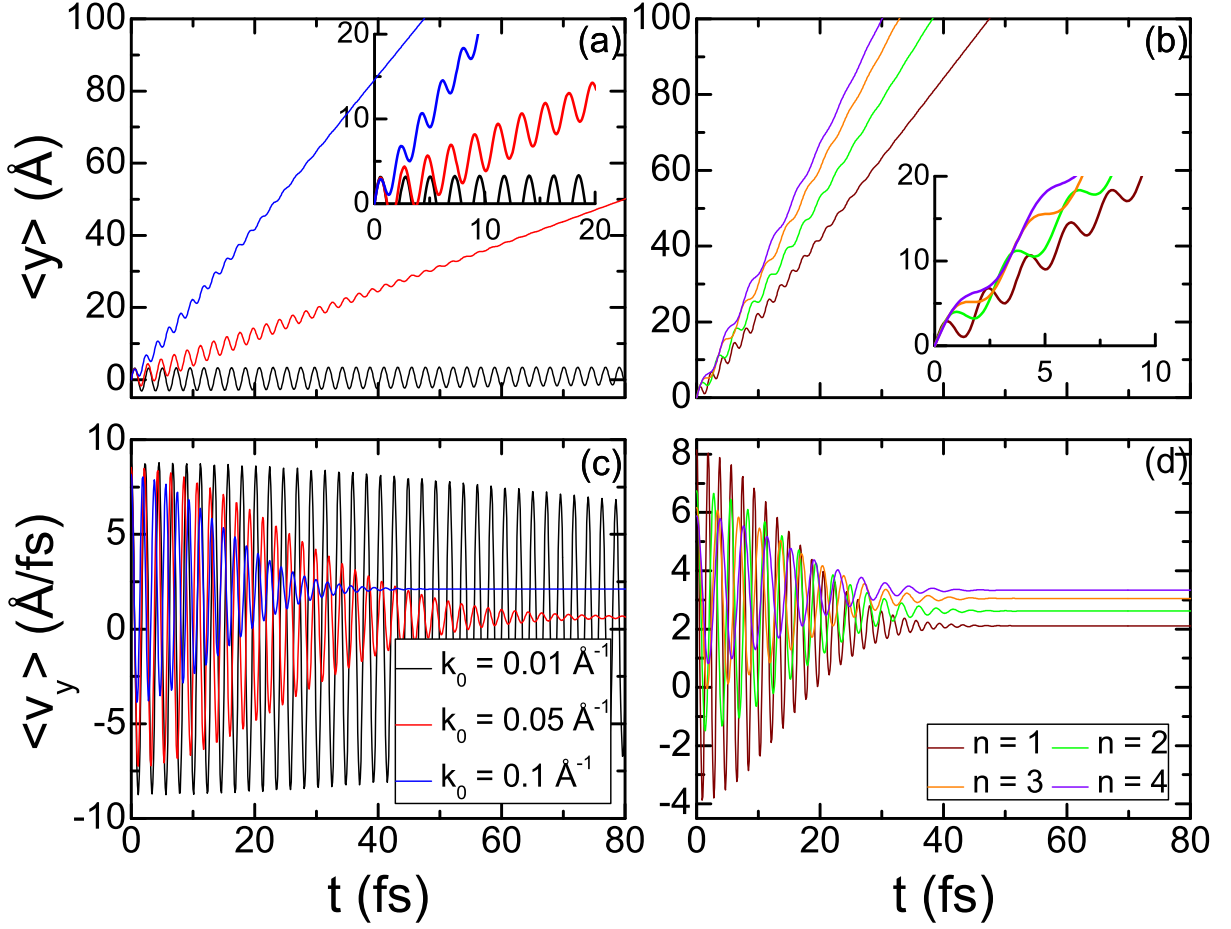
Figure 6.6: (Color online) The same as in Fig. 6.2, but now for the case $c_1 = 1$ and $c_2 = i$.

one obtains

$$
\langle x(t) \rangle = -\frac{ie^{-a^2}}{\pi} \int_0^\infty \int_{-\pi}^{\pi} e^{-q^2 + 2aq\sin\beta} \Bigg\{ dq^2 \cos\beta + \frac{2it\eta_x^n q^2 \cos\beta}{\hbar d}
$$

$$
- \frac{i\chi^n \gamma_x^n \hbar^4 d^2 q^3 \sin(2\beta) \sin(2\varepsilon_2(q,\beta)t/\hbar) \cos\theta_k(q,\beta)}{\left[\delta^n \hbar^2 d^2 + (\gamma_x^n \cos^2\beta + \gamma_y^n \sin^2\beta)q^2\hbar^2\right]^2 + d^2(\chi^n)^2 \hbar^4 q^2 \sin^2\beta}
$$

$$
+ i\sin\theta_k(q,\beta) \left(\frac{2t\gamma_x q^2 \cos\beta [\delta\hbar^2 d^2 + (\gamma_x \cos^2\beta + \gamma_y \sin^2\beta)q^2\hbar^2]}{\hbar^3 d^3 \varepsilon_2(q,\beta)} \right) \Bigg\} d\beta dq, \quad (6.30a)
$$

$$
\langle y(t) \rangle = -\frac{ie^{-a^2}}{\pi} \int_0^\infty \int_{-\pi}^{\pi} e^{-q^2 + 2aq\sin\beta} \Bigg\{ -adq + dq^2 \sin\beta + \frac{2it\eta_y^n q^2 \sin\beta}{\hbar d}
$$

$$
+ \frac{iq\chi^n \hbar^2 d^2 \left[\delta^n \hbar^2 d^2 + \left(\gamma_x^n \cos^2\beta - \gamma_y^n \sin^2\beta\right)q^2\hbar^2\right] \sin(2\varepsilon_2(q,\beta)t/\hbar) \cos\theta_k(q,\beta)}{2\left[\delta^n \hbar^2 d^2 + (\gamma_x^n \cos^2\beta + \gamma_y^n \sin^2\beta)q^2\hbar^2\right]^2 + 2d^2(\chi^n)^2 \hbar^4 q^2 \sin^2\beta}
$$

$$
- itq^2 \sin\theta_k(q,\beta) \left(\frac{2\gamma_x^n \cos\beta[\delta^n \hbar^2 d^2 + (\gamma_x^n \cos^2\beta + \gamma_y^n \sin^2\beta)q^2\hbar^2] + (\chi^n)^2 \hbar^2 d^2 \sin\beta}{\hbar^3 d^3 \varepsilon_2(q,\beta)} \right) \Bigg\} d\beta dq.
$$

$$
(6.30b)
$$
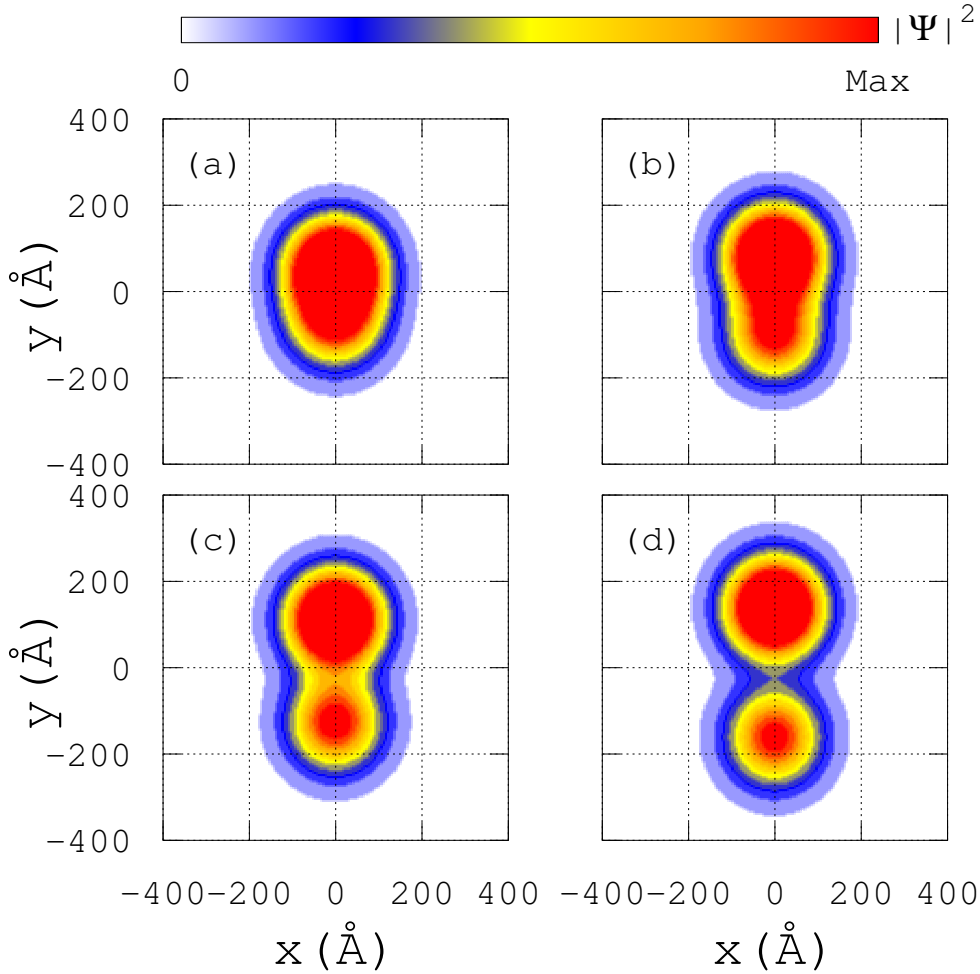
Figure 6.7: (Color online) The same as in Fig. 6.3, but now for the case $c_1 = 1$ and $c_2 = i$.

As in the previous cases, $\langle x(t) \rangle$ is unchanged with time due to initial configuration $k_0^x = 0$ in Eq. (6.13b). The results for $\langle y(t) \rangle$ and $\langle v_y(t) \rangle$ for different initial wave vectors and number of BP layers are shown in Figs. 6.6(a, b) and 6.6(c, d), respectively. As seen, these results also exhibit very pronounced ZBW and are more similar to the results shown in Fiqs. 6.2(a) and 6.2(b) for the case $[1, 0]^T$ concerning the large oscillation amplitudes, high oscillation frequency and small oscillation period, as compared to the ones shown in Fiqs. 6.4(a) and 6.4(b) for the $[1, 1]^T$ case. The reason for the pronounced ZBW effect in the cases $[1, 0]^T$ and $[1, i]^T$ can be linked to the unbalance and/or phase difference of the different pseudospin components. On the other hand, $\langle y(t) \rangle$ is shifted with time to positive y values, as in case $[1, 1]^T$ shown in Fiqs. 6.4(a) and 6.4(b), that suggests that the overall wave packet is propagating along the positive y direction. It is confirmed by the contour plots shown in Fig. 6.7 for the time evolution of the squared modulus of the wave function for different time steps. Similar to the previous cases, as the ZBW disappears, two separate parts of the initial wave packet are seen to move along the y axis with opposite velocities. Figure 6.7(d) shows that the two subpackets have different widths

and thus the total wave packet symmetry in y direction for a fixed time is not preserved,
i.e. $|\Psi(x, y, t)|^2 \neq |\Psi(x, -y, t)|^2$, similar to the case $[1, 1]^T$. The dominant contribution to
the total wave function is responsible for the positive shift in the average position $\langle y(t) \rangle$
and also for the the non-zero values for the converging average velocities at large time
steps.

In order to check the agreement between the results obtained by using the two frame-
works adopted here, namely, Green's function formalism (Sec. 6.3) and the split-operator
technique (Sec. 6.4), we plot in Fig. 6.8 the comparison between them for two pseudospin
configurations: (a, b) for the case $c_1 = 1$ and $c_2 = 1$, and (c, d) the case $c_1 = 1$ and $c_2 = i$.
We have omitted such comparison for the case $c_1 = 1$ and $c_2 = 0$, since for the time
scale, initial momentum values, and wave packet width investigated in the current work,
no difference at all was observed. It is really clear that both analytical (dashed curves)
and numerical (solid curves) methods give similar qualitative results and illustrate similar
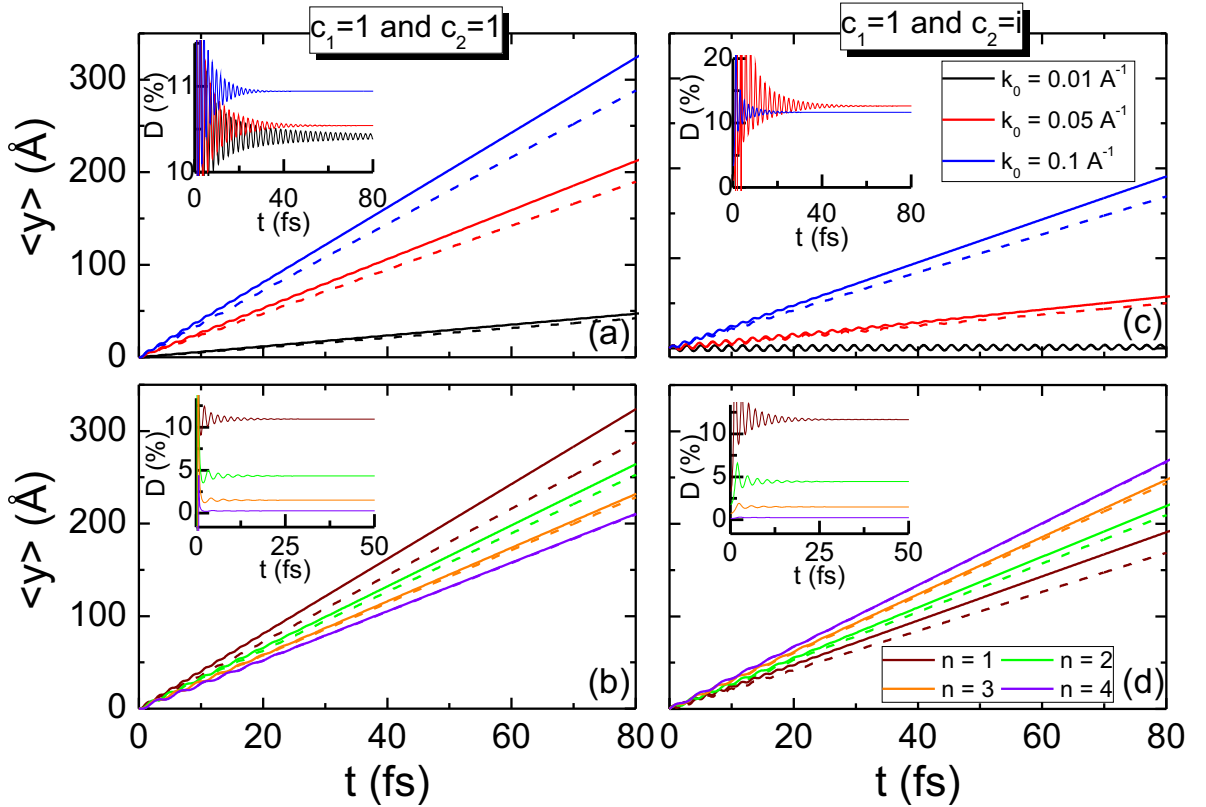
Figure 6.8: (Color online) Comparison between the results of the average position of a
Gaussian wave packet of width $d = 100$ Å as a function of time obtained by (solid curves)
the split-operator technique derived in Sec. 6.4 and (dashed curves) analytical calculations
derived in Sec. 6.3, for (a, b) the case $c_1 = 1$ and $c_2 = 1$, and (c, d) the case $c_1 = 1$ and
$c_2 = i$. (a, c) Wave packet propagating in a monolayer phosphorene sheet ($N = 1$) with
different wave vectors: $k_0 = 0.01$ Å^{-1} (black), $k_0 = 0.05$ Å^{-1} (red) and $k_0 = 0.1$ Å^{-1}
(blue). (b, d) Wave packet propagating in multilayer phosphorene ($N = 1, 2, 3, 4$) for
fixed wave vector $k_0 = 0.1$ Å^{-1}.

ZBW. They have a good quantitative agreement, exhibiting a small discrepancy, for the worst case of $\approx 11\%$ at maximum, as shown in the insets, and that occurs, in general, for much larger values of wave vector, and only after long time steps (see panels (a) and (b)), as well as fewer numbers of layers (see panels (c) and (d)). The reason for such discrepancy for these two pseudopsin configuration must be related to inaccuracy in numerical integration to obtain the expectation values of the analytically derived position operators, since expressions (6.28a), (6.28b), (6.30a) and (6.30b) are more complicated as compared to the ones (6.26a) and (6.26b) for the case $[1,0]^T$, in which both methods agree 100%, giving rise to these small deviations.

6.6 Velocity operator

Let us now obtain the velocities along the x and y directions and verify whether v_x and v_y are constants of motion or not, which also indicates the directions where the ZBW manifests. To understand how this affects the velocity along certain directions, we use the Hamiltonian Eq. (7.1), or equivalently Eq. (6.3), for electrons in multilayer phosphorene, and calculate the commutators $[\mathcal{H}, v_x]$ and $[\mathcal{H}, v_y]$. According to the Heisenberg picture, the velocity operator is given by

$$\vec{v} = \frac{\partial \mathcal{H}}{\partial \vec{p}} = \frac{1}{\hbar} \frac{\partial \mathcal{H}}{\partial \vec{k}} = \frac{1}{i\hbar} [\vec{r}, \mathcal{H}], \tag{6.31}$$

with $\vec{v} = (v_x, v_y)$ and $\vec{r} = (x, y)$, yielding

$$v_x = \frac{2k_x}{\hbar} \left(\eta_x^n 1 + \gamma_x^n \sigma_x \right), \tag{6.32a}$$

$$v_y = \frac{2k_y}{\hbar} \left(\eta_y^n 1 + \gamma_y^n \sigma_x - \frac{\chi^n}{k_y} \sigma_z \right). \tag{6.32b}$$

Let us now verify whether v_x and v_y are constants of motion, and if there is any situation where v_x and v_y are not affected by the zitterbewegung. Evaluating $[\mathcal{H}, v_i]$ by making use of Eqs. (6.3) and (6.32), one obtains

$$[\mathcal{H}, v_x] = \frac{4i\epsilon_2}{\hbar} k_x \gamma_x^n \sin\theta_k \begin{pmatrix} -1 & 0 \\ 0 & 1 \end{pmatrix}, \tag{6.33a}$$

$$[\mathcal{H}, v_y] = \frac{4i\epsilon_2}{\hbar} \left[k_y \gamma_y^n \sin\theta_k + \chi^n \cos\theta_k \right] \begin{pmatrix} -1 & 0 \\ 0 & 1 \end{pmatrix}. \tag{6.33b}$$

Equation (6.33a) suggests that $[\mathcal{H}, v_x] = 0$ when:

(i) $k_x = |k|\cos\beta = 0$ [that implies either $|k| = 0 \to k_x = k_y = 0$, i.e zero initial momentum, or $\cos\beta = 0$ $(\sin\beta = \pm 1) \to \beta = \pm(2l+1)\pi/2$, with $l \in N$],

(ii) $\sin\theta_k = 0 \to \theta_k = \pm l\pi$, with $l \in N$ and consequently, by the definition of θ_k in Eq. (6.4c), one has $k_y = |k|\sin\beta = 0$ [that implies either $|k| = 0 \to k_x = k_y = 0$, i.e zero initial momentum, or $\sin\beta = 0$ $(\cos\beta = \pm 1) \to \beta = \pm l\pi$, with $l \in N$].
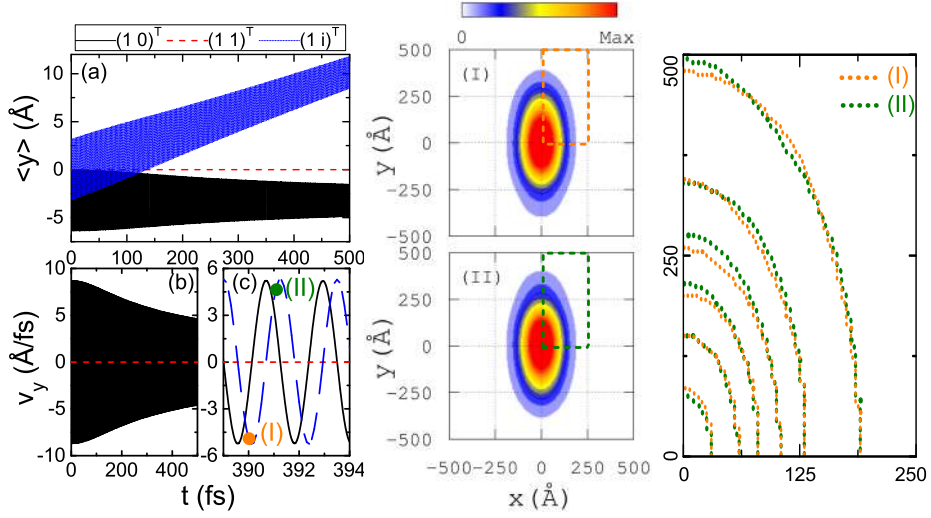
Figure 6.9: (Color online) (a) Average position and (b, c) expectation value of the velocity along y direction as a function of time for the case $[c_1, c_2]^T = [1, 0]^T$ (black), $[c_1, c_2]^T = [1, 1]^T$ (red), and $[c_1, c_2]^T = [1, i]^T$ (blue). (c) A magnification of the results in (b) for large time steps showing the oscillatory behavior of v_y. (right panels) Contour plots of the squared modulus of the wave function at (I) $t = 390$ fs and (II) $t = 391$ fs, and a zoom emphasized by the dahsed curves showing the isosurfaces at the two time steps.

Thus, v_x will be a constant of motion if $(k_x, k_y) = (0, \pm|k|)$ or $(k_x, k_y) = (\pm|k|, 0)$, corresponding to a constant motion along the y and x directions, respectively. On the other hand, $[\mathcal{H}, v_y]$ should be null if and only if k_y and $\cos\theta_k$ are both null, i.e. $\theta_k = \pm(2l+1)\pi/2$, with $l \in N$. However, as mentioned in Sec. 6.2 and shown in Figs. 6.1(c)-6.1(e), the phase angle of the pseudospin varies in the range $-\theta_k^{max} \leq \theta_k \leq \theta_k^{max}$, where θ_k^{max} corresponds to the value of θ_k for $k_x = 0$ and $k_y = \pm 1$, being equivalent to $\beta = \pi/2$ (see Figs. 6.1(c)-6.1(e)). Therefore, one concludes that $[\mathcal{H}, v_y] \neq 0$, suggesting that: v_y is never a constant of motion, and the trembling motion along the y direction at small times for the wave packet propagation in phosphorene systems is unavoidable, even for the case where one assumes $k_x = k_y = 0$, which yields

$$[\mathcal{H}, v_y]|_{k_x=k_y=0} = \frac{4i\delta^n\chi^n}{\hbar} \begin{pmatrix} -1 & 0 \\ 0 & 1 \end{pmatrix}, \qquad (6.34)$$

and, therefore, the wave packet will also move in the y direction. Similar behavior has been observed in previous works for graphene, where it was demonstrated both numerically[9, 173] and analytically [144] within the Dirac and tight-binding models that even when $k_x = k_y = 0$ the wave packet motion is still observed due to zitterbewegung effects. Considering the three different pseudospin configurations used here, one observes in Fig. 6.9 that this also holds for the electron motion in phosphorene for (black curve) $[c_1, c_2]^T = [1, 0]^T$ and (blue curve) $[c_1, c_2]^T = [1, i]^T$, exhibiting oscillations in the [Fig. 6.9(a)] average position and [Fig. 6.9(b, c)] velocity along y direction, similarly to the ones observed in Figs. 6.2

and 6.6 for small momentum values, but now with a much higher oscillation frequency and shorter period, that is clearly a consequence of the reduction of the momentum value. To understand the nature of such oscillations that counter intuitively appear even for the case with null initial momentum, we illustrate on the right panels of Fig. 6.9 the electron probability density (I) at $t = 390$ fs and (II) at $t = 391$ fs nearby a valley and a peak of the average velocity curve, corresponding to points with negative and positive velocities, respectively, as labeled in Fig. 6.9(c). It can be observed that the dispersion of the wave packet is just along the y direction, keeping its radius along x direction practically unchanged from the initial circularly symmetric shape, and thus, for longer times, it becomes distorted into an elliptical shape. One can see by comparing panels (I) and (II) that for positive and negative points of the average velocity curve, the wave packet oscillates along y, such that the symmetry of the probability density concerning this axis changes over time, i.e. $|\Psi(x, y, t)|^2 \neq |\Psi(x, -y, t)|^2$. In the right panel, we show the isosurfaces at these two time steps [orange and green curves represent the states (I) and (II)], in order to emphasize that in fact the wave packet shakes around $y = 0$ while distorting along y direction. On the other hand, for the case $[c_1, c_2]^T = [1, 1]^T$ (red curves in Fig. 6.9) with null initial momentum $|k| = 0$, both the position and velocity averages along both x and y directions remain unchanged over time, although the wave packet also distorts for this case along the y direction, exhibiting an elliptical shape for large time, but it deforms keeping the symmetry $|\Psi(x, y, t)|^2 = |\Psi(x, -y, t)|^2$.

6.7 Conclusions of this chapter

In summary, we have studied the dynamics of free electrons described by an initial Gaussian wave packet in multilayer phosphorene samples by using the Green's function representation [116, 144] and the continuum model [169] for low-energy electrons in N-layer BP. We performed analytical calculations to investigate the time evolution of some physical observables and, by considering an arbitrary pseudospin amplitude for the BP sublattices, we obtained explicit analytical expressions for the two components of wave function and the expectation values of the x and y position operators. A numerical method based on the split-operator technique for N-layer BP system was also used, and its results were compared to the analytical ones. Both analytical and numerical methods illustrated similar effects, such as the packet splitting and ZBW oscillation, with good quantitative agreement. The methods exhibited a quantitative discrepancy for the worst case of $\approx 11\%$ at maximum and it occurs, in general, for large values of wave vector and after long time steps, as well as fewer numbers of layers. The errors are primarily due to: (i) inaccuracy in numerical integration to obtain the expectation values of the analytically derived position operators, and (ii) small numerical errors accumulated over the temporal evolution in split-operator technique.

The results obtained for monolayer, bilayer, trilayer and tetralayer phosphorene clearly

demonstrate that the time evolution of wave function is accompanied by ZBW oscillations, which strongly depend on the initial pseudospin polarization, and decay of the wave packet amplitude. The trembling motion and transient character of the ZBW were verified in the average position and average group velocity of the center mass of the propagated wave packet. The amplitude, frequency and duration time of the transient ZBW are shown to decay faster with increasing wave vector, due to wave packet dispersion. It was also found that for the three investigated configurations of initial pseudospin, the oscillation amplitude of average position is more pronounced for the case $[c_1, c_2]^T = [1, 0]^T$, being related to the unbalance of the probability amplitude on the BP sublattices. Moreover, we showed that electrons moving in N-layer phosphorene exhibit qualitatively similar results as the ones observed in the monolayer BP case, except for the oscillation phase difference and final group velocity achieved after the transient behavior. This is caused by the different curvature of the energy bands for the different N-layer phosphorene, and consequently different effective masses and Hamiltonian parameters in the continuum model. In addition, the anisotropic character of the N-layer BP energy bands and their effective masses along the x (zigzag) and y (armchair) directions imply an elliptical shape for the propagated wave packet, since the group velocity is also consequently anisotropic, i.e. it is greater in one direction than the other leading to a non-uniform propagation along the different directions.

In order to understand in more details the nature of the transient character of the ZBW effect in multilayer BP systems, we investigated numerically also the spatial evolution of the initial wave packet by showing snapshots for $t > 0$ of the probability density of the wave function. We demonstrated the effect of the packet splitting is associated to the ZBW. This splitting of the wave packets in two parts appears due to the presence of the electron states with a Gaussian distribution of negative and positive momenta, which propagate with different group velocity in opposite directions. Furthermore, based on the Heisenberg picture and by the calculation of the velocity operators, we demonstrated that the trembling motion along the y direction at small times for the wave packet propagation in phosphorene systems is unavoidable even for null initial momentum.

7

Electronic and transport properties of anisotropic semiconductor quantum wires

Within the effective-mass approximation, we theoretically investigated the electronic and transport properties of 2D semiconductor quantum wires (QWs) with anisotropic effective masses and different orientations with respect to the anisotropic axis. The energy levels in the absence and presence of an external magnetic field are analytically calculated, showing: (i) a strong dependence on the spacing of energy levels related to the alignment QW angle and the anisotropy axis; and (ii) for non-null magnetic field, the quantum Hall edge states are significantly affected by the edge orientation. Moreover, by means of the split-operator technique, we analyzed the time evolution of wavepackets in straight and V-shaped anisotropic QWs and compared the transmission probabilities with those of isotropic systems. In the anisotropic case we found damped oscillations in the average values of velocity in both x and y directions for a symmetric Gaussian wavepacket propagating along a straight wide QW, with the oscillation being more evident as the non-collinearity between the group velocity and momentum vectors increases.

7.1 Motivation

In the last two decades, the production of graphene has led to a significant level of interest on the physics of layered materials [3, 70, 62, 142, 153, 183, 184, 185, 186, 187, 188]. This interest is not only due to its possible future technological applications, but also because it provides the possibility to probe interesting phenomena predicted by quantum field theories not found in conventional semiconductors and metals. Along with the investigation of basic properties of these materials, there has also been a significant effort to develop devices that can benefit from their two-dimensional (2D) character. In that respect, the introduction of additional confinement by creating 1D (quantum wires (QWs)) and 0D (quantum dots) structures becomes relevant [169, 99, 174, 189, 190, 191, 192, 193, 194, 195], since these are known to modify the electronic spectra and the transport properties of the structure in comparison with the pristine sample.

Most recently, there is a growing interest in single layers of black phosphorus (BP), also known as phosphorene [93, 39, 46, 19, 20, 32, 31] which is a semiconductor with a puckered structure, due to sp^3 hybridization and displays a tunable bandgap [46, 19]. In addition, phosphorene presents a highly anisotropic band structure and thus an anisotropic effective mass [153, 169, 93, 39, 46, 19, 20, 32, 31]. Another material that has attracted attention due to its anisotropic properties is single layer Arsenic (arsenene) [196, 197, 198, 199, 200, 201], a semiconductor also with a puckered structure. Due to the highly anisotropic band structures of such crystals, their electrical conductivity, thermal conductivity and optical responses are found to be strikingly dependent on the crystallographic directions [20, 32, 156, 47, 157, 158, 160, 161, 164, 165, 166]. In particular, one possible consequence of the anisotropy may be seen in the electronic confinement caused by the presence of constraints such as external gates or crystal terminations. In that case, a dependence of the confined states on the direction of the alignment of the constraint may arise.

In this chapter we investigate the electronic and transport properties of anisotropic materials in which a 1D confining potential has been imposed. The work proceeds as follows: Initially we investigate the case of 1D confinement in an anisotropic system (i.e. a QW) in which the QW orientation may not match the anisotropy axis of the sample. In order to do that, we employ an effective mass model in which the anisotropy is encoded in the direction-dependent effective mass. Next, we show results for the spectra of confined states for different orientation angles of QW edges in the presence of an external magnetic field. By using the split-operator technique [99, 174, 170, 171, 79, 172, 173, 175, 110, 176, 177, 178, 179, 180, 202, 203, 204], we then present results for the time-evolution of a Gaussian wavepacket propagating in an anisotropic QW that presents a "bend", i.e. the orientation of the QW with regards to the anisotropy axes changes along the longitudinal direction. We numerically investigate the electronic scattering of the propagated wavepacket at the bend caused by the mismatch between the electronic subbands at each QW region, which is an evidence of their dependence on the orientation angle. In addition, we calculate the average velocity values for the x and y directions of an initially symmetrical Gaussian wavepacket propagating along a large QW in order to analyze the non-specular reflections at the QW edges and the combination of effects due to the anisotropy and system geometry.

Initially we present the analytical model for anisotropic classic systems taking as starting point an effective mass model. We show the spectrum of confined states for QWs anisotropic systems with different orientation angles with and without an external magnetic field. The influence of an anisotropic QW formed by leads with different alignment angles in the scattering initial Gaussian wavepacket is also studied.

7.2 Anisotropic classic systems

Let us consider an anisotropic 2D system in which the anisotropy is introduced as direction-dependent effective masses. Among an extensive list of anisotropic materials, such as BP [93, 39, 46, 19, 20, 32, 31], arsenene [196, 197, 198, 199, 200, 201], ReS$_2$ [205], TiS$_3$ [205], and others, the first two are the most prominent ones, and for that reason why, we henceforth assume parameters suitable for these materials. Similar qualitative results discussed along this work are expected for any of the above mentioned anisotropic materials. Effective mass models have been shown to give a reasonable description of the low-energy spectrum of phosphorene and arsenene. [206, 207] In general, in the theoretical analysis of such system, it is convenient to chose coordinate axes in such a way that they match the anisotropy directions (henceforth known as the x and y directions, with m_x and m_y being the effective masses along each direction, respectively). Table I presents the values of electron effective masses for both phosphorene and arsenene. However, as shown below, it is necessary in the present case to consider a more general configuration. Thus, in general the Hamiltonian is given by

$$H = \frac{p_x^2}{2m_x} + \frac{p_y^2}{2m_y}. \tag{7.1}$$

A curve of constant energy in momentum space is then an ellipse. A more complicated but also more interesting case is when the coordinate axes are not parallel to the anisotropy axes. We can obtain that by rotating the coordinate system in momentum space, such that the semi-major axis of the elliptical constant energy curve is rotated by an angle α around the z axis. That give us: $p_x = p'_x \cos\alpha - p'_y \sin\alpha$ and $p_y = p'_x \sin\alpha + p'_y \cos\alpha$, where the primed terms correspond to the new, rotated coordinate system. Thus, we can now obtain the Hamiltonian as

$$H = \frac{p_x'^2}{2\mu_1} + \frac{p_y'^2}{2\mu_2} + \frac{p'_x p'_y}{\mu_3}, \tag{7.2}$$

Table 7.1: Electron effective masses in the x and y directions for phosphorene and arsenene in units of free electron mass (m_0).[39]

	phosphorene	arsenene
m_x/m_0	1.01	0.23
m_y/m_0	0.19	1.22

with

$$\frac{1}{\mu_1} = \frac{\cos^2 \alpha}{m_x} + \frac{\sin^2 \alpha}{m_y}, \tag{7.3a}$$

$$\frac{1}{\mu_2} = \frac{\sin^2 \alpha}{m_x} + \frac{\cos^2 \alpha}{m_y}, \tag{7.3b}$$

$$\frac{1}{\mu_3} = \left(\frac{1}{m_y} - \frac{1}{m_x} \right) \sin \alpha \cos \alpha. \tag{7.3c}$$

From Eq. (7.2) we find

$$p'_y = \pm \sqrt{ 2\mu_2 E - \left(\frac{\mu_2}{\mu_1} - \frac{\mu_2^2}{\mu_3^2} \right) p_x'^2 } - \frac{\mu_2}{\mu_3} p'_x. \tag{7.4}$$

It can be immediately seen that for $m_x = m_y$ (i.e. $1/\mu_3 = 0$) we obtain $p'_y = \sqrt{2\mu E - p_x'^2}$, with $\mu_1 = \mu_2 = \mu$, as expected for the isotropic case. Let us now obtain the components of the velocity vector. An important feature of anisotropic systems is the fact that the velocity is usually not collinear with the momentum vector, as shown below by computing $v'_i = \partial E / \partial p'_i$ for $i = x$ and y. Thus, the velocity components are given by

$$v'_x = \frac{p'_x}{\mu_1} + \frac{p'_y}{\mu_3} \quad , \quad v'_y = \frac{p'_y}{\mu_2} + \frac{p'_x}{\mu_3}, \tag{7.5}$$

where it is seen that v'_x (v'_y) can be non-zero even if p'_x (p'_y) vanishes.
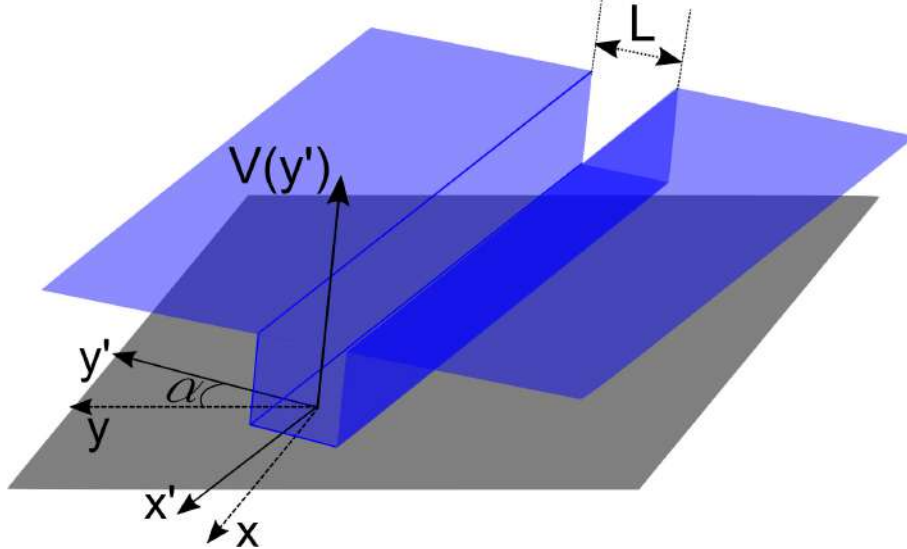
Figure 7.1: Schematic representation of the rotated QW defined electrostatically by the 1D square-well potential $V(y') = V_0 \left[\Theta(-y') + \Theta(y' - L) \right]$ with width L and $V_0 > 0$. α is the rotation angle with respect to the crystallographic directions (x and y), defining the new primed coordinates (x' and y').

7.3   Anisotropic quantum wires

7.3.1   In the absence of magnetic field

Let us consider the case of a QW with infinite potential walls ($V_0 \to \infty$ in $V(y')$), for interfaces aligned along an arbitrary direction, i.e. non-zero $1/\mu_3$ (see Fig. 7.1). Without loss of generality, we will assume that the walls are parallel to the x' direction, the assumed translational symmetry direction of the system, allowing us to write the wavefunction as $\Psi = \phi(y')e^{ik_x'x'}$. Using the Hamiltonian given by Eq. (7.2) and the substitutions $\vec{p'} = \hbar\vec{k'}$ and $\vec{k'} \to -i\nabla'$, the resulting time-independent Schrödinger equation for the rotated QW becomes

$$-\frac{\hbar^2}{2\mu_2}\frac{d^2\phi}{dy'^2} - i\frac{\hbar^2 k_x'}{\mu_3}\frac{d\phi}{dy'} + \frac{\hbar^2 k_x'^2}{2\mu_1}\phi = E\phi. \tag{7.6}$$

We obtain a solution by assuming linear combinations of incident and reflected states as

$$\Psi(x',y') = \left[A\exp(ik_y'^+ y') + B\exp(ik_y'^- y')\right]e^{ik_x'x'}, \tag{7.7}$$

with

$$k_y'^\pm = \pm\theta_1 - \theta_2, \tag{7.8a}$$

$$\theta_1 = \sqrt{\frac{2\mu_2 E}{\hbar^2} - \left(\frac{\mu_2}{\mu_1} - \frac{\mu_2^2}{\mu_3^2}\right)k_x'^2}, \tag{7.8b}$$

$$\theta_2 = \frac{\mu_2}{\mu_3}k_x', \tag{7.8c}$$

where the plus (minus) sign refers to incident (reflected) waves. Now, one has to introduce the boundary conditions, i.e. the vanishing of ϕ at the interfaces, for $y' = 0$ and $y' = L$ in Eq. (7.7). That leads to the conditions $B = -A$ and $\sin(\theta_1 L) = 0$, resulting in the following quantization condition $\theta_1 = n\pi/L$ with $n \in \mathcal{Z}$. Therefore, the wavefunction and the energy levels are found as

$$\Psi(x',y') = A\sin\left(\frac{n\pi}{L}y'\right)\exp\left[i\left(x' - \frac{\mu_2}{\mu_3}y'\right)k_x'\right], \tag{7.9a}$$

$$E = \frac{\hbar^2 n^2 \pi^2}{2\mu_2 L^2} + \frac{\varrho\hbar^2 k_x'^2}{2\mu_1}, \tag{7.9b}$$

respectively, where $\varrho = 1 - \frac{\mu_1\mu_2}{\mu_3^2}$. It is seen that both the wavefunction, Eq. (7.9a), and the energy spectrum, Eq. (7.9b), show a striking dependence on the QW orientation α in relation to the anisotropy axes.

Figure 7.2 depicts the dependence of electronic energy levels of phosphorene and arsenene QWs with respect to the QW width L, by using Eq. (7.9b) with $k_x' = 0$ and the effective masses of Table I. In panel (a) the energy levels for three different QW angles are shown for monolayer BP material, and in panel (b) we compare the electronic confined states of (solid curves) phosphorene and (dashed curves) arsenene with the fixed
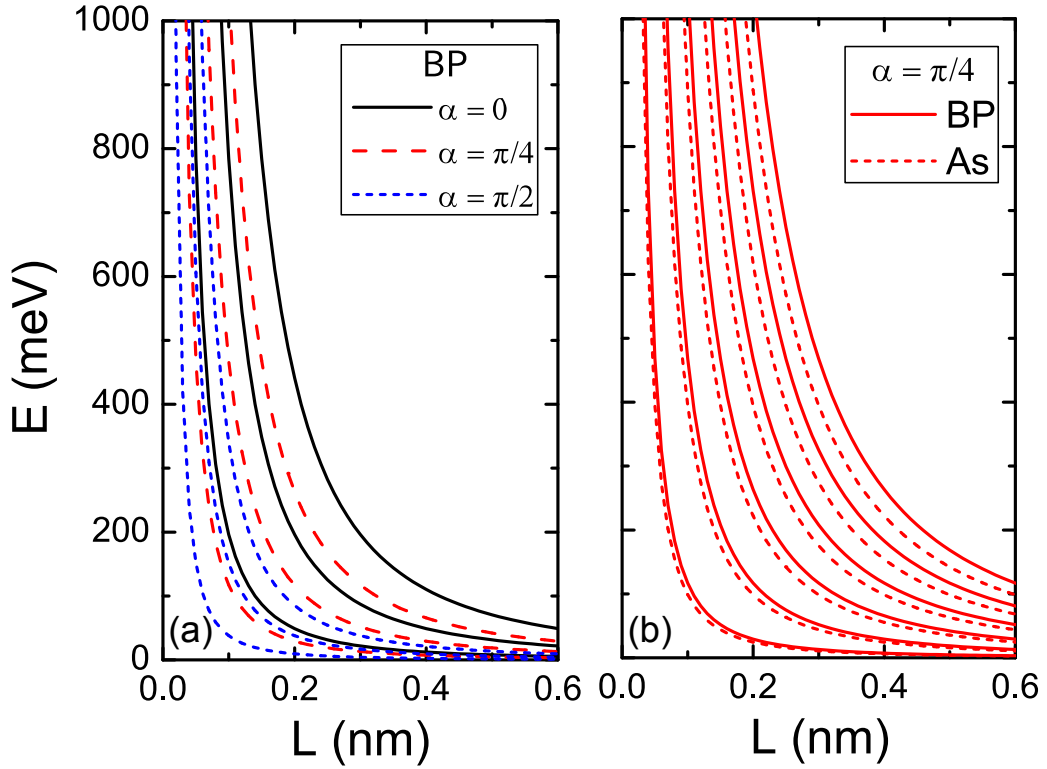
Figure 7.2: Energy levels as function of QW width with $k'_x = 0$ in Eq. (7.9b) (a) for different rotation angle α with respect to the anisotropy axes and taking the effective masses of monolayer BP, and (b) for a fixed angle $\alpha = \pi/4$ and assuming (solid curves) phosphorene and (dashed curves) arsenene parameters.

angle $\alpha = \pi/4$. It is seen that the energy levels decrease quadratically with increasing QW width, something already expected when we make $k'_x = 0$ in Eq. (7.9b), scaling as $\approx 1/L^2$ in a similar way as observed for confined states in 1D squared quantum well and widely presented in quantum mechanic text books. A consequence of the change of QW alignment, as shown in Fig. 7.2(a), is a shift of the energy levels, together with a change of level spacing. By comparing the cases of a QW made of arsenene and phosphorene for a given value of rotation angle, shown in Fig. 7.2(b) it is seen that the behavior of the electronic levels of the two samples is similar. A difference that is evident in the dispersion relation in Figs. 7.3(a) and 7.3(b), for QW with width $L = 1$ nm for BP and As, respectively, is the fact that the confined states in BP QWs present higher energy values than those of arsenene. This is caused by the different effective masses of the materials (see Table I). Moreover, Fig. 7.3 shows that, as α increases the energy levels are shifted to lower (upper) values for phosphorene (arsenene) and the spacing between them decreases (increases) too, which in turn increases (decreases) in the number of accessible electronic states. This result is emphasized in Fig. 7.4, which shows the energy levels as function of the alignment angle α for (blue solid curves) phosphorene and (dashed red curves) arsenene QW, maintaining the QW width $L = 1$ nm and $k'_x = 0$ in Eq. (7.9b). Note that these behaviors of the confined QW energy levels with respect to the rota-

tion angle strongly resemble to those for 1D quantum well in Schrödinger equation with isotropic masses by varying the QW width instead of the alignment angle, i.e. the change of alignment QW angle with a fixed width L for the anisotropic case works similarly as the isotropic case by varying the QW width. Phosphorene and arsenene energy levels exhibit opposite behaviors due to highest effective mass being along opposite directions in these materials (see Table 7.1). These results suggest that a connection of QWs with different rotation angles acts similarly to constrictions in quantum point contact systems, due to the mismatch of the energy levels in the different sections of the QW junction. Such kind of QW junction system shall be explored latter in Sec. 7.4.
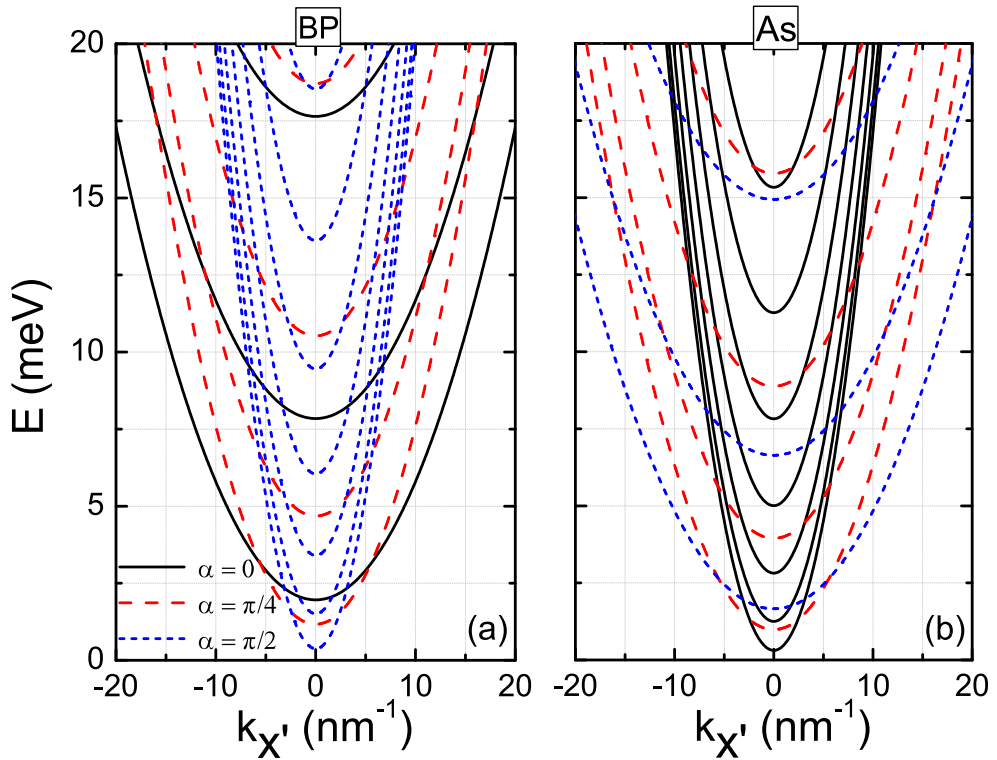
Figure 7.3: Dispersion relation of QW with width $L = 1$ nm for (a) phosphorene and (b) arsenene (As), and taking different rotation angle α with respect to the anisotropy axes.

7.3.2 In the presence of magnetic field

Let us now study the effect of an external magnetic field perpendicular to the plane containing the QW, by considering the substitution $\vec{p'} \to \vec{p'} + e\vec{A}$ in Eq. (7.6). A convenient choice of gauge is $\vec{A} = \left(-By', B\frac{\mu_2}{\mu_3}y', 0\right)$. In this case, one finds $\vec{\nabla} \cdot \vec{A} = (\mu_2/\mu_3)B$. Since we assume an uniform magnetic field, in this gauge the vector potential corresponds to an uniform rotation of the vector potential obtained from the Landau gauge by an angle of $\arctan(\mu_2/\mu_3)$. It is seen that for the isotropic case (i.e. $1/\mu_3 = 0$), as well as for $\alpha = 0$ and $\alpha = \pi/2$ one recovers the usual vector potential of the Landau gauge. Then, the
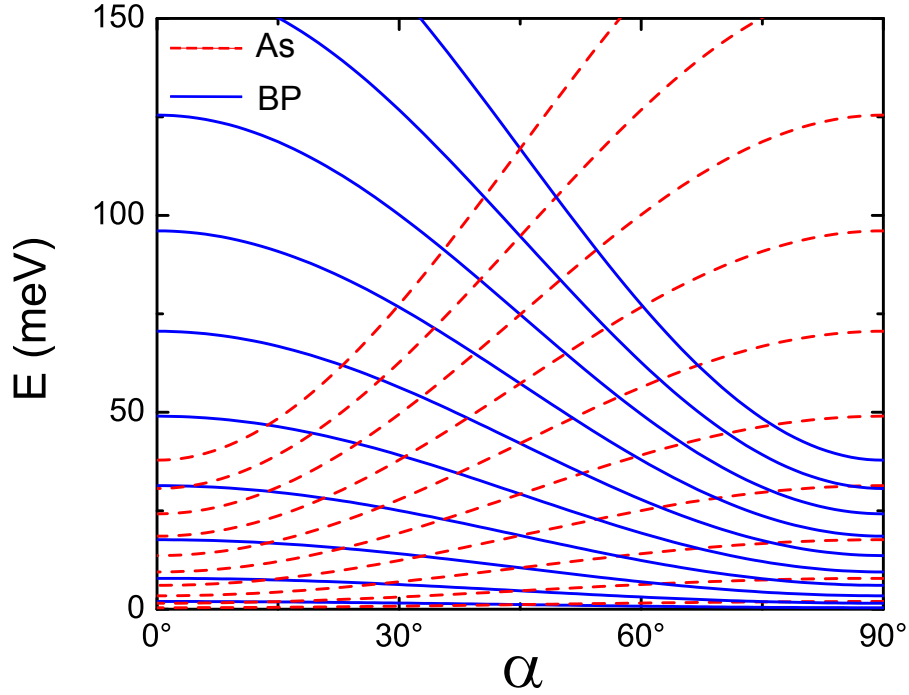
Figure 7.4: Energy levels as a function of the rotation angle α with respect to the anisotropy axes (see Fig. 7.1) for (blue lines curves) phosphorene and (red dashed curves) arsenene QWs. It was taken $L = 1$ nm and $k'_x = 0$.

Schrödinger equation for rotated QW in the presence of a perpendicular magnetic field can be written as

$$\frac{-\hbar^2}{2\mu_2}\frac{d^2\Psi}{dy'^2} - i\frac{\hbar^2 k'_x}{\mu_3}\frac{d\Psi}{dy'} + \frac{\varrho}{2\mu_1}(eBy' + \hbar k'_x)^2 + (1-\varrho)\frac{\hbar^2 k'^2_x}{2\mu_1} = E\Psi. \tag{7.10}$$

Performing the coordinate transformation $y^* = y' + \frac{\hbar k'_x}{eB}$, defining the cyclotron frequency for the rotated anisotropic system as $w_c^2 = \varrho\left(\frac{eB}{\mu_1}\right)^2$ and the new energies as $E' = E - (1-\varrho)\frac{\hbar^2 k'^2_x}{2\mu_1}$, one can rewrite Eq. (7.10) as

$$\frac{-\hbar^2}{2\mu_2}\frac{d^2\Psi}{dy^{*2}} - i\frac{\hbar^2 k'_x}{\mu_3}\frac{d\Psi}{dy^*} + \frac{\mu_1 w_c^2 y^{*2}}{2}\Psi = E'\Psi. \tag{7.11}$$

By assuming the following ansatz $\Psi(x', y^*) = \exp\left(-i\mu_2 k'_x y^*/\mu_3\right)\phi(x', y^*)$ in order to eliminate the first derivative in Eq. (7.11), it becomes

$$\frac{-\hbar^2}{2m^*}\frac{d^2\phi}{dy^{*2}} + \frac{m^*}{2}w_c^2 y^{*2}\phi = \sqrt{\frac{\mu_2}{\mu_1}}E\phi, \tag{7.12}$$

where $m^* = \sqrt{\mu_1\mu_2}$. Solving Eq. (7.12) numerically we obtain the energy levels for a QW in the presence of external magnetic field and different system parameters. Figure 7.5 shows the dispersion relation for different alignment angles (black solid curves) $\alpha = 0$, (red dashed curves) $\alpha = \pi/4$, and (blue short-dashed curves) $\alpha = \pi/2$, and fixed QW width $L = 100$ nm and external magnetic field $B = 5$ T. It is seen that similarly to
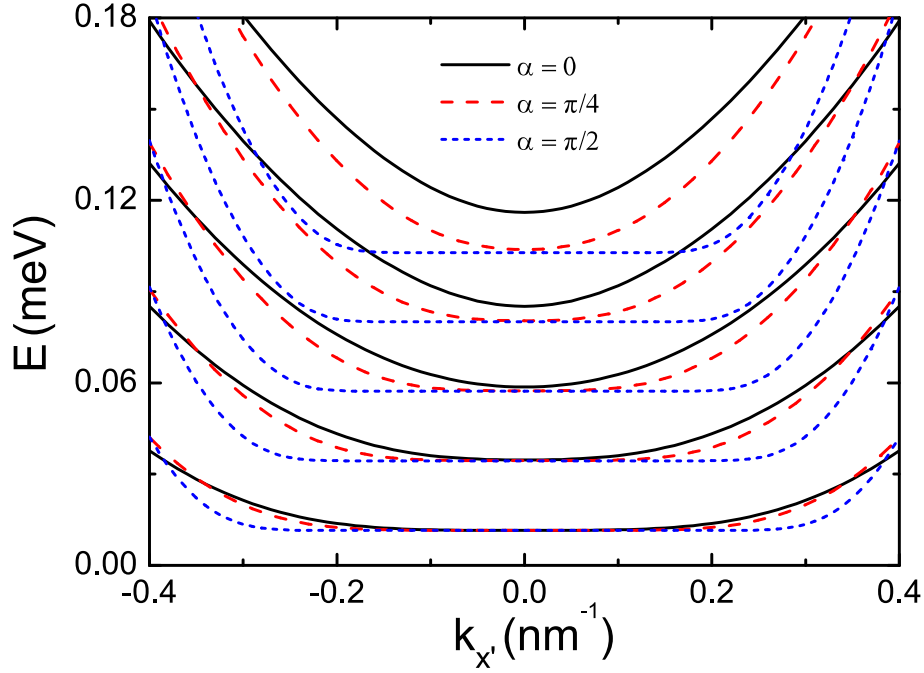
Figure 7.5: Dispersion relation of phosphorene QW for different alignment angles α with respect to the anisotropy axes and fixed QW width $L = 100$ nm and magnetic field amplitude $B = 5$ T. Black solid, red dashed, and blue short-dashed curves correspond to the spectrum for rotation angles $\alpha = 0$, $\alpha = \pi/4$, and $\alpha = \pi/2$, respectively.

an isotropic semiconductor structure with two boundaries, there is a momentum region around $k'_x = 0$ where the energy levels are flat (i.e. $dE/dk_{x'} = 0$). These states correspond to quantum Hall states, being more dispersive the higher the energy value, owing to the fact that the lower energy states are more strongly confined by the magnetic field. The presence of the edges gives rise to propagating states, resulting in the quantum Hall edge states. These states are related to the dispersive region of the energy spectrum in Fig. 7.5, i.e. for momentum values away from the plateaus. [208, 209, 210, 211, 212] In addition to the mentioned features, for the anisotropic QW case: (i) the quantum Hall edge states are significantly affected by the alignment of the QW, and (ii) as α increases, the energy states are found to be less dispersive, that is caused by the fact that the wavefunctions become more localized, as it will be discussed next in Fig. 7.6. Consequently, the group velocities of the quantum Hall edge states show a striking dependence on the edge alignment.

In order to understand the effects of the rotation angle changes and the magnetic field on the electronic confined states, we show in Fig. 7.6 the probability density of the ground state for different rotation angles with and without a magnetic field, taking the same system parameters as in Fig. 7.5. Since Eq. (7.11) is a quantum harmonic oscillator type equation, the ground state wavefunction of a rotated anisotropic QW in the presence of a magnetic field is given by

$$\Psi(x', y*) = \left(\frac{m^* \omega_c}{\pi \hbar}\right)^{1/4} \exp\left(-\frac{m^* \omega_c y^{*2}}{2\hbar} - i\frac{\mu_2}{\mu_3} k'_x y^*\right). \tag{7.13}$$
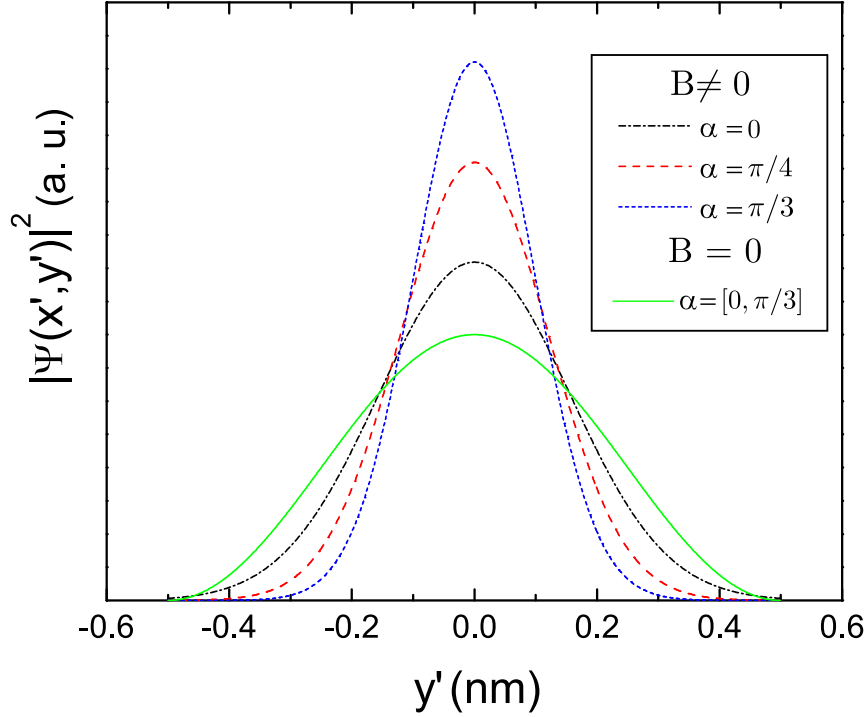
Figure 7.6: Squared total wavefunction for anisotropic rotated QWs in the presence of an external magnetic field, $B = 5$ T, with a fixed QW width $L = 100$ nm and wave vector $k'_x = 0$. Black dashed-dot, red dashed, and blue short-dashed curves correspond to the case for rotation angles $\alpha = 0$, $\alpha = \pi/4$, and $\alpha = \pi/2$, respectively. For comparison, $|\Psi|^2$ for $B = 0$ is shown by green solid curve.

Similar to the case for zero magnetic field (see Eq. (7.9a)), the wavefunction not only contains plane wave term but depends on the QW alignment in relation to anisotropy axes, which is contained into y^* term. One can note that: (i) for a fixed rotation angle, the total wavefunction is more localized for $B \neq 0$ than $B = 0$, as already expected, (ii) for $B \neq 0$, as α increases $|\Psi|^2$ becomes more localized, and (iii) for $B = 0$, the QW rotations do not affect the wavefunction profile, as shown by the green solid curve in Fig. 7.6 for $\alpha = 0$ and $\alpha = \pi/3$.

A complementary way to see the magnetic field dependence of the confined states in anisotropic QWs is shown in Fig. 7.7. The spectra for null and non-null wave vectors are present in panels (a) and (b), respectively, for three different rotation angles. Note that, as the magnetic field increases, the magnetic length becomes smaller than the system size, so that confinement effects are strongly reduced, and the magnetic levels in the phosphorene QW converge to the Landau levels of an infinite phosphorene sheet, given by: $E = \hbar\omega (n + 1/2)$, with $n = 0, 1, 2, \ldots$, and $\omega = eB/m_g = \omega_c \sqrt{\mu_1/\mu_2}$ being the cyclotron frequency calculated with the geometric mean of the masses $m_g = \sqrt{m_x m_y}$. [169, 93] Moreover, one can realize that the energy levels spacing is strongly affected by the mag-
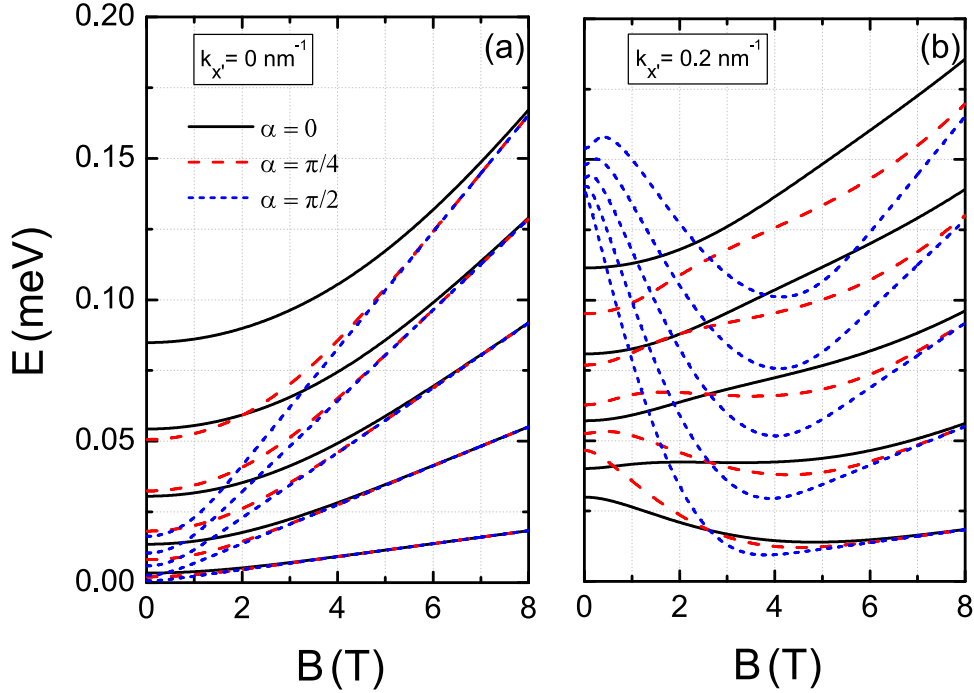
Figure 7.7: Energy levels of a phosphorene QW with width $L = 100$ nm as function of the magnetic field for wave vector values (a) $k'_x = 0$, and (b) $k'_x = 0.2$ nm^{-1} for different rotation angles α with respect to the anisotropy axes.

nitude of the applied magnetic field, and with increasing magnetic field the confinement effects due to QW rotation discussed in Sec. 7.3.1 are less evident, such that regardless the wave vector amplitude (see, e.g. panels 7.7(a) and 7.7(b)) and QW rotation angle the energy levels converge to the Landau levels of an infinite system.

7.4   Wave-packet propagation and scattering in anisotropic quantum wires

As the previous results have shown, the electronic spectrum of anisotropic QWs is strongly dependent on the relative orientation of the QW in relation to the anisotropic axes. Therefore, it can be expected that a change of orientation angle (α) along the length of the QW may give rise to an energy mismatch, as illustrated in Fig. 7.8(a), which can in turn lead to electron scattering. In order to investigate that, let us now calculate the transport properties of a QW in which an abrupt change of α is introduced, forming a elbow-like feature in an otherwise straight QW. For this purpose, let us now consider electrons in the (x, y) plane moving from left to right in a region with a V-shaped QW formed by a straight section with $\alpha = 0$ and a section with $\alpha \neq 0$ as illustrated in Fig. 7.8(b). The electrons are confined by a step like potential, i.e. $V(x, y) = 0$ inside
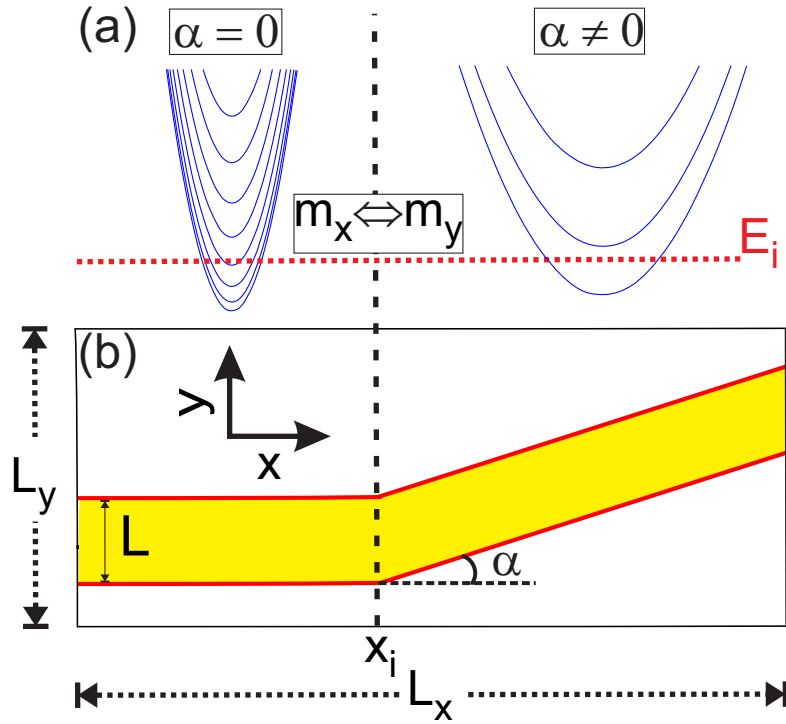
Figure 7.8: Illustration of (a) the energy bands for each QW section of (b) the V-shaped anisotropic QW due to an abrupt change of orientation angle α along the QW length. For $x < x_i$ ($\geq x_i$), one has $\alpha = 0$ ($\alpha \neq 0$). The two QW sections are made up of a phosphorene QW with width L. The energy bands for each QW section exhibit different energy levels spacing and minimum, and consequently leading to an energy mismatch in the junction. E_i and x_i indicate the initial wavepacket energy and the position of the QW corner. L_x (L_y) is system length along the x (y) direction.

the QW and $V(x, y) = V_0$ otherwise. Moreover, we assume that the electrons are always in the conduction band and that conduction-to-valence band transitions are negligible, which is a reasonable approximation when dealing with low-temperature systems and also once that the conduction-to-valence energy distance, i.e. the energy gap, is large for phosphorene systems [169, 93, 39]. It was considered QWs with width $L = 3$ nm and $L = 10$ nm, abrupt borders, and made out of phosphorene. For simplicity sake, throughout this section the effective masses along the x and y directions were exchanged as the ones referred in Table 7.1.

The injected electrons are described by a combination of a Gaussian function with a plane wave along the x direction and the ground state wavefunction of the QW in the y direction $\phi_0(y)$. Then, at $t = 0$ the initial wavepacket is defined by

$$\Psi_0(x, y) = \exp\left[ik_x^i x - \frac{(x - x_0)^2}{2d^2}\right]\phi_0(y), \tag{7.14}$$

where $k_x^i = \sqrt{2m_x E_i/\hbar^2}$ is the wave vector corresponding to the packet kinetic energy E_i (see dotted line in Fig. 7.8(a)), d is the initial wavepacket width in the x direction

that is chosen as the same QW width L, and x_0 is the initial postion in the x direction of the wave packet maximum, set up far from the corner of the bent QW, such as $x_0 = -32.5$ nm and $x_0 = -8.6$ nm for the QW width cases $L = 10$ nm and $L = 3$ nm, respectively. It is important to stress out that the ground state wavefunction $\phi_0(y)$ is given by Eq. (7.9a) which is closely related to the initial QW alignment angle, since it contains angle-dependent anisotropic effective masses terms.

With the aim of solving the time-dependent Schrödinger equation to obtain the propagating wavepacket through the evolved time steps and thus to get the transport properties of the analyzed system, one applies the split-operator technique. For this, we follow the approach described in Refs. [99, 174, 170, 171, 79, 172, 173, 175, 110, 176, 177, 178, 179, 180, 202, 203, 204]. This allows us to separate the exponential of the time evolution operator (that for the case in which the Hamiltonian does not explicitly depend on time, this operator can be written as $\hat{U}(t', t) = \exp\left[-\frac{i}{\hbar} H(t' - t)\right]$) into two parts: one of them involves only the potential operator $\hat{V}$, whereas the other contains only the kinetic operator $\hat{T}$, as well as, enabling to split also the kinetic terms for each direction. Therefore, the time evolved wavefunction is obtained by successively applying the operation $\hat{U}$ such as

$$\Psi(\vec{r}, t + \Delta t) = e^{-i\hat{V}\Delta t/2\hbar} e^{-i\hat{T}_x\Delta t/\hbar} e^{-i\hat{T}_y\Delta t/\hbar} e^{-i\hat{V}\Delta t/2\hbar} \Psi(\vec{r}, t), \qquad (7.15)$$

where $\hat{T}_{x(y)}$ is the kinetic-energy operator for $x(y)$ direction and we neglect terms of order $\mathcal{O}\left(\Delta t^3\right)$ and higher, being such error a consequence of the noncommutativity of kinetic and potential terms. This error can be minimized as smaller the time step. We assume a small time step of $\Delta = 0.7$ fs. Here, we opted for the split-operator technique, because it allows us to track the position and velocity of the center of mass trajectories, see reflection patterns and scattering on the edges, and obtain the transmission and reflection coefficients (which will be important to the analysis in this section).

To numerically solve this problem, we discretized the (x, y) plane with a square grid, assuming $\Delta x = \Delta y = 0.4$ nm and $\Delta x = \Delta y = 0.12$ nm for the cases where $L = 3$ nm and $L = 10$ nm, respectively, and used the finite difference scheme to solve the derivatives in the kinetic energy terms of the Hamiltonian. In addition, as suggested in Ref. [213] and successfully used in Refs. [172, 173, 175, 202] we added an absorbing (imaginary) potential on the boundaries of our computational box in order to avoid spurious reflections and backscattering when the wavepacket reaches the limits of our system.

For each investigated system configuration, we run the simulation and calculate: (i) the transmission probability $T(t)$ for each time step by integrating the square modulus of the normalized wavepacket in the region after the elbow-like QW corner, i.e. for $x > x_i$, given by

$$T(t) = \int_{-L_y/2}^{L_y/2} dy \int_{x_i}^{L_x/2 - |x_i|} dx \, |\Psi(x, y, t)|^2, \qquad (7.16)$$
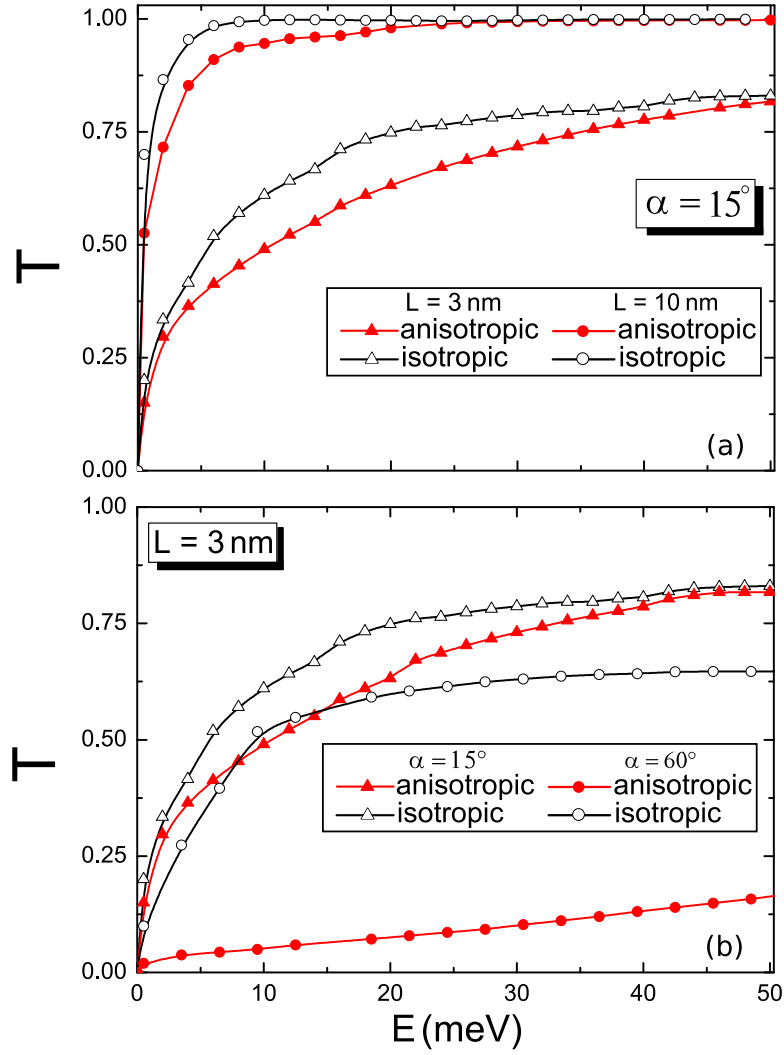
Figure 7.9: Transmission probabilities as a function of the initial wavepacket energy by assuming the elbow-like QW with: (a) a fixed rotation angle $\alpha = 15°$ and QW widths $L = 3$ nm (triangles) and $L = 10$ nm (circles); and (b) a fixed QW width $L = 3$ nm and rotation angles $\alpha = 15°$ (triangles) and $\alpha = 60°$ (circles). Red (filled) and black (open) curves (symbols) correspond to the anisotropic and isotropic QW cases.

(ii) the total average position, i.e., the trajectory of the wavepacket center of mass, that is calculated for each time step by computing

$$\langle x(t) \rangle = \int_{-L_y/2}^{L_y/2} dy \int_{-L_x/2}^{L_x/2} dx \, |\Psi(x,y,t)|^2 \, x, \qquad (7.17\text{a})$$

$$\langle y(t) \rangle = \int_{-L_x/2}^{L_x/2} dx \int_{-L_y/2}^{L_y/2} dy \, |\Psi(x,y,t)|^2 \, y, \qquad (7.17\text{b})$$
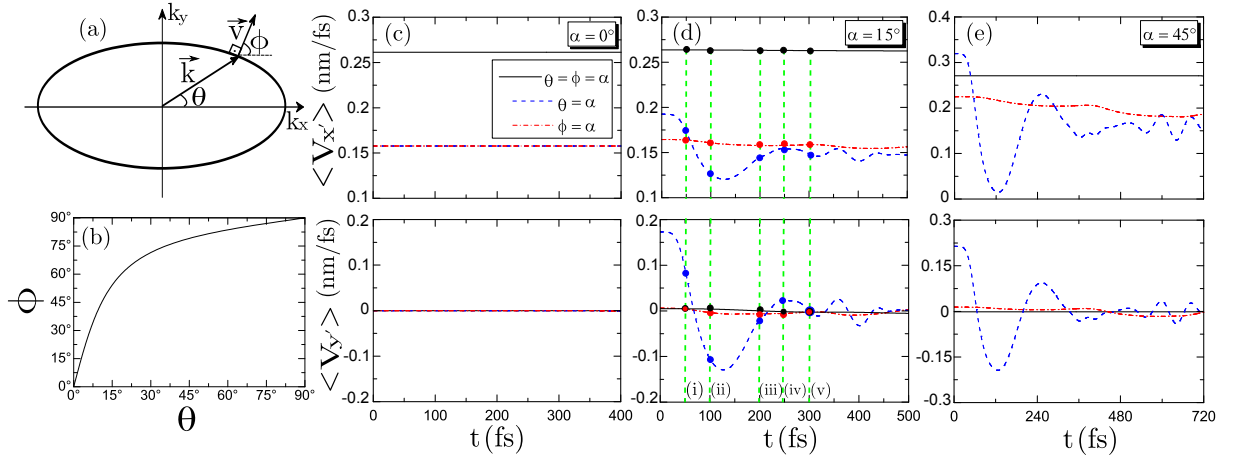
Figure 7.10: (a) Isoenergy curve in momentum space of the electronic band for a non-rotated anisotropic system, that corresponds to $\alpha = 0$. θ and ϕ are the minimum angles with respect to k_x axis that are associated with the orientation of the wave vector $\vec{k}$ and group velocity vector $\vec{v}$, respectively. (b) Values of angle ϕ as a function of angle θ given by the following equation: $\tan\phi = (\tan\theta/\mu_2 - 1/\mu_3) / (\tan\theta/\mu_3 + 1/\mu_1)$. (c)-(e) Average velocities for the (top panels) x' and (bottom panels) y' directions by considering (black solid curve that corresponds to $\theta = \phi = \alpha$) the isotropic case, the anisotropic case with the QW parallel to (blue dashed curve that corresponds to $\theta = \alpha \neq \phi$) the wave vector, and (red dashed-dot curve that corresponds to $\phi = \alpha \neq \theta$) to the group velocity vector. The rotation angle was assumed as (c) $\alpha = 0°$, (d) $\alpha = 15°$, and (e) $\alpha = 45°$.

and (iii) the average velocity, by

$$\langle v_x(t) \rangle = \frac{d\langle x(t) \rangle}{dt}, \tag{7.18a}$$

$$\langle v_y(t) \rangle = \frac{d\langle y(t) \rangle}{dt}, \tag{7.18b}$$

where the limits of the computational box are defined by $x \in [-L_x/2, L_x/2]$ and $y \in [-L_y/2, L_y/2]$. The reflection probability R is obtained by similar integration as Eq. (7.16) but for the region before the QW corner ($x < x_i$). For larger t, the value of the transmission (reflection) probability integral increases (decreases) with time until it converges to a number. This number is then considered to be the transmission (reflection) probability of such a system configuration.

Transmission probabilities for the bent QW computed by using the split-operator technique are presented in Fig. 7.9 as function of the initial wavepacket energy. In Fig. 7.9(a) the transmission was obtained for a QW rotated by a fixed angle $\alpha = 15°$ and QW width $L = 3$ nm (triangles) and $L = 10$ nm (circles) both in isotropic (open symbols) and anisotropic cases (filled symbols). In Fig. 7.9(b), it was fixed the QW width $L = 3$ nm and analyzed two different rotation angles: $\alpha = 15°$ (triangles) and $\alpha = 60°$ (circles). From Fig. 7.9(a), one can notice that: (i) since the energy levels become closer for wider QWs, the wavepacket has a larger transmission probability for wider channels in both
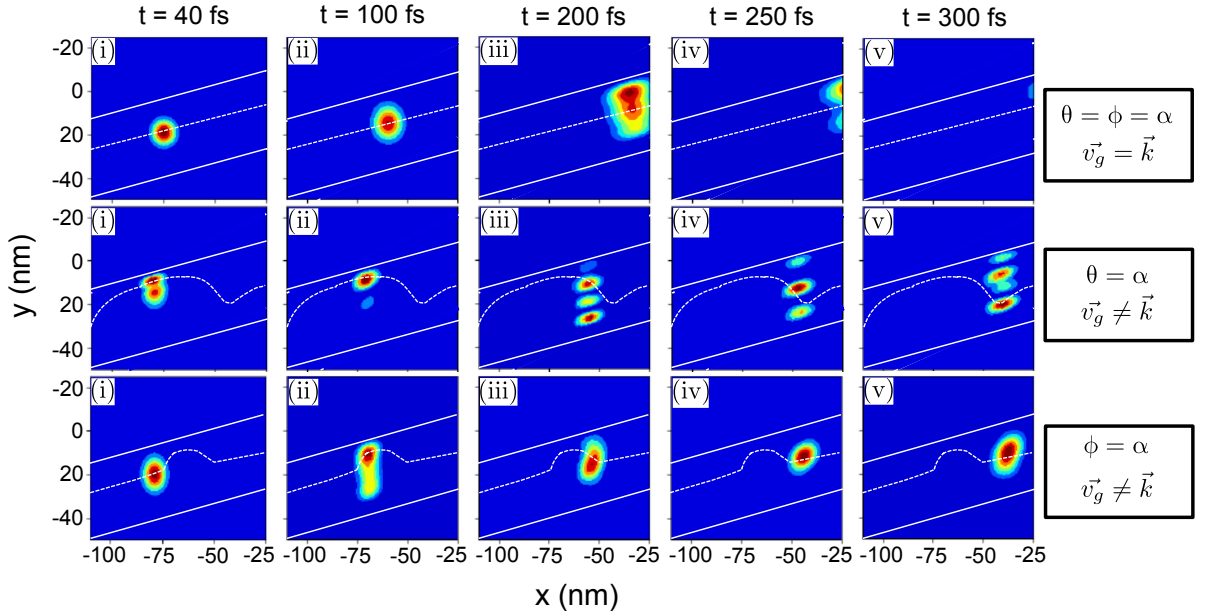
Figure 7.11: Snapshots of the total evolved wavefunction through the QW rotated by $\alpha = 15°$ at the time steps (i) $t = 40$ fs, (ii) $t = 100$ fs, (iii) $t = 200$ fs, (iv) $t = 250$ fs, and (v) $t = 300$ fs as labeled by roman letters in Fig. 7.10(d) and considering (upper panels) $\theta = \phi = \alpha$, (middle panels) $\theta = \alpha$, and (bottom panels) $\phi = \alpha$.

isotropic and anisotropic systems, as well as, it also explains the rapid convergence of the transmission to 1 for wider QWs as a consequence of the larger number of accessible electronic states; (ii) the quantitative difference between anisotropic and isotropic curves for each fixed QW width case is due to the difference on their subbands energy values. Note that the energy bands in both straight and rotated sections of the V-shaped QW are (non-)identical for (an)isotropic case, and thus as a consequence of this energy mismatch caused by the QW bending one has a greater reflection probability for anisotropic case. In both isotropic and anisotropic cases, due to the channel geometry the wavepacket is more reflected when reaches the bend that connects the two leads represented in Fig. 7.8(b), and as the right-arm of QW is rotated the transmission decreases, as can be seen in Fig. 7.9(b). The introduction of a bend in the QW can reduce the transmission even in the isotropic case, due to the fact that it breaks the translational symmetry of the system. For instance, compare black triangular and circular symbols in Fig. 7.9(b), in which the transmission for $\alpha = 15°$ is larger than the case for $\alpha = 60°$ for any initial wavepacket energy. Although the energy bands for the isotropic case are identical for any rotation angles, the QW geometry has an important role on the total transmission probability. Thus, in order to separate this purely geometric effect from the effect of the anisotropy, all the results in Fig. 7.9 show a comparison between the transmission for isotropic and anisotropic cases for different values of L (Fig. 7.9a) and α (Fig. 7.9b).

Another aspect of the transport in anisotropic QWs that was investigated was the effect

of the interaction between the electrons and the QW edges as function of α. A semiclassical analysis suggests that the non-collinearity of the group velocities and the momentum vectors (see Eq. (7.5)) may give rise to a group velocity oscillation. In order to investigate that, we have analyzed the wavepacket dynamics simulating electrons that propagate through a straight QW as the one represented in Fig. 7.1. For this, we considered an initial circularly symmetric Gaussian wavepacket centered in $\vec{r} = (x_0, y_0)$ and multiplied by a pulse with initial wave vector $\vec{k}_0$, given by

$$\Psi(x, y) = \exp\left[-\frac{(x - x_0)^2}{2d^2} - \frac{(y - y_0)^2}{2d^2} + i\vec{k}_0 \cdot \vec{r} \right]. \tag{7.19}$$

In this analysis, it was assumed that the QW width is much larger than the wavepacket width, being taken $d = 5$ nm and $L = 30$ nm, and that the wavepacket is injected from left to right into the channel with initial position $(x_0, y_0) = (-32.5, -8.6)$ nm and initial energy $E = 200$ meV.

Figure 7.10 shows the wavepacket average velocities as function of time for both x and y directions that were obtained by computing the first order derivative of the average positions Eqs. (7.17a) and (7.17b) at each time step, being given by Eqs. (7.18a) and (7.18b), respectively. The wavepacket evolution through the straight QW with different values of rotations angle α was analyzed for both isotropic and anisotropic cases, taking into account the non-collinearity of the wave vector $\vec{k}$ and group velocity vector $\vec{v}$. The wave vector and group velocity are here associated with the angles θ and ϕ, respectively, as illustrated in Fig. 7.10(a), being $\vec{v}$ always perpendicular to the isoenergy in momentum space. It is easy to see from Eq. (7.5) that for isotropic case $(1/\mu_3 = 0)$, one has $\vec{v}' \parallel \vec{k}'$ and the isoenergies are circular. However, as mentioned in Sec. 7.2, for anisotropic semiconductors whose isoenergies are ellipses, this is not the case. Figure 7.10(b) shows the relation between the angles θ and ϕ that differs for almost every angle, except for $\theta = 0°$ and $\theta = 90°$ in which the wave vector and group velocity are aligned, similarly to the isotropic case. Figures 7.10(c) to 7.10(e) depict the average velocities (top panels) v'_x and (bottom panels) v'_y for the following rotation angles: [Fig. 7.10(c)] $\alpha = 0°$, [Fig. 7.10(d)] $\alpha = 15°$, and [Fig. 7.10(e)] $\alpha = 45°$. The black solid, blue dashed, and red dashed-dot curves correspond to $\theta = \phi = \alpha$, i.e. the isotropic case, to $\theta = \alpha \neq \phi$, i.e. the anisotropic case with the QW parallel to the wave vector, and to $\phi = \alpha \neq \theta$, i.e. the anisotropic case with the QW parallel to the group velocity vector, respectively. According to Figs. 7.10(c)-7.10(e), one can realize that: (i) the average velocities for both x and y directions remain unchanged for isotropic case ($\theta = \phi = \alpha$, black solid curves), irrespective to the QW rotation angle, as well as for the anisotropic case in which the wave vector and the group velocity are collinear as shown by the blue dashed and red dashed-dot curves in Fig. 7.10(c). Qualitative similar results can be obtained for $\alpha = 90°$, instead of $\alpha = 0°$; (ii) for $\theta \neq \phi$ and $\alpha \neq 0°, 90°$ that corresponds to non-collinear cases between the wave vector and the group velocity, the average velocities oscillate, as expected by the semiclassical picture due to the non-specular reflections on the edges in an anisotropic media. This can

be seen by the blue dashed and red dashed-dot curves in Figs. 7.10(d) and 7.10(e); (iii) the oscillations are more evident as $|\theta - \phi|$ increases, exhibiting an increasing oscillation amplitude the greater the non-collinearity between the vectors $\vec{k}$ and $\vec{v}$. This can be seen by comparing the oscillation amplitudes of the blue dashed curves in Figs. 7.10(d) and 7.10(e), and also for a fixed rotation angle by comparing the $\theta = \alpha$ and $\phi = \alpha$ cases. Note from Fig. 7.10(b) that for $\theta = \alpha = 15°$ one has $\phi \approx 55°$, whereas for $\phi = \alpha = 15°$ one implies $\theta \approx 4°$, and consequently the difference $|\theta - \phi|$ is larger for former case with $\theta = \alpha$ (blue dashed curves) that indeed exhibits the large oscillation amplitude for the presented cases.

In order to clarify how the non-collinearity between the group velocity and wave vector in anisotropic case affects the wavepacket evolution, it is displayed in Fig. 7.11 snapshots of the time evolution of the probability density propagating through the QW rotated by the angle $\alpha = 15°$ at times (i) $t = 40$ fs, (ii) $t = 100$ fs, (iii) $t = 200$ fs, (iv) $t = 250$ fs, and (v) $t = 300$ fs as labeled in Fig. 7.10(d), and considering the isotropic case (upper panels, $\theta = \phi = \alpha$) and the anisotropic case with the QW orientation parallel to the wave vector (middle panels, $\theta = \alpha \neq \phi$) and to the group velocity (bottom panels, $\phi = \alpha \neq \theta$). By analyzing the snapshots, it is clear that for the isotropic case (upper panels) when the wavepacket evolves it disperses but keeping the average position (white dashed lines) and consequently the average velocity unchanged, as observed in Fig. 7.10(d). Since the propagation direction and the wave vector are collinear for this case, after the reflections at the potential edges the direction of the group velocity vector remains the same over time. However, for the anisotropic case in which the wave vector and the group velocity are non-collinear, when the wavepacket reaches the QW edges it undergoes non-specular reflections [214]. As a consequence, for the case where $\theta = \alpha$, this interaction with the edges results a subpackage splitting with different propagation directions that leads to an average velocity oscillation with large amplitudes that are damped over time, as shown by the blue dashed curves in Fig. 7.10(d). On the other hand, for the anisotropic case where $\phi = \alpha$, no subpackage splitting is observed and the average velocity oscillation amplitude is less pronounced, as shown by red dashed-dot curves in Fig. 7.10(d). This is linked to the fact that in this case the group velocity is aligned with the QW orientation and then the total wavepacket evolves in parallel to QW boundaries exhibiting a straight trajectory and dispersing over time similarly to the isotropic snapshots case, but here owing to the non-specular reflections its interaction with the QW edges implies a slightly different average position and barely affecting the total propagation velocity.

7.5 Conclusions of this chapter

In summary, we developed an analytical model for classical anisotropic systems using the effective mass model and applied this formalism to obtain the electronic properties of QWs made up of arsenene and phosphorene and with the length direction rotated

in relation to its anisotropy axes. The energy levels in the presence and absence of an external magnetic field perpendicular to the QW plane were analyzed for different system parameters. In the absence of a magnetic field, we found an analytical expression for the QW energy levels that contains a term analog to the ones for isotropic quantum wells with a $1/L^2$ dependence, and another term that carries the system anisotropy. Our results showed that the spacing of the energy levels for both samples is strongly affected by the alignment angle between the QW and the crystallographic directions, such that as the angle increases, the spacing between the energy levels is lowered (raised) for phosphorene (arsenene), as well as, observing a shifted to lower (upper) energy values. For the non-null magnetic field case, the electronic wavefunctions obey a harmonic oscillator type equation but for a modified mass and modified cyclotron frequency that depends on the alignment angle between the QW and its anisotropy axes. Numerical calculations showed that the energy spectrum is significantly affected by the confining potential edges and that the quantum Hall edge states are less pronounced the greater the rotation angle. With respect to the wavefunction localization, for large QW rotation angles, the wavefunction becomes more confined, whereas in the absence of a magnetic field it remains unchanged under rotations.

Since the electronic energy levels of anisotropic QWs are strongly affected by rotation, we studied their transport properties by using the split-operator technique and compared the isotropic and anisotropic results for the transmission probability, average position, average group velocity, and snapshots of the time evolved wavepacket. By considering a circularly symmetric Gaussian wavepacket propagating inside of a wide anisotropic QW rotated by α with respect to the anisotropic axes, one observed oscillations in the average velocity for the case when the initial wave vector and the group velocity vector are not collinear, and the oscillation amplitude is more pronounced the greater the non-collinearity between them, i.e. the greater the $\theta - \phi$ value. The snapshots at different time steps demonstrated that for the anisotropic QWs the interaction between the wavepacket and the QW edges gives rise to subwavepackets with different momentum orientations, whereas for isotropic QWs the wavepacket disperses over time without splitting and its interaction with the QWs edges does not change the orientation of the average group velocity. In the case of a bent QW, as a consequence of the energy mismatching in different sections of the QW and the anisotropy of the system, one expects that electrons traveling through the bend can be scattered. The results showed that the transmission probabilities are greater the lower the rotation angle of the right-arm and the wider the QW, regardless of the anisotropic character of the system, and the nature of the quantitative difference of the transmission probabilities between the isotropic and anisotropic QWs is linked to the difference on their subband values. The differences in propagation for different orientations of the QW may be experimentally measured by attaching perpendicular leads to the system, one expecting different Hall conductances between isotropic and anisotropic cases, as well for collinear and non-collinear situations between the group velocity and

momentum vectors. This direction-dependent Hall conductance will be investigated in a future project. Finally, we hope that our electronic and transport results will prove useful for designing anisotropic semiconductor based quantum confinement devices.

8

Dirac fermions in graphene using the position-dependent translation operator formalism

Within the position-dependent translation operator formalism for quantum system, we obtain analytical expressions for the eigenstates and the Landau levels spectrum of Dirac fermions in graphene under the presence of a perpendicularly applied magnetic field and, as a consequence of the formalism, with a generalized form of the momentum operator. Moreover, we explore the behavior of wave packet dynamics in such system, by considering different initial pseudospin polarization and metric parameter. Our findings show that the Landau levels, the wave packet trajectories and velocities are significantly affected by the choice of the metric in the non-Euclidean space of the deformed momentum operator, exhibiting a tunable energy level spacing. In the dynamics analysis, one observes an enhance of the oscillation amplitude of the average positions for all investigated pseudospin polarizations due to the non-symmetric evolution of the wave packet induced by the different metric in the system. The present formalism shows to be a theoretical platform to describe the effects of two scenarios due to: (i) a lattice deformation in graphene, giving rise to a natural Fermi velocity renormalization; or even (ii) a non-uniform mass-term, induced by specific substrate, that varies on a length scale much greater than the magnetic field length.

8.1   Motivation

During the last two decades, many studies have been carried out to understand the unique properties of graphene, a single atomic-thin layer of graphite. [3, 62] A plethora of its exotic features, such as: Klein tunneling effect and unusual quantum Hall effect, originate from the fact that low energy charge carriers in graphene obey the zero mass Dirac equation, providing a favorable environment to probe interesting phenomena predicted by quantum field theories not found in conventional semiconductors and metals. One consequence of its gapless linear dispersion, under the presence of a perpendicular magnetic field, is the $\sqrt{B}$ dependence to the Landau levels in contrast to the linear dependence on

B observed in conventional two-dimensional (2D) electron gas spectrum for Schrödinger fermions. [215, 57, 216, 217]

Other very interesting property of massless Dirac fermions in graphene is that it experiences zitterbewegung, a trembling motion caused by interference between positive and negative energy states [111, 112] that was predicted by Schrödinger for the motion of relativistic electrons in vacuum governed by the Dirac equation. Therefore, stimulated by Schrödinger's idea, numerous theoretical works have investigated the dynamics of wave packets in 2D electron gas [111, 112, 13, 123, 127, 129] and more recently in 2D materials, as examples: single-layer [143, 144, 145, 146, 147, 14, 148, 152, 150, 151] and bilayer [143, 147, 15] graphene, silicene, [167] transition metal dichalcogenide, [168] and multilayer phosphorene [203].

From the theoretical point of view in the analysis of quantum systems, in the last years one observed a growing literature dealing with systems consisting of particles with position-dependent mass. [218, 219, 220, 221, 222, 223, 224, 225, 226, 227, 228, 229, 230, 231, 232, 233, 234] Most of the previous approaches [218, 219, 220, 221, 222, 223, 224, 225, 226, 227, 228, 229, 230] considered a modification of canonical commutation relations or even modifications in the underlying space, which leads to the problem of the ordering in the kinetic energy operator, since in this formalism mass is mapped into an operator that does not commute with the momentum operator. [235] To overcome this issue, Costa Filho et al. [231] in 2011 proposed a new method that consists of a generalized translation operator which produces infinitesimal spatial displacements, such that $T(dx)|x\rangle = |x + g_{xx}^{-1/2}dx\rangle$, where $g_{xx}^{-1/2}$ is a function of the position and related to the metric. It changes the momentum and, consequently, the commutation relation between momentum and position into a more generalized form and leads to a modified Schrödinger equation that resembles the standard Schrödinger equation to describe charge carriers with a position-dependent effective masses. Thereafter, a series of recent studies have done by using this position-dependent translation operator formalism. [231, 232, 233, 234, 236, 237, 238, 239, 240]

Based on the Costa Filho formalism [231, 232, 233, 234] and motivated by the great interest on 2D materials due to their colossal possible future technological applications, in this work we extend the previous reported analysis for the case of graphene under the presence of a perpendicular magnetic field and we show that the metric in this formalism can be viewed as an additional mechanism for controlling the electronic and transport properties of low energy electrons in graphene, as well as we discussed it in view of two scenarios due to the lattice deformation and to a position-dependent mass term induced by specific substrate. To perform this investigation, we analytically solve the Dirac equation with a generalized momentum operator and discuss the role the metric in the eigenstates and energy spectrum. Moreover, we time evolve a Gaussian wave packet, describing charge carriers traveling through the system, and calculate the expectation values of the position operator and velocity operator as a function of time, discussing the main features of the zitterbewegung effect for different initial pseudospin polarization and metric.

In this chapter we discuss the position-dependent translation operator formalism, showing the analytical solution of the Dirac equation for monolayer graphene in the presence of a perpendicularly applied magnetic field and with a deformed momentum along the x-direction due to a general metric originated from the position-dependent translation operator formalism. Results of the analytically calculated Landau levels for a generic metric is also shown and compared with the non-deformed case. Moreover, we investigate the wave packet dynamics and how some physical quantities, such as average positions and average velocities, evolve in time for the studied graphene system with a generic metric. Results for different metrics, for different initial pseudospin polarizations, as well as the manifestation of the zitterbwegung on the wave packet motion in graphene with this deformed metric are discussed.

8.2 Position-dependent translation operator formalism

Matter curves the space-time in all directions leading two particles, traveling parallel to each other, to get closer or far apart as if there is a force acting between them. This is the definition of gravity in the realm of general relativity, where the space is curved in the vicinities of large densities of mass or energy. In general relativity, the metric tensor determines the geometric local structure of the curved space-time. For example, the Minkowski metric is the one used in special relativity, while the Schwarzschild metric is the most general solution to the Einstein's equation. Non-Euclidean metrics appear naturally also in very small scales where Quantum Mechanics is valid. For example, it has been used as an attempt to merge general relativity and quantum mechanics [**?, ?, ?, ?, ?**], as well as in the study of quantum systems problems with constraints [**?, ?, ?**]. More recently, a Schwarzschild-like metric has been used to find the quantum wave equations [**?**].

In a curved surface the shortest path between two points is a geodesic and the squared distance between two infinitesimally close points is given by

$$ds^2 = \sum_{\mu\nu} g_{\mu\nu} dx^\mu dx^\nu, \tag{8.1}$$

where $g_{\mu\nu}$ is the metric of the curved space under consideration. Here, we use a diagonal metric,

$$ds^2 = g_{xx}dx^2 + g_{yy}dy^2 + g_{zz}dz^2, \tag{8.2}$$

to show that an inertial force appears naturally in the quantum mechanics framework leading to a modified Ehrenfest theorem. More importantly, it is shown that the metric is responsible for a minimum momentum leading naturally to what is called extended uncertainty principle (EUP) [**?**].

As a first consequence of adopting Eq. (8.2), the space curvature leads to an internal product of the wave function given by

$$\langle\phi|\psi\rangle \equiv \int \phi^*(x,y,z)\psi(x,y,z)\sqrt{|g|}dxdydz, \tag{8.3}$$

where $g = \det(g_{\mu\nu})$ is the determinant of the matrix of components of the metric tensor. In this context, a particle in the vicinities of a point with coordinate x can be described by the ket $|x\rangle$ where $\hat{x}|x\rangle = x|x\rangle$. As the set $\{|x\rangle\}$ is complete, the identity operator can be written as

$$1 = \int \sqrt{|g|}dxdydz|x,y,z\rangle\langle x,y,z|, \tag{8.4}$$

and the scalar product in this metric for one dimension is given by $\langle x|x'\rangle = g(x)^{-1/2}\delta(x-x')$. With this metric, for a particle to go from a point x to $x + g_{xx}^{-1/2}dx$ it has to get a translation like $T_g(dx)|x\rangle = |x + g_{xx}^{-1/2}dx\rangle$. This translation is clearly non-additive and the operator can be written as

$$T_g(\vec{dr}) \equiv 1 - i\frac{\vec{\mathcal{P}}}{\hbar}\cdot\vec{dr}, \tag{8.5}$$

where $\vec{\mathcal{P}}$ is a generalized momentum that generates the translation, with $[x,\mathcal{P}_x] = i\hbar g_{xx}^{-1/2}$. As a consequence, it is straightforward to show that the momentum component can be written as $\mathcal{P}_\nu = -i\hbar g_{\nu\nu}^{-1/2}\partial_\nu$ leading to an stationary equation of motion for a particle $\mathcal{H}\psi = E\psi$ or,

$$-\frac{\hbar^2}{2m}\mathcal{D}^2\psi(\mathbf{r}) + V(\mathbf{r})\psi(\mathbf{r}) = E\psi(\mathbf{r}), \tag{8.6}$$

where $\mathcal{D} = \sum_\nu g_{\nu\nu}^{-1/2}\partial_\nu$, and

$$\mathcal{D}^2 \equiv \frac{1}{\sqrt{g}}\sum_\nu \partial_\nu\sqrt{g}g^{\nu\nu}\partial_\nu, \tag{8.7}$$

with $g^{\nu\nu}g_{\nu\nu} = 1$, and $\nu = x,y,z$. At this point, it is important to mention that the Hamiltonian defined by

$$\mathcal{H} \equiv -\frac{\hbar^2}{2m}\mathcal{P}^2 + V(\mathbf{r}) \tag{8.8}$$

is Hermitian due to Eq. (8.4). As consequence, the probability density $\rho = \Psi(x,t)\Psi(x,t)^*$ obeys the continuity equation,

$$\frac{\partial\rho}{\partial t} + \mathcal{D}\mathcal{J} = 0, \tag{8.9}$$

where the probability current is now written as $\mathcal{J} = g_{xx}^{-1/2}J$. We emphasize that the translation is non-additive in this diagonal metric, the associated Schrödinger-like equation remains linear, second-order in space and first-order in time, and that the probability density is conserved in terms of a continuity equation of the same form as the standard one in Euclidean space.

8.3 Electronic properties of graphene with a generic metric

The energy spectrum of an infinite undoped graphene sheet in the presence of a magnetic field and in the vicinity of the Dirac cones can be obtained by solving the eigenvalue equation $H_D \Psi(x, y) = E \Psi(x, y)$ with following Dirac-Weyl Hamiltonian[241, 242]

$$H_D = v_F \vec{\sigma} \cdot \left(\vec{\mathcal{P}} + e\vec{A} \right) + \tau \Delta \sigma_z, \tag{8.10}$$

where v_F is the Fermi velocity, e is the electron charge, $\vec{A}$ is the electromagnetic vector potential, $\vec{\sigma} = (\sigma_x, \sigma_y, \sigma_z)$ denotes the Pauli matrix, Δ $(-\Delta)$ is the on-site potential induced by the substrate on the A (B) sublattice, which can be seen as a mass term within the continuum model, and τ is the valley index, being 1 (-1) for K (K') Dirac point. Based on the position-dependent translation operator formalism, [231, 232, 233, 234] the generalized position-dependent momentum operator associated with a spatial displacement that generates the translation from a point ν to $\nu + g_{\nu\nu}^{-1/2} d\nu$ can be written as $\mathcal{P}_\nu = -i\hbar g_{\nu\nu}^{-1/2} \frac{\partial}{\partial \nu}$, with $\nu = x$, y, and z, being $g_{\nu\nu}^{-1/2}$ a function of the position and related to the metric. In fact, $g_{\nu\nu}^{-1/2}$ is an element of a diagonal metric of the non-Euclidean space under consideration. The eigenstates of the Hamiltonian (8.10) are the two-component spinors $\Psi = [\Psi_A, \Psi_B]^T$, where Ψ_A (Ψ_B) are the envelope functions associated with the probability amplitudes at the sublattice A (B).

For convenience, we choose the Landau gauge $\vec{A} = (0, B_0 x, 0)$, such that the system has translational invariance only along y-direction (i.e. $\mathcal{P}_y = \hbar k_y$). Thus, one can assume solutions as the following ansatz

$$\Psi(x, y) = e^{ik_y \int g_{yy}^{1/2} dy} \begin{pmatrix} \psi_+(x) \\ \psi_-(x) \end{pmatrix}. \tag{8.11}$$

By acting the Hamiltonian (8.10) on the two-component wave function (8.11), one obtains the following set of coupled differential equations

$$\left[\frac{1}{\sqrt{g_{xx}}} \frac{d}{dx} + \frac{(x - x_0)}{l_B^2} \right] \psi_- = i \frac{(E - \tau\Delta)}{\hbar v_F} \psi_+, \tag{8.12a}$$

$$\left[\frac{1}{\sqrt{g_{xx}}} \frac{d}{dx} - \frac{(x - x_0)}{l_B^2} \right] \psi_+ = i \frac{(E + \tau\Delta)}{\hbar v_F} \psi_-, \tag{8.12b}$$

where $x_0 = -\frac{\hbar k_y}{e B_0} = -l_B^2 k_y$ and $l_B = \sqrt{\frac{\hbar}{e B_0}}$ is the magnetic length.

Decoupling the above set of equations (8.12) with respect to ψ_+, we arrive at

$$\frac{d^2 \psi_+(\eta)}{d\eta^2} + \left[\frac{(E^2 - \Delta^2)}{\hbar^2 v_F^2} - \frac{e^{\sqrt{g} \frac{\eta}{l_B}}}{l_B^2} - \frac{(e^{\sqrt{g} \frac{\eta}{l_B}} - 1)^2}{g l_B^2} \right] \psi_+(\eta) = 0, \tag{8.13}$$

where one considers the spatial metric as the linear function

$$g_{xx}^{-1/2} = 1 + \frac{\sqrt{g}}{l_B} (x - x_0), \tag{8.14}$$
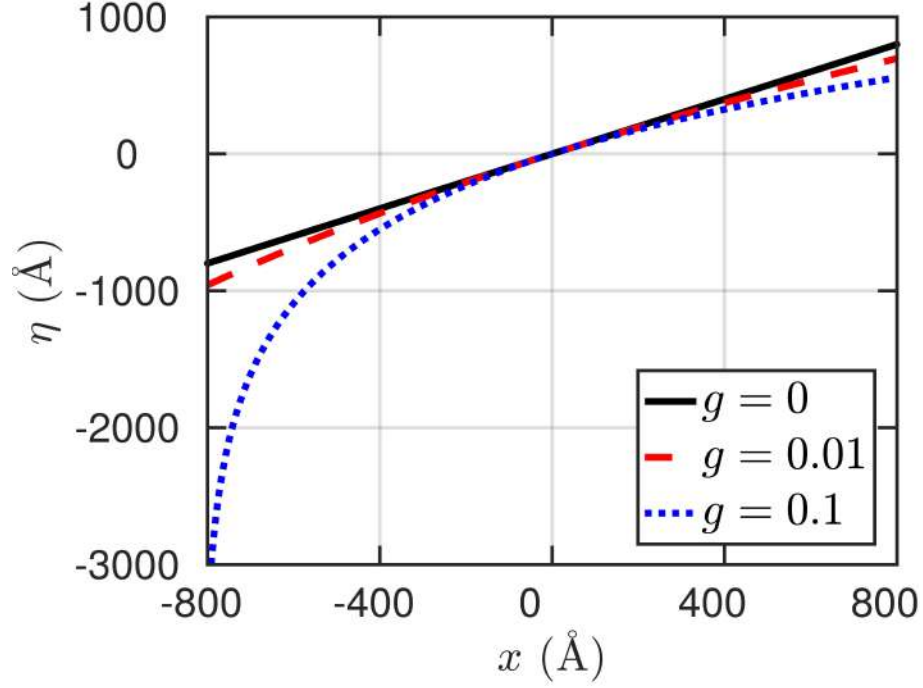
Figure 8.1: Deformed η-coordinate as a function of the non-deformed x-coordinate in real space [see Eq. (8.15)] for three different metric parameters: (black solid line) $g = 0$, (red dashed line) $g = 0.01$, and (blue dotted line) $g = 0.1$. It was assumed a magnetic field amplitude of $B = 1$ T.

and the application of the transformation

$$\eta(x) = \int g_{xx}^{1/2} dx = \frac{l_B}{\sqrt{g}} \ln\left[1 + \frac{\sqrt{g}}{l_B}(x - x_0)\right], \tag{8.15}$$

in order to eliminate the first derivative in Eq. (8.13). Notice that g is a dimensionless parameter that is associated with the effect of space modification. It is easy to note that for $g = 0$ one recovers the non-modified Dirac equation with the metric equal to 1 (i.e. $\mathcal{P}_\nu \to -i\hbar \frac{\partial}{\partial \nu}$). Therefore, the appropriated length scale for the problem is the magnetic length l_B. To illustrate this spatial deformation in η axis, Fig. 8.1 depicts the η's dependence as a function of the real and non-deformed x-coordinate [Eq. (8.15)] in the case of a linear metric as given by Eq. (8.14). Three different metric parameters g were assumed and it was taken a fixed magnetic field amplitude $B = 1$ T. One can realize from Fig. 8.1 that the introduction of a non-null metric parameter g induces a deformation in the η's space, such that η is moving away from a linear relation with respect to the x-coordinate to higher values of g, as can be seen by comparing the cases $g = 0$ and $g = 0.1$, as well as $\eta < 0$ is the most affected direction.

From Eq. (8.13), one can obtain the wave functions ψ_+ and ψ_- given, respectively, by

$$\psi_+(\eta) = A_n \beta^s e^{-\beta} L_n^{2s}(2\beta), \tag{8.16a}$$

$$\psi_-(\eta) = \frac{A_n \beta^s e^{-\beta} i\hbar v_F}{l_B \sqrt{g}(E + \tau\Delta)} \times$$
$$\left\{ 2e^{\frac{\sqrt{g}\eta}{l_B}} L_{n-1}^{2s+1}(2\beta) + \left[2e^{\frac{\sqrt{g}\eta}{l_B}} - (1+gs) \right] L_n^{2s}(2\beta) \right\}, \tag{8.16b}$$

where $\beta = \frac{1}{g} e^{\sqrt{g}\eta/l_B}$, $s = \frac{1}{g} - (n+1)$, L_n^{2s} is the generalized Laguerre polynomial, and A_n is the normalization constant. The corresponding energy levels read as

$$E_n = \pm\hbar v_F \sqrt{ \frac{\Delta^2}{\hbar^2 v_F^2} + \frac{2}{l_B^2}(n+1) - \frac{g}{l_B^2}(n+1)^2 }, \tag{8.17}$$

with $n \in \mathcal{N}$. The positive values correspond to electrons (conduction band), while the negative values correspond to holes (valence band). Repeating the same decoupling procedure of the set of equations (8.12) but now for the ψ_- component, one finds

$$E_n = \pm\hbar v_F \sqrt{ \frac{\Delta^2}{\hbar^2 v_F^2} + \frac{n(2 - gn)}{l_B^2} }. \tag{8.18}$$

By taking $g = 0$ in Eqs. (8.17) and (8.18), one can easily obtain the Landau level energies for the non-deformed graphene which depend on the square root of both the level index n and the magnetic field B, and exhibit a different dependence on the energy levels for sublattices A ($E_n \propto \sqrt{2(n+1)}$) and B ($E_n \propto \sqrt{2n}$). It is in contrast to the standard 2D electron gas, whose the Landau levels are equally spaced. Notice that for the graphene case with $g \neq 0$, one has an additional contribution term for the Landau levels that is proportional to the metric g and has a n^2-dependence. It is easy to realize from Eqs. (8.17) and (8.18) that there is a range of valid g values in order to obtain real energy levels, given by $g \leq \left(\frac{\Delta l_B}{\hbar v_F n'} \right)^2 + \frac{2}{n'}$, with $n' = 0, 1, 2, \ldots$, i.e. for a fixed g parameter only some n' values are allowed. As we shall discuss further, this term is responsible for changing the charge carrier electronic properties in graphene with a generic metric, when compared to the non-deformed case, and also it causes a shift into the energy spectrum. For $\Delta = 0$, note that Eq. (8.17) lacks the level with $E = 0$ that is present in Eq. (8.18), and the introduction of a different metric does not lift the degeneracy of the two-fold zeroth Landau levels since $E_0 = 0$ by Eq. (8.18), unlike the mass-term Δ that opens a gap of 2Δ in the spectrum and in addition the presence of Δ shifts the Landau levels spectrum for $n \neq 0$. The existence of a zeroth Landau level $E_0 = 0$ is a direct consequence of the zero gap in the energy spectrum for Dirac fermions in graphene and due to its chiral symmetry. [243] An important remark about Eqs. (8.17) and (8.18) is that the Landau levels are independent of the valley index, and therefore the Landau level for $n \neq 0$ ($n = 0$) has four-fold (two-fold) degeneracy, being two-fold associated with the electron-hole symmetry and the another two-fold because of valley symmetry. [57, 216, 217]
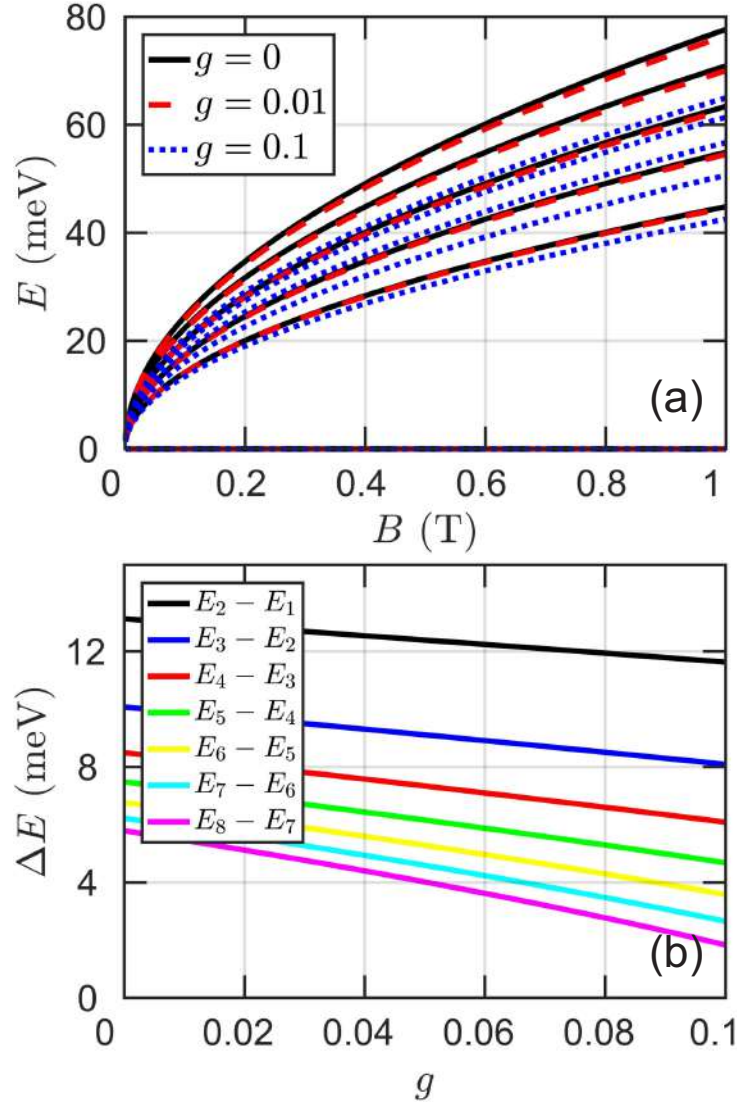
Figure 8.2: (a) The lowest five Landau levels for electrons as a function of perpendicular magnetic field for metric (solid black lines) $g = 0$, (dashed red lines) $g = 0.01$, and (dotted blue lines) $g = 0.1$. (b) Energy levels spacing between two adjacent states $E_{n+1} - E_n$ as a function of the metric for a fixed magnetic field amplitude $B = 1$ T and a null mass term $\Delta = 0$.

The dependence of the lowest energy levels on the magnetic field for the unbiased graphene system for $g = 0$ (solid black lines) and for $g \neq 0$ (being dashed red lines for $g = 0.01$ and dotted blue lines for $g = 0.1$) is shown in Fig. 8.2(a). A consequence of the metric change is a shift of the energy levels, together with a change of level spacing, as emphasized in Fig. 8.2(b) which depicts the behavior of the level spacing as a function of the metric g, maintaining the magnetic field amplitude $B = 1$ T. It is seen that as the metric increases, the energy levels are shifted to lower values and the spacing between them decreases too, which in turn increases in the number of accessible electronic states for a fixed energy range. Note that these behaviors of the deformed Landau levels with respect to the metric resemble those observed in the following two scenarios: (i) a strained

graphene, such that both the lattice and Dirac cones are distorted which leads to a spatial-dependence and anisotropy of the Fermi velocity induced by the lattice change through a renormalized linear momentum; [244, 245, 246, 247, 248] and (ii) a single-layer graphene sheet deposited on a specific deformed substrate, such that the substrate-induced mass-term is non-uniform and that varies on a length scale much greater than the magnetic field length. [249] In the both scenarios, the Landau levels change qualitatively in a similar way as shown in Fig. 8.2(a), i.e. exhibiting a contraction effect of the Landau levels spectra. With respect to the first scenario, it is worth mentioning that a more direct analogy with the considered position-dependent spatial metric given by the linear function Eq. (8.14) is an uniaxially strained graphene. In this context, a recent work[244] described such unidirectional deformation by using a renormalized linear momentum in an effective Dirac-like Hamiltonian that similarly to the current work can capture the feature of the contraction of the Landau levels but as a function of the deformation amplitude, instead of the metric as treated here. In both cases owing to the strain or metric change, the contraction of the Landau level energies can be understood by the renormalization of the Fermi velocity. From this point-of-view, one can get an explicit relation showing quantitatively a direct correspondence between the spatial metric g and the different types of the strain in graphene, such that it is possible to find $g \equiv g(\epsilon)$, being ϵ the amplitude of the lattice deformation.
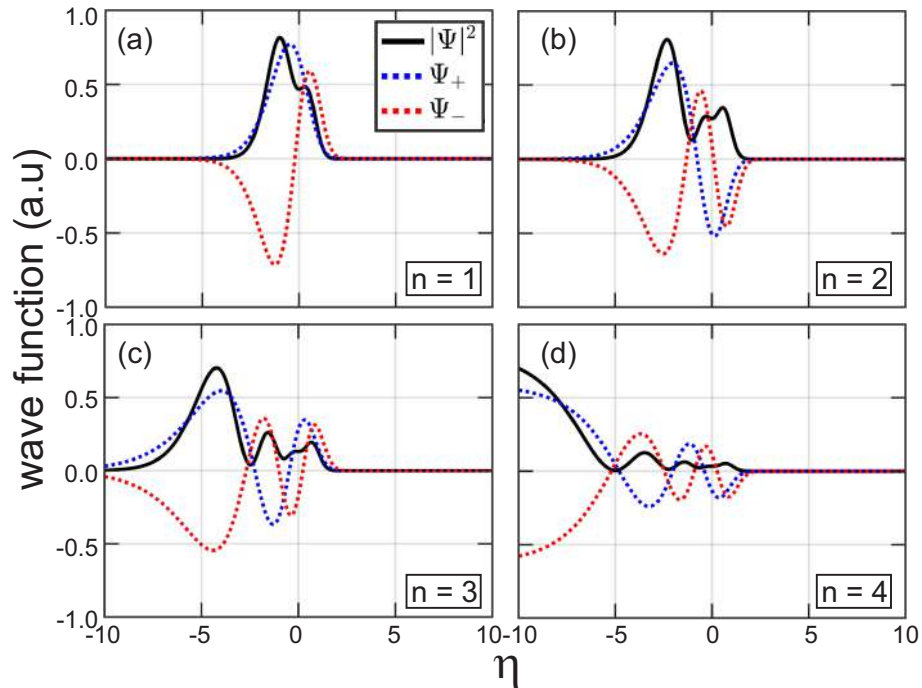
Figure 8.3: The wave function amplitude for the first four excited levels (a) $n = 1$, (b) $n = 2$, (c) $n = 3$, and (d) $n = 4$. The black solid, dashed blue and red lines correspond to the total wave function and the two pseudospin components ψ_+ and ψ_-, respectively. The metric is $g = 0.25$ and the assumed magnetic field was $B = 1$ T. It is shown $\Im\{\psi_-\}$, since it is pure imaginary. The η unit is angstrom.

From the analytical expressions (8.16a) and (8.16b), we plot in Fig. 8.3 the four first excited wave functions for graphene case with a non-null metric assumed as $g = 0.25$ and a fixed magnetic field amplitude $B = 1$ T. The solid black, dashed blue and red lines correspond to the total wave function $|\Psi|^2$ and the two pseudopsin components ψ_+ and ψ_-, respectively. For the non-deformed graphene case, it is well-known [57, 216, 217, 6] that solutions in the presence of an external magnetic field are given by the Hermite polynomials and $|\Psi|^2$ is symmetric with respect to $\eta = 0$. Note that the total wave function, as well as the two components of the pseudospinor are no longer spatially symmetric when one assumed a non-null parameter g. By an analogy with the strained graphene, such lack of spatial symmetry of the wave functions can be understood by the lattice deformation in graphene that causes in the microscopic point-of-view changes in the interatomic distances and in the hopping energies of the carbon atoms and, consequently, a modification in the electronic band structure. Such distortions on the Dirac cones can lead to an anisotropic position-dependent Fermi velocity which, in turn, can be seen as an anisotropy and a position-dependence on the effective masses of the system. Therefore, within this analogy, the wave function is more (less) localized at the regions where the kinetic energy is lowest (highest) due to the highest (lowest) effective mass along certain direction. Note from Fig. 8.3 that due to the non-null metric, the wave functions with higher energetic states exhibit a strong localization for $\eta < 0$ that can be associated with the region with higher effective mass, lower renormalized Fermi velocity, and most affected η-direction as demonstrated in Fig. 8.1. Similar results for deformed graphene systems have been already reported in the literature such strong localization along the deformed direction. [244, 245, 246, 247, 248] A very interesting aspect about the spatial distribution of the two-components wave functions is that, even for the non-deformed case ($g = 0$), the occupation of the sublattices displays a natural asymmetric occupation which is originated from asymmetry in positions of the nearest neighbors for atoms at A and B sublattices due to the different dependence of the energy levels for sublattices A [Eq. (8.17)] and B [Eq. (8.18)], which differs in the index n for 1. Moreover, Eq. (8.13) resembles a differential equation of a particle subjected to an effective Morse-type potential [?] in $\eta-$space i.e. $[d^2/d\eta^2 + V_{eff}(\eta)]\,\psi_+ = E'\psi_+$, being the effective potential the term inside the brackets in Eq. (8.13) without the energy term $E' = (E/\hbar v_F)^2$. Note also that Fig. 8.3 shows a strong asymmetry in the probability density, which implies that it is more probable to find the particle in the regions of maximum potential. In Refs. [250, 251], the authors showed that such asymmetry can be obtained when a particle is subjected to an exponential-type magnetic field. However, in the current work one obtains similar results by applying a constant magnetic field in $\{x, y\}$-space.

In addition to the wave function analysis for graphene system with a generic metric, in Fig. 8.4 contour plots of the (a) first ($n = 1$), (b) second ($n = 2$), (c) third ($n = 3$) and (d) fourth ($n = 4$) excited total wave functions are shown by varying the magnetic field amplitude but keeping a fixed value of metric as $g = 0.25$. As already expected, as
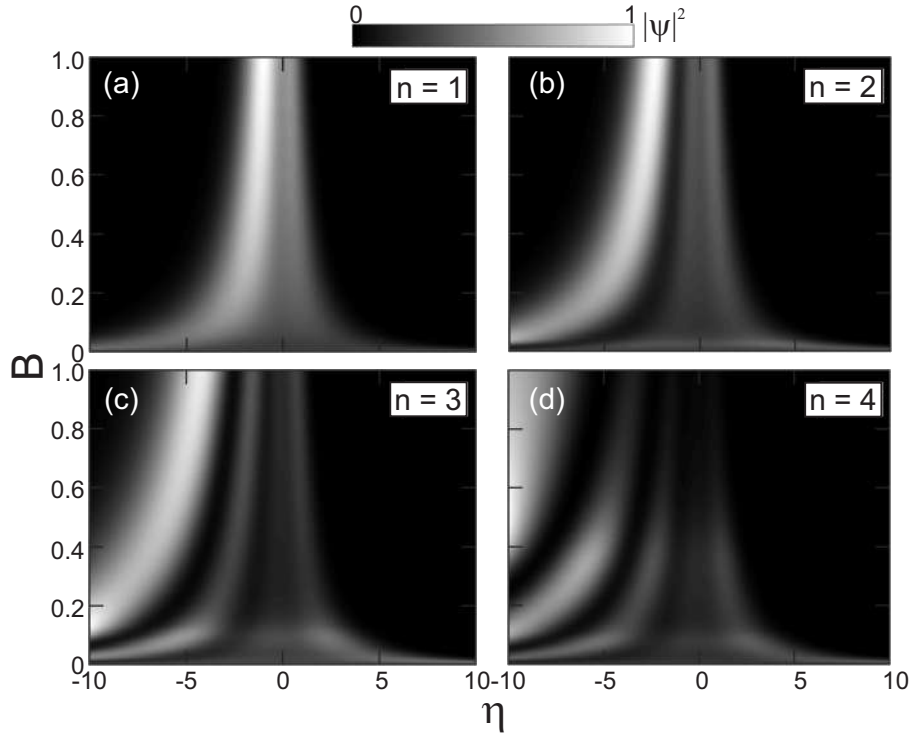
Figure 8.4: The dependence of the wave function on the magnetic field for metric $g = 0.25$ and for the first four excited levels: (a) $n = 1$, (b) $n = 2$, (c) $n = 3$, and (d) $n = 4$. The amplitude increases from black to white. The units of the magnetic field amplitude and η are Tesla and angstrom, respectively.

the magnetic field increases the magnetic length decreases and, consequently, the wave functions become more confined. Hence, although the introduction of a different metric (i.e. $g \neq 0$) delocalizes the wave function, giving rise a spatial asymmetry, the effect of strong magnetic fields is able to overcome such delocalization.

8.4 Wave-packet dynamics in graphene with a generic metric

Let us now investigate the effect on the wave packet dynamics under the presence of external magnetic field due to a non-unitary metric (i.e. for $g_{\nu\nu} \neq 1$ or equivalently for $g \neq 0$ in Eq. (8.14)), owing to a generalized position-dependent momentum operator in the considered formalism, and we shall also discuss the results of the role of a different metric in association with different physical scenarios already reported in the literature [244, 245, 246, 247, 249] and also discussed in the previous Sec. 8.3. In this analysis, we explore the time-dependent average positions and velocities, and the snapshots in real space of the wave packet evolution by taking different metric parameter g and different initial pseudospin polarization. To do this, we use the well-known split-operator technique [110, 170, 171, 79, 99, 173, 176, 177, 178, 179, 180, 202, 203, 252, 253] for

wave packet propagation in the real time that consists in the solution of time-dependent Schrödinger equation $i\hbar\partial\Psi(\vec{r}, t) = H\Psi(\vec{r}, t)$, by taking a separation of the time-evolution operator $\hat{U} = \exp[-iH\Delta t/\hbar]$ in a series of matrices, such that the propagated wave function after a time step $\triangle t$ can be calculated by applying the expanded exponential time-evolution operator on the wave packet at any instant t, i.e. $\Psi(\vec{r}, t + \Delta t) = \hat{U}\Psi(\vec{r}, t)$.

Similarly to the previous Sec. 8.3, now to calculate the quantum electronic trajectories using a wave packet within the split-operator technique, we consider: (i) the continuum model Hamiltonian H_D given by Eq. (8.10) for the description of low-energy massless Fermions, (ii) a deformed momentum along the x-direction given by $\mathcal{P}_x = -i\hbar g_{xx}^{-1/2}\frac{\partial}{\partial_x}$, and (iii) the linear function for the metric given by Eq. (8.14). The initial wave packet is assumed as a circularly symmetric Gaussian distribution, multiplied by a pseudospinor $[c_1, c_2]^T$ that accounts for the probability distributions over the two sublattices of graphene (labeled A and B), and by a plane wave with wave vector $\vec{k} = (k_x, k_y)$, which gives the wave packet a non-zero average momentum, defined as

$$\Psi(\vec{r}, 0) = N \begin{pmatrix} c_1 \\ c_2 \end{pmatrix} \exp\left[-\frac{(x-x_0)^2 + (y-y_0)^2}{d^2} + i(\vec{k}\cdot\vec{r})\right], \tag{8.19}$$

where N is a normalization factor, (x_0, y_0) are the coordinates of the center of the Gaussian wave packet, and d is its width. For our study, the initial position of the wave packet is at $(x_0, y_0) = (0, 0)$, its width is assumed as $d = l_B$, with $l_B = \sqrt{\hbar/eB_0}$ corresponding to the magnetic length for a fixed magnetic field amplitude considered as $B_0 = 10$ T and thus $l_B = 81.13$ Å, and its initial momentum as $(k_x^0, k_y^0) = (0.035, 0)$Å^{-1}.

In order to exemplify the effect of the metric in the wave packet dynamics, we shall discuss next the results for the two most considered, in the study of wave packet propagation, Gaussian distributions along the subalttices: (Sec. 8.4.1) $[c_1, c_2]^T = [1, 0]^T$ and (Sec. 8.4.1) $[c_1, c_2]^T = [1, 1]^T$. Since such analysis for undeformed monolayer graphene has been reported in details in Refs. [144, 110, 252], here we focus mainly on the differences that arises due to the different metric.

8.4.1 Case $c_1 = 1$, $c_2 = 0$

We first consider the simple case where the lower component of the initial electronic wave function is zero, i.e., taking $c_1 = 1$ and $c_2 = 0$. This corresponds to the situation in which the electron probability is initially located only at the A sublattice of graphene monolayer.

The trajectory drawn by $\vec{r(t)} = (\langle x(t)\rangle, \langle y(t)\rangle)$ for such a packet in the xy plane after a $t = 1600$ fs propagation time is shown in Fig. 8.5(a). As expected due to the effect of an external perpendicular magnetic field, the charge carrier travels in a cyclotron orbit, and moreover, by assuming a non-null g parameter, the radii of these orbits are strongly affected, as we shall discuss below. The expectation values of position and velocity as a function of time for different metric are depicted in Figs. 8.5(b,d) and 8.5(c,
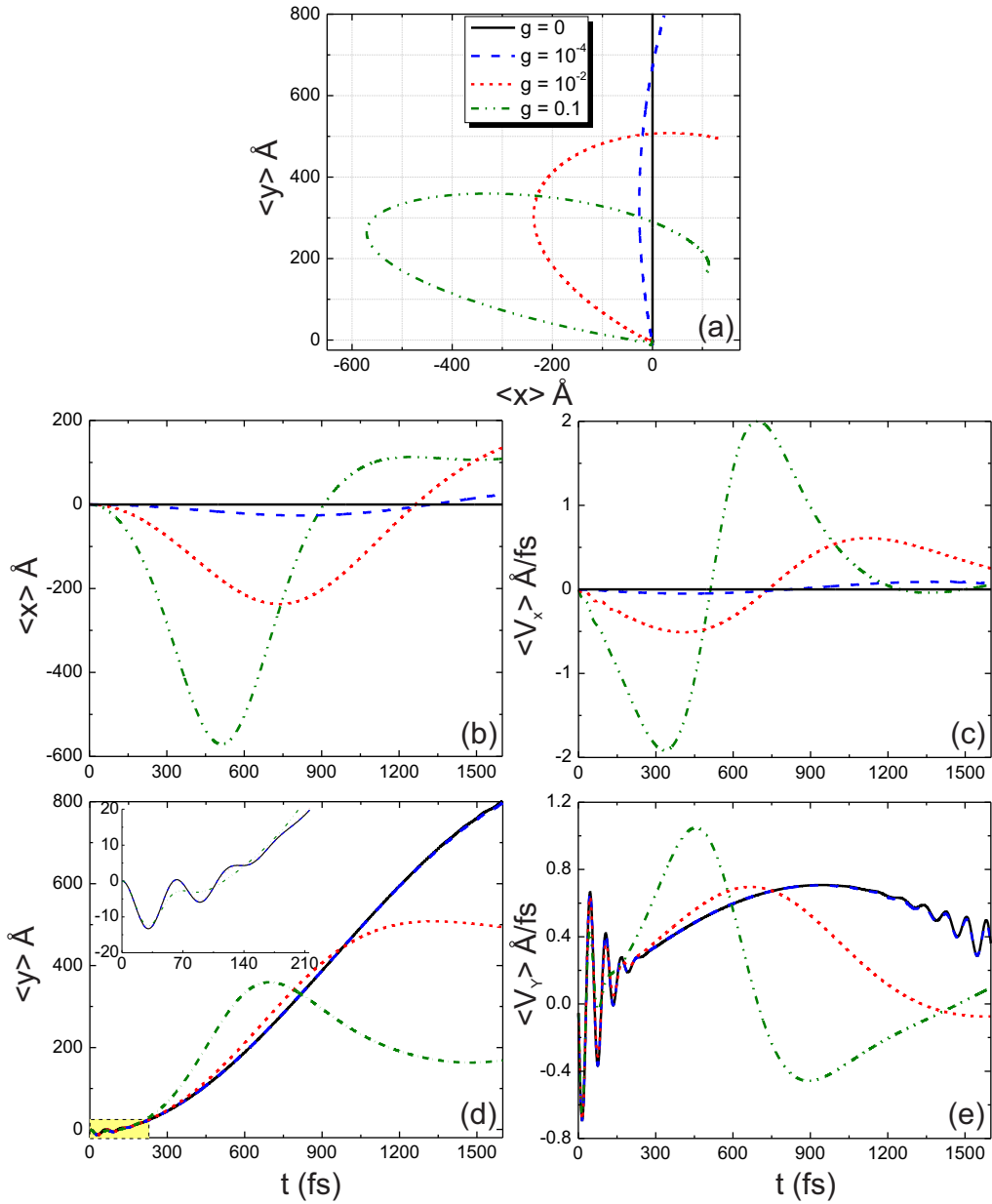
Figure 8.5: (a) Trajectories drawn by $\langle x \rangle$ and $\langle y \rangle$ within $t = 1600$ fs propagation time. [(b) and (d)] Average positions and [(c) and (e)] expectation values of the velocities in x and y directions, respectively, as a function of time for a Gaussian wave packet with initial pseudospin polarization $[c_1, c_2]^T = [1, 0]^T$, width $d = l_B = 81.13$ Å and initial momentum $k_x = 0.035$ Å^{-1}. The results are obtained for different metric: $g = 0$ (solid black lines), $g = 10^{-4}$ (dashed blue lines), $g = 10^{-2}$ (red dotted lines), and $g = 0.1$ (green dashed-dotted lines). The inset in panel (d) is an enlargement for the first time steps.

e), respectively. Results for metric $g = 0$, $g = 10^{-4}$, $g = 10^{-2}$ and $g = 0.1$ are shown in solid black lines, dashed blue lines, dotted red lines, and green dashed-dotted lines, respectively. One can realize that the average values of position and velocity in the x-direction remain constant for the undeformed graphene case ($g = 0$). However, when a

non-null g is considered, the averages position and velocity in the x direction are no longer zero and exhibit variations with the time evolution that are more evident the greater the metric amplitude. This can be easily understood keeping in mind that the introduction of a different metric induces a renormalization of the Fermi velocity, as discussed in the previous Sec. 8.3, leading to non-null value for $\langle v_x \rangle$. Moreover, it will be clarified next when we discuss about the symmetries of the total probability density for different time steps. On the other hand, by analyzing the average values of position and velocity in the y-direction, one observes a clear oscillation even for $g = 0$, as emphasized in the inset of Fig. 8.5(d), in the first time steps of the wave packet evolution that are damped as time evolves. This oscillatory behavior indicates the manifestation of the zitterbewegung effect along the y direction, as already reported [144, 110, 252, 148] in the literature for this pseudospin configuration for undeformed graphene case and confirmed here for $g = 0$ (see black line in 8.5(d)). Moreover, one notices that such oscillations exhibit a transient character, disappearing after a few hundred femtoseconds, and that the duration time and amplitude of the transient zitterbewegung for $\langle y \rangle$ decays faster as the metric value increases.
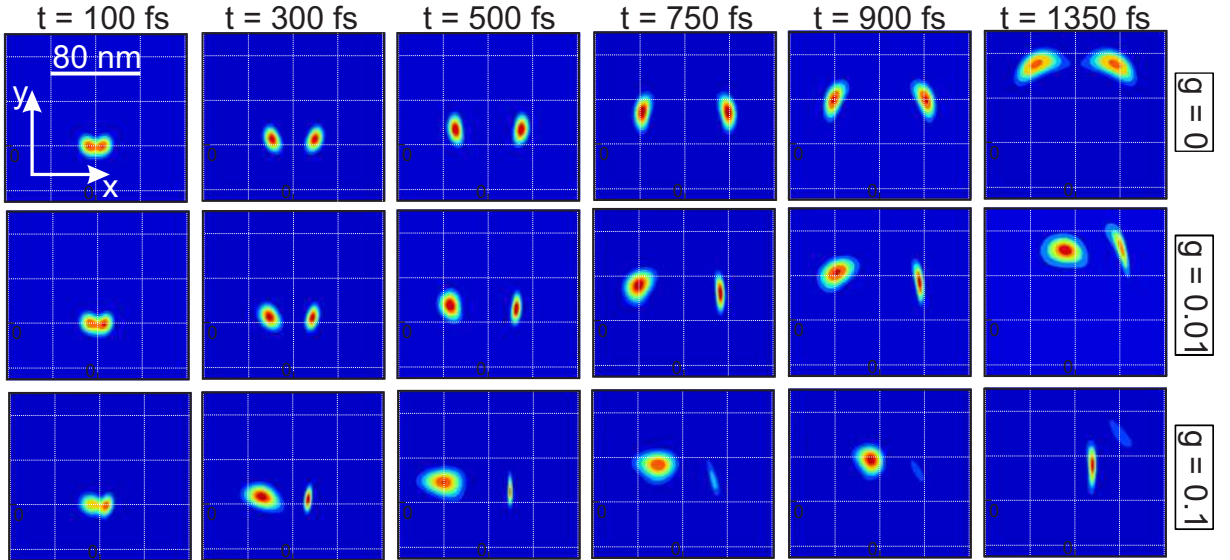
Figure 8.6: Time evolution of electronic wave packet for the case $[c_1, c_2]^T = [1, 0]^T$ for the same parameters of Fig. 8.5 at the time steps (first column) $t = 100$ fs, (second column) $t = 300$ fs, (third column) $t = 500$ fs, (fourth column) $t = 750$ fs, (fifth column) $t = 900$ fs, and (sixth column) $t = 1350$ fs and assuming the metric as (upper panels) $g = 0$, (middle panels) $g = 0.01$, and (bottom panels) $g = 0.1$. The wave packet starts at $(x_0, y_0) = (0, 0)$ Å.

For a better understanding of the average position and velocity behaviors in the x and y directions of Fig. 8.5, we analyze the contour plots of the squared modulus ($|\Psi|^2$) of the propagated wave functions at different time steps. The results are depicted in Fig. 8.6 for cases $g = 0$ (upper painels), $g = 0.01$ (middle painels), and $g = 0.1$ (bottom painels)

and for the following time steps: (first column) $t = 100$ fs, (second column) $t = 300$ fs, (third column) $t = 500$ fs, (fourth column) $t = 750$ fs, (fifth column) $t = 900$ fs, and (sixth column) $t = 1350$ fs. Note that as the time evolves the Gaussian wave packet, that start with circularly symmetric shape, splits in two parts moving with opposite velocities along x axis. This splitting leads to vanishing oscillations in the average position and expectation values of velocity along y-direction (see Figs. 8.5(d) and 8.5(e)) after $t \approx 180$ fs, which explains the transient behavior of the zitterbewegung. The trajectory of the wave packet is described by a circular cyclotron orbit as clearly visible in Fig. 8.5(a) and also evident in Fig. 8.6 from the fact that the wave packet bends for large time steps (see latest columns in Fig. 8.6) and by the average position for y-coordinate that has an extra oscillation with a large amplitude associated with the radius of the cyclotron orbit. Therefore, from Figs. 8.5 and 8.6 one can see that the higher the amplitude of the g parameter the smaller the radius of the cyclotron orbit. For the undeformed graphene case (top panels for $g = 0$), the two propagating subpackets move symmetrically with respect to $x = 0$, i.e. $|\Psi(x, y, t)|^2 = |\Psi(-x, y, t)|^2$ for a fixed time step. In contrast, for non-null g case (see middle and bottom panels for $g = 0.01$ and $g = 0.1$) the portions of probability amplitudes and widths of the two subpackets are noticeably different and they are increasingly distorted into an elliptic shape to higher g values. This strong asymmetry in the total probability density is due to the assumed position-dependent spatial metric that in turn can be linked with a strong anisotropy in the Fermi velocity and linear momentum to the electron motion, such that the momentum contributions along the negative and positive x-directions are different and thus giving rise to two propagating subpackets asymmetric with respect to each other, being one of them more elliptical. Moreover, it is interesting to note that this large asymmetry in the probability density explains the less evident zitterbewegung effect and the reduction of the transient time, as well as is related to the reason why one gets a non-null average position for x coordinate. Note that, since the probability densities of the two subpackages for $g \neq 0$ are not the same, the contribution to the total average position value of the center-of-mass will be different, causing changes in the trajectories and average values of position and velocity as shown in Fig. 8.5.

8.4.2 Case $c_1 = 1$, $c_2 = 1$

We now investigate the case in which the wave function is equally distributed in the sublattices A and B, which is equivalent as choosing $c_1 = c_2 = 1$. Similar to the previous case (Sec. 8.4.1), we analyze the time evolution of average values of position and velocity along the x and y direction, the trajectories evolved in time, as well as the snapshots of the total probability density in different time steps, with the results displayed in Figs. 8.7 and 8.8, respectively, for the same parameters assumed in Sec. 8.4.1.

The trajectories drawn by $\vec{r(t)} = (\langle x(t) \rangle, \langle y(t) \rangle)$ and the expectation values of the position and velocities along the two x and y coordinates shown in Fig. 8.7 are non-null
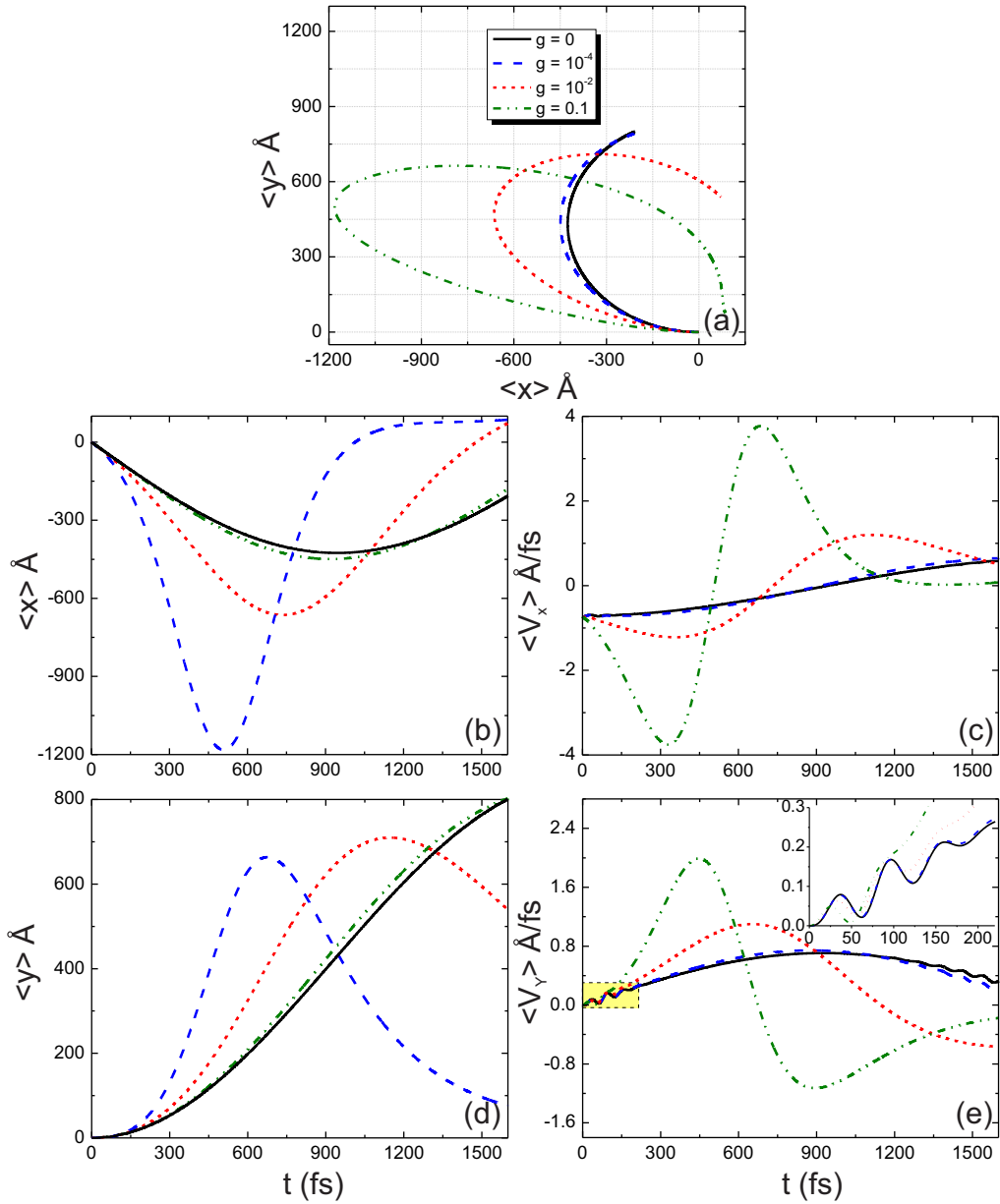
Figure 8.7: The same as in Fig. 8.5, but now for Gaussian wave packet with pseudospin polarization $[c_1, c_2]^T = [1, 1]^T$. The inset in panel (e) is an enlargement to emphasize the oscillatory behavior of $\langle v_y \rangle$ for the first time steps.

for $t > 0$ and do not remain constant as a function of time even for the undeformed graphene case (compare Fig. 8.7 with 8.5), unlike the previous case for $[1, 0]^T$. Note from Figs. 8.7(d) and 8.7(e) that the average values of position and velocity along the y-direction exhibit less pronounced oscillations, as emphasized in the inset of Fig. 8.7(e). In order to understand the origin of this weak (or absent) oscillation in the average physical variables for this chosen of pseudopsin polarization, we verified how is the spatial time evolution of the initial wave packet by showing snapshots for $t > 0$ of the total probability density, as shown in Fig. 8.8. Notice that regardless of the g value, the wave packet for

this pseudospin configuration does not split in two subpackets as it does for the previous configuration (see Fig. 8.6), being the reason why the electronic motion for this case does not exhibit zitterbewegung. In the current case, the electronic trajectory is similar to the one for left subpacket in Fig. 8.6, deforming and varying the packet width as the time evolves due to the position-dependent spatial metric that works in a similar way as position-dependent effective masses and anisotropic Fermi velocity. Also similarly to the previous pseudospin case, here the trajectory of the Gaussian wave packet center-of-mass is given by a cyclotronic orbit that drastically changes by increasing the metric amplitude, leading to a deformed elliptic orbit, being more squeezed the greater the g parameter (see Fig. 8.7(a)). The oscillation in Fig. 8.7(d) for the $\langle v_y \rangle$ is related to the asymmetric spreading over time of the wave packet.
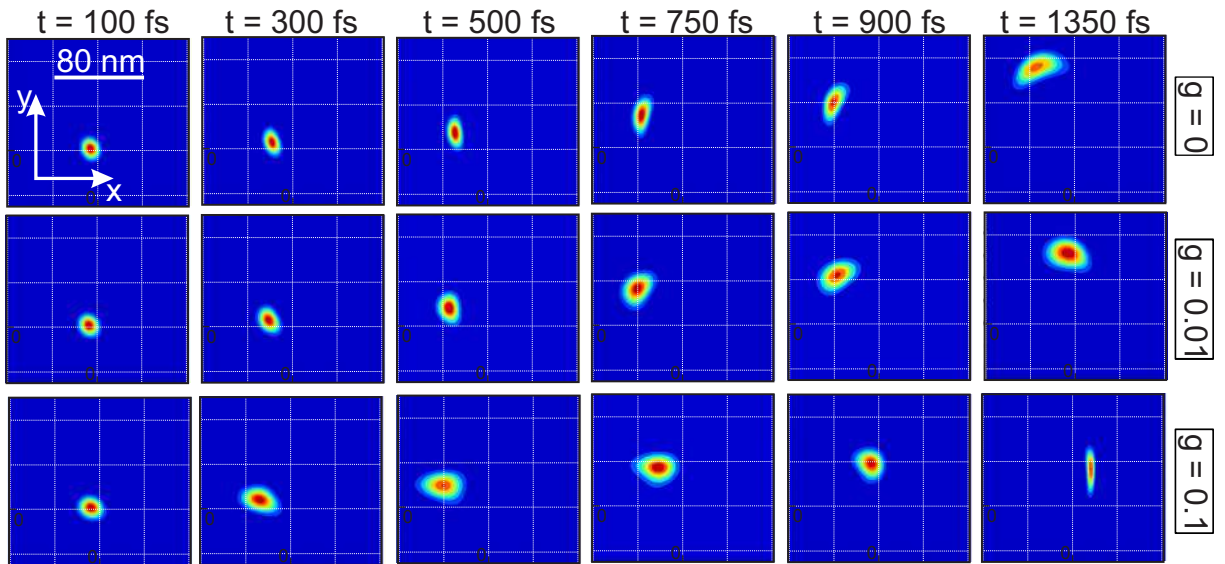
Figure 8.8: The same as in Fig. 8.6, but now for Gaussian wave packet with pseudospin polarization $[c_1, c_2]^T = [1, 1]^T$.

8.5 Conclusions of this chapter

In summary, we have investigated the effects of metric changes in the electronic properties and in the time evolution of a low-energy two-dimensional Gaussian wave packet for graphene by means the position-dependent translation operator formalism. We showed that such formalism is able to introduce additional control of such properties and that the studied system mimics two different physical scenarios: a deformed graphene due to strain and a non-uniform mass-term, induced by specific substrate, that varies on a length scale much greater than the magnetic field length. A more direct analogy with the position-dependent spatial metric in this formalism is done with the first scenario when takes in account an unidirectional deformation that induces renormalized and position-dependent linear momentum and Fermi velocity.

With respect to the electronic properties, we analytically derived the Landau levels and its respective wave functions. An additional contribution term for the Landau levels was found with a $\sqrt{g}$-dependence and we showed that this term is responsible for performing a contraction of the levels, i.e. the metric changes shift the Landau level to lower values and decreases the level spacing. The total wave function, as well as the two pseudospin components, are strongly affected by a non-null metric g, leading a delocalization of the wave function.

By using the well-known split-operator technique and the deformed Dirac Hamiltonian in the presence of an external magnetic field developed in the position-dependent translation operator formalism, we investigated the wave packet dynamics for different metric and for different choices of the initial pseudospin polarization. We analyzed the results for the expectation values of center-of-mass coordinates, the trajectories, the spreading of the wave packet in real space, as well as their oscillations due to zitterbewegung. In general, we demonstrated that the non-null metric leads to an asymmetry for the wave packet evolution and therefore in some cases it brings up oscillations in the average of the physical observables and in other cases it suppresses the zittebewegung. The strong asymmetry in the total probability density is due to the position-dependent spatial metric that in turn can be linked with a strong anisotropy in the Fermi velocity and linear momentum to the electron motion. We observed that the higher the amplitude of the g parameter the smaller the radius of the circular cyclotron orbit described by the electron due to magnetic field presence and more deformed it becomes.

The theoretical formalism used here can be useful for comparison and analogy to other two-dimensional based system, and we believe that the discussions about the results found in this work will be contribute to a better understanding of the position-dependent translation operator formalism applied for two-dimensional materials.

9

Band-gap formation and morphing in $\alpha - T_3$ superlattices

Electrons in $\alpha - T_3$ lattices behave as condensed-matter analogies of integer-spin Dirac Fermions. The three atoms making up the unit cell bestow the energy spectrum with an additional energy band that is completely flat, providing unique electronic properties. The interatomic hopping term, α, is known to strongly affect the electronic spectrum of the 2D lattice, allowing it to continuously morph from graphene-like responses to the behaviour of Fermions in a Dice lattice. For pristine lattice structures, the energy bands are gapless, however small deviations in the atomic equivalence of the three sublattices will introduce gaps in the spectrum. It is unknown how these affect transport and electronic properties such as the energy spectrum of superlattice mini-bands. Here we investigate the dependency of these properties on the parameter α accounting for different symmetry-breaking terms and show how it affects band gap formation. Furthermore, we find that superlattices can force band gaps to close and shift in energy. Our results demonstrate that $\alpha - T_3$ superlattices provide a versatile material for 2D band gap engineering purposes.

9.1 Motivation

The isolation of a stable single layer of carbon atoms arranged in a hexagonal lattice, known as graphene, in 2004 [3] combined with the extraordinary electronic and transport properties observed in the atomically thin material [3, 254, 8, 255] has motivated many researchers to investigate and produce other two-dimensional (2D) materials [3, 19, 256, 257]. The peculiar electronic properties of graphene are the result of charge carriers described by an equation analogous to the Dirac one for relativistic particles but here the presence of a variable similar to a spinor representation, differently from the "real" one, results only from the crystal structure instead from an intrinsic property of the particles. Therefore the charge carriers in graphene are commonly referenced as pseudospin-1/2 particles [258, 259]. These particles have a linear energy dispersion where valence and conduction bands touch each other in special points in reciprocal space called

Dirac points [254, 8, 258, 259].

2D materials can be subjected to electrostatic potentials with a periodicity significantly larger than the inter-atomic distance [76, 77, 74, 78]. Because one can easily change the strength of the electrostatic potential, this method has been thoroughly investigated as a way to tune electronic properties of the charge carriers in these 2D systems [260, 261, 86, 262, 84, 263, 264]. Superlattice potentials are known to increase the number of Dirac points of graphene [261, 86, 262, 80, 83, 82, 265, 87] and as such introduce new physical modes at zero energy, as recently observed in Ref. [91]. Some relevant applications originated from the periodic structures are electron beam supercollimation and electron wave filter [265, 87].

Recently, novel and distinctive physics has emerged from 2D systems when adding an additional atom in their crystal structure [266, 267, 268, 269, 52, 56, 58, 270], which leads to their charge carriers in a low-energy approach to be described as enlarged pseudospin Dirac Fermions [52, 56, 53, 54, 271]. Among these systems we have Lieb lattice with the additional atom at edges of a square-lattice, which was recently obtained by adding carbon monoxide molecules to a substrate [267] and the T_3 or dice lattice which has an additional atom at the center of the hexagonal structure. In both, different from graphene, the massless Dirac Fermions are described as spin-1 particles and an additional flat-band touching the top of the valence and the bottom of the conduction linear bands [55, 272]. This flat band has important and unusual effects on the electronic properties due to its dispersionless nature and thus an infinity effective mass [271, 55, 272, 273, 274, 96, 275, 276, 98]. Moreover, flat bands are predicted to be important in the search for room-temperature superconductivity [277, 278].

The graphene hexagonal lattice and T_3 or dice lattice are incorporated in the $\alpha - T_3$ model [55, 96, 275, 276, 279, 98]. It allows a tuning between the central atom arrangement and the hexagonal structure by varying the parameter α. Graphene and T_3 are the limiting cases $\alpha = 0$ and $\alpha = 1$, respectively.

The $\alpha - T_3$ model has been useful to investigate physical systems presenting Dirac Fermions with a larger pseudo-spin value. The $\alpha - T_3$ model was originally proposed to describe the dia- to paramagnetic transition in the orbital susceptibility in an optical lattice of cold atoms [136, 280]. The limiting case $\alpha = 1$ corresponds to the dice lattice which can be obtained by stacking three layers of $SrTiO_3/SrIrO_3/SrTiO_3$ [50], or be generated by controlling three laser beams propagating in towards a two-dimensional layer of cold atoms [51]. Likewise this model with appropriate doping and for the case $\alpha = 1/\sqrt{3}$ can be used to describe the three-dimensional $Hg_{1-x}Cd_xTe$ system [281, 282].

Curiously, systems with charge carriers described as spin-1 massless Dirac Fermions, for certain energy conditions have an angular independent Klein tunneling through rectangular electrostatic barriers which is called super-Klein tunneling (SKT). This isotropic transmission is unlike single and bilayer graphene that show highly anisotropic transmission across such barriers. In addition, the tunneling into the flat band across a potential

step for generalized pseudospin has been discussed as well [52, 54]. Previous studies considering Dirac Fermions across electrostatic potentials in systems with intermediate values of α reveal perfect transmission for normal incidence, and a general trend of enhanced transmission with increasing α [54, 279, 98]. Moreover, when more barriers are considered, in the case of the dice lattice the tunneling shows little dependence on the number of barriers, whereas for graphene the number of barriers strongly affects the tunneling [283].

Several studies have been published aiming at a way to create a band gap in these structures [275, 97, 284, 285, 286, 287].This is necessary for practical electronic applications such as the fabrication of quantum information devices. It was demonstrated that an additional mass term in $\alpha - T_3$ systems distorts the linear bands around the Dirac cone and produces an energy gap with a third band in it which could be flat or dispersive [275, 276]. The position of this band inside the band gap has important consequences for Klein tunneling of massive Dirac Fermions across potential barriers.

Motivated by the richness of the tunneling properties and the peculiar electronic properties of Dirac Fermions with integer pseudospin, and aiming at understanding how the band gap in $\alpha - T_3$ systems varies as function of the tuning parameter α in the presence of super periodicity, we investigate the energy spectra and density of states (DOS) first in ungapped $\alpha - T_3$ superlattices, and subsequently we take into account the effect of different symmetry-breaking terms. In both cases we pay special attention to the appearance of mini-bands, its band flatness, and its dependence on the coupling parameter α.

In this chapter we discuss the electronic properties of charge carriers in $\alpha - T_3$ lattices and how this is affected by small deviations in the atomic equivalence between the sites and the presence of mass terms. We develop the transfer matrix approach to analyze the energy spectra of Dirac Fermions in $\alpha - T_3$ in the presence of a one-dimensional(1D) periodic potential. The band gap morphing and its dependence on (i) the coupling parameter, and (ii) the symmetry-breaking between the atomic sites by the inclusion of different mass terms are also discussed.

9.2 Fermions in $\alpha - T_3$ lattices

9.2.1 Energy spectrum and eigenstates

An $\alpha - T_3$ lattice is formed by the superposition of three triangular sublattices [56]. Two of them are formed by atom sites A and B arranged in a hexagonal lattice with hopping term t. The additional site C is connected only to sites B by a hopping term tuned by a parameter α, which is the parameter that provides a continuous transition from the honeycomb ($\alpha = 0$) to the dice ($\alpha = 1$) lattice and determines the strength of coupling between the C atoms at the center of the honeycomb lattice, as shown in Fig. 10.1. The distance between the A, B and C atoms are the same and denoted by a_0. The hopping parameters t, α and a_0 depend on the specific atomic composition of the
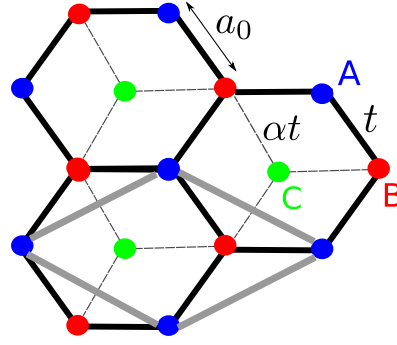
Figure 9.1: Schematic of the $\alpha - T_3$ lattice where the sites of the three sublattices are coloured differently. The limit $\alpha = 0$ corresponds to the honeycomb lattice (graphene-like), and $\alpha = 1$ corresponds to the dice lattice. The hopping amplitude between the different atoms is indicated. The region bounded by the grey lines corresponds to the unit cell.

lattice under consideration and completely determine the properties of the $\alpha - T_3$ lattice.

The presence of the additional site C centered in the honeycomb lattice results in some interesting electronic properties, like e.g. the presence of a flat band in addition to the linear bands and the larger value of pseudospin of charge carriers in these lattices [52, 56, 55, 96, 98, 50, 51, 281, 282].

The lattice structure determines the kinetic energy of the Fermions in the material. The low-energy Hamiltonian of Fermions in a $\alpha - T_3$ lattice around the K point is given by the 3×3 matrix expressed in the sublattice basis $|\Psi\rangle = (|\psi_A\rangle, |\psi_B\rangle, |\psi_C\rangle)$ as [56, 96]

$$\hat{H}_{\text{kin}} = \begin{pmatrix} 0 & f_\xi(\vec{k}) \cos\theta & 0 \\ f_\xi^*(\vec{k}) \cos\theta & 0 & f_\xi(\vec{k}) \sin\theta \\ 0 & f_\xi^*(\vec{k}) \sin\theta & 0 \end{pmatrix} . \tag{9.1}$$

In Eq. (10.1) we introduced the parameter $\theta = \tan^{-1}\alpha$, where $\theta = 0$ and $\theta = \pi/4$ corresponds to honeycomb and dice lattices, respectively. The function $f_\xi(\vec{k}) = v_F(\xi k_x - ik_y)$ with $v_F = 3a_0 t/2\hbar$ the Fermi velocity and $\vec{k} = (k_x, k_y)$ the wave vector. Here, $\xi = \pm 1$ is the valley index for the K and K' valleys, respectively [56, 96]. In the absence of external potentials, the eigenstates of the Hamiltonian are given by

$$|\Psi_\pm\rangle = \begin{pmatrix} \cos\theta e^{i\phi_k} \\ \pm 1 \\ \sin\theta e^{-i\phi_k} \end{pmatrix}, \tag{9.2}$$

with eigenvalues $E_\pm = \pm\hbar v_F k$, where $\pm$ indicates the conduction and valence bands, respectively. The angle $\phi_k = \tan^{-1}(k_y/k_x)$ corresponds to the angle associated with the momentum vector. In addition, a flat band state is found

$$|\Psi_0\rangle = \begin{pmatrix} \cos\theta e^{i\phi_k} \\ 0 \\ \sin\theta e^{-i\phi_k} \end{pmatrix}, \tag{9.3}$$
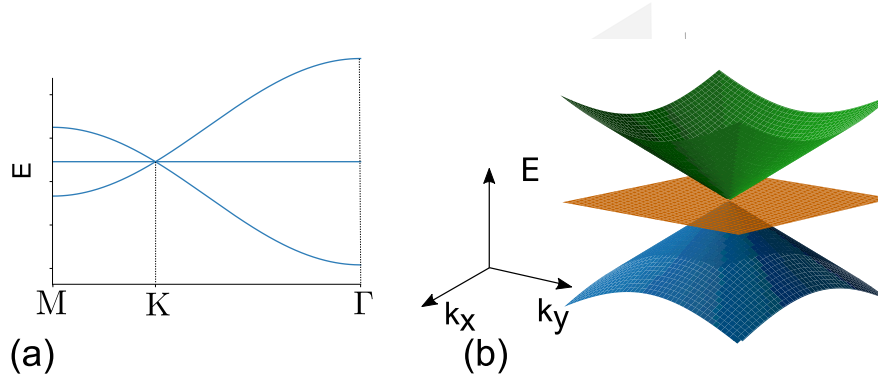
Figure 9.2: Energy spectrum of massless Dirac fermions in the $\alpha - T_3$ lattice (a) in the full first Brillouin zone, and (b) around the K point.

with eigenvalue $E = 0$ corresponding to strongly degenerate states [52, 50, 51], as represented in Fig. 9.2. Notice that the energy eigenvalues E do not depend on θ. The parameter is solely affecting the eigenstates.

9.2.2 Introduction of a band gap

The Dirac point at $E = 0$ in the pristine $\alpha - T_3$ lattice is triple degenerate as seen in Fig. 9.2. This degeneracy is produced by the equivalence of the three sub-lattices. Breaking this equivalence will lead to a lifting of the degeneracy and the introduction of a band gap. In general, one can include this in the Hamiltonian by a term proportional to $\hat{U}$ that enters as follows:

$$\hat{H} = \hat{H}_{\text{kin}} + \Delta \hat{U} \ , \tag{9.4}$$

with $\hat{H}_{\text{kin}}$ given by Eq. (10.1), and Δ measures the strength of the symmetry breaking. The Hamiltonian in Eq. (10.4) is obtained from an expansion of the tight-binding model to nearest neighbors of the $\alpha - T_3$ lattices around the K point of the first Brillouin zone when different on-site energies are considered [55, 96, 51]. In this work, we consider two different forms of $\hat{U}$, respectively, given by

$$\hat{U}_1 = \begin{pmatrix} 1 & 0 & 0 \\ 0 & -1 & 0 \\ 0 & 0 & 1 \end{pmatrix} \ , \quad \hat{U}_2 = \begin{pmatrix} 1 & 0 & 0 \\ 0 & 0 & 0 \\ 0 & 0 & -1 \end{pmatrix} . \tag{9.5}$$

The effects of the inclusion of the terms $\hat{U}_1$ and $\hat{U}_2$ on the energy spectrum are shown in Fig. 9.3 and Fig. 9.4, respectively.

The term $\hat{U}_1$ introduces a site energy on the different sub-lattices as has been discussed for photonic crystals and optical lattices [97, 284]. The solution of $\hat{H}\Psi = E\Psi$ for this case gives the eigenenergies

$$E_0 = \Delta \ , \quad E = \pm\sqrt{\Delta^2 + \hbar^2 v_{\text{F}}^2 k^2} \ . \tag{9.6}$$
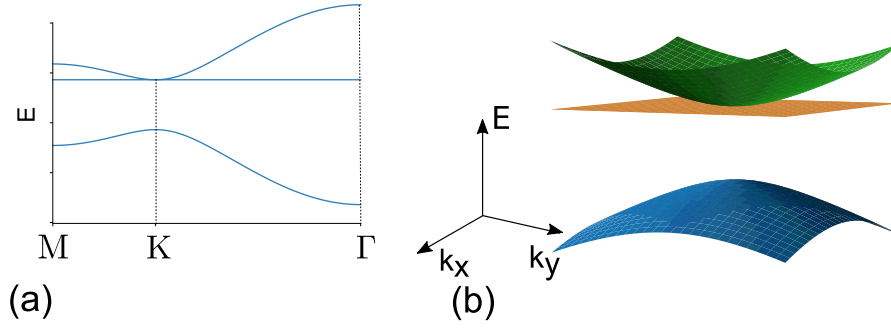
Figure 9.3: Energy spectrum of Dirac Fermions for arbitrary values of the parameter θ in the $\alpha - T_3$ lattice when the symmetry-breaking term $\hat{U} = \hat{U}_1$ is used in Eq. (10.4). (a) Full first Brillouin zone, and (b) spectrum around the K point.

Correspondingly, the wave-functions in this case are given by

$$|\psi_0\rangle = \begin{pmatrix} \cos\theta e^{i\phi_k} \\ 0 \\ \sin\theta e^{-i\phi_k} \end{pmatrix} \quad , \quad |\psi_\pm\rangle = \begin{pmatrix} \alpha\cos\theta e^{-i\phi_k} \\ \gamma \\ \alpha\sin\theta e^{i\phi_k} \end{pmatrix}, \tag{9.7}$$

where $\alpha = \sqrt{E + \Delta}$, and $\gamma = \sqrt{E - \Delta}$.

Similar sublattice symmetry breaking systems have been discussed suggesting that such mass potential term is attainable by depositing graphene on specif substrates, such SiC [288, 289], and h-BN [290]. In Eq. (10.6) we find the presence of a gap 2Δ opening in the energy spectrum. This results in massive Dirac Fermions with an effective mass defined as $m = \Delta/v_F^2$. Since Eq. (10.6) does not depend on the parameter θ the energy spectrum remains the same for all $\alpha - T_3$ lattices, as shown in Fig. 9.3. Moreover, as long as the equivalence between the sites A and C is maintained, the flatband is shifted and touches only the bottom of the conduction band. Notice that now the bottom of the conduction band and the top of the valence band are quadratic in $\vec{k}$.

On the other hand, the term $\hat{U}_2$ defined in Eq. (9.5) has been used to describe the effect of a pseudomagnetic field [285, 286], and the dispersion relations for this case are obtained from a solution of the non-linear equation

$$E(\Delta^2 - E^2) + k^2(\Delta\cos 2\theta + E) = 0, \tag{9.8}$$

and the eigenstate for the conduction and valence band are given by

$$|\psi\rangle = \begin{pmatrix} \alpha'\cos\theta e^{i\phi_k} \\ \gamma' \\ \beta\sin\theta e^{-i\phi_k} \end{pmatrix}, \tag{9.9}$$

with $\alpha' = \sqrt{1 + 2\Delta/(E - \Delta)}$, $\gamma' = \sqrt{1 + \Delta\cos(2\theta)/E}$ and $\beta = \sqrt{1 - 2\Delta/(E + \Delta)}$.

Unlike the previous case, there is no longer equivalence between the site C and the other sites of the crystal structure, which means that small deviations of the coupling
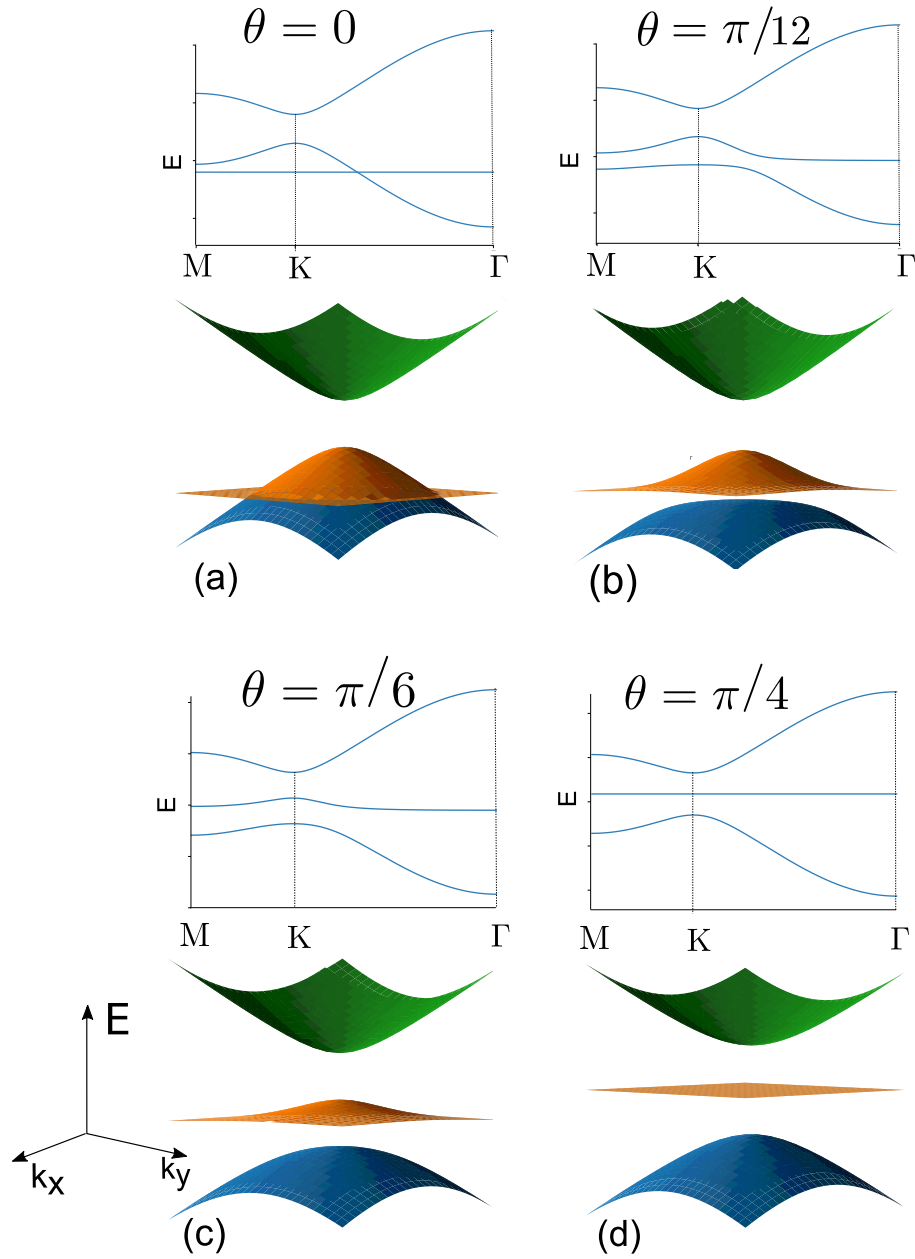
Figure 9.4: Energy spectrum of Dirac Fermions in the $\alpha - T_3$ lattice for different values of θ when the symmetry-breaking term $\hat{U} = \hat{U}_2$ is used in Eq. (10.4). The full first Brillouin zone is shown at the top and bellow the energy spectrum around the K point for (a) $\theta = 0$ (graphene-like case), (b) $\theta = \pi/12$, (c) $\theta = \pi/6$, and (d) $\theta = \pi/4$ (dice case).

parameter α results in different eigenenergies as depicted in Fig. 9.4. In this case the flat band is dispersionless only when $\theta = \pi/4$ (dice lattice) and is located in the center of the energy gap [286, 287], as shown in Fig. 9.4(a).
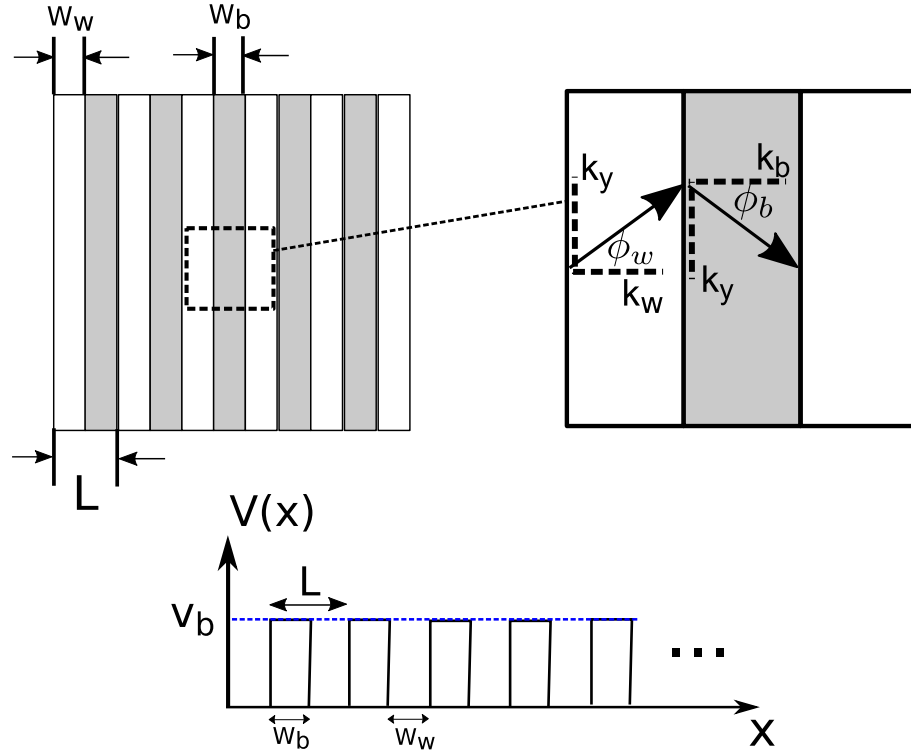
Figure 9.5: Schematic representation of the superlattice potential in $x - y$ plane. Dark regions denote the barrier region with height $V(x) = V_b$ and the white region represents the well with zero potential. The angles ϕ_w and ϕ_b in the inset, respectively, denote the angles of the carriers in the wells and barriers regions. The profiles of the 1D periodic potential is given by the figure at the bottom.

9.3   Superlattice

In this chapter one of our goals is investigate how fermions in $\alpha - T_3$ lattices are affected by a one-dimensional periodic electrostatic potential. In casu, we investigate one-dimensional potentials with a periodicity much larger than the interatomic distance, i.e. $L/a_0 \ll 1$. We consider an infinite number of barriers periodically spaced with unit cell length $L = W_w + W_b$, with $W_w(W_b)$ the width of well(barrier), as illustrated in Fig. 9.5. The general Hamiltonian taking into account the presence of symmetry-breaking terms is now given by [54, 96, 98]

$$\hat{H} = \hat{H}_{\text{kin}} + V(x)\hat{I} + \Delta\hat{U}_i, \tag{9.10}$$

with $\hat{H}_{\text{kin}}$ given by Eq. (10.1), $V(x) = V_b$ the periodic potential, and $\Delta\hat{U}_i$ represent the symmetry-breaking term which can be translated into a mass term. Due to translation invariance in the y direction the wave-functions have the form $\Psi_j(x,y) = \Psi_j(x)e^{ik_y y}$ with label $j = w$ or $j = b$ used to denote the region of well(barrier), and $\Psi_j(x)$ is given by:

$$\psi_j(x) = \frac{A}{\sqrt{2}} \begin{pmatrix} \alpha_j \cos\theta e^{i\phi_j} \\ \gamma_j \\ \beta_j \sin\theta e^{-i\phi_j} \end{pmatrix} e^{ik_j x} + \frac{B}{\sqrt{2}} \begin{pmatrix} -\alpha_j \cos\theta e^{-i\phi_j} \\ \gamma_j \\ -\beta_j \sin\theta e^{i\phi_j} \end{pmatrix} e^{-ik_j x}. \tag{9.11}$$

The angles $\phi_w = \tan^{-1}(k_y/k_w)$ and $\phi_b = \tan^{-1}(k_y/k_b)$ are the angles associated with the direction of the momentum of the electron in the well and barrier regions, respectively, as depicted in the inset of Fig. 9.5, and both in addition to the terms α_j, γ_j, and β_j are obtained from the eigenstates equation using the Hamiltonian Eq. (10.10).

Moreover, the constants A, B, C, D are determined by requesting continuity of the wave-functions. Writing the wave-functions given by Eq. (10.11) in the general form $\Psi(x) = (\psi_A(x), \psi_B(x), \psi_C(x))$ and by integrating the eigenvalue equation $\hat{H}\Psi = E\Psi$ over a small interval $x = [-\epsilon, \epsilon]$ and allowing the interval to approach zero, we obtain the following matching conditions for the wave-function on either side of the superlattice

$$\psi_B(-\epsilon) = \psi_B(\epsilon), \tag{9.12a}$$

and

$$\cos\theta\psi_A(-\epsilon) + \sin\theta\psi_C(-\epsilon) = \cos\theta\psi_A(\epsilon) + \sin\theta\psi_C(\epsilon). \tag{9.12b}$$

These matching conditions are different from those of the two limiting cases in the $\alpha - T_3$ model, i.e. graphene-like ($\alpha = 0$) and dice lattice ($\alpha = \pi/4$) [78, 98]. Whereas for graphene which has pseudospin-1/2 the matching conditions simply require the continuity of each two-component of the wave-function, however for the dice lattice which has integer pseudospin, the matching condition takes into account a sum of the first and last component of the three-components of the wave-function, as indicated in Eq. (10.12) by setting $\cos\theta = \sin\theta = 1/\sqrt{2}$. Applying the matching conditions given by Eq. (10.12) into Eq. (10.11) we obtain the transfer matrix for the $\alpha - T_3$ superlattice

$$T = \Omega_{k_w}(L)\Omega_{k_w}^{-1}(W_b)\Omega_{k_b}(W_b)\Omega_{k_b}^{-1}(0), \tag{9.13}$$

where

$$\Omega_{k_j}(x) = \begin{pmatrix} \gamma_j e^{ik_j x} & \gamma_j e^{-ik_j x} \\ \lambda_j e^{ik_w x} & -\lambda_j^* e^{-ik_w x} \end{pmatrix}, \tag{9.14}$$

with

$$\lambda_j = \cos^2\theta e^{i\phi_j} + \sin^2\theta e^{-i\phi_j}. \tag{9.15}$$

Inserting Eq. (10.15) into Eq. (10.13) we get:

$$T = \frac{1}{a_b a_w}\begin{pmatrix} c_+\lambda_b^\dagger + c_-\lambda_b & \gamma_b(c_+ - c_-) \\ d_+\lambda_b^\dagger + d_-\lambda_b & \gamma_b(d_+ - d_-) \end{pmatrix}, \tag{9.16}$$

where

$$a_j = \gamma_j(\lambda_j^* + \lambda_j), \tag{9.17a}$$

$$c_+ = e^{ik_b W_b}\gamma_w\left(\gamma_b b_1 + \lambda_b b_2\right),$$
$$c_- = e^{-ik_b W_b}\gamma_w\left(\gamma_b b_1 - \lambda_b^* b_2\right), \tag{9.17b}$$

$$d_+ = e^{ik_bW_b} \left(\gamma_b \lambda_w \lambda_w^* b_2 + \gamma_w \lambda_b b_3 \right),$$
$$d_- = e^{-ik_bW_b} \left(\gamma_b \lambda_w \lambda_w^* b_2 - \gamma_w \lambda_b^* b_3 \right) \tag{9.17c}$$

with $b_1 = \lambda_w^* e^{ik_wW_w} + \lambda_w e^{-ik_wW_w}$, $b_2 = e^{ik_wW_w} - e^{-ik_wW_w}$ and $b_3 = \lambda_w e^{ik_wW_w} + \lambda_w^* e^{-ik_wW_w}$.

According to Bloch's theorem and requiring $\det[T] = 1$ the electronic dispersion at any incident angle is given by $2\cos(K_xL) = Tr(T)$, where $K_x = 2\pi n/L$ expresses the periodicity of the superlattice structure. This results into the following nonlinear equation for the dispersion relation

$$\begin{aligned}\cos(K_xL) = {} & \cos(k_bW_b)\cos(k_wW_w) \\ & - G_U \sin(k_bW_b)\sin(k_wW_w),\end{aligned} \tag{9.18}$$

where G_U differs by the presence or absence of the symmetry-breaking term. It is denoted by G_0 for the gapless case, G_1, and G_2 when $\hat{U}_1$, and $\hat{U}_2$ are taken into account, respectively. As we will demonstrate further on, since the dispersion relation given in Eq. (9.18) depends on the symmetry between the atomic sites of the crystal structure, the inclusion of small deviations between them lead to large changes in the energy spectra and the band gap.

The allowed states for the superlattice is obtained when $-1 \leq \cos(K_xL) \leq 1$ in Eq. (9.18) which corresponds to the energy spectra for this system in the k_y plane. In addition, we can derive the density of states (DOS) represented by D(E) and given by

$$D(E) = \sum_{n,k_y} \delta(E - E_{n,k_y}), \tag{9.19}$$

and expressed in units of $D_0 = L/\hbar v_F$, which corresponds to the amount of states per unit area and L is the period of the superlattice.

9.4 Pristine system

To start, we consider the pristine system corresponding to $\hat{U}_i = 0$ in Eq. (10.10). The solution of $\hat{H}\Psi_j = E\Psi_j$ in this case leads to $\alpha_j = \gamma_j = \beta_j = 1$ in the wave-functions given by Eq. (10.11). Moreover, from the secular equation $\det(\hat{H} - E) = 0$ we obtain, respectively, the wave-vectors in the $x-$direction in the well and barrier regions

$$k_w = \sqrt{\left(\frac{E}{\hbar v_F}\right)^2 - k_y^2} \quad , \quad k_b = \sqrt{\left(\frac{E - V_b}{\hbar v_F}\right)^2 - k_y^2}, \tag{9.20}$$

with $\hbar v_F = 3a_0 t/2$.

From the transfer matrix in Eq. (9.16) we find the dispersion relation given by Eq. (9.18) with $G_U = G_0$ where

$$G_0 = \frac{1}{k_w k_b} \left[\frac{E(E - V_b)}{\hbar^2 v_F^2} + \frac{(E^2 + (E - V_b)^2)k_y^2(\cos^2(2\theta) - 1)}{2E(E - V_b)} - k_y^2 \cos^2(2\theta) \right]. \tag{9.21}$$

An electrostatic superlattice is capable of multiplying the number of Dirac points [80]. These are points in reciprocal space where the valence and conduction bands touch each other and around which the energy spectrum is linear. Therefore, it is interesting to calculate how the $\alpha - T_3$ lattice Dirac point is affected by the superlattice potential.

In order to determine the location of the Dirac points for the symmetric case $W_b = W_w = W$ we take $K_x = 0$, and $k_b = k_w$ in Eq. (9.18). Inserting this latter condition into Eq. (10.21), we have $E = V_b/2$. Thus, Eq. (9.18) becomes

$$1 = \cos^2(k_b W) + \sin^2(k_b W)$$
$$\left[\frac{V_0^2/4\hbar^2 v_F^2 + 2k_y^2 \cos^2(2\theta) - k_y^2}{V_0^2/4\hbar^2 v_F^2 - k_y^2} \right]. \tag{9.22}$$

This equation has solutions when the term between brackets is equal to 1, or $\sin^2(k_b W) = 1$. The first possibility is obtained for $k_y = 0$ and corresponds to the main Dirac point at $k_y = 0$. The second possibility leads to $k_b W = n\pi$ with n being a positive integer. This last possibility determines the position of the extra Dirac points in k_y space from Eq. (10.21),

$$k_y = \sqrt{\frac{V_b^2}{4\hbar^2 v_F^2} - \left(\frac{n\pi}{W}\right)^2}. \tag{9.23}$$

Note from Eq. (9.22) that for the symmetric case the condition to determine the position of Dirac points is regardless of the parameter θ. Note that when $\theta = 0$, Eq. (9.22) reduces to

$$1 = \cos^2(k_b W) + \sin^2(k_b W) \left[\left(V_b^2/4\hbar^2 v_F^2 + k_y^2 \right) / \left(V_b^2/4\hbar^2 v_F^2 - k_y^2 \right) \right], \tag{9.24}$$

which is consistent with the equation that determines the Dirac points for graphene [80]. As discussed above, there is no real solution for Eq. (9.24) unless $k_y = 0$ that represents the usual Dirac point, or $k_b W = n\pi$ [84, 80, 83].

On the other hand, when we set $\theta = \pi/4$, Eq. (9.22) leads to

$$\cos^2(k_b W) + \sin^2(k_b W) = 1. \tag{9.25}$$

Unlike the graphene-like case, Eq. (9.22) has many solutions and the condition for allowed states in the dispersion relation of Eq. (9.18) is always satisfied for arbitrary k_y.

In Figs. 9.6(a-d) we show the electronic band structures at $K_x L = 0$ for some values of the parameter θ assuming $W_w = W_b = L/2$ and $V_b = 7E_L$, where $E_L = \hbar v_F/L$ and $L/a_0 = 1200$. As discussed above, one Dirac point appears at $E = V_b/2$ and $k_y L = 0$ for $0 \leq \theta < \pi/4$ as shown in Figs. 9.6(a-c), moreover the upper and lower bands gradually becomes closer as the structure reaches $\theta = \pi/4$ (dice lattice), when the Dirac point disappears and all states at $E = 3.5E_L$ are allowed regardless of the values of $k_y L$, as shown in Fig. 9.6(d).

Figure 9.6: Electronic band structures at $K_xL = 0$ for (a) $\theta = 0$ (graphene-like case), (b) $\theta = \pi/12$, (c) $\theta = \pi/6$, (d) $\theta = \pi/4$ (dice case) with $V_b = 7E_L$, $W_w = W_b = L/2$, where $L/a_0 = 1200$, and $E_L = \hbar v_F/L$

Figure 9.7: Density of states for $\theta = 0$ (black solid curve), $\theta = \pi/12$ (blue dashed curve), $\theta = \pi/6$ (red dash-dotted curve), $\theta = \pi/4$ (magenta dotted curve) for the same parameters as in Fig. 9.6.

The dependence on the parameter θ observed in the energy spectra can be better understood from the density of states (DOS) shown in Fig. 9.7 for the same parameters as in Fig. 9.6. For the dice case, depicted by the magenta dotted curve, we notice the presence of a pronounced peak, which agrees with Eq. (9.25) representing the manifestation of the

Figure 9.8: Valence and conduction bands of the spectrum of a superlattice considering $\theta = 0$ (graphene-like), and $\theta = \pi/4$ (dice) with $V_b = 21E_L$, $W_w = W_b = L/2$, where $L/a_0 = 1200$, and $E_L = \hbar v_F/L$.
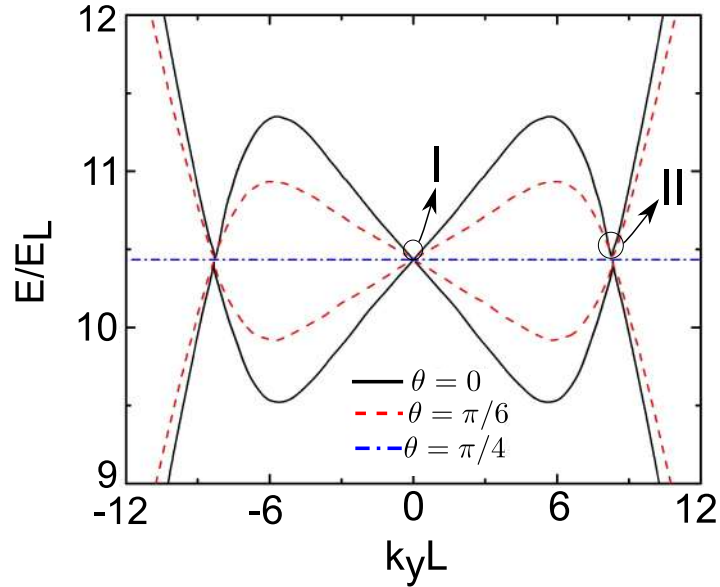
Figure 9.9: Electronic band structures for $K_x L = 0$ with $\theta = 0$ (black solid curve), $\theta = \pi/6$ (red dashed curve), and $\theta = \pi/4$ (blue dot-dashed curve) for $K_x L = 0$ with $V_b = 21E_L$, $W_w = W_b = L/2$, where $L/a_0 = 1200$, and $E_L = \hbar v_F/L$.

flat band and, therefore, an enhancement of the number of states.

In Fig. 9.8 the spectrum resulting from Eq. (9.18) using Eq. (9.21) for equal barrier and well width is plotted taking $L/a_0 = 1200$, and $V_b = 21E_L$ for $\theta = 0$ and $\theta = \pi/4$. We observe for the honeycomb case, i.e. $\theta = 0$, the appearance of extra Dirac points localized to the left and to the right of the main one at the energy corresponding to $V_b = 10.5E_L$ for $K_x L = 0$. However, at this same point for the dice case the Dirac points disappear giving rise to a flat band, which can be observed clearer in Fig. 9.9 where we show the superlattice spectrum along $k_y L$ for $K_x L = 0$ for different values of θ. We notice that as θ increases the spacing between the upper and lower bands around the Dirac points decreases.

Moreover, the group velocity along the $k_y L$ direction around the main and the extra Dirac points denoted in Fig. 9.9 by the labels I and II is shown in Fig. 9.10. Notice that the slope of the dispersion relation around these points is strongly reduced as compared to the value v_F when no superlattice is imposed. This result is similar to the collimation effect observed in graphene as new extra Dirac points are to arise when the height of the potential V_b increases as discussed in Ref. [80]. But now, the collimation effect results from changing the coupling constant θ.
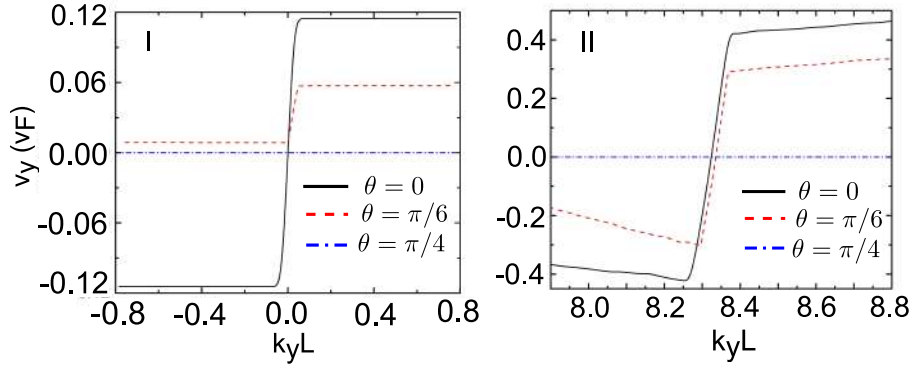
Figure 9.10: Group velocity along k_y direction around the main Dirac point (I), and around the extra Dirac point (II) indicated in Fig. 9.9.

9.5 Introduction of gaps in the superlattice energy spectrum

Using the transfer matrix formalism from Sec. 9.3, we analyze the appearance and morphing in $\alpha - T_3$ superlattices when including deviations in the atomic equivalence of the three sublattices and by adding the terms $\hat{U}_1$ or $\hat{U}_2$.

9.5.1 Gapped case $\hat{U}_1 =$diag$(1, -1, 1)$

Assuming $\hat{U} = \hat{U}_1$ in Eq. (10.10), we obtain the wave-functions expressed in Eq. (10.11) in the well $(j = w)$ and barrier $(j = b)$ with $\alpha_w = \beta_w = \sqrt{E + \Delta}, \alpha_b = \beta_b = \sqrt{E - V_b + \Delta}, \gamma_w = \sqrt{E - \Delta}$ and $\gamma_b = \sqrt{E - V_b - \Delta}$.

The wave-vectors in $x-$ direction in the well and barrier regions are

$$k_w = \sqrt{\frac{E^2 - \Delta^2}{\hbar^2 v_F^2} - k_y^2}, \tag{9.26a}$$

$$k_b = \sqrt{\frac{(E - V_b)^2 - \Delta^2}{\hbar^2 v_F^2} - k_y^2}. \tag{9.26b}$$

From the transfer matrix method we get the dispersion relation in Eq.(9.18) with $G_U = G_1$

$$G_1 = -\frac{1}{2}\left[\left(\frac{\eta_{w_1}}{\eta_{b_1}} + \frac{\eta_{b_1}}{\eta_{w_1}}\right) + \cos^2(2\theta)\left(\frac{k_y^2}{k_b^2}\frac{\eta_{b_1}}{\eta_{w_1}} + \frac{k_y^2}{k_w^2}\frac{\eta_{w_1}}{\eta_{b_1}}\right) - 2\frac{k_y^2}{k_w k_b}\cos^2(2\theta)\right], \quad (9.27)$$

with $\eta_{w_1} = k_w\hbar v_F/(E - \Delta)$ and $\eta_{b_1} = k_b\hbar v_F/(E - V_b - \Delta)$.

In order to analyze the effects on the energy spectrum, and investigate how the Dirac points are affected due to the presence of this symmetry-breaking term, we consider $W_b = W_W = W$, and $k_w W = -k_b W$ in Eq. (9.18) at the energy $E = V_b/2$ where, for gap-less case, the Dirac points are found. When we take into account these considerations and we assume $\theta = 0$, the dispersion relation becomes

$$\cos(K_x L) = \cos^2(k_b W) + \sin^2(k_b W)\left[\frac{(V_b^2/4 + \Delta^2)/\hbar^2 v_F^2 + k_y^2}{(V_b^2/4 - \Delta^2)/\hbar v_F^2 - k_y^2}\right], \quad (9.28)$$

which has no real solution regardless of the value of k_y, indicating the presence of a band gap in the energy spectrum. This result can be extended to other cases where $\cos 2\theta \neq 0$ in Eq. (9.27).

Assuming the particular case $\theta = \pi/4$ we get

$$\cos(K_x L) = \cos^2(k_b W) + \sin^2(k_b W)\left[\frac{(V_b^2/4 + \Delta^2)/\hbar^2 v_F^2 - k_y^2\left((V_b^2/4 + \Delta^2)/(V_b^2/4 - \Delta^2)\right)}{(V_b^2/4 - \Delta^2)/\hbar^2 v_F^2 - k_y^2}\right],$$
$$(9.29)$$

which has a real solution for two touching points $k_y = \pm\sqrt{V_b^2/4 - \Delta^2}/\hbar v_F$. Unlike the dice case in the absence of a mass term discussed in Sec. 9.3, the energy allowed states in the presence of a symmetry-breaking term is no longer independent of k_y at $E = V_b/2$.

This becomes more clear when we calculate the electronic band structure for some particular values of the parameter θ, the effective mass term $\Delta = 0.1V_b$, $V_b = 7E_L$, and $L/a_0 = 1200$. The results are depicted in Fig. 9.11, where $E_L = \hbar v_F/L$. As discussed from Eq. (9.28) and Eq. (9.29), we can observe the presence of a band gap in the energy spectra at $E = V_b/2$, or, in terms of the unit E_L, $E \approx 3.5E_L$. Except for $\theta = \pi/4$, where the band gap is closed at the touching points $k_y = \pm\sqrt{V_b^2/4 - \Delta^2}/\hbar v_F$, but we observe the formation of another band gap at energy $E \approx 5E_L$. Moreover, the mini-bands present in the energy spectra for intermediate values of θ are no longer symmetric around the band gap, as shown in Figs. 9.11(b)-(c). The band gap morphing and its dependence on θ can be observed when we analyze the density of states (DOS) of those systems shown in Fig. 9.12. The appearance of asymmetric mini-bands, and the band gap shifting observed in Fig. 9.11(d) becomes clearly apparent. In addiction, unlike the graphene-like case, when we assume $\theta \neq 0$ a new allowed energy state arises which appears as a new peak localized in the energy range $7E_L$ to $8E_L$ as observed in Fig. 9.12 .

On the other hand, when we take a large value for the mass term $\Delta = 0.4V_b$ maintaining the other parameters used in Fig. 9.11, beyond the increased gap, we found that
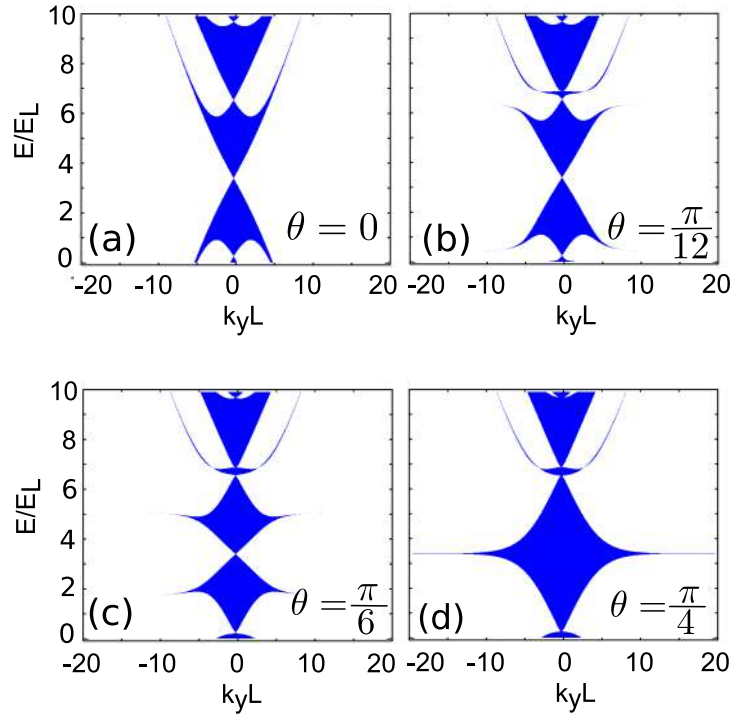
Figure 9.11: Electronic band structures at $K_x L = 0$ for (a) $\theta = 0$ (graphene-like case), (b) $\theta = \pi/12$, (c) $\theta = \pi/6$, (d) $\theta = \pi/4$ (dice case) with $V_b = 7E_L$, $W_w = W_b = L/2$, $\Delta = 0.1V_b$ and $\hat{U} = \hat{U}_1$, where $L/a_0 = 1200$, and $E_L = \hbar v_F/L$ in all cases.
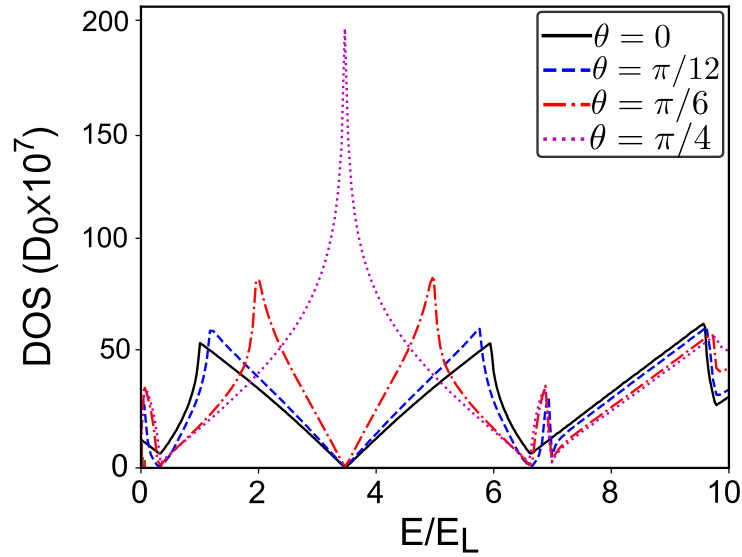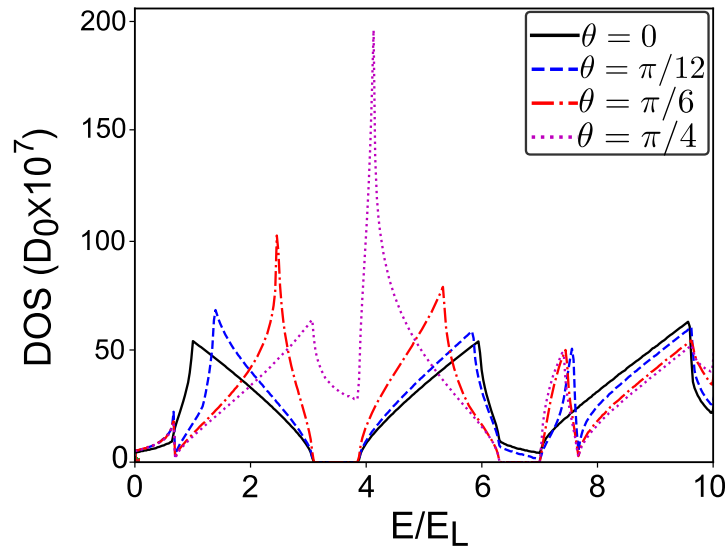

Figure 9.12: Density of states for $\theta = 0$ (black solid curve), $\theta = \pi/12$ (blue dashed curve), $\theta = \pi/6$ (red dash-dotted curve), $\theta = \pi/4$ (magenta dotted curve) for the same parameters as in Fig. 9.11.

the mini-bands change drastically. When $\theta \neq 0$, the energy spectra exhibit significant modifications in a large range of energy, as shown in Figs. 9.13(b)-(d), where it is possible to see the appearance of new mini-bands inside the band gap region, unlike

the graphene-like case. The appearance of new allowed states inside the region where for the graphene-like case there is only a band gap, is clearly seen from the density of states, as shown in Fig. 9.14. In addition, the position of the touching points given by $k_y = \pm\sqrt{V_b^2/4 - \Delta^2}/\hbar v_F$ depends on the mass term value, and these points are shifted, as shown in Fig. 9.13(d). From Fig. 9.14 we observe that there is a prominent peak when
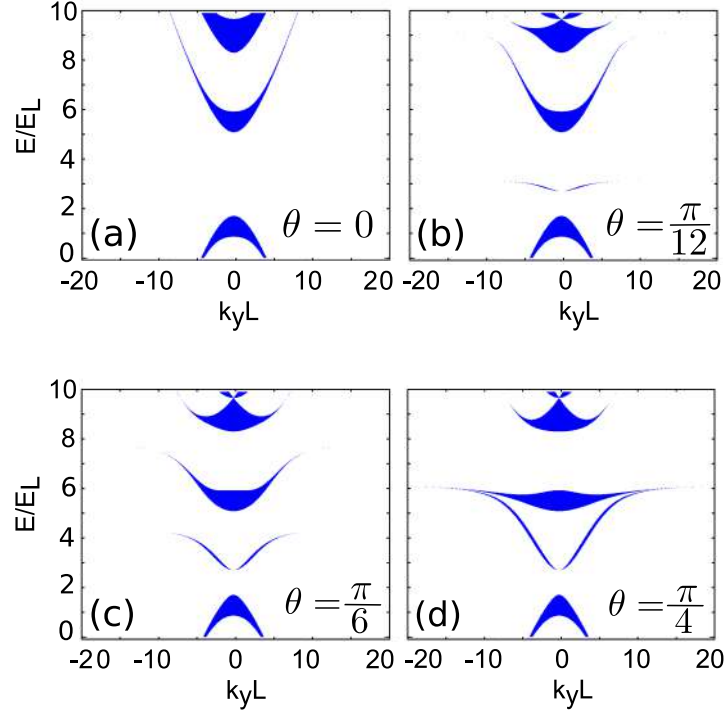
Figure 9.13: Electronic band structures at $K_x L = 0$ for (a) $\theta = 0$ (graphene-like case), (b) $\theta = \pi/12$, (c) $\theta = \pi/6$, (d) $\theta = \pi/4$ (dice case) with $V_b = 7E_L$, $W_w = W_b = L/2$, $\Delta = 0.4V_b$ for $\hat{U} = \hat{U}_1$, where $L/a_0 = 1200$, and $E_L = \hbar v_F/L$ in all cases.

the dice case is considered similar to Fig. 9.12 but localized at different energy, which results from the increase of the mass term Δ. Moreover, it is evident that there are more allowed states in the energy range $2E_L$ to $5E_L$ for $\theta \neq 0$.

In Fig. 9.15 we show the dispersion relation obtained from Eq. (9.21) and Eq. (9.27) assuming equal barrier and well widths, $L/a_0 = 1200$, $V_b = 21E_L$, and $\Delta = 0.4V_b$ for $\theta = 0$ and $\theta = \pi/4$. Unlike the gap-less case, for $\theta = 0$ the main Dirac point at $k_y L = 0$ is no longer observed, although the extra Dirac points on both sides remains. Similarly, for the dice case, the upper and lower mini-bands touch each other at two-points $k_y L \neq 0$, similar as in Fig. 9.11(d) and Fig. 9.13(d).

Moreover, when we assume the superlattice spectrum along $k_y L$ direction for $K_x L = 0$ in Fig. 9.15 we find that the dispersion gradually changes around the point $k_y L = 0$, becoming flat for $\theta = \pi/4$, as shown in Fig. 9.16. In addition, around the touching points the slope of the dispersion decreases as θ increases.
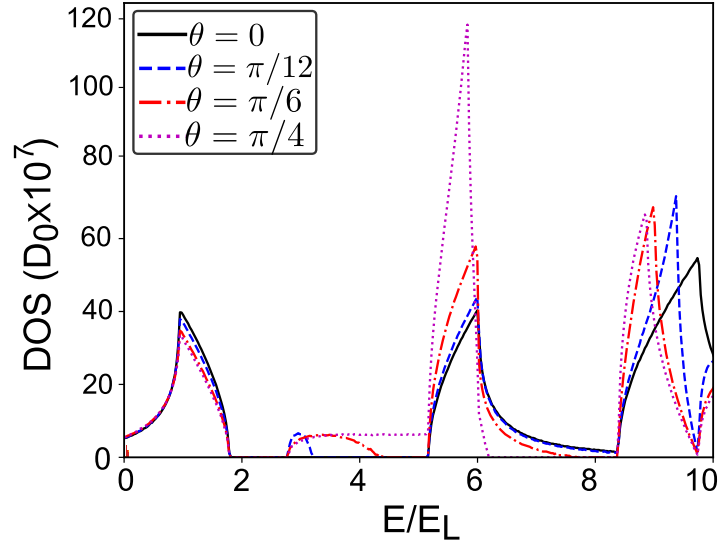
Figure 9.14: Density of states for $\theta = 0$ (black solid curve), $\theta = \pi/12$ (blue dashed curve), $\theta = \pi/6$ (red dash-dotted curve), $\theta = \pi/4$ (magenta dotted curve) for the same parameters as in Fig. 9.13.
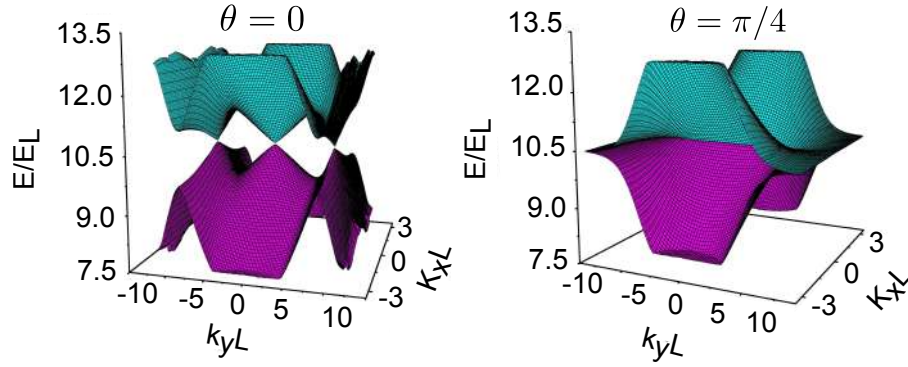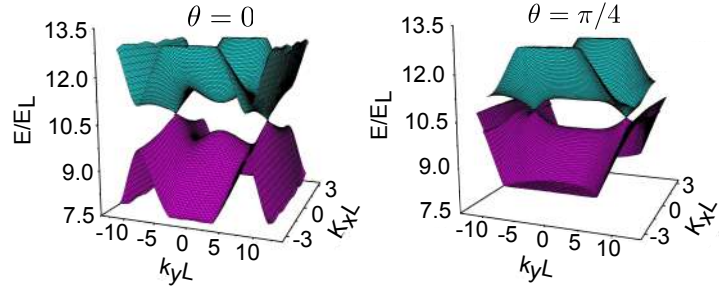

Figure 9.15: Valence and conduction bands of the spectrum of a superlattice considering $\theta = 0$ (graphene-like), and $\theta = \pi/4$ (dice) with $V_b = 21E_L$, $W_w = W_b = L/2$, $\hat{U} = \hat{U}_1$, and $\Delta = 0.4V_b$. Where $L/a_0 = 1200$, and $E_L = \hbar v_F/L$.

9.5.2 Gapped case $\hat{U}_2 = \text{diag}(1, 0, -1)$

For the other symmetry-breaking term denoted by $\hat{U} = \hat{U}_2$ in Eq. (10.10), we have $\alpha_w = \sqrt{1 + 2\Delta/(E - \Delta)}, \alpha_b = \sqrt{1 + 2\Delta/(E - V_b - \Delta)}, \gamma_w = \sqrt{1 + \Delta\cos(2\theta)/E}, \gamma_b = \sqrt{1 + \Delta\cos(2\theta)/(E - V_b)}, \beta_w = \sqrt{1 - 2\Delta/(E + \Delta)}$, and $\beta_b = \sqrt{1 - 2\Delta/(E - V_b + \Delta)}$. Consequently, the wave-functions k_w and k_b are given by

$$k_w = \sqrt{\frac{(E^2 - \Delta^2)E}{(\hbar^2 v_{\mathrm{F}}^2)(E + \Delta\cos 2\theta)} - k_y^2}, \tag{9.30a}$$

$$k_b = \sqrt{\frac{((E - V_b)^2 - \Delta^2)(E - V_b)}{(\hbar^2 v_{\mathrm{F}}^2)(E - V_b + \Delta\cos 2\theta)} - k_y^2}. \tag{9.30b}$$
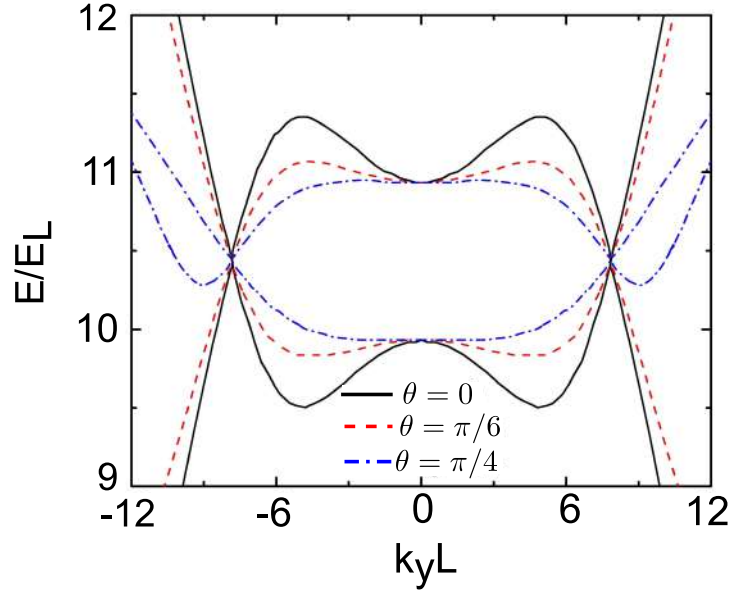
Figure 9.16: Electronic band structures at $K_x L = 0$ for $\theta = 0$ (black solid curve), $\theta = \pi/6$ (red dashed curve), and $\theta = \pi/4$ (blue dot-dashed curve) with $V_b = 21E_L$, $W_w = W_b = L/2$, $\Delta = 0.4V_b$ where $L/a_0 = 1200$, and $E_L = \hbar v_F/L$.

For this case we have

$$G_2 = -\frac{1}{2}\left[\left(\frac{\eta_{w_2}}{\eta_{b_2}} + \frac{\eta_{b_2}}{\eta_{w_2}}\right) + \left(\frac{k_y^2 \eta_{b_2}}{k_b^2 \eta_{w_2}} \frac{((E - V_b)\cos 2\theta + \Delta)^2}{(E - V_b + \Delta\cos 2\theta)^2} + \frac{k_y^2 \eta_{w_2}}{k_w^2 \eta_{b_2}} \frac{(E\cos 2\theta + \Delta)^2}{(E + \Delta\cos 2\theta)^2}\right) \right.$$
$$\left. - \frac{2k_y^2}{k_w k_b} \frac{((E - V_b)\cos 2\theta + \Delta)(E\cos 2\theta + \Delta)}{(E - V_b + \Delta\cos 2\theta)(E + \Delta\cos 2\theta)}\right], \tag{9.31}$$

and

$$\eta_{w_2} = \frac{k_w}{(E^2 - \Delta^2)(E + \Delta\cos 2\theta)}, \tag{9.32a}$$

$$\eta_{b_2} = \frac{k_b}{[(E - V_b)^2 - \Delta^2][(E - V_b) + \Delta\cos 2\theta]}. \tag{9.32b}$$

From Eq. (10.10) assuming $\Delta = 0.1V_b$ for $\hat{U} = \hat{U}_2$, and the same values of L and V_b as in Fig. 9.6, we get the energy spectra shown in Fig. 9.17 for different values of θ. Similar to the case $\hat{U} = \hat{U}_1$ we observe the presence of a band gap for all values of $\theta \neq \pi/4$ around $E = V_b/2$, i.e $E = 3.5E_L$, and the mini-bands tend to reach each other around this energy as θ increases until the band gap is completely closed for the dice case, as shown in Fig. 9.17(d). Like the gapless case, all energy states when $\theta = \pi/4$ are allowed regardless of the k_y value, which results in a prominent peak in the density of states depicted in Fig. 9.18. This result can be expected when we assume the condition $W_b = W_w = W$, $E = V_b/2$, and $\theta = \pi/4$ in the dispersion relation for this case. Under these conditions, the dispersion relation for the dice lattice reduces to the same one for the gapless case represented in Eq. (9.25).
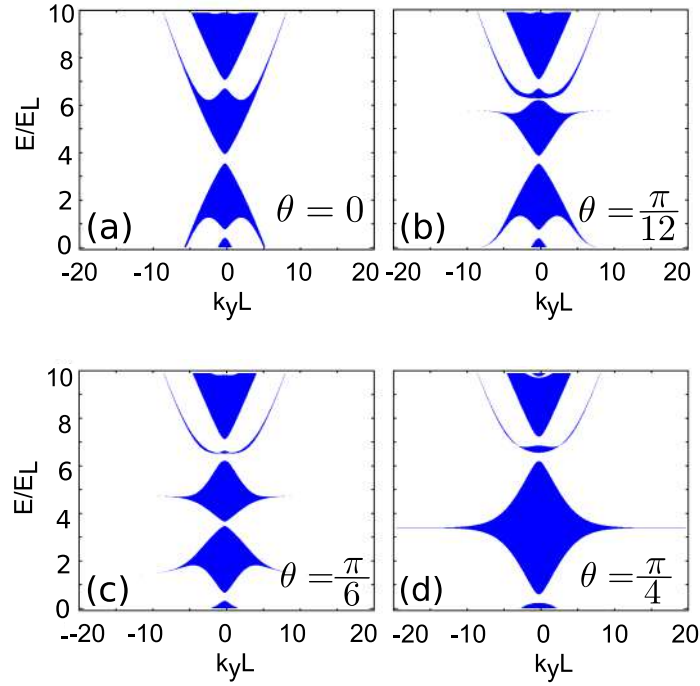
Figure 9.17: Electronic band structures at $K_xL = 0$ for (a) $\theta = 0$ (graphene-like case), (b) $\theta = \pi/12$, (c) $\theta = \pi/6$, (d) $\theta = \pi/4$ (dice case) with $V_b = 7E_L$, $W_w = W_b = L/2$, $\Delta = 0.1V_b$ when $\hat{U} = \hat{U}_2$, where $L/a_0 = 1200$, and $E_L = \hbar v_F/L$ in all cases.
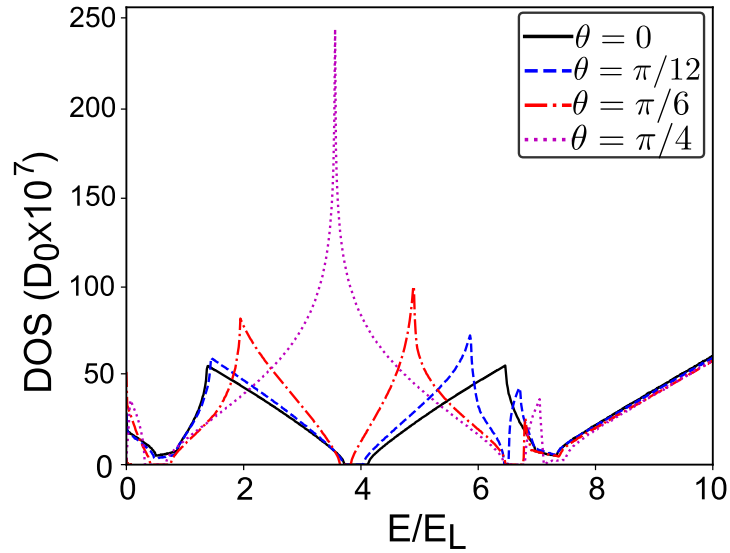
Figure 9.18: Density of states for $\theta = 0$ (black solid curve), $\theta = \pi/12$ (blue dashed curve), $\theta = \pi/6$ (red dash-dotted curve), $\theta = \pi/4$ (magenta dotted curve) for the same parameters as in Fig. 9.17.

Moreover, comparing the band gap width observed in Fig. 9.17 to the one in Fig. 9.11 the band gap is reduced and shifted up, as observed in Fig. 9.18.

Similar to the previous gapped case, if we consider a larger value of the mass term $\Delta = 0.4V_b$ the band gap is increased and other allowed states appear inside them when
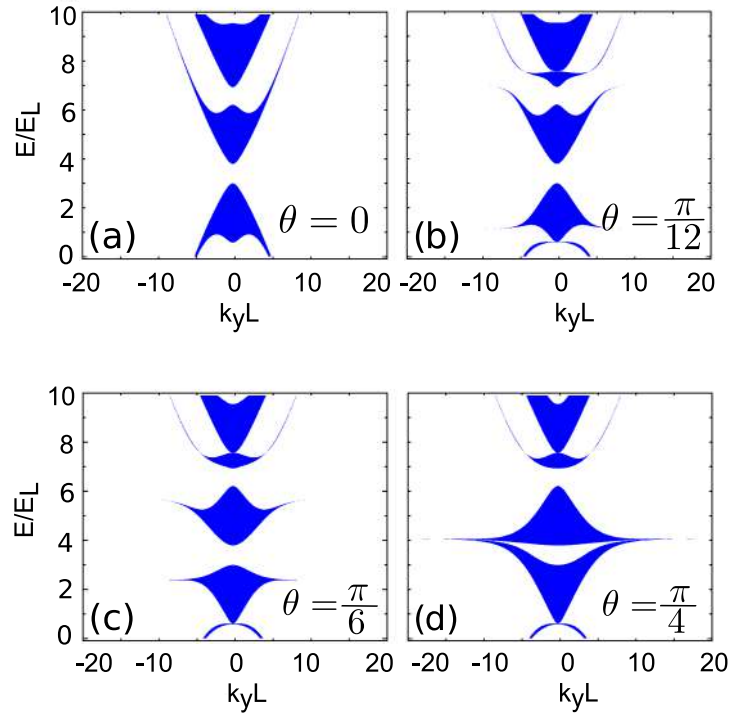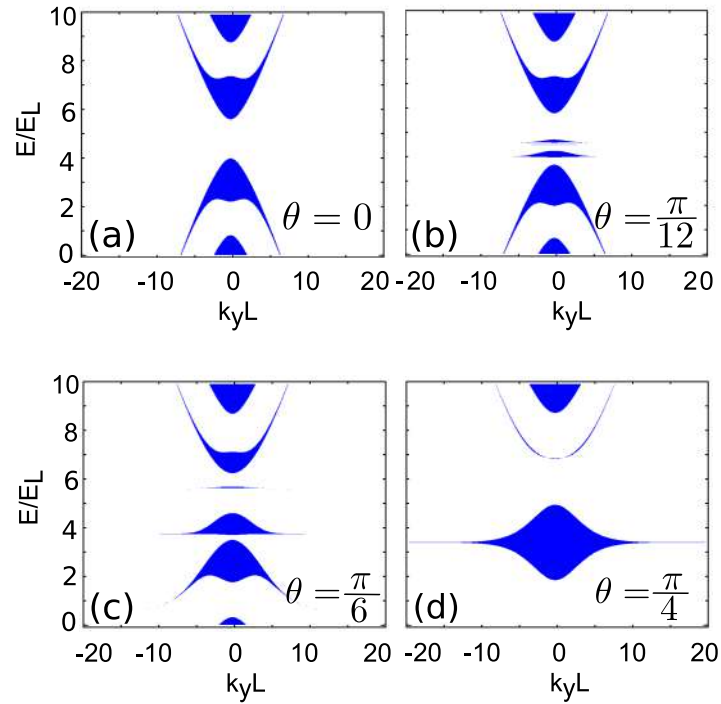
Figure 9.19: Electronic band structures at $K_x L = 0$ for (a) $\theta = 0$ (graphene-like case), (b) $\theta = \pi/12$, (c) $\theta = \pi/6$, (d) $\theta = \pi/4$ (dice lattice) with $V_b = 7E_L$, $W_w = W_b = L/2$, $\Delta = 0.4V_b$ when $\hat{U} = \hat{U}_2$, where $L = 1200$, and $E_L = \hbar v_F/L$ in all cases.
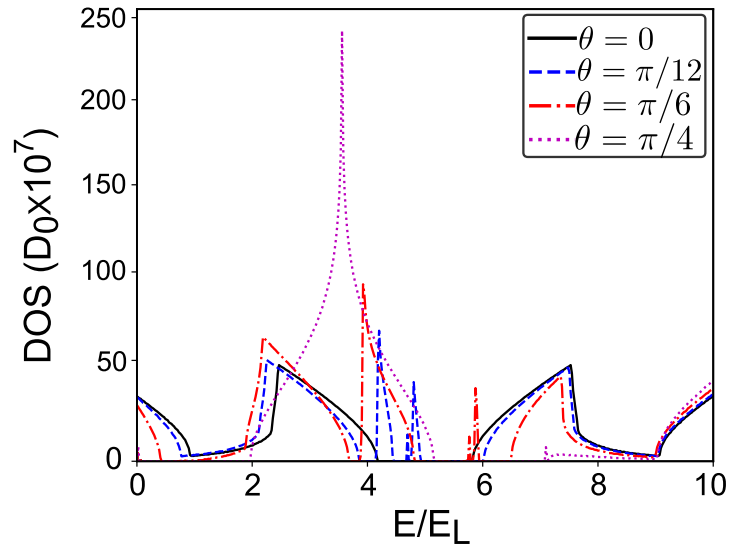
Figure 9.20: Density of states for $\theta = 0$ (black solid curve), $\theta = \pi/12$ (blue dashed curve), $\theta = \pi/6$ (red dash-dotted curve), $\theta = \pi/4$ (magenta dotted curve) for the same parameters as in Fig. 9.19.

intermediate values of θ are considered, as shown in Fig. 9.19. However the allowed state for arbitrary values of k_y at $E = V_b/2$ for the dice lattice is preserved and a peak in the density of states is observed for $\theta = \pi/4$, as shown in Fig. 9.20, since this condition is independent of the value of the effective mass. The spectrum obtained from Eq. (9.18)
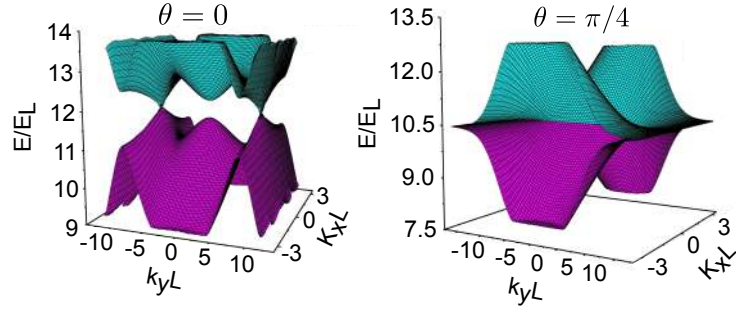
Figure 9.21: Valence and conduction bands of the spectrum of a superlattice considering $\theta = 0$ (graphene-like), and $\theta = \pi/4$ (dice) with $V_b = 21E_L$, $W_w = W_b = L/2$, $\hat{U} = \hat{U}_2$, and $\Delta = 0.4V_b$. Where $L/a_0 = 1200$, and $E_L = \hbar v_F/L$.

and Eq. (9.31) considering equal barrier and well widths, $L/a_0 = 1200$, $V_b = 21E_L$, and $\Delta = 0.4V_b$ for $\theta = 0$ and $\theta = \pi/4$ are shown in Fig. 9.21. Similar to previous gapped case, for $\theta = 0$ the upper and lower mini-bands touch each other in two-points, and at $k_yL = 0$ there is a gap. However, as discussed above, the energy where the touching points are localized is no longer at $E = V_b/2$. On the other hand, for the dice lattice the spectrum is completely flat at $k_yL = 0$ and $E = V_b/2$, similar to Fig. 9.8.
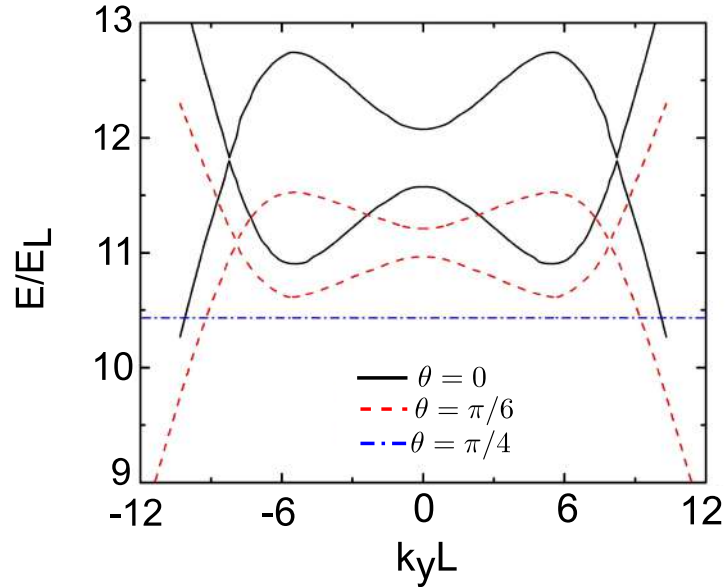
Figure 9.22: Electronic band structures at $K_xL = 0$ for $\theta = 0$ (black solid curve), $\theta = \pi/6$ (red dashed curve), and $\theta = \pi/4$ (blue dot-dashed curve) with $V_b = 21E_L$, $W_w = W_b = L/2$, $\Delta = 0.4V_b$ where $L/a_0 = 1200$, and $E_L = \hbar v_F/L$.

In Fig. 9.22 we show the superlattice spectrum considering $K_xL = 0$ along k_yL direction for some values of θ. Notice that the energy where the touching points are localized depends on θ. Moreover, like the gapless case, as $\theta \to \pi/4$ the dispersion becomes flat and shifted to lower values of energy.

9.6 Conclusions of this chapter

We investigated the energy spectrum and the density of states (DOS) of $\alpha - T_3$ lattices for different values of interlattice hopping parameter $\theta = \tan^{-1}\alpha$ in the presence of a 1D superlattice. We consider both the case of equivalence between the three sub-lattices, and how the band gap is affected by small deviations of this equivalence in the limit $\Delta \ll t$ by considering two cases of symmetry-breaking terms denoted by $\hat{U}_1$ and $\hat{U}_2$.

For the pristine system, when no symmetry-breaking term are present, we found the condition for the appearance of Dirac points that depends on the cosine function of the parameter θ, indicating that the energy level where they are located remains the same for all cases when $\cos(2\theta) \neq 1$. When $\theta = \pi/4$ all energies are allowed for arbitrary k_y. Moreover, the mini-bands for intermediate values of θ tends to close around the energy level where Dirac points are localized. In addition, when we considered higher values of the potential, we observed extra Dirac points localized on the right and on the left of the main one positioned at $k_y = 0$ for all values of $\theta \neq \pi/4$.

When we introduce symmetry-breaking terms into the system, we observed the appearance of a band gap, whose creation depends on the deviation on the equivalence between the three sub-lattices. When we considered the case $\hat{U}_1 = \text{diag}(1, -1, 1)$, a band gap appears at energy $E = V_b/2$. However for the dice case, around this energy, there is no longer a band gap and the mini-bands touch at two points. This result can be observed either in the energy spectra and in their corresponding DOS.

In addition, the mini-bands for larger values of the mass term was shifted up, which is a consequence of the fact that the sites A and C remain equivalent, leading to twofold degeneracy of the energy spectra, as in the case when there is no periodic potential present. Moreover, for larger values of the potential the main Dirac point for all θ values is no longer present, only the extra ones appear and are localized at the energy $E = V_b/2$.

When $\hat{U}_2 = \text{diag}(1, 0, -1)$, the dispersion relation, and consequently, the energy spectrum is strongly altered. For the dice case, we found that the condition for the allowance of the energy states at $E = V_b/2$ is always satisfied regardless of k_y, similarly as in the gapless case. However a band gap is still present but now localized at another energy. In addition, we noticed that the band gap is smaller than the one observed when $\hat{U}_1$. Moreover, for larger values of the effective mass new energy states were observed inside the band gap as confirmed from the density of states. In addition, for higher values of the potential considering $\theta \neq \pi/4$ only the extra Dirac points are observed, like for the previous gapped case, but now the energy value where they are localized depends on the hopping parameter.

The theoretical formalism and results obtained in this work are useful for a better understanding of the band-gap behaviour of $\alpha - T_3$ lattices, and consequently demonstrate that these materials are versatile for purposes of band-gap engineering in 2D materials, since the band-gap is tunable by changing the interlattice hopping parameter and their symmetry.

10

Tunneling properties in $\alpha - T_3$ lattices: effects of symmetry-breaking terms

The $\alpha - T_3$ lattice model interpolates a honeycomb (graphene-like) lattice and a T_3 (also known as dice) lattice via the parameter α. These lattices are made up of three atoms per unit cell. This gives rise to an additional dispersionless flat band touching the conduction and valence bands. Electrons in this model are analogous to Dirac fermions with an enlarged pseudospin, which provides unusual tunneling features like omnidirectional Klein-tunneling, also called super-Klein tunneling (SKT). However, it is unknown how small deviations in the equivalence between the atomic sites, i.e. variations in the α-parameter, and the number of tunnel barriers changes the transmission properties. Moreover, it is interesting to learn how tunneling occurs through regions where the energy spectrum changes from linear with a middle flat band to a hyperbolic dispersion. In this paper we investigate these properties, its dependence on the number of square-barriers and the α-parameter for either gapped and gapless cases. Furthermore, we compare these results to the case where electrons tunnel from a region with linear dispersion to a region with a band-gap. In the latter case, contrary to tunneling through a potential barrier, the SKT is no longer observed. Finally, we find specific cases where transmission is allowed due to a symmetry breaking of sublattice equivalence.

10.1   Motivation

The probability for a particle to cross potential barriers even through a classically forbidden region with a tiny probability is a quantum phenomenon. This counterintuitive aspect of the transmission takes place when a particle, with some probability, can create a 'tunnel' that enables it to traverse a potential barrier even when it is higher than its energy. Although such tunneling is not expected in a classical particle dynamics approach, an analogous effect called evanescent wave coupling takes place in optics, in which an electromagnetic wave is transmitted through a region where the solution of the corresponding wave equation is exponentially decaying. In quantum mechanics, likewise,

the tunneling of a particle can be said to arise due to the coupling of the propagating solutions of Schrödinger's equation at either sides of the potential barrier with decaying solutions in the barrier region, leading to non-zero transmission probabilities [291].

However, counterintuitive effects emerge in the tunneling of relativistic particles [67, 68, 69]. One example is the total transmission of relativist particles through large potential steps at certain values of momentum which is known as the *Klein paradox* [68, 69]. Although it was first described by Klein, experimental realization of a similar effect known as the "Klein tunneling" (KT), an usual tunneling property characterized by the suppression of backscattering by potential barriers [8, 72, 73], has only recently become possible [74, 75, 76, 77] following the isolation of stable-single layer (graphene) and bilayer carbon crystals where the carbon atoms are arranged on a honeycomb lattice (HCL) [3, 254, 8, 255]. Since electrons in graphene at low-energy are well described by the two-dimensional (2D) massless Dirac equation, i.e. the Dirac-Weyl equation with pseudospin $S = 1/2$, graphene boosted the exploration of fundamental research in 2D materials [292], bridging condensed matter physics, relativistic quantum mechanics, and quantum field theory, resulting in the probing of interesting relativistic predictions, such as KT [74, 75, 76, 77, 8, 255] and Zittebewegung [148, 111, 203, 252].

The KT observed in graphene is strongly related to the conservation of chirality for carriers in this material and the nature of its pseudospin [78, 79]. Instigated by such unusual properties lying on the 2D panorama, the search for new graphene-based materials has been intensified in the past two decades. Examples of these 2D materials is T_3 or dice lattice [56], Lieb [267] and Kagome [268]. These lattices result from altering the HCL of graphene by adding an atom at the center of the hexagons of the unit cell [266, 267, 268, 269, 52, 56, 58, 270]. As a consequence, the charge carriers are described as enlarged pseudospin Dirac fermions [52, 56, 53, 54, 271] and a flatband appears touching the top of the valence and the bottom of the conduction linear bands in the energy spectrum [55, 272]. This flatband has important and unusual effects on the electronic properties due to its dispersionless nature [271, 55, 272, 273, 274, 96, 275, 276, 98].

The $\alpha - T_3$ model interpolates between the HCL and the dice lattice by varying the parameter $\alpha = \tan\theta$, corresponding to the strength between the HCL and the central site, from $\alpha = 0$ to $\alpha = 1$, respectively, with the limiting cases of the HCL ($\theta = 0$) and the dice lattice ($\theta = \pi/4$) [55, 96, 275, 276, 98]. Unlike graphene, charge carriers in $\alpha - T_3$ lattices are described as massless Dirac fermions only in the limiting case $\alpha = 1$, i.e. dice. For certain energy conditions, it presents an angular independent Klein tunneling through rectangular electrostatic barriers called super-Klein tunneling (SKT) [54, 98]. In addition, an extraordinary Snell law is found allowing a refracted particle beam to be focused at one point, such as occurs in a Veselago lens [293, 294]. Furthermore, there is a general trend of enhanced transmission when increasing the α-parameter [54, 279, 98]. Moreover, in the case of the dice lattice the tunneling is less sensitive to the number of barriers for certain values of energy [283], whereas for graphene the number of barriers

strongly affects the tunneling [262].

Nonetheless, for practical electronic applications such as the fabrication of quantum information devices the creation of a band-gap is necessary. It was demonstrated that an additional mass term in $\alpha - T_3$ systems distorts the linear bands around the Dirac cone and produces an energy gap with a third band in it which could be flat or dispersive [275, 276]. In the present work and using the theoretical formalism developed in Ref. [295], we theoretically study the emergence of SKT and under what conditions this phenomena is affected when the equivalence between the sublattices is broken and by increasing the number of barriers. We find that as a consequence of the enlarged pseudospin and the symmetry between the three sublattices, for dice the increasing of the number of barriers effects is less in the transmission properties for electrons with incident energy around half the height of the potential and omnidirectional tunneling is observed regardless the number of barriers. Additionally, we investigate the role of the location of the flat band in the transmission properties of charge carriers across potential barriers for some values of α when different symmetry-breaking terms are taken into account. In both cases we find that small deviations in the symmetry between the sublattices, followed by modifications in the electronic band structures as discussed in Ref. [295], result in strong modifications on the nature of wave-vectors inside the barriers, consequently, affecting the tunneling properties of charge carriers. Subsequently, we analyze the transmission of chiral electrons in $\alpha - T_3$ lattice through a region where the electronic spectrum changes from linear dispersion to hyperbolic dispersion with a band-gap and we compare these results with those for HCL [296]. We highlight that KT is prevented to take place and the transmission probability is less than 1 for all values of θ, although the peaks of resonant transmission becomes smooth as θ increases and a perfect transmission is observed for larger values of incident angle.

In this chapter we discuss the electronic properties of charge carriers in $\alpha - T_3$ lattices, and how this is affected by small deviations in the atomic equivalence between the sites. The consequences of the presence of mass terms on the energy spectrum are also discussed. We develop the transfer-matrix approach to analyze the tunneling of Dirac fermions in $\alpha - T_3$ lattices through a 1D periodic potential. Using this approach we analyze the transmission properties of massless fermions and the effects of symmetry-breaking on the tunneling properties. Furthermore we investigate the tunneling through spatial regions where the energy spectrum of fermions in $\alpha - T_3$ changes from linear to hyperbolic dispersion.

10.2 Fermions in $\alpha - T_3$ lattice

The low-energy Hamiltonian for the $\alpha - T_3$ model, a crystallographic lattice composed by three atoms per unit cell as illustrated in Fig. 10.1(a), around the K point in the first Brillouin zone can be written as
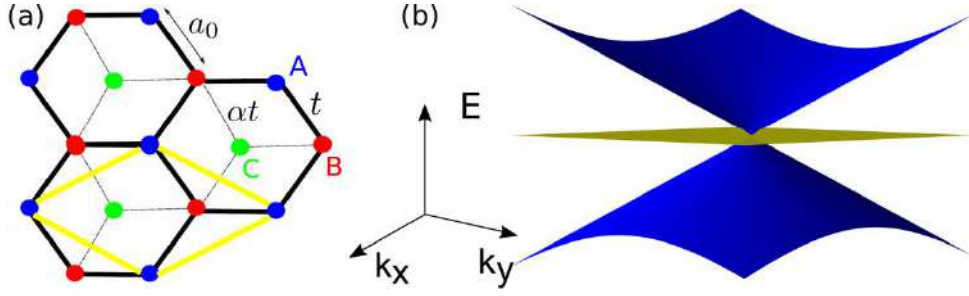
Figure 10.1: (a) Illustration of the $\alpha - T_3$ lattice with three atomic sites (A, B, and C) per unit cell (yellow rhombus) is shown. $\alpha = 0$ and $\alpha = 1$ limits correspond to HC (graphene-like) and dice lattices. $A - B$ and $B - C$ sites are connected by the hopping amplitude t and αt, respectively. (b) Low energy spectrum of massless Dirac fermions in the $\alpha - T_3$ lattice, composed by a linear dispersion and a flat-band.

$$\hat{H}_{kin} = \begin{pmatrix} 0 & f_k(\tau)\cos\theta & 0 \\ f_k^*(\tau)\cos\theta & 0 & f_k(\tau)\sin\theta \\ 0 & f_k^*(\tau)\sin\theta & 0 \end{pmatrix}, \tag{10.1}$$

where $\theta = \tan^{-1}\alpha$ is the angle that provides a continuous evolution from the honeycomb graphene-like ($\alpha = 0$) to the dice ($\alpha = 1$) lattice via the parameter α. The tuning parameter is proportional to the strength of the coupling between B sites with the additional atoms C at the center of the HCL, as shown in Fig. 10.1(a), and the other two atomic sites A and B are connected by the hopping parameter t. In Eq. (10.1) we defined the function $f_k(\tau) = v_F(\tau k_x - ik_y)$, with $v_F = 3a_0t/2\hbar$ the Fermi velocity, a_0 the lattice constant, $\vec{k} = (k_x, k_y)$ the wave vector, and $\tau = +1(-1)$ is the valley index for the K and K' valleys, respectively. In the absence of external potentials, the eigenstates of the Hamiltonian are given by

$$|\Psi_\pm\rangle = \begin{pmatrix} \cos\theta e^{i\phi_k} \\ \pm 1 \\ \sin\theta e^{-i\phi_k} \end{pmatrix}, \tag{10.2}$$

with eigenvalues $E_\pm = \pm\hbar v_F k$, where $+(-)$ indicates the conduction and valence bands, respectively, resulting in graphene-like conical energy bands. The angle $\phi_k = \tan^{-1}(k_y/k_x)$ corresponds to the polar angle associated with the momentum-vector. In additional to the linear dispersion, a third energy band, with eigenvalue $E = 0$, is also found, being a highly degenerate state, as shown in Fig. 10.1(b). It is associated to the flat-band state

$$|\Psi_0\rangle = \begin{pmatrix} \cos\theta e^{i\phi_k} \\ 0 \\ \sin\theta e^{-i\phi_k} \end{pmatrix}, \tag{10.3}$$

with eigenvalues that do not depend on the θ parameter, which affects only the eigenstates.
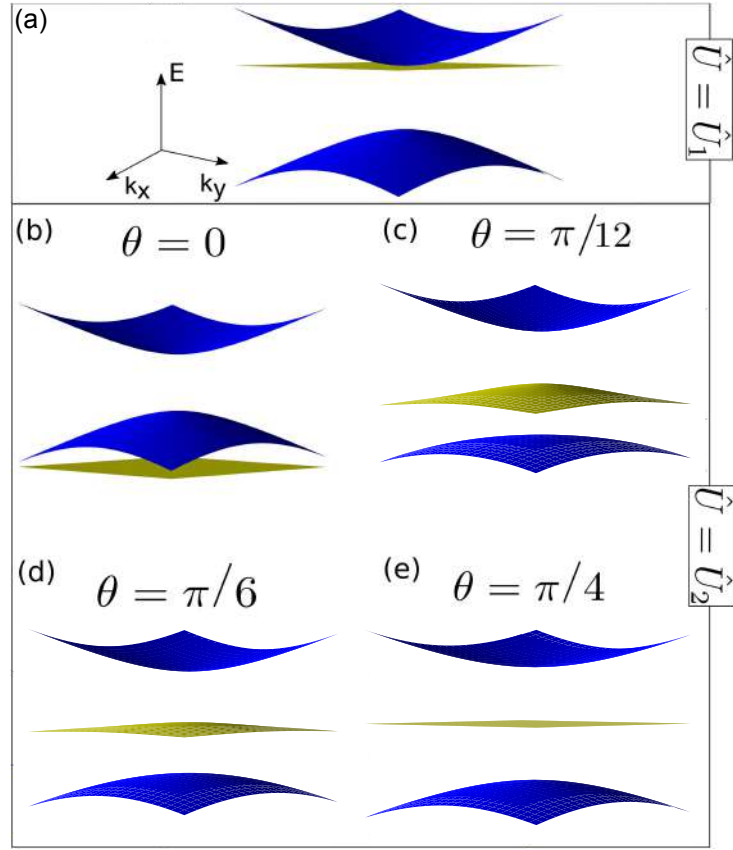
Figure 10.2: Energy spectrum of Dirac fermions around the K point for different values of the parameter θ in the $\alpha - T_3$ lattices when (a) the sublattice symmetry-breaking term $\hat{U} = \hat{U}_1$ is taken in Eq. (10.4), and for the symmetry-breaking term $\hat{U} = \hat{U}_2$ when (b) $\theta = 0$ (graphene-like), (c) $\theta = \pi/12$, (d) $\theta = \pi/6$, and (e) $\theta = \pi/4$ (dice).

10.3 Introduction of band-gap

The degeneracy observed at $E = 0$ in the energy spectrum shown in Fig. 10.1(b) is lifted when the equivalence between the three sub-lattices is broken, and a gap is introduced into the energy spectrum. In general, we can include this in the Hamiltonian by a term $\hat{U}$, as follows:

$$\hat{H} = \hat{H}_{kin} + \Delta \hat{U}, \tag{10.4}$$

with the kinetic term $\hat{H}_{kin}$ given by Eq. (10.1), and Δ measures the strength of the sub-lattice symmetry breaking. We consider two different forms of the $\hat{U}$ matrix, respectively, given by

$$\hat{U}_1 = \begin{pmatrix} 1 & 0 & 0 \\ 0 & -1 & 0 \\ 0 & 0 & 1 \end{pmatrix}, \quad \hat{U}_2 = \begin{pmatrix} 1 & 0 & 0 \\ 0 & -1 & 0 \\ 0 & 0 & -3 \end{pmatrix}. \tag{10.5}$$

The effects of the inclusion of the terms $\hat{U}_1$ and $\hat{U}_2$ on the energy spectrum are shown in Fig. 10.2(a) and Figs. 10.2(b)-10.2(e), respectively.

The solution of $\hat{H}\Psi = E\Psi$ when $\hat{U} = \hat{U}_1$ gives the eigenenergies

$$E_0 = \Delta, \quad E = \pm\sqrt{\Delta^2 + \hbar^2 v_{\mathrm{F}}^2 k^2} \; . \tag{10.6}$$

Correspondingly, the wave-functions in this case are given by

$$|\psi_0\rangle = \begin{pmatrix} \cos\theta e^{i\phi_k} \\ 0 \\ \sin\theta e^{-i\phi_k} \end{pmatrix}, \quad |\psi_\pm\rangle = \begin{pmatrix} \alpha\cos\theta e^{-i\phi_k} \\ \gamma \\ \alpha\sin\theta e^{i\phi_k} \end{pmatrix}, \tag{10.7}$$

where $\alpha = \sqrt{E + \Delta}$ and $\gamma = \sqrt{E - \Delta}$.

According to Eq. (10.6), one obtains an energy spectrum with a band-gap opening of 2Δ. It is worth mentioning that the format of $\hat{U}_2$ in Eq. (10.5) was chosen in order that both sublattice symmetry-breaking terms $\hat{U}_1$ and $\hat{U}_2$ give rise to the same 2Δ band-gap opening. This results in massive Dirac fermions with an effective mass defined as $m = \Delta/v_F^2$. Since Eq. (10.6) does not depend on the parameter θ, the energy spectrum remains the same for all $\alpha - T_3$ lattices, as shown in Fig. 10.2(a). Moreover, as long as the equivalence between the sites A and C is maintained, the flat-band is shifted and touches only the bottom of the conduction band. Notice that now the bottom of the conduction band and the top of the valence band are quadratic in k.

When we assume $\hat{U} = \hat{U}_2$ in Eq. (10.4), the energy dispersion relation is obtained from a non-linear equation

$$(E + 3\Delta)(E^2 - \Delta^2) - k^2(\Delta\cos 2\theta + E + 2\Delta\cos^2\theta) = 0, \tag{10.8}$$

and the eigenstates for the conduction and valence bands are given by

$$|\psi\rangle = \begin{pmatrix} \alpha'\cos\theta e^{i\phi_k} \\ \gamma' \\ \beta\sin\theta e^{-i\phi_k} \end{pmatrix}, \tag{10.9}$$

with $\alpha' = \sqrt{(E + 3\Delta)/(E - \Delta)}$, $\gamma' = \sqrt{(E + \Delta\cos(2\theta) + 2\Delta\cos^2\theta)/(E + \Delta)}$, and $\beta = \sqrt{(E - \Delta)/(E + 3\Delta)}$.

Like the previous case, a 2Δ band-gap opening is still observed for all values of θ, but now the previous flat-band no longer touches the bottom of the conduction band. In addition, the dispersion of the middle band depends on the θ parameter, being flat only when $\theta = \pi/4$ (dice lattice - Fig. 10.2(e)). Note that for the specific case $\theta = 0$ (graphene-like) the energy spectra for $\hat{U}_1$ (Fig. 10.2(a)) and $\hat{U}_2$ (Fig. 10.2(b)) differ only by the localization of the flat band. As we shall discuss later, this results in similar tunneling properties for both gapped cases when one-dimensional square potentials are applied to these systems.
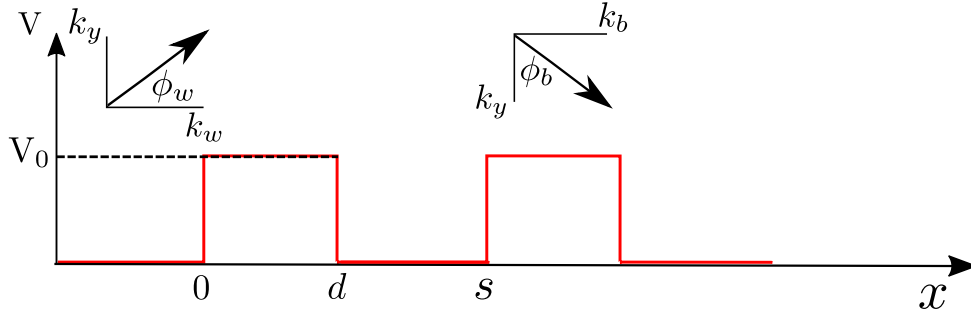
Figure 10.3: Schematic illustration (see top insets) of the wavevectors in the tunneling process through an electrostatic finite superlattice formed by rectangular barriers of height V_0 and width d. The well width, i.e. the inter-barrier distance, is $s - d$.

10.4 Transmission through one-dimensional periodic barriers

First, we investigate the transmission probability of fermions in $\alpha - T_3$ lattice through a finite number N of electrostatic rectangular barriers of constant height V_0, width d and inter-barrier distance $s - d$, as depicted in Fig. 10.3. We consider both gapless and gapped cases as obtained from the presence of sublattice symmetry-breaking terms given by Eq. (10.5). The general Hamiltonian taking into account both the presence of the symmetry-breaking term and electrostatic potential is now given by

$$\hat{H} = \hat{H}_{\text{kin}} + V(x)\hat{I} + \Delta\hat{U}, \tag{10.10}$$

where $\hat{H}_{\text{kin}}$ is given by Eq. (10.1), $V(x)$ denotes the superlattice potential with translational symmetry breaking along the x-direction, and $\Delta\hat{U}$ represents the previous sublattice symmetry-breaking term assumed here by Eq. (10.5). Due to the translation invariance in the y-direction the wave-functions have the form $\Psi_j(x, y) = \Psi_j(x)e^{ik_y y}$, where the j index is related to the different potential regions along the x-direction being outside ($j = w$) and inside ($j = b$) of the barrier. Therefore, the wave-function can be written as

$$\psi_j(x) = \frac{A_j}{\sqrt{2}}\begin{pmatrix} \alpha_j \cos\theta e^{i\phi_j} \\ \gamma_j \\ \beta_j \sin\theta e^{-i\phi_j} \end{pmatrix} e^{ik_j x} + \frac{B_j}{\sqrt{2}}\begin{pmatrix} -\alpha_j \cos\theta e^{-i\phi_j} \\ \gamma_j \\ -\beta_j \sin\theta e^{i\phi_j} \end{pmatrix} e^{-ik_j x}. \tag{10.11}$$

The angles $\phi_j = \tan^{-1}(k_y/k_j)$ (with $j = \omega, b$) are the angles associated with the direction of the momentum of the electron in the regions inside and outside of the potential, as depicted in the insets of Fig. 10.3. In addition, the terms α_j, γ_j, and β_j, are obtained from the eigenstates equation using the Hamiltonian Eq. (10.10).

In order to obtain the transmission probability through electrostatic barriers, we need to solve the scattering problem by matching wave functions given in Eq. (10.11) at the interfaces inside and outside the barrier. We assume potential variations that are smooth

on the length scale of the lattice constant a_0 but sharp on the scale of the Fermi wavelength $\lambda_F = 2\pi v_F/|E|$.

Writing the wave-functions given by Eq. (10.11) in its general form as $\Psi(x) = [\psi_A(x), \psi_B(x), \psi_C(x)]^T$ and by integrating the eigenvalue equation $\hat{H}\Psi = E\Psi$ over a small interval $x = [-\epsilon, \epsilon]$, in the limit $\epsilon \to 0$, we obtain the following matching conditions for the wave-function in each region

$$\psi_B(-\epsilon) = \psi_B(\epsilon), \tag{10.12a}$$

$$\cos\theta\psi_A(-\epsilon) + \sin\theta\psi_C(-\epsilon) = \cos\theta\psi_A(\epsilon) + \sin\theta\psi_C(\epsilon). \tag{10.12b}$$

Applying these matching conditions into Eq. (10.11), we obtain the transfer matrix for a single-barrier

$$\mathcal{T}^{(1)} = \mathcal{M}_b(d) \cdot \mathcal{M}_w(0) = \begin{pmatrix} w & z \\ z* & w* \end{pmatrix}, \tag{10.13}$$

where $\mathcal{M}_b$ and $\mathcal{M}_w$ correspond to the transfer matrix into the well and barrier, respectively, and are given by

$$\mathcal{M}_b(d) = \Omega_{k_w}^{-1}(d)\Omega_{k_b}(d), \tag{10.14a}$$

$$\mathcal{M}_w(0) = \Omega_{k_b}^{-1}(0)\Omega_{k_w}(0), \tag{10.14b}$$

with

$$\Omega_{k_j}(x) = \begin{pmatrix} \gamma_j e^{ik_j x} & \gamma_j e^{-ik_j x} \\ \lambda_j e^{ik_j x} & -\lambda_j^* e^{-ik_j x} \end{pmatrix}, \tag{10.15}$$

and $\lambda_j = \alpha_j \cos^2\theta e^{i\phi_j} + \beta_j \sin^2\theta e^{-i\phi_j}$. Using Eqs. (10.14) and (10.15), one can obtain explicitly the terms w and z in Eq. (10.13) as

$$w = \frac{1}{a}[e^{-i(k_w-k_b)d}\left(\lambda_w^*\lambda_b^* + \eta_1\lambda_w^*\lambda_w + \eta_2\lambda_b^*\lambda_b + \lambda_w\lambda_b\right)$$
$$+ e^{-i(k_w+k_b)d}\left(\lambda_w\lambda_b^* - \eta_1\lambda_w^*\lambda_w - \eta_2\lambda_b^*\lambda_b + \lambda_w^*\lambda_b\right)], \tag{10.16a}$$

$$z = \frac{1}{a}[e^{-i(k_w-k_b)d}\left(\lambda_w^*\lambda_b^* - \gamma_b^2\lambda_w^*\lambda_w + \gamma_w^2\lambda_b^*\lambda_b - \lambda_w^*\lambda_b\right)$$
$$+ e^{-i(k_w+k_b)d}\left(\lambda_w^*\lambda_b + \gamma_b^2\lambda_w^*\lambda_w - \gamma_w^2\lambda_b^*\lambda_b - \lambda_w^*\lambda_b^*\right)], \tag{10.16b}$$

where $a = (\lambda_w^* + \lambda_w)(\lambda_b^* + \lambda_b)$, $\eta_1 = \gamma_b/\gamma_w$ and $\eta_2 = \gamma_w/\gamma_b$.

Correspondingly, the transfer matrix considering double barriers with an inter-distance s between them is

$$\mathcal{T}^{(2)} = \mathcal{M}_b(2d+s) \cdot \mathcal{M}_w(s+d)\mathcal{T}^{(1)}. \tag{10.17}$$

Thus, we can extend this result to N identical barriers which is given by the product of transfer matrices:

$$\mathcal{T}^{(N)} = \prod_{l=1}^{N} \mathcal{M}_b(l(d+s) - s) \cdot \mathcal{M}_w((l-1)(d+s)). \tag{10.18}$$

Once $\mathcal{T}^{(N)}$ is an unimodular matrix and the electron wave originates from the left of the system in Fig. 10.3, the transmission probability is obtained as $T = 1/|\mathcal{T}_{22}^{(N)}|^2$. After some algebraic calculations, we found the transmission probability through N barriers as

$$T = \frac{1}{1 + |z|^2 \left(\frac{\sin N\xi}{\sin \xi}\right)^2}, \tag{10.19}$$

where ξ corresponds to the Bloch wave-function of the whole system and is given by

$$\xi = \cos^{-1}[\mathbb{R}(w)\cos(k_w(d+s)) - \mathbb{C}(w)\sin(k_w(d+s))], \tag{10.20}$$

with z given by Eq. (10.16b), $\mathbb{R}(w)$ and $\mathbb{C}(w)$ correspond respectively to the real and imaginary terms of w in Eq. (10.16a).

10.5 Transmission of massless Dirac fermions

Initially, we consider the symmetry-breaking free case, i.e. taking $\hat{U}_i = 0$ in Eq. (10.10). The solution of $\hat{H}\Psi_j = E\Psi_j$ in this case leads to $\alpha_j = \gamma_j = \beta_j = 1$, as can be seen by comparing Eqs. (10.11) and Eqs. (10.2) for the wave-functions of the dispersion bands, and consequently, it implies $\eta_1 = \eta_2 = 1$ in Eq. (10.16a). Moreover, from the secular equation $\det(\hat{H} - E) = 0$ we obtain the wave-vectors in the $x-$direction in the well and barrier regions, k_w and k_b, respectively as

$$k_w = \sqrt{\left(\frac{E}{\hbar v_{\mathrm{F}}}\right)^2 - k_y^2} \quad , \quad k_b = \sqrt{\left(\frac{E - V_0}{\hbar v_{\mathrm{F}}}\right)^2 - k_y^2}, \tag{10.21}$$

with the eigenvalues in each region respectively given by

$$E = \pm\sqrt{\hbar^2 v_{\mathrm{F}}^2(k_w^2 + k_y^2)}, \tag{10.22a}$$

$$E - V_0 = \pm\sqrt{\hbar^2 v_{\mathrm{F}}^2(k_b^2 + k_y^2)}. \tag{10.22b}$$

Figure 10.4 shows the transmission probabilities using Eq. (10.19) for a single barrier as a function of the incident wave energy E and its transverse wave vector k_y for different values of the θ parameter: (a) $\theta = 0$, (b) $\theta = \pi/12$, (c) $\theta = \pi/6$, and (d) $\theta = \pi/4$. The potential height is set to $V_0 = 0.2$ eV and the barrier width is $d = 30$ nm. The possible non-null transmission regions in the $(k_y d, E/V_0)$ plane of Fig. 10.4 can be explained by identifying which modes are propagating inside and outside the potential barrier. The borders between these regions are indicated by dashed curves superimposed on the density plots, where the black and grey lines correspond to the energy spectrum outside and inside of the barrier which are given by Eqs. (10.22a) and (10.22b), respectively. Since wave-functions interfere inside the barrier, we observe for all values of θ when $E/V_0 < 1$ the appearance of resonance peaks marked by $T = 1$. In addition, when the incoming wave-function is perpendicular to the barrier, i.e. $k_y d = 0$, the transmission is total

Figure 10.4: Transmission probability through a single-barrier in the $(k_y, E/V_0)$ plane for (a) $\theta = 0$ (graphene-like), (b) $\theta = \pi/12$, (c) $\theta = \pi/6$, and (d) $\theta = \pi/4$ (dice) in the symmetry-breaking free case ($\hat{U} = 0$) for barrier height and width assumed as $V_0 = 0.2$ eV and $d = 30$ nm, respectively.

and the barrier is completely transparent regardless of the potential width and height. This perfect transmission at normal incidence is a consequence of the conservation of the pseudo-spin at scattering on the barrier which results in the absence of backscattering of wave-functions, an effect referred as KT which has been noted previously for the two limiting cases $\theta = 0$ [78] and $\theta = \pi/4$ [96].

We note that for $0 < E/V_0 < 0.5$ sharp resonances in the transmission probabilities become softer and less pronounced as θ increases, leading to a general enhancement trend of transmission probability for $\theta \neq 0$. This result is more evident in Fig. 10.5, which shows the transmission probability in the $(\phi_w, E/V_0)-$plane. We observe the broadening of transmission as θ increases in the energy region $0 < E/V_0 < 0.5$, indicating that the barrier becomes more transparent, as depicted in Fig. 10.6(a) for a fixed energy $E/V_0 = 0.25$. Furthermore, the special case $\theta = \pi/4$ (dice) at $E/V_0 = 0.5$ the barrier becomes fully transparent leading to an omnidirectional total transmission, as observed in Fig. 10.5(d) and Fig. 10.6(b) and discussed in Refs. [96, 98].

However, as shown in Fig. 10.5 when the energy of incoming waves is $0.5 < E/V_0 < 1$

Figure 10.5: Contour plot of transmission probability through a single-barrier in the $(\phi_w, E/V_0)$ plane for (a) $\theta = 0$ (graphene-like), (b) $\theta = \pi/12$, (c) $\theta = \pi/6$, and (d) $\theta = \pi/4$ (dice) for the same potential parameters as in Fig. 10.4.

for all values of θ there is a reduction of the transmission probability with increasing incident energy and the transmission curves almost coincide, indicating that, analogously to the total reflection effect observed in optics, there is an incident critical angle such that above it the incident wave-function is fully reflected and an evanescent wave-function is found inside the potential. This angle is determined from the conservation of momentum in the y direction

$$\sin \phi_k = \frac{V_0 - E}{E} \sin \phi_q. \tag{10.23a}$$

Since the condition for total reflection of incoming wave-function is $\sin \phi_q = 1$, the incident critical angle ϕ_{kc} is determined by

$$\sin \phi_{kc} = \frac{V_0 - E}{E}. \tag{10.24}$$

Note that the critical angles do not depend on the parameter θ, and the transmission probabilities are almost the same for $E/V_0 > 0.5$ regardless of θ.

From Eq. (10.19) we analyze the effects of the number N of barriers on the transmission probabilities in the $(\phi_w, E/V_0)$−plane. The results for transmission assuming $N = 2$ and

Figure 10.6: Transmission probability through a single-barrier as function of incident angle ϕ_w at incident energy values (a) $E/V_0 = 0.25$, and (b) $E/V_0 = 0.5$ for $\theta = 0$ (solid black curve), $\theta = \pi/12$ (dotted magenta curve), $\theta = \pi/6$ (dashed red curve), and $\theta = \pi/4$ (dash-dotted blue curve) assuming the same potential parameters as in Fig. 10.4.

$N = 6$ are depicted in Figs. 10.7 and 10.8, respectively. For all these cases the inter-barrier distance is 30 nm. One notices more resonance peaks in the transmission as the number of barriers increases as a consequence of the fact that the wave-function interferes more with itself inside the barriers. Beside that, a perfect transmission $T = 1$ for normal or near-normal incidence is observed, which is a signature of the KT. Unlike graphene-like and for intermediate values of θ, the increase in the number of barriers is much less effective for dice when $0 < E/V_0 < 1$ and the SKT at $E/V_0 = 0.5$ is still observed regardless the number of barriers, as shown in Figs. 10.7(d) and 10.8(d). However, for incident energies $E/V_0 > 1$ and $E/V_0 < 0$ the effect of the number of barriers in the transmission is evident for all values of θ.

Moreover, like the single-barrier case and for $0 < E/V_0 < 0.5$, as θ increases there is a broadening of the transmission resonant peaks. Since the increase of the number of barriers does not affect the nature of pseudo-spin, which depends only on the crystal structure, the KT and the SKT, beside the enhancement of transmission as θ increases, are maintained regardless the number of barriers.

10.6   Symmetry-breaking effects into the tunneling properties

As discussed in Sec. 10.3, within the low-energy approach, the presence of small deviations in the equivalence of the atoms generate a band-gap in the energy spectrum resulting in charge carriers that are described as massive Dirac fermions. Now, we shall discuss the
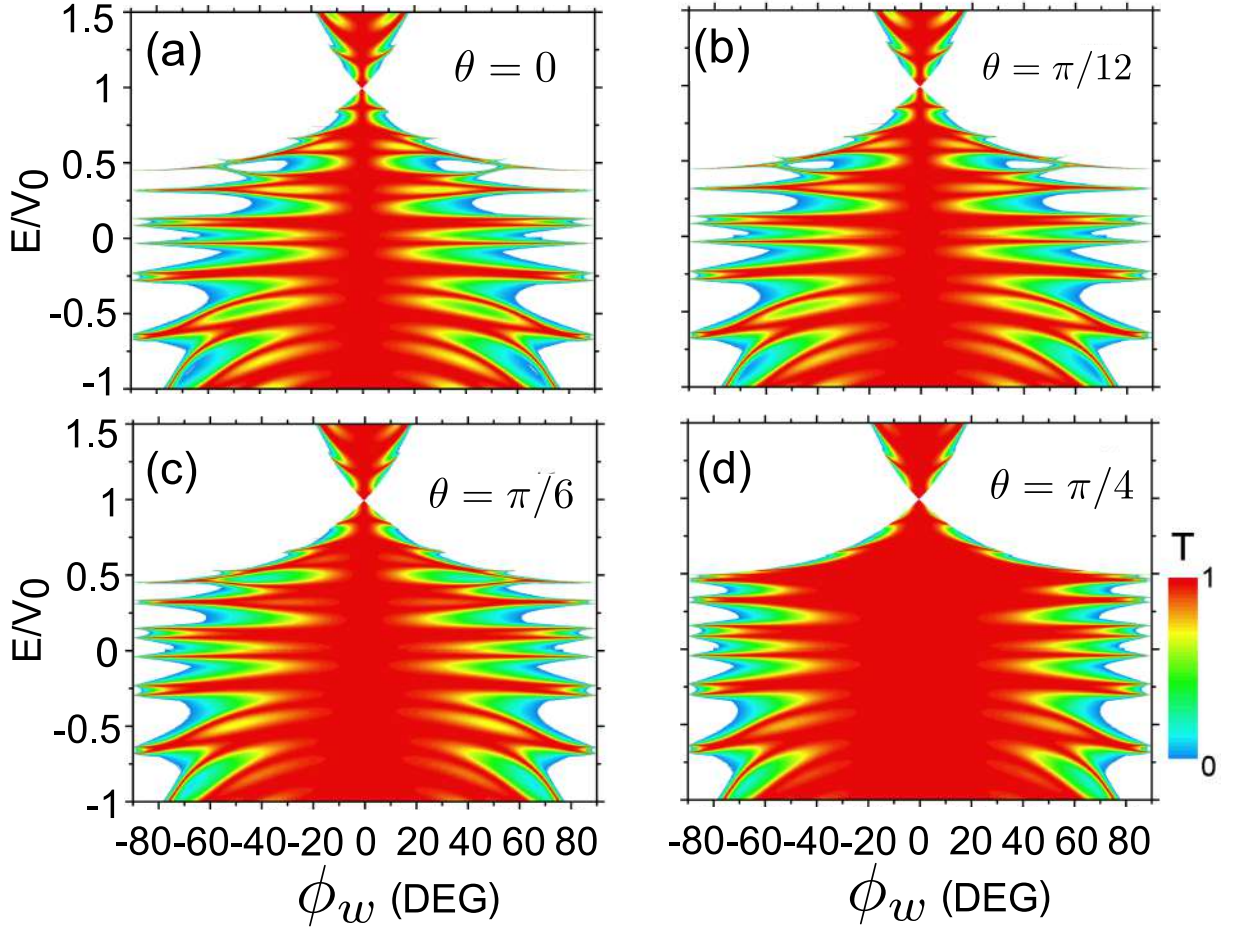
Figure 10.7: Contour plot of transmission probability, shown in the $(\phi_w, E/V_0)$ plane, through a double-barrier ($N = 2$) for (a) $\theta = 0$ (graphene-like), (b) $\theta = \pi/12$, (c) $\theta = \pi/6$, and (d) $\theta = \pi/4$ (dice) for the same potential parameters as in Fig. 10.5 and with a inter-barrier distance of 30 nm.

tunneling properties of those massive fermions in $\alpha - T_3$ lattices under the presence of single and multiple barriers by considering the symmetry-breaking terms $\hat{U}_1$ and $\hat{U}_2$ given by Eq. (10.5).

10.6.1   Case $\hat{U} = \hat{U}_1$

Assuming $\hat{U} = \hat{U}_1$ in Eq. (10.10), we obtain the wave-functions expressed in Eq. (10.11) in the barrier and well regions with $\alpha_w = \beta_w = \sqrt{E + \Delta}, \alpha_b = \beta_b = \sqrt{E - V_0 + \Delta}, \gamma_w = \sqrt{E - \Delta}$, and $\gamma_b = \sqrt{E - V_0 - \Delta}$. The wave-vectors in the $x-$direction inside and outside of the barrier are

$$k_w = \sqrt{\frac{E^2 - \Delta^2}{\hbar^2 v_{\mathrm{F}}^2} - k_y^2}, \tag{10.25a}$$

$$k_b = \sqrt{\frac{(E - V_0)^2 - \Delta^2}{\hbar^2 v_{\mathrm{F}}^2} - k_y^2}. \tag{10.25b}$$
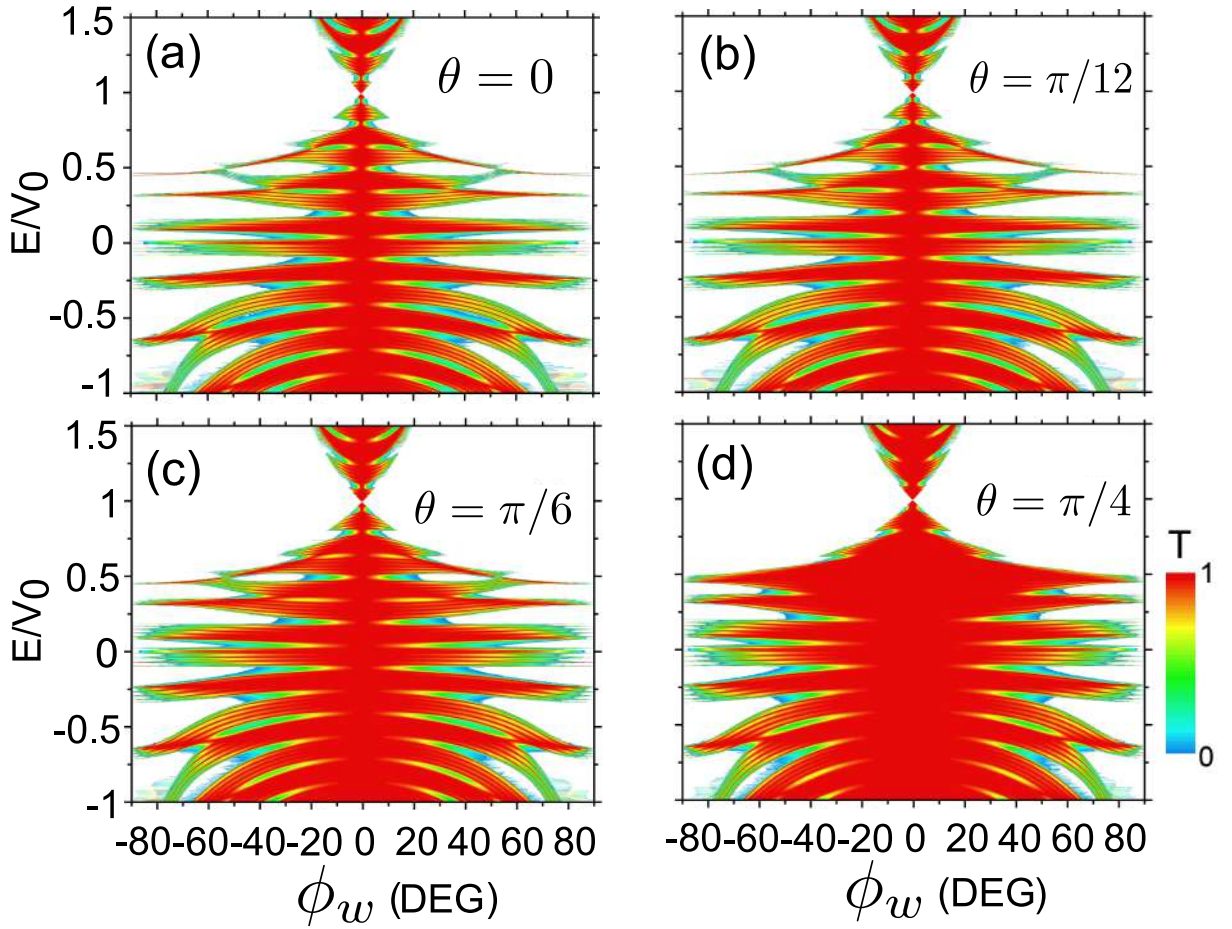
Figure 10.8: The same as Fig. 10.7, but now for $N = 6$ barriers.

The transmission probability is given by Eq. (10.19), and the terms η_1 and η_2 in Eq. (10.16a) are

$$\eta_1 = \sqrt{\frac{(E + \Delta)(E - V_0 - \Delta)}{(E - V_0 + \Delta)(E - \Delta)}}, \tag{10.26a}$$

$$\eta_2 = \sqrt{\frac{(E - \Delta)(E - V_0 + \Delta)}{(E - V_0 - \Delta)(E + \Delta)}}. \tag{10.26b}$$

The transmission probabilities for single-barrier as function of $(k_y d, E/V_0)$, assuming $V_0 = 0.2$ eV, $d = 30$ nm, and $\Delta = 0.04$ eV for different values of θ are shown in Fig. 10.9. The non-zero transmission zones are bounded by the energy levels inside and outside of barrier, corresponding to the grey and black dashed curves, respectively. It is clearly seen that the presence of the sublattice symmetry-breaking induced band-gap in the energy spectrum lead to a suppression of the transmission for all values of the parameter θ, as well as the "fishbone" transmission shape in the energetic region $\Delta < E < 4\Delta$ is suppressed. Beside, the conservation of chirality does not take place due to the introduction of small deviation in the equivalence between the atoms and total transmission for normal or near-normal incident angles, or equivalently smaller $k_y d$, is no longer observed indicating that for all values of θ KT is destroyed, as depicted in Figs. 10.9 and 10.10.
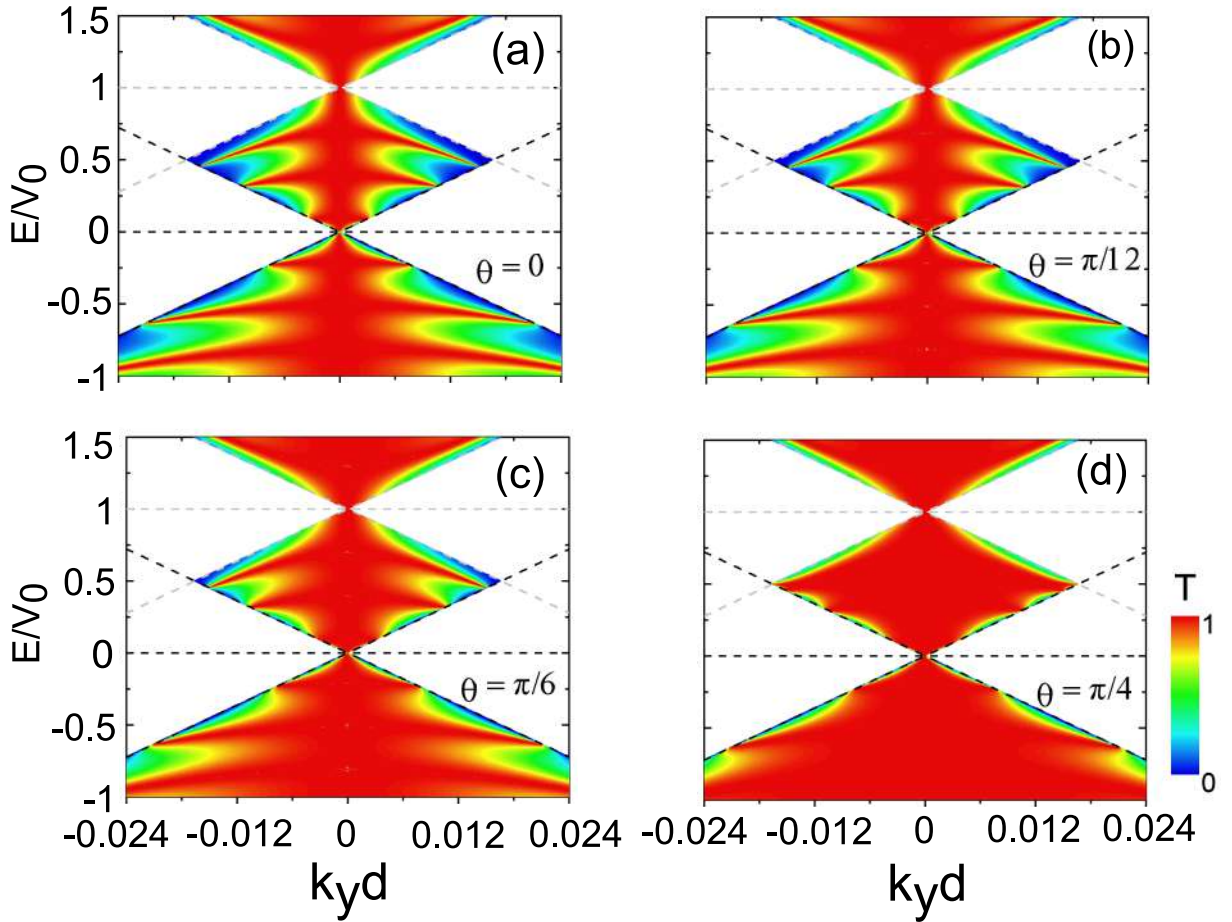
Figure 10.9: Transmission probability through a single-barrier in the $(k_y, E/V_0)$ plane for (a) $\theta = 0$ (graphene-like), (b) $\theta = \pi/12$, (c) $\theta = \pi/6$, and (d) $\theta = \pi/4$ (dice) by assuming the symmetry-breaking term as $\hat{U} = \hat{U}_1$, with sublattice unbalance strength $\Delta = 0.04$ eV, for barrier height $V_0 = 0.2$ eV and width $d = 30$ nm.

However, while the KT is no longer observed, from Fig. 10.9(d) one notices perfect transmission when $\theta = \pi/4$ at $0 < E/V_0 < 0.5$ for large $k_y d$ values, or equivalently for large incident angles as shown in Fig. 10.10(d). In fact, when θ is tuned from the correspondent value of graphene-like to dice at incident energy $E/V_0 = 0.25$ the transmission curves tend to exhibit a completely opposite feature: incident waves nearly parallel to the barrier are completely transmitted, as shown in Fig. 10.11(a). On the other hand, for $\theta = 0$ and oblique incident angles at incident energy $E/V_0 = 0.5$ there is a narrow resonance peak which widens as θ increases, whereas for dice lattice beyond the broadening of this peak a new total transmission peak appears for incident angles parallel to the barrier as noticed in Fig. 10.11(b).

Figure 10.12 shows the transmission contour plots considering now double-barrier systems with the same width and potential height used in single-barrier case and an interdistance barrier of 30 nm. Comparing to Fig. 10.10, we observe that beyond total reflection of waves for smaller incident angles at $E/V_0 = 0.5$, the energy scale where there is non-
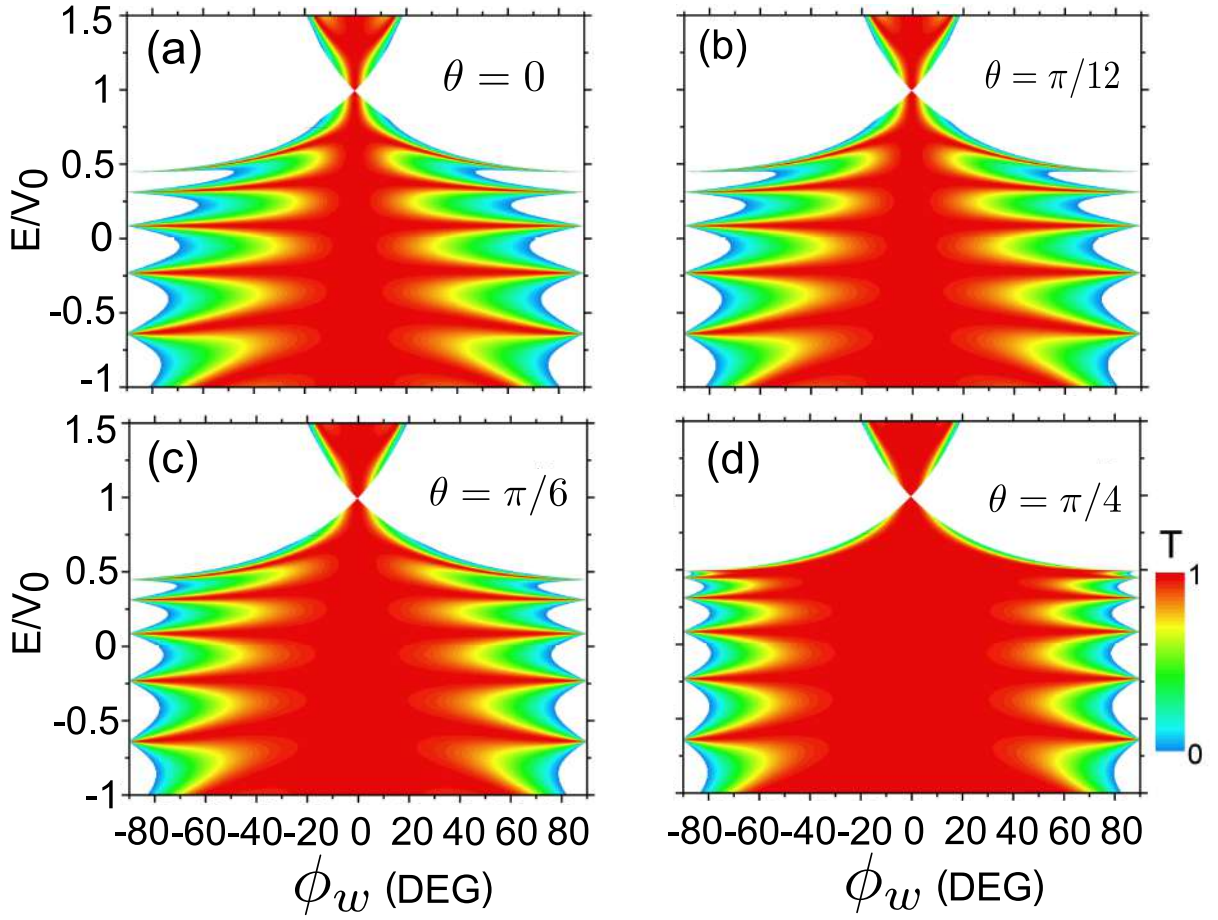
Figure 10.10: Contour plot of transmission probability through a single-barrier in the $(\phi_w, E/V_0)$ plane for (a) $\theta = 0$ (graphene-like), (b) $\theta = \pi/12$, (c) $\theta = \pi/6$, and (d) $\theta = \pi/4$ (dice) for the same system parameters as in Fig. 10.9.

null transmission is reduced and for graphene-like and intermediate values of θ there is no transmission at incident energies close to the value of Δ, i.e $E/V_0 = 0.2$. Nonetheless, for dice lattice the perfect transmission of waves near-parallel or parallel to barriers is still observed in the range $E/V_0 \in [0.2, 0.5]$ and for energies immediately above the potential energy, i.e. $1.2 < E/V_0 < 1.3$ a peak of transmission occurs for critical incident angle, like in the single-barrier case. This result is clear when we analyse the transmission curves in Fig. 10.13 for incident energies $E/V_0 = 1.3$ for single and double-barriers. While for $\theta = \pi/4$ and $N = 1$ there is a peak of total transmission for incident angles around $\pm 10°$, which corresponds to the critical angle for this value of incident energy. For the other values of θ the transmission is reduced and falls to zero. Moreover, when $N = 2$, beyond the peak of total transmission for dice, there is a peak of almost-total transmission for $\theta = \pi/6$.

The perfect transmission at large values of $k_y d$, or incident angles parallel and near-parallel to the barrier, for $\theta = \pi/4$ is explained when we analyse Fig. 10.14(a), where we depict the electronic band structure along $k_y d$ direction of a system consisting of an infinite
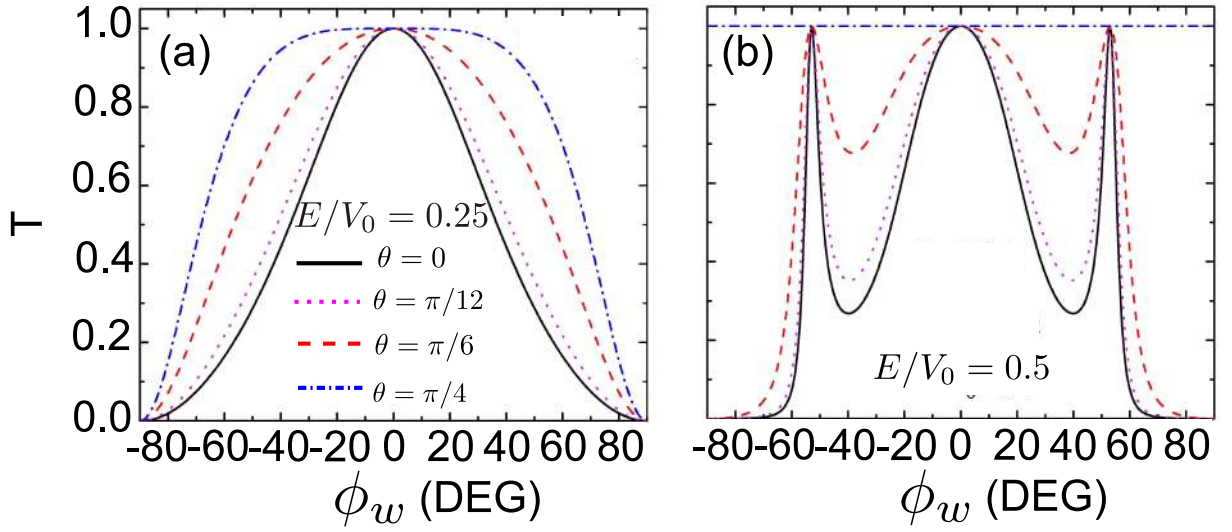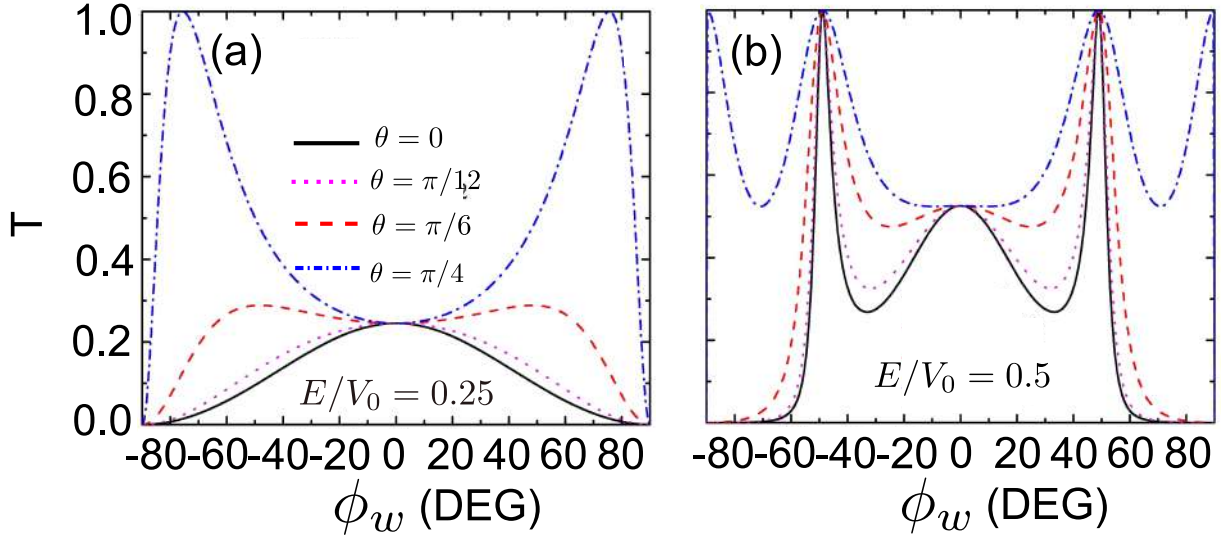
Figure 10.11: Transmission probability through a single-barrier as function of incident angle ϕ_w at incident energy values (a) $E/V_0 = 0.25$ and (b) $E/V_0 = 0.5$ for $\theta = 0$ (solid black curve), $\theta = \pi/12$ (dotted magenta curve), $\theta = \pi/6$ (dashed red curve), and $\theta = \pi/4$ (dash-dotted blue curve) for the same system parameters as in Fig. 10.9.

number of barriers with the same parameters of potential height, width and inter-barrier distance used in Fig. 10.12. We note that for energies at the interval $0.2 < E/V_0 < 0.5$ the mini-bands touch each other at large values of $k_y d$, indicating the presence of degenerate states, which is represented by prominent peaks in the density of states (DOS) in the same energetic range in Fig. 10.14(b). Therefore, since more allowed energy states arise, an enhancement of the transmission probability of electrons under these initial conditions of momentum and energy is observed.

10.6.2   Case $\hat{U} = \hat{U}_2$

For the other symmetry-breaking term denoted by $\hat{U} = \hat{U}_2$ in Eq. (10.10), we have $\alpha_w = \sqrt{(E + 3\Delta)/(E - \Delta)}$, $\alpha_b = \sqrt{(E - V_0 + 3\Delta)/(E - V_0 - \Delta)}$, $\gamma_w = \sqrt{(E + \Delta\cos(2\theta) + 2\Delta\cos^2}$ $\gamma_b = \sqrt{(E - V_0 + \Delta\cos(2\theta) + 2\Delta\cos^2\theta)/(E - V_0 + \Delta)}$, $\beta_w = \sqrt{E - \Delta/(E + 3\Delta)}$, and $\beta_b = \sqrt{E - V_0 - \Delta/(E - V_0 + 3\Delta)}$.

Consequently, the wave-vectors k_w and k_b are given by

$$k_w = \sqrt{\frac{(E^2 - \Delta^2)(E + 3\Delta)}{\hbar^2 v_{\mathrm{F}}^2(E + \Delta\cos 2\theta + 2\Delta\cos^2\theta)} - k_y^2}, \tag{10.27a}$$

$$k_b = \sqrt{\frac{((E - V_0)^2 - \Delta^2)(E - V_0 + 3\Delta)}{\hbar^2 v_{\mathrm{F}}^2(E - V_0 + \Delta\cos 2\theta + 2\Delta\cos^2\theta)} - k_y^2}. \tag{10.27b}$$

For this case, the transmission of fermions through N one-dimensional barriers is
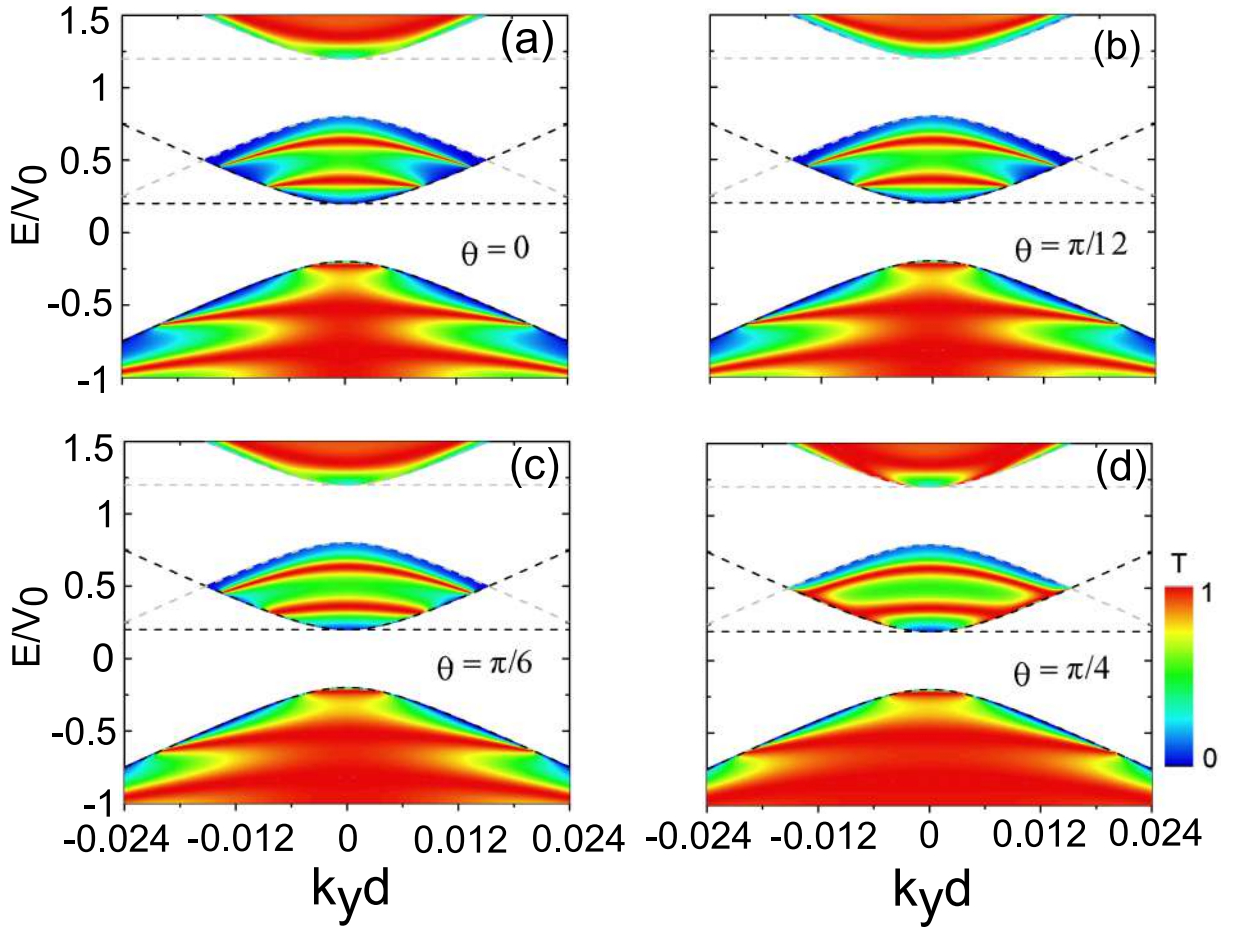
Figure 10.12: Contour plot of transmission probability through a double-barrier in the $(\phi_w, E/V_0)$ plane for (a) $\theta = 0$ (graphene-like), (b) $\theta = \pi/12$, (c) $\theta = \pi/6$, and (d) $\theta = \pi/4$ (dice) when $\hat{U} = \hat{U}_1$, $V_0 = 0.2$ eV, $\Delta = 0.04$ eV, $d = 30$ nm, and an inter-barrier distance $s = 30$ nm.

obtained using Eq. (10.19) with η_1 and η_2 in Eq. (10.16a) given by

$$\eta_1 = \sqrt{\left[\frac{E - V_0 + \Delta \cos 2\theta + 2\Delta \cos^2 \theta}{E + \Delta \cos 2\theta + 2\Delta \cos^2 \theta}\right]} \eta_{12}, \qquad (10.28a)$$

$$\eta_2 = \sqrt{\left[\frac{E + \Delta \cos 2\theta + 2\Delta \cos^2 \theta}{E - V_0 + \Delta \cos 2\theta + 2\Delta \cos^2 \theta}\right]} \eta_{21}, \qquad (10.28b)$$

with $\eta_{12} = \frac{E + \Delta}{E - V_0 + \Delta}$ and $\eta_{21} = \frac{E - V_0 + \Delta}{E + \Delta}$. The transmission probabilities as function of $(k_y d, E/V_0)$ for this case are depicted in Fig. 10.15. Similar to previous cases, the zones where waves are able to propagate and therefore the transmission is non-null are bounded by the energy levels inside and outside of the barrier indicated by the grey and black dashed curves superimposed on the transmission contour plot. As observed in Figs. 10.2(a) and 10.2(b), the energy spectrum for both symmetry-breaking terms $\hat{U}_1$ and $\hat{U}_2$ for $\theta = 0$ differs only by the position of the flat band maintaining the conduction and valence bands with the same dispersion and position. Since the dispersionless bands do not contribute
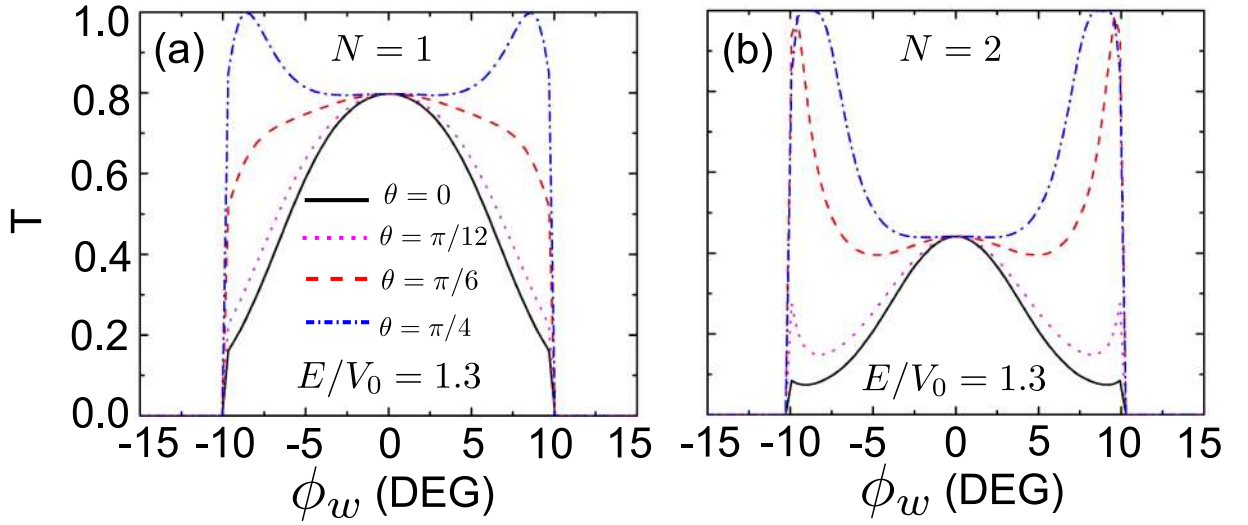
Figure 10.13: Transmission probability through a (a) single-barrier ($N = 1$) and (b) double-barrier ($N = 2$) as function of incident angle ϕ_w at incident energy $E/V_0 = 1.3$ for $\theta = 0$ (solid black curve), $\theta = \pi/12$ (dotted magenta curve), $\theta = \pi/6$ (dashed red curve), and $\theta = \pi/4$ (dash-dotted blue curve) for the same system parameters as in Fig. 10.9 and an inter-barrier distance of 30 nm for double-barrier system.
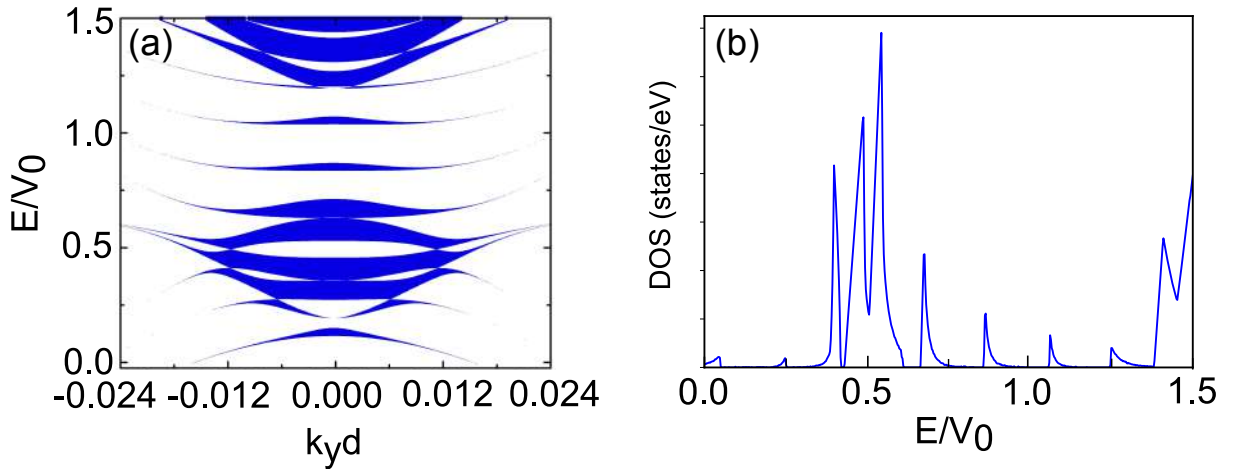
Figure 10.14: (a) Electronic band structure along the $k_y d$ direction for $\theta = \pi/4$ (dice case) superlattices taking the same system parameters as in Fig. 10.12. (b) The corresponding DOS of (a) is shown.

to the transmission, the effects observed in the tunneling properties for both symmetry-breaking terms for $\theta = 0$ are similar, as noticed when we compare Fig. 10.15(a) and Fig. 10.9(a). However, for $\theta \neq 0$ the transmission contour plots are quite different from the previous gapped case, as depicted in Figs. 10.15(b)-10.15(d). We note that for incident energies $0 < E/V_0 < 1$ depending on θ new zones where there is no propagation of waves appear in the $(k_y, E/V_0)$ plane. To understand this result we plot in Fig. 10.16 a diagram for the wave-vector k_b inside the barrier using the relation given in Eq. (10.27a) for the
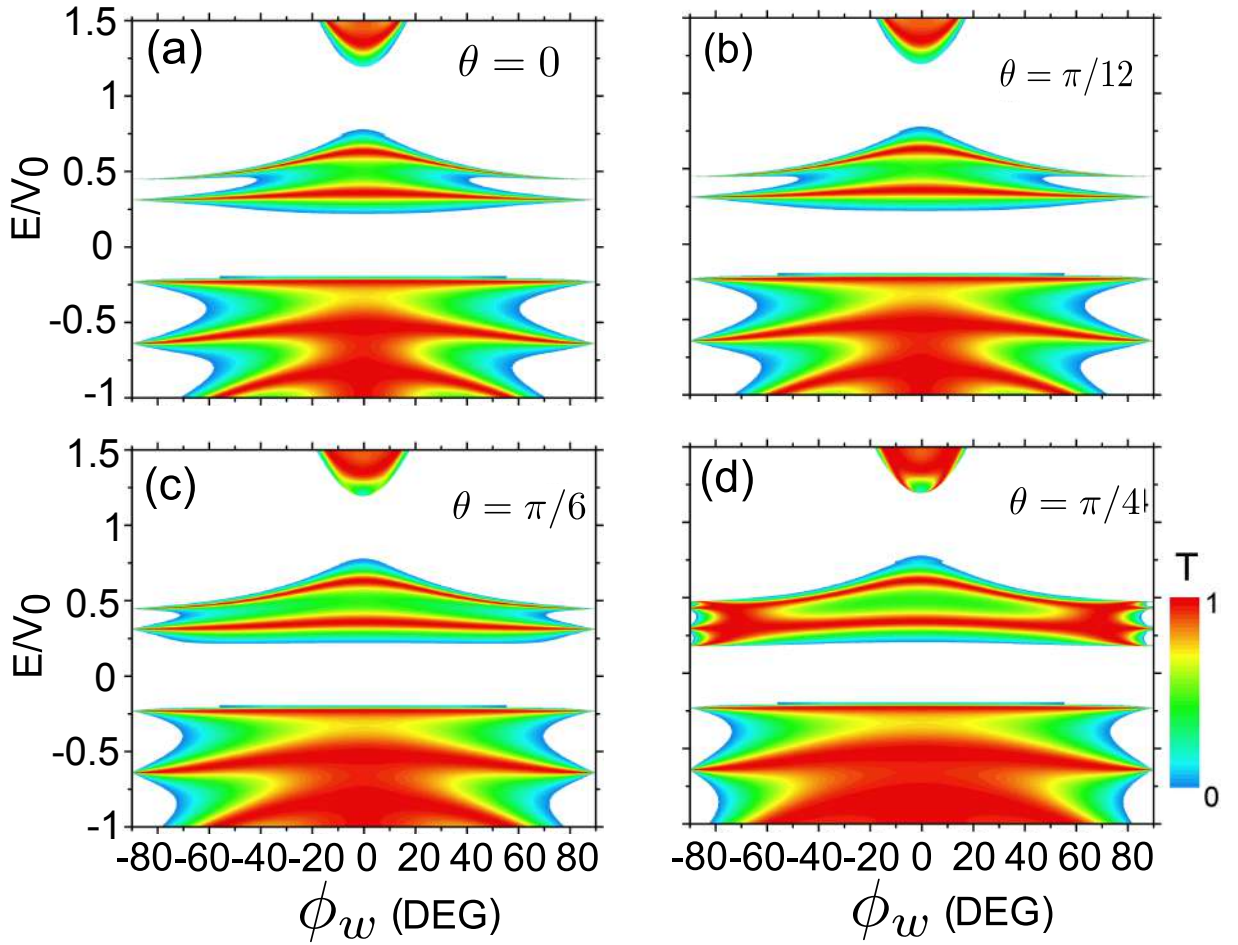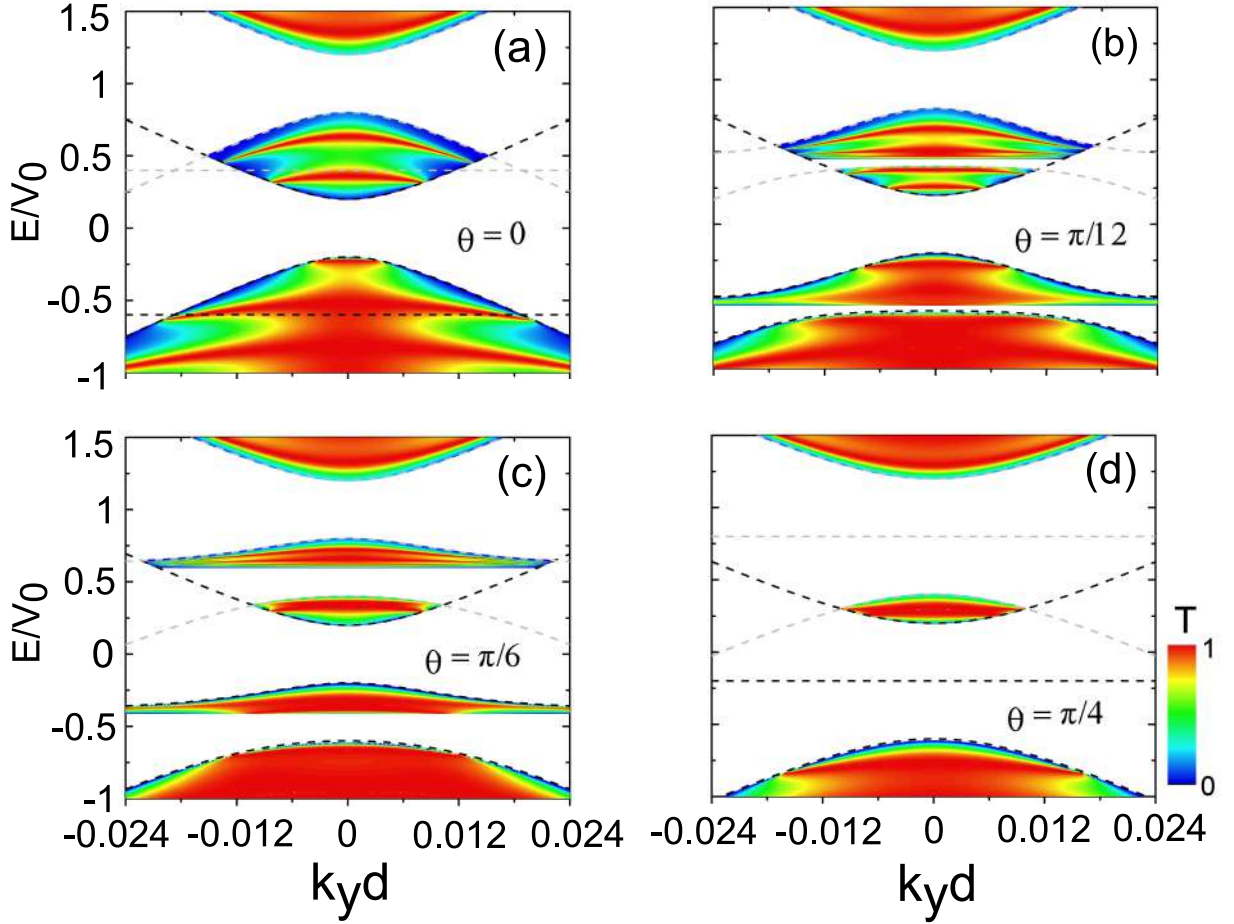
Figure 10.15: Transmission probability through a single-barrier in the $(k_y, E/V_0)$ plane for (a) $\theta = 0$ (graphene-like), (b) $\theta = \pi/12$, (c) $\theta = \pi/6$, and (d) $\theta = \pi/4$ (dice) when $\hat{U} = \hat{U}_2$, $V_0 = 0.2$ eV, $\Delta = 0.04$ eV, and $d = 30$ nm.

same parameters used in Fig. 10.15. The blue zones indicate where the transmission is due to propagating waves, i.e. k_b is real, in that case the incoming waves might interfere with itself between the two interfaces of barrier-well, leading to the transmission resonances.

When k_b is purely imaginary, indicated by the grey zone in the phase diagram, the transmission is still possible via evanescent waves but with a reduced amplitude. Furthermore, the condition to have an evanescent wave is determined by the incident critical angle, so from the conservation of momentum in the y direction and using Eq. (10.27) we get the expression of a critical incident angle ϕ_{kc}

$$\sin \phi_{kc} = \sqrt{E_\theta \left[\frac{((E - V_0)^2 - \Delta^2)(E - V_0 + 3\Delta)}{(E^2 - \Delta^2)(E + 3\Delta)} \right]}, \tag{10.29}$$

where

$$E_\theta = \frac{(E + \Delta \cos 2\theta + 2\Delta \cos^2 \theta)}{(E - V_0 + \Delta \cos 2\theta + 2\Delta \cos^2 \theta)}. \tag{10.30}$$

According to Eq. (10.29) and as shown in Fig. 10.17, unlike the gapless and previous
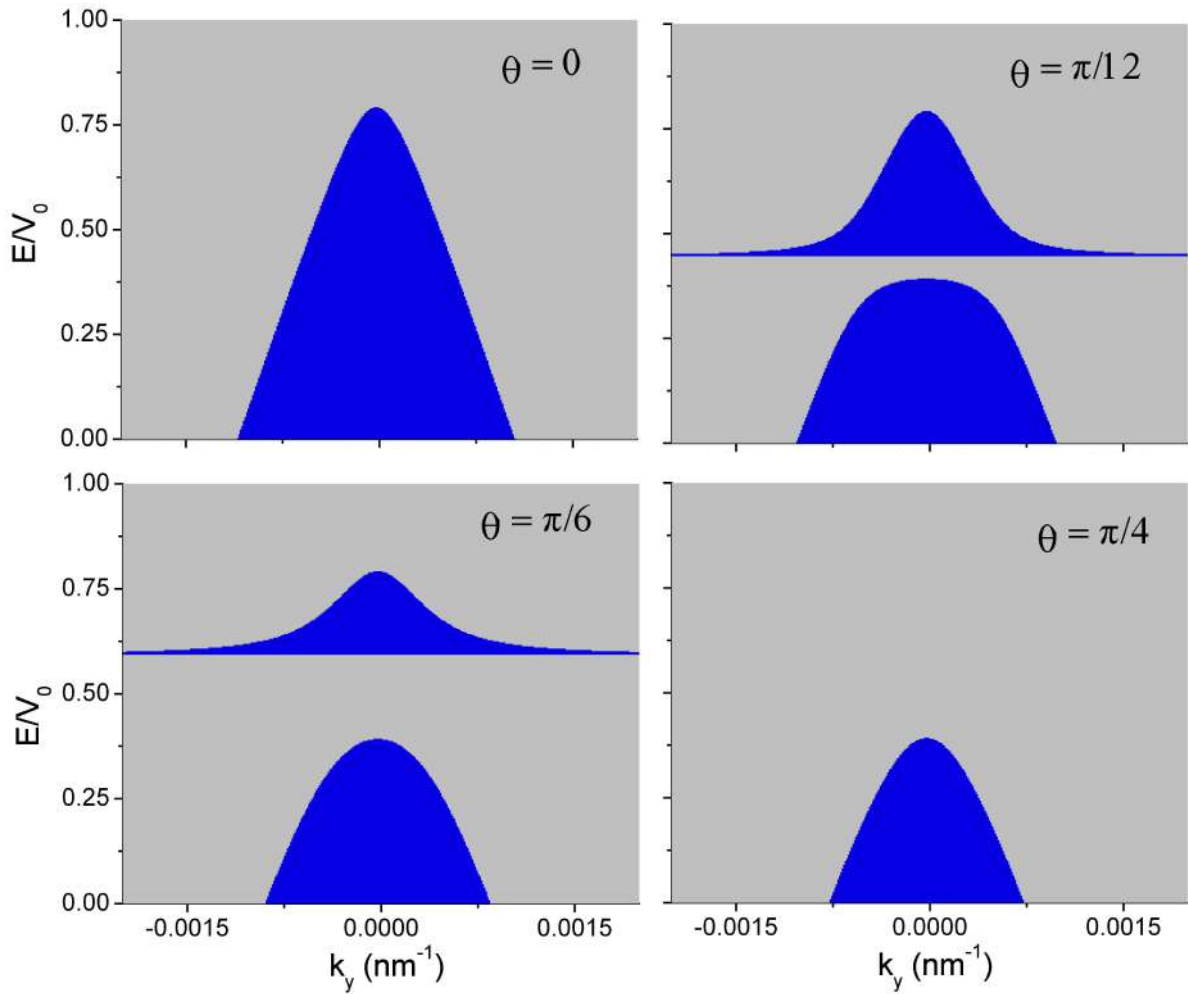
Figure 10.16: Diagram obtained from the relation given in Eq. (10.27a) representing the wave nature inside the barrier plotted in the $(k_y, E/V_0)$ plane for (a) $\theta = 0$ (graphene-like), (b) $\theta = \pi/12$, (c) $\theta = \pi/6$, and (d) $\theta = \pi/4$ (dice) when $\hat{U} = \hat{U}_2$, $\Delta = 0.04$ eV, $V_0 = 0.2$ eV, and $d = 30$ nm. The blue area is the zone of propagating waves corresponding to a real wave-vector k_b, the grey area is the zone where k_b is purely imaginary indicating evanescent waves.

gapped case, the critical incident angle for transmission and consequently the condition for evanescent or propagating waves depends on the value of θ, indicating the appearance of new transmission zones as θ is tuned from graphene-like to dice.

In Fig. 10.17 we observe at $E/V_0 = 0.25$ that while the transmission probability is nearly perfect for $\theta = \pi/12$ and $\theta = \pi/4$, for $\theta = \pi/6$ it becomes smaller, as shown in Fig. 10.18(a). In addition, in Fig. 10.18(b) we note that there is no transmission for $\theta = \pi/6$ and $\theta = \pi/4$ at $E/V_0 = 0.5$, since under these conditions the incident waves are evanescent and localized into the grey zone in the phase diagram in Fig. 10.16(c) and Fig. 10.16(d), respectively.

Furthermore, for double-barrier systems assuming graphene-like and intermediate values of θ, the transmission is in general reduced for large incident angles and there are
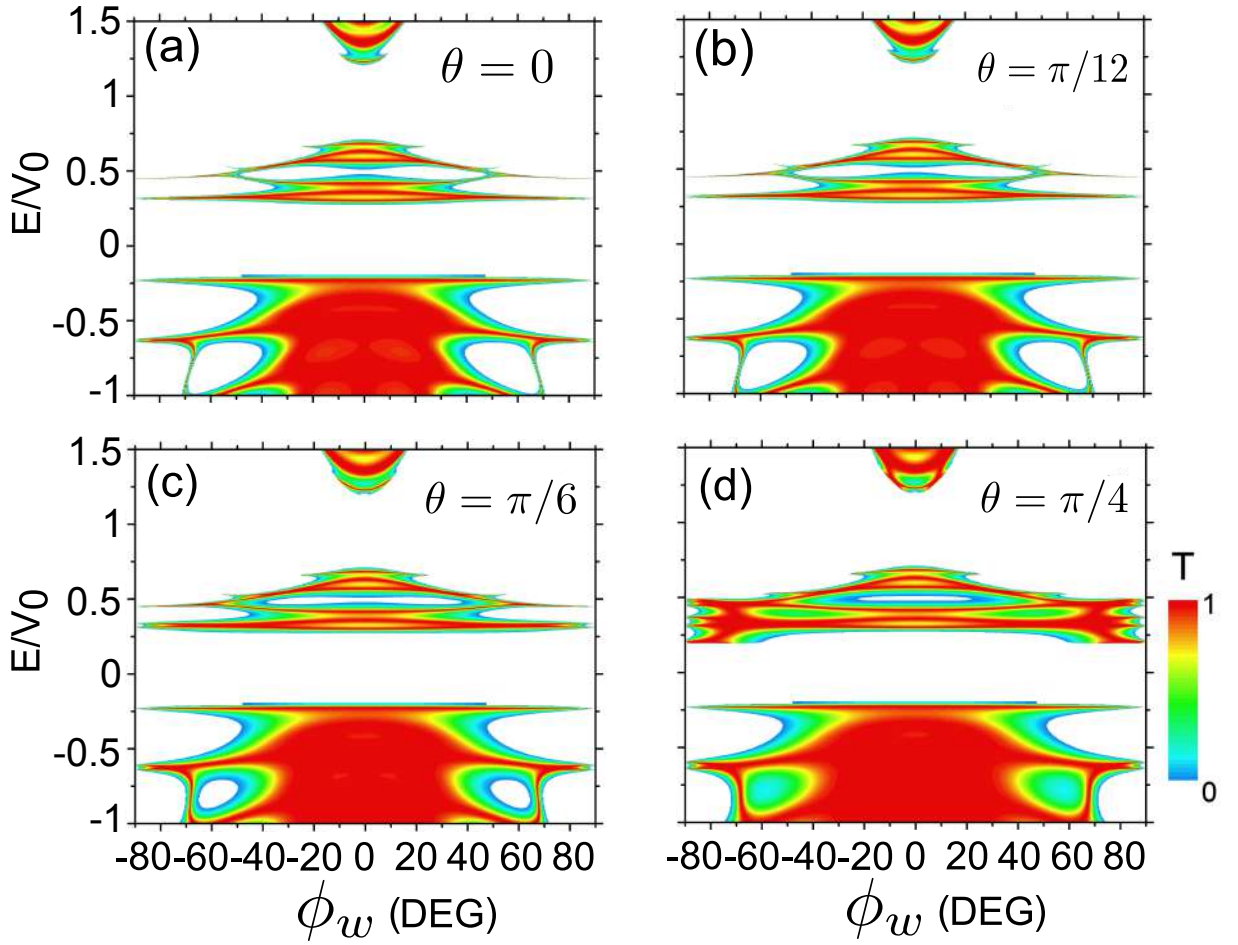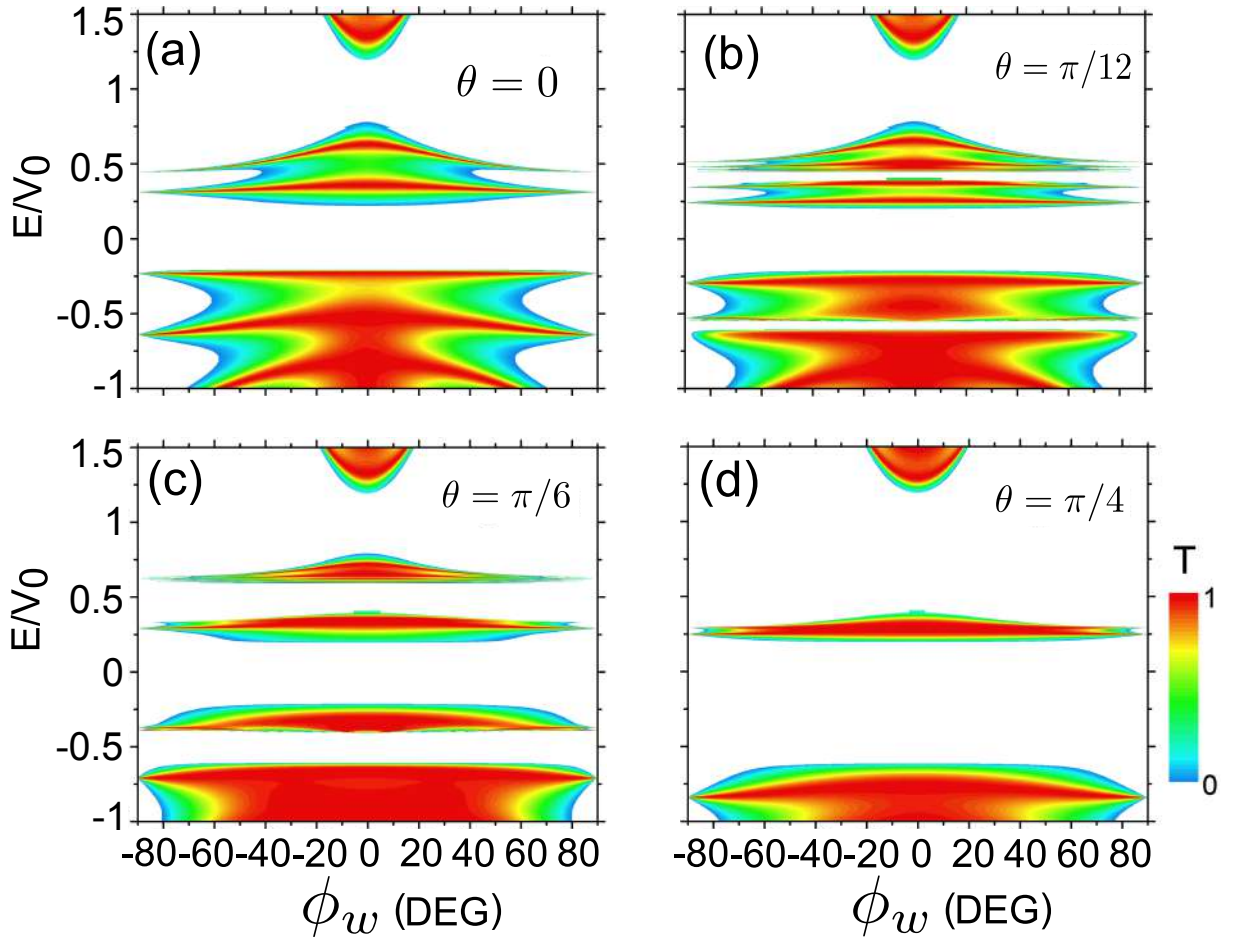
Figure 10.17: Contour plot of transmission probability through a single-barrier in the $(\phi_w, E/V_0)$ plane for (a) $\theta = 0$ (graphene-like), (b) $\theta = \pi/12$, (c) $\theta = \pi/6$, and (d) $\theta = \pi/4$ (dice) when $\hat{U} = \hat{U}_2$, $V_0 = 0.2$ eV, $\Delta = 0.04$ eV, and $d = 30$ nm.

more resonant peaks, as shown in Fig. 10.19. However, for dice lattice we observe the enhancement of the transmission, which is almost perfect for all values of incident energy $0.2 < E/V_0 < 0.4$ and large values of incident angle, as shown in Fig. 10.19(d).

10.7 Tunneling through spatial regions of finite mass

Now we investigate the tunneling properties of electrons in $\alpha - T_3$ lattices when we assume a region where the electronic spectrum changes from the usual linear dispersion to a hyperbolic dispersion, due to the presence of a gap originating from the presence of the symmetry-breaking term $\hat{U}_1$, as depicted in Fig. 10.20. The transmission expression is obtained in a similar way as in previous section. The wave-function $\Psi(x)$ corresponding
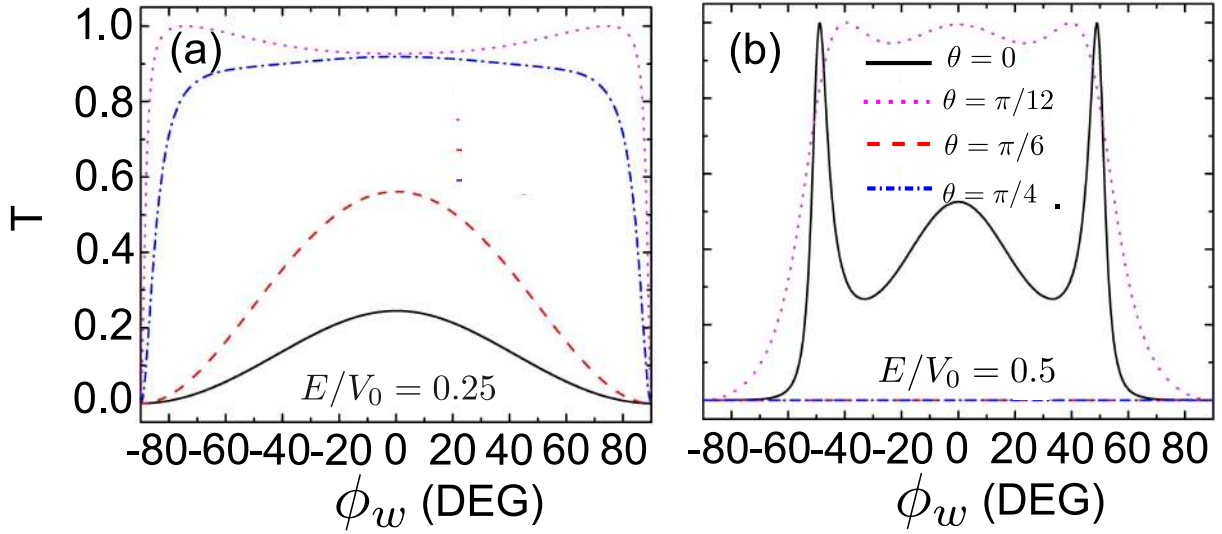
Figure 10.18: Transmission probability through a single-barrier as function of incident angle ϕ_w at incident energy values (a) $E/V_0 = 0.25$, and (b) $E/V_0 = 0.5$ for $\theta = 0$ (solid black curve), $\theta = \pi/12$ (dotted magenta curve), $\theta = \pi/6$ (dashed red curve), and $\theta = \pi/4$ (dash-dotted blue curve) when $\hat{U} = \hat{U}_2$, $V_0 = 0.2$ eV, $\Delta = 0.04$ eV, and $d = 30$ nm.

to eigenstates with linear dispersion in region I and III depicted in Fig. 10.20 is

$$\psi(x)_{I,III} = \frac{A}{\sqrt{2}} \begin{pmatrix} \cos\theta e^{i\phi_k} \\ 1 \\ \sin\theta e^{-i\phi_k} \end{pmatrix} e^{ik_x x} + $$
$$\frac{B}{\sqrt{2}} \begin{pmatrix} -\cos\theta e^{-i\phi_k} \\ 1 \\ -\sin\theta e^{i\phi_k} \end{pmatrix} e^{-ik_x x}. \tag{10.31}$$

Consequently, the wave-function in region II corresponding to the hyperbolic and gapped energy spectrum at $0 \leq x \leq d$ is given by

$$\psi_{II}(x) = \frac{A'}{\sqrt{2}} \begin{pmatrix} \alpha\cos\theta e^{i\phi_q} \\ \gamma \\ \alpha\sin\theta e^{-i\phi_q} \end{pmatrix} e^{iq_x x} + $$
$$\frac{B'}{\sqrt{2}} \begin{pmatrix} -\alpha\cos\theta e^{-i\phi_q} \\ \gamma \\ -\alpha\sin\theta e^{i\phi_q} \end{pmatrix} e^{-iq_x x}, \tag{10.32}$$

The incident angles into the different regions with linear dispersion and band-gap are $\phi_k = \tan^{-1} k_y/k_x$ and $\phi_q = \tan^{-1} k_y/q_x$, respectively, with momentum along the $x-$ direction given by

$$k_x = \sqrt{\frac{E^2}{\hbar^2 v_{\rm F}^2} - k_y^2}, \qquad q_x = \sqrt{\frac{E^2 - \Delta^2}{\hbar^2 v_{\rm F}^2} - k_y^2}. \tag{10.33}$$
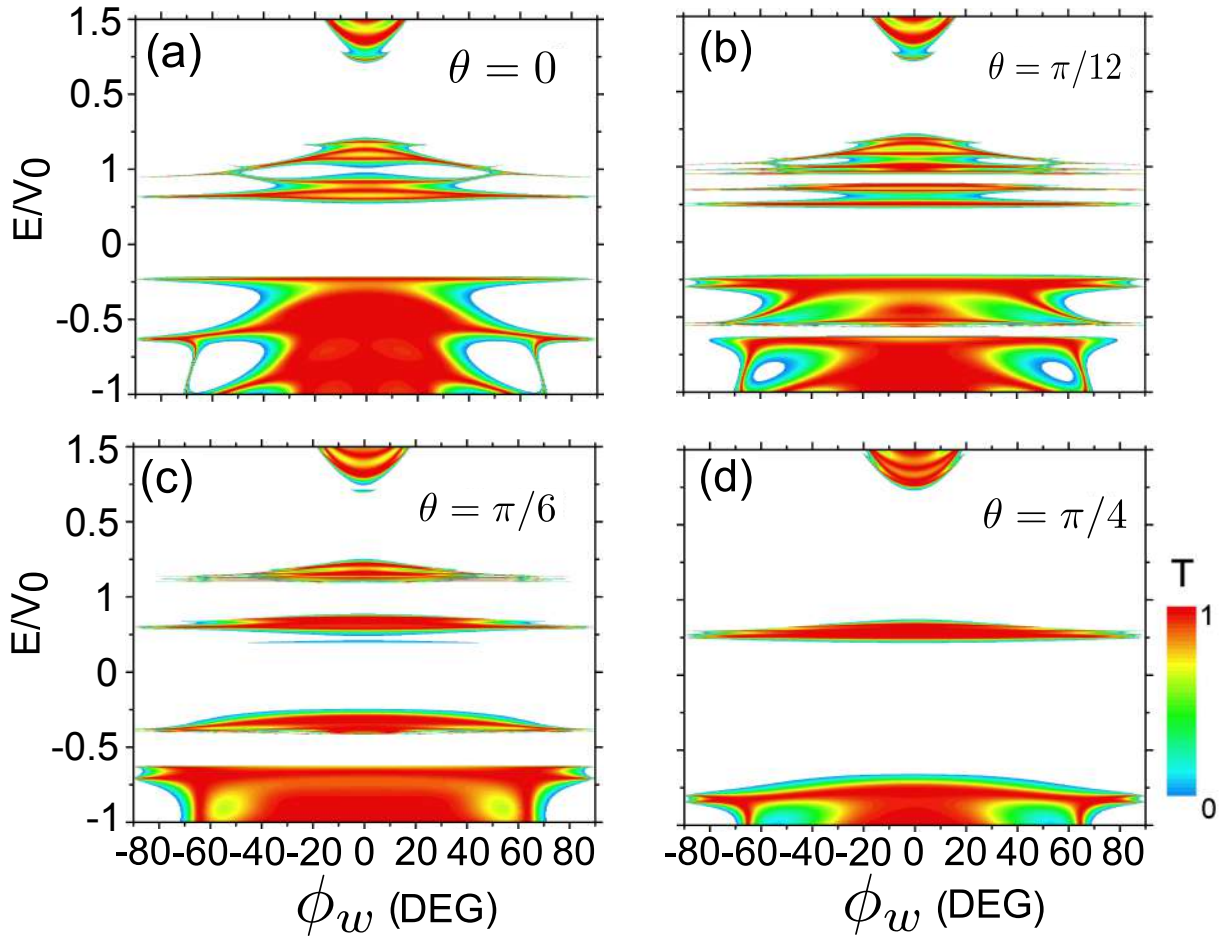
Figure 10.19: Contour plot of transmission probability through a double-barrier in the $(\phi_w, E/V_0)$ plane for (a) $\theta = 0$ (graphene-like), (b) $\theta = \pi/12$, (c) $\theta = \pi/6$, and (d) $\theta = \pi/4$ (dice) when $\hat{U} = \hat{U}_2$, $V_0 = 0.2$ eV, $\Delta = 0.04$ eV, $d = 30$ nm, and inter-barrier distance $s = 30$ nm
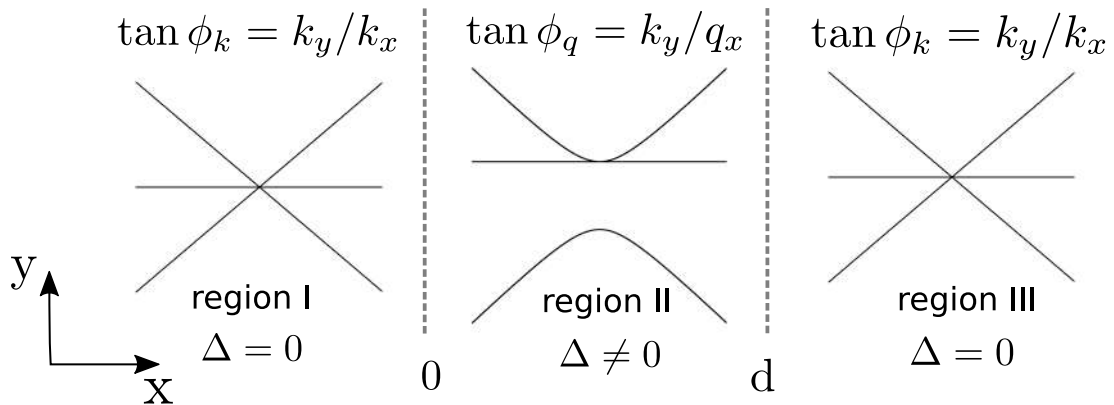
Figure 10.20: Schematic illustration of the electronic energy spectrum in $\alpha - T_3$ lattice at different spatial regions. In Region II $(0 \leq x \leq d)$, there is a band-gap in the energy spectrum induced by the presence of the symmetry-breaking term $\Delta \hat{U}_i = \hat{U}_1$.

Using the matching conditions in Eq. (10.12) and the same procedure to get the transfer matrix in Eq. (10.13), we determine the transmission probability through the spatial
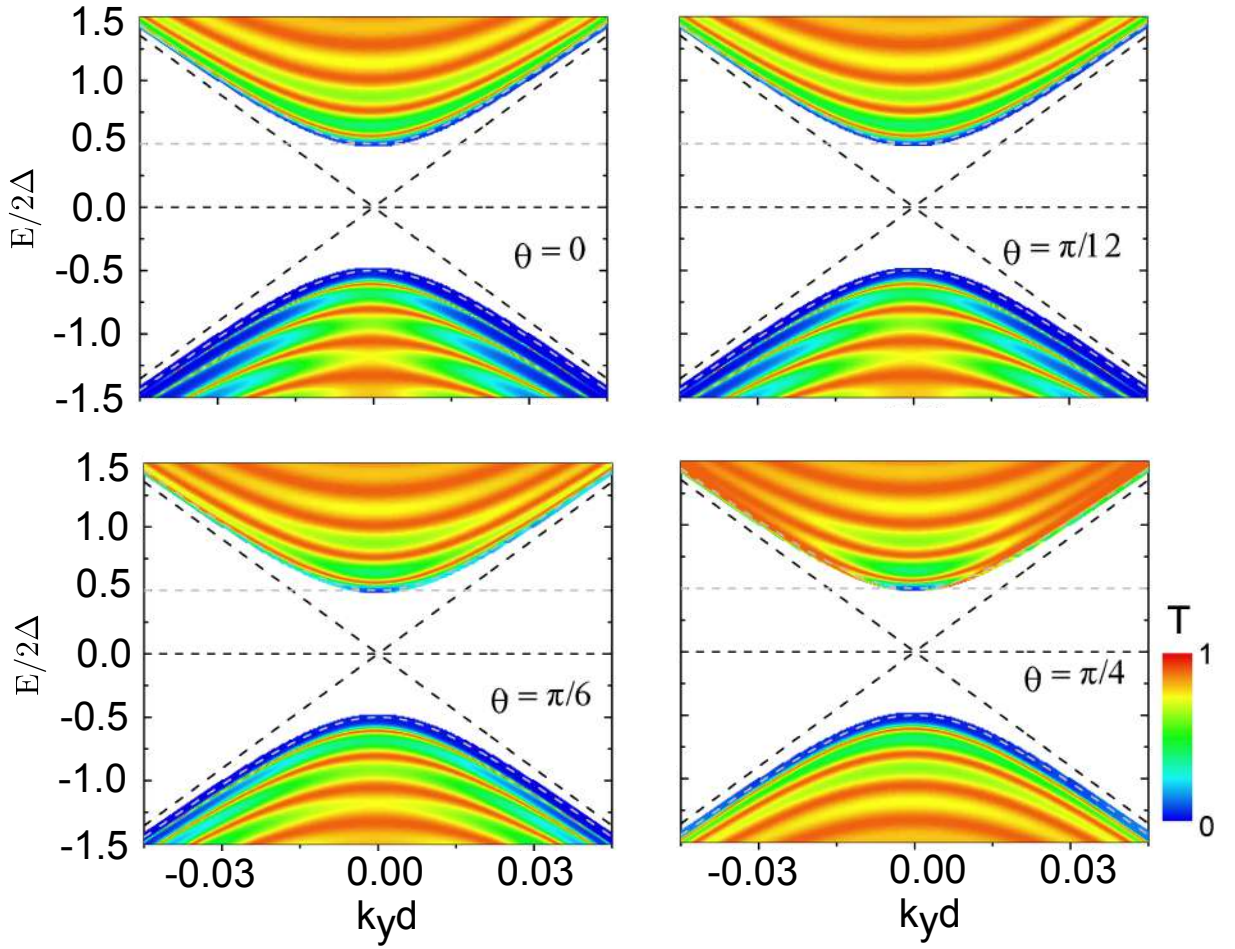
Figure 10.21: Transmission contour plots as function of $k_y d$ of electrons in $\alpha - T_3$ lattice through a spatial region that begins at $x = 0$ and width $d = 30$nm where there is a band-gap 2Δ in the energy spectrum induced by the presence of the symmetry-breaking term $\Delta \hat{U}_i = \hat{U}_1$ with $\Delta = 0.1$eV and for (a) $\theta = 0$, (b) $\theta = \pi/12$, (c) $\theta = \pi/6$, and (d) $\theta = \pi/4$.

regions of finite mass using the relation $T = 1/|\mathcal{T}_{22}^{(1)}|^2$:

$$T = \frac{1}{a_k a_q} \big[e^{i(k_x + q_x)d} \left(\Lambda_k \Lambda_q^* - \eta_1 \Lambda_k \Lambda_k^* - \eta_2 \Lambda_q \Lambda_q^* + \Lambda_k^* \Lambda_q \right)$$
$$+ e^{i(k_x - q_x)d} \left(\Lambda_k \Lambda_q + \eta_1 \Lambda_k \Lambda_k^* + \eta_2 \Lambda_q \Lambda_q^* + \Lambda_k^* \Lambda_q^* \right) \big], \tag{10.34}$$

where $\Lambda_j = \cos^2 \theta e^{\phi_j} + \sin^2 \theta e^{-\phi_j}$, $a_j = \Lambda_j + \Lambda_j^*$ with $j = k$ and $j = q$ denoting the linear energy spectrum and gapped regions, respectively. In that case $\eta_1 = \sqrt{(E - \Delta)/(E + \Delta)}$ and $\eta_2 = \sqrt{(E + \Delta)/(E - \Delta)}$.

Figure 10.21 shows the transmission probabilities plotted in the $(k_y d, E/2\Delta)$ plane for different θ, using $d = 30$ nm, and $\Delta = 0.1$ eV, resulting in a band-gap opening of $2\Delta = 0.2$ eV into Region II. Since our motivation is to compare the transmission results obtained in this section to the previous one assuming transmission through potential barriers, here we assume a band-gap with the same energy of that height of potential used in the previous sections.
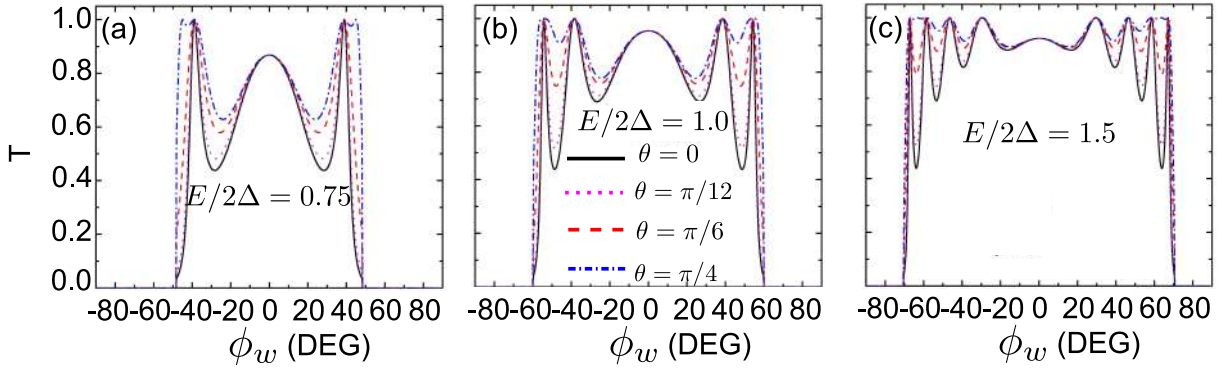
Figure 10.22: Transmission probability as function of incident angle ϕ_k, and incident energy (a) $E = 0.15$ eV, (b) $E = 0.20$ eV, (c) $E = 0.30$ eV for $\theta = 0$ (solid black curve), $\theta = \pi/12$ (dotted magenta curve), $\theta = \pi/6$ (dashed red curve), and $\theta = \pi/4$ (dash-dotted blue curve) when $\hat{U} = \hat{U}_1$ in the Region II in Fig. 10.20 with $\Delta = 0.1$ eV and $d = 30$ nm.

The energy spectrum in the different regions, i.e. in the region with linear dispersion and in the region with hyperbolic dispersion are indicated by dashed curves superimposed on the contour plots. We note that due to the band-gap opening in Region II, when incident energies are inside the gap $-0.1 < E < 0.1$ the transmission is exponentially small and for $k_y d = 0$ the transmission $T < 1$. Unlike the case of tunneling through barriers discussed in Sec. 10.5, there is absence of KT. Moreover, beyond the enhancement of the transmission as θ increases, the transmission curves are almost the same as incident energy increases only for smaller incident angles ϕ_k, as observed in Fig. 10.22.

From Fig. 10.22 we observe, in general, that there is a broadening of transmission curves for greater values of θ, like the barrier system case. However, for energies $E < 2\Delta$, which is analogous to incident energies bellow the potential barrier in the previous sections, the number of peaks in the transmission curves is the same regardless of the parameter θ, as shown in Fig. 10.22(a). In addition, the transmission continues to be enhanced even for incident energy above the band-gap energy 2Δ, as represented in Fig. 10.22(b) and 10.22(c). This result is opposite to the one observed for tunneling through potential barriers, where the transmission is reduced for energies above the one associated to the critical angle. Besides, the difference between the transmission curves as θ is tuned from graphene-like to dice is more evident for values $E > 2\Delta$, as shown in Fig. 10.22(c), where for $\theta = \pi/4$ the transmission curve is more smooth for larger values of ϕ_k.

10.8   Conclusions

In summary, using the transfer matrix approach, we investigated the tunneling properties in $\alpha - T_3$ lattices of electrons across square barriers and through regions of space where the energy spectrum has a finite band-gap. For tunneling across one-dimensional square barriers, we consider both the case of equivalence between the three sub-lattices,

and the ones where band-gaps originate due to small deviations of this equivalence by including symmetry-breaking terms. We also investigated tunneling of electrons from regions with a linear to a hyperbolic dispersion.

For the massless Dirac fermion case, when no symmetry-breaking terms are present, besides a general trend of enhanced transmission with increasing α, KT at normal incidence is found for all values of θ, regardless the number of barriers. At oblique incidence, the transmission increases with increasing θ. For a particular case, $E/V_0 = 0.5$ and $\theta = \pi/4$ (dice), an omnidirectional transmission is observed which is called *super-Klein tunneling* (SKT) effect, and preserved regardless of the number of barriers. Although the increase in the number of barriers gives rise to additional resonances in the transmission for all values of θ, this increase is much less pronounced for the dice lattice, whereas for a graphene-like lattice the transmission probability is strongly modified. Moreover, we found that, similar to total reflection in optics, above an incident angle ϕ_k there is total reflection of the incident wave-functions. This critical angle depends only on the incident energy and potential barrier and remains the same for all values of θ.

The presence of additional symmetry-breaking term in the Hamiltonian distorts the linear dispersion around the Dirac point and changes the location of the flat band, whose occurrence depends on the deviation of the equivalence between the three sublattices. The symmetry-breaking term destroys the KT and SKT in the $\alpha-T_3$ model. It is demonstrated that the additional term in general suppresses the transmission probabilities for both cases $\hat{U}_1$ and $\hat{U}_2$. When the flat band is located at the band edge, i.e. when $\hat{U}_1 = \text{diag}(1, -1, 1)$, resonant tunneling is considerably suppressed and at incident energies $0 < E/V_0 < 0.5$ the transmission is perfect for larger values of incident angle, as a consequence of the presence of degenerate states around large values of k_y observed from the electronic band structure. In addition, when we consider the double-barrier system at $E/V_0 = 0.5$, unlike the single-barrier, the transmission is reduced for smaller ϕ_w, and perpendicular or near-perpendicular incident wave-functions are totally reflected.

When $\hat{U}_2 = \text{diag}(1, -1, -3)$, since the nature of wave-vector k_b inside the potential depends on the coupling parameter we note that for $0 < E/V_0 < 1$ and intermediate values of θ new zones with total reflection of the wave-function appears as θ is tuned from graphene-like to dice, indicating the strong relation between the transmission properties and both location and distortion of the energy band inside the gap. However, the transmission probabilities are much less affected by an increase of the number of barriers as θ increases.

We also discussed the tunneling properties of electrons in $\alpha - T_3$ lattices when they traverse a region of space where the spectrum exhibits a finite energy gap. In the case we considered here, the gap is induced by inclusion of a symmetry-breaking term $\hat{U}_1$, rendering the sub-lattice C non-equivalent. The consequence is the opening of a gap in the energy spectrum. We have shown that the existence of an energy gap prevents the KT and SKT from taking place for all values of θ, and the transmission for perpendicular

or near-perpendicular waves are less than 1, unlike the transmission through a potential barrier. Moreover, at larger values of incident energy we noted a broadening of the transmission curves as θ increases. For dice the transmission peaks are smoothed as incident energy increases, and at large incident angles the transmission is perfect as a consequence of degenerate states at large values of k_y, as observed in the potential barrier case when $\hat{U}_1$ term was considered.

The results obtained in this work are useful to understand the effects in the transmission properties due to small deviations in the equivalence between the three sublattices in $\alpha - T_3$ lattices, as well as the role of location and dispersion of the band-inside the gap in the occurrence of KT and SKT. We discussed a versatile engineering to control and prevent the SKT and KT, which is a necessary condition for nanoelectronic applications, by changing the symmetry between the atomic sites of the crystal and consequently, controlling the dispersion of the middle band.

11

Final considerations and perspectives

In this thesis, we developed two methods for wave packet propagation based on the Green's function formalism and the split-operator technique adapted for multilayer phosphorene within the continuum model for low-energy electrons, which have not been published before, to our knowledge. Both theoretical models are then used to study the dynamics of Gaussian wave packets with different initial wave vectors and different initial pseudospin polarizations in N-layer phophorene. By calculating the time-dependent average position and velocity, we observed transient oscillations in these observables due to the effect known as ZBW and verified that these oscillations are directly related to the splitting of the wave packet into two parts moving with opposite velocities. We discussed the similarities and discrepancies between the results for multilayer phosphorene with those ones reported in the literature for graphene and conventional semiconductors. By comparing the results for different number of BP layers, we showed that electrons moving in N-layer BP exhibit qualitatively similar results as the ones observed in monolayer case, except for the oscillation phase difference and final group velocity achieved after the transient behavior, that is caused by the different curvature of the energy levels for different N-layer BP. Due to the highly anisotropic band structur, the wave packet propagates non-uniformly along the different x and y directions and deforms into an elliptical shape, as a consequence of the different group velocities, effective masses along x and y direction and the linear k_y term on the off-diagonal elements of the continuum Hamiltonian. We believe that the theoretical descriptions for the time evolution of wave packet propagation in multilayer BP systems will make possible further investigations of transport properties in many different BP-based materials in the presence or absence of external fields.

Further on, we theoretically explored the electronic and transport properties of QWs of anisotropic 2D semiconductors in the presence and in the absence of a perpendicular magnetic field. In the first part, the energy levels were analytically calculated by means of the effective mass approximation and analyzed for different parameters, such as: QW width, orientation angle α with respect to the anisotropy axes, and the magnetic field amplitude. Our results showed that the energy spectrum is strongly dependent on the alignment angle α, as for instance: the greater this angle, the smaller the energy levels

spacing, implying an increase of the accessible electronic states; and that in the presence of magnetic field the quantum Hall edge states are less pronounced the larger the angle α and consequently the plateaus are more evident in the magnetic dispersion relation. In the second part of this work, the transmission probability, the average position, the average velocity, and snapshots of the squared total wavefunction were numerically computed by using the split-operator technique for two different configurations: (i) a straight QW rotated and (ii) an elbow-like QW formed by a junction of two QWs with $\alpha = 0$ and $\alpha \neq 0$. For (i), we demonstrated that the average velocity oscillates for the anisotropic case in which the initial wave vector and group velocity are not collinear, whereas the average velocity remains constant for the isotropic case. Such oscillations are due to the non-specular reflections of the wavepacket at the QW edges and owing the emergence of subwavepackets with different momentum orientations in this interaction with the edges, whereas for isotropic QWs the wavepacket disperses over time without splitting. For the latter system (ii), as a consequence of the energy band mismatching of the two QWs sections and the system anisotropy, the electrons traveling through the bended QW exhibit scattering processes coming from the QW geometry itself and the anisotropic angle-dependent confinement, leading to a QW aligned angle dependence of transmission probability. We believe that the theoretical calculations and the found results for anisotropic systems with arbitrary alignment direction will make possible further investigations of transport and electronic properties in a variety of anisotropic materials in the presence or absence of external fields, which may be useful for designing anisotropic semiconductor based quantum confinement devices.

We also investigated the consequences on the electronic properties and on the dynamics of electronic states in graphene due to a generic position-dependent metric, as well as we made a parallel with analogous quantum systems that exhibit similar results. To do this, we applied the position-dependent translation operator formalism that leads to a generalized momentum operator and, consequently, a modification in the Dirac equation used here to describe the massless Dirac fermions at low-energy regime. We showed that such formalism is able to introduce additional control of such properties and that the studied system mimics two different physical scenarios: a deformed graphene due to strain and a non-uniform mass-term, induced by specific substrate. Within this generalized formalism, we analytically obtained the eigenstates and the modified Landau levels of the graphene system with a generic metric and under the presence of a perpendicular magnetic field. We showed that where the metric changes it shifts the Landau level to lower values, decrease the energy level spacing, and strongly affect the spatial distribution of the total wave function as well as the two pseudospin components. For the study of 2D Gaussian wave packet dynamics in graphene with a generic metric, we considered the well-known split-operator technique that allows us to calculate the time dependence of physical observables, such as average position and velocity, and, therefore, to track the wave packet evolution in order to understand the influence of the metric on the transport properties

of electrons in this system. In this context, we demonstrated for a different metric and for different choices of the initial pseudospin polarization that the non-null metric leads to an asymmetry for the wave packet evolution and therefore in some cases it brings up oscillations in the average of the physical observables and in other cases it suppresses the ZBW, as well as we showed the consequences on the cyclotron orbit of the electronic trajectory for different metric parameters. We also discussed the origin of this strong asymmetry in the total probability density that can be linked with a strong anisotropy in the Fermi velocity and linear momentum to the electron motion due to the position-dependent spatial metric. This theoretical formalism can be useful for comparison and analogy to other 2D based system, and we believe that the discussions about the results found in this work will contribute to a better understanding of the position-dependent translation operator formalism applied for 2D materials.

Regarding the dice or $\alpha - T_3$ lattices, since they can support flat bands that are currently a very hot topic in the study of electronic transport properties of materials and these bands are very sensitive to perturbations, its transport properties can be changed and controlled making possible the development of new electronic devices. Motivated by these properties we showed that the inclusion of symmetry-breaking terms translate into deviations in the atomic equivalence between the atomic sites of the $\alpha - T_3$ lattice which affects for example the number and appearance of Dirac points and band-gap morphing in their energy spectra. Furthermore, we demonstrate that the band-gap is strongly dependent on the symmetry between the atomic sites and the hopping parameter of these lattices. New allowed states in the energy spectrum are predicted in regions where previously there were band-gaps, which is important for electronic and transport applications. The theoretical formalism and results obtained are useful to gain a better understanding of the band-gap behavior of $\alpha - T_3$ lattices, and consequently demonstrate that these materials are versatile for purposes of band-gap engineering in 2D materials. The band-gap is tunable by changing the interlattice hopping parameter and their symmetry.

Also, since these lattices present a flat-band in their energy spectra, unusual transmission properties emerge under certain conditions. We show that small deviations in the equivalence between the atomic sites in $\alpha - T_3$ lattices, as well as the number of barriers can strongly change the transmission properties in these lattices, leading to a general suppression of the transmission for example. We demonstrate that by adjusting the symmetry between the atomic sites, new tunneling regions are possible. The presence of degenerate states and the dispersion of a quasi-flat band in the energy spectrum are associated to the enhancement of the transmission. This indicates that the electronic and transport properties can be controlled by altering the interlattice hopping parameter, which is a necessary condition for applications in nanoelectronics. The theoretical formalism and results obtained can be useful to a better understanding of the role of the location and dispersion of the energy-band-inside the gap in the occurrence of total transmission in $\alpha - T_3$ lattices, and consequently demonstrate that these materials are versatile to control

the transmission properties in 2D materials. The dispersion of the middle band can be controlled by changing the interlattice hopping parameter and their symmetries.

Regarding the study of electronic and transport properties of the charge carriers in 2D materials, in particular, to multi-layer $\alpha - T_3$-related systems, we envision a set of interesting ideas to be developed in the near future, following the examples of previously investigated problems in graphene, that in turn, will be covered by assuming $\alpha = 0$ (honeycomb) and in addition, it will allow investigating the continuously morphing from graphene-like to dice ($\alpha = 1$) systems by an one-parameter simple model, as presented throughout this thesis. Most interesting is that such systems possess the coexistence of quasi-flat bands and Dirac cones which make them even more exciting, exhibiting unconventional properties. In this context and as a short-term perspective, we intend to study the following problems:

- chiral states and their localization that could be originated from the breaking of the sublattice symmetry due to an asymmetric mass potential or even by the inclusion of a defect line between two regions of $\alpha - T_3$ material. Such states were investigated in monolayer graphene [297];

- chiral states and extra Dirac cone formation in superlattices composed by electrostatic kink and anti-kink potential profiles in the bilayer of $\alpha - T_3$. Such structures for single and double interfaces of electrostatic kinks have been already investigated for bilayer graphene [298], and we propose to develop an extension of this investigation to check the role of α variation, number, and widths of interfaces of the kink-anti-kink-like potentials. Such structures can be created by applying an asymmetric potential to the upper and the lower layers of the bilayer system;

- twisted bilayer $\alpha - T_3$ system, checking the interplay between the α parameter and the rotation angle between the two layers of $\alpha - T_3$ material.

It is worth mentioning that suggestions for similar analogies to the graphene-like system reported in the last two decades can be easily developed/extended to $\alpha - T_3$ case, as we intend to do in the near future.

Appendix A
Publications related to this thesis

- **S. M. Cunha**, D. R. da Costa, G. O. de Sousa, Andrey Chaves, J. Milton Pereira, Jr., and G. A. Farias, *Wave-packet dynamics in multilayer phosphorene*, Phys. Rev. B **99**, 235424 (2019).

Wave-packet dynamics in multilayer phosphorene

S. M. Cunha,[*] D. R. da Costa,[†] G. O. de Sousa,[‡] Andrey Chaves,[§] J. Milton Pereira, Jr.,[∥] and G. A. Farias[¶]

Departamento de Física, Universidade Federal do Ceará, Caixa Postal 6030, Campus do Pici, 60455-900 Fortaleza, Ceará, Brazil

We investigate the dynamics of Gaussian wave packets in multilayer black phosphorus (BP). Time-dependent average position and velocity are calculated analytically and numerically by using a continuum model and a method based on the split-operator technique, respectively. By analyzing the wave-packet trajectories with nonvanishing initial momentum along y direction, we observed transient spatial oscillations due to the effect known as zitterbewegung (ZBW). We also demonstrated, based on the Heisenberg picture and by the calculation of the velocity operators, that the trembling motion along the y direction at small times is unavoidable even for null initial momentum. We verified that the ZBW is directly related to the splitting of the wave packet into two parts moving with opposite velocities, as similar to graphene, and the linear dependence on k_y in out-of-diagonal terms in the Hamiltonian. In addition for phosphorene systems, the two portions of the propagated wave packets have an asymmetric shape for unbalanced ($[1, 0]^T$) and phased different ($[1, i]^T$) initial pseudospin components, playing an important role in the amplitude, frequency and duration time of the transient oscillations. Electrons in the vicinity of the Fermi energy traveling in N-layer phosphorene also exhibit qualitatively similar trembling motion and transient character as found in the monolayer case, except by the oscillation phase difference and final group velocity achieved after the transient behavior. As a consequence of the anisotropy on the N-layer BP energy bands, effective masses and group velocities along the x and y directions, the wave packet propagates nonuniformly along the different directions and deforms into an elliptical shape. By comparing our analytical results with those ones obtained by the split-operator technique, we verified a good qualitative and quantitative agreement between them, except for very larger values of wave vector and after long time steps.

I. INTRODUCTION

The well-known zitterbewegung (ZBW) phenomenon, a trembling motion caused by interference between positive and negative energy states [1,2], was predicted by Schrödinger in 1930 for the motion of relativistic electrons in vacuum

a relativistic effect, it may arise even for a nonrelativistic particle moving in crystalline solids if their band structures could be represented by a two-band model reminiscent of the Dirac equation [11–13], or for quasiparticles governed by the Bogoliubov-de Gennes equations in superconductors [14,15],

- **S. M. Cunha**, D. R. da Costa, L. C. Felix, Andrey Chaves, and J. Milton Pereira, Jr., *Electronic and transport properties of anisotropic semiconductor quantum wires*, Phys. Rev. B **102**, 045427 (2020).

Electronic and transport properties of anisotropic semiconductor quantum wires

S. M. Cunha,[*] D. R. da Costa,[†] L. C. Felix, Andrey Chaves, and J. Milton Pereira Jr.[‡]

Departamento de Física, Universidade Federal do Ceará, Campus do Pici, 60455-900 Fortaleza, Ceará, Brazil

Within the effective-mass approximation, we theoretically investigated the electronic and transport properties of 2D semiconductor quantum wires (QWs) with anisotropic effective masses and different orientations with respect to the anisotropic axis. The energy levels in the absence and presence of an external magnetic field are analytically calculated, showing (i) a strong dependence on the spacing of energy levels related to the alignment QW angle and the anisotropy axis, and (ii) for non-null magnetic fields, the quantum Hall edge states are significantly affected by the edge orientation. Moreover, by means of the split-operator technique, we analyzed the time evolution of wave packets in straight and V-shaped anisotropic QWs and compared the transmission probabilities with those of isotropic systems. In the anisotropic case, we found damped oscillations in the average values of velocity in both x and y directions for a symmetric Gaussian wave packet propagating along a straight wide QW, with the oscillation being more evident as the noncollinearity between the group velocity and momentum vectors increases.

I. INTRODUCTION

In the last two decades, the production of graphene has led to a significant level of interest on the physics of layered materials [1–11]. This interest is not only due to its possible future technological applications, but also because it provides the

caused by the presence of constraints such as external gates or crystal terminations. In that case, a dependence of the confined states on the direction of the alignment of the constraint may arise.

In the present paper, we investigate the electronic and transport properties of anisotropic materials in which a 1D

- V. Aguiar, **S. M. Cunha**, D. R. da Costa, and Raimundo N. Costa Filho, *Dirac fermions in graphene using the position-dependent translation operator formalism*, Phys. Rev. B **102**, 235404 (2020).

Dirac fermions in graphene using the position-dependent translation operator formalism

V. Aguiar, S. M. Cunha, D. R. da Costa,[*] and Raimundo N. Costa Filho[†]

Departamento de Física, Universidade Federal do Ceará, Campus do Pici, 60455-760 Fortaleza, Ceará, Brazil

Within the position-dependent translation operator formalism for quantum systems, we obtain analytical expressions for the eigenstates and the Landau level spectrum of Dirac fermions in graphene in the presence of a perpendicularly applied magnetic field and, as a consequence of the formalism, with a generalized form of the momentum operator. Moreover, we explore the behavior of wave packet dynamics in such a system by considering different initial pseudospin polarizations and metric parameters. Our findings show that the Landau levels, the wave packet trajectories, and velocities are significantly affected by the choice of the metric in the non-Euclidean space of the deformed momentum operator, exhibiting a tunable energy level spacing. In the dynamics analysis, one observes an enhancement of the oscillation amplitude of the average positions for all investigated pseudospin polarizations due to the nonsymmetric evolution of the wave packet induced by the different metrics in the system. The present formalism is shown to be a theoretical platform to describe the effects of two scenarios due to (i) a lattice deformation in graphene, giving rise to a natural Fermi velocity renormalization, or even (ii) a nonuniform mass term, induced by a specific substrate, that varies on a length scale much greater than the magnetic field length.

I. INTRODUCTION

During the past two decades, many studies have been carried out to understand the unique properties of graphene, a single atomic thin layer of graphite [1,2]. A plethora of its body of literature dealing with systems consisting of particles with position-dependent mass [27–43]. Most of the previous approaches [27–39] considered a modification of canonical commutation relations or even modifications in the underlying space, which leads to the problem of ordering in the kinetic

- **S. M. Cunha**, D. R. da Costa, J. Milton Pereira, Jr., R. N. Costa Filho, B. Van Duppen, and F. M. Peeters, *Band-gap formation and morphing in $\alpha - T_3$ superlattices*, Phys. Rev. B **104**, 115409 (2021).

Band-gap formation and morphing in α-T_3 superlattices

S. M. Cunha[1,2,*] D. R. da Costa[2] J. Milton Pereira, Jr.,[2] R. N. Costa Filho[2] B. Van Duppen,[1,†] and F. M. Peeters[1]

[1]*Department of Physics, University of Antwerp, Groenenborgerlaan 171, B-2020 Antwerp, Belgium*
[2]*Departamento de Física, Universidade Federal do Ceará, Campus do Pici, Fortaleza, Ceará, Brazil*

Electrons in α-T_3 lattices behave as condensed-matter analogies of integer-spin Dirac fermions. The three atoms making up the unit cell bestow the energy spectrum with an additional energy band that is completely flat, providing unique electronic properties. The interatomic hopping term, α, is known to strongly affect the electronic spectrum of the two-dimensional (2D) lattice, allowing it to continuously morph from graphenelike responses to the behavior of fermions in a dice lattice. For pristine lattice structures the energy bands are gapless, but small deviations in the atomic equivalence of the three sublattices will introduce gaps in the spectrum. It is unknown how these affect transport and electronic properties such as the energy spectrum of superlattice minibands. Here we investigate the dependency of these properties on the parameter α accounting for different symmetry-breaking terms, and we show how it affects band-gap formation. Furthermore, we find that superlattices can force band gaps to close and shift in energy. Our results demonstrate that α-T_3 superlattices provide a versatile material for 2D band-gap engineering purposes.

I. INTRODUCTION

The isolation of a stable single layer of carbon atoms arranged in a hexagonal lattice, known as graphene [1], combined with the extraordinary electronic and transport properties observed in the atomically thin material [1–4], has motivated many researchers to investigate and produce other two-dimensional (2D) materials [1,5–7]. The peculiar electronic properties of graphene are the result of charge

Recently, novel and distinctive physics has emerged from 2D systems when adding an additional atom in their crystal structure [27–34], which leads to their charge carriers in a low-energy approach being described as enlarged pseudospin Dirac fermions [31,32,35–37]. Among these systems, we have a Lieb lattice with the additional atom at the edges of a square lattice, which was recently obtained by adding carbon monoxide molecules to a substrate [28], and the T_3 or dice lattice, which has an additional atom at the center of the hexagonal

- **S. M. Cunha**, D. R. da Costa, J. Milton Pereira, Jr., R. N. Costa Filho, B. Van Duppen, F. M. Peeters, *Tunneling properties in $\alpha - T_3$ lattices and effects of symmetry-breaking terms*, manuscript submitted to PRB in November 2021.

Tunneling properties in $\alpha - T_3$ lattices: effects of symmetry-breaking terms

S. M. Cunha,[1,2,*] D. R. da Costa,[2] J. Milton Pereira Jr.,[2] R. N. Costa Filho,[2] B. Van Duppen,[1] and F. M. Peeters[1]

[1]*Department of Physics, University of Antwerp, Groenenborgerlaan 171, B-2020 Antwerp, Belgium*
[2]*Departamento de Física, Universidade Federal do Ceará, Campus do Pici, Fortaleza, Ceará, Brazil*

The $\alpha - T_3$ lattice model interpolates a honeycomb (graphene-like) lattice and a T_3 (also known as dice) lattice via the parameter α. These lattices are made up of three atoms per unit cell. This gives rise to an additional dispersionless flat band touching the conduction and valence bands. Electrons in this model are analogous to Dirac fermions with an enlarged pseudospin, which provides unusual tunneling features like omnidirectional Klein-tunneling, also called super-Klein tunneling (SKT). However, it is unknown how small deviations in the equivalence between the atomic sites, i.e. variations in the α-parameter, and the number of tunnel barriers changes the transmission properties. Moreover, it is interesting to learn how tunneling occurs through regions where the energy spectrum changes from linear with a middle flat band to a hyperbolic dispersion. In this paper we investigate these properties, its dependence on the number of square-barriers and the α-parameter for either gapped and gapless cases. Futhermore, we compare these results to the case where electrons tunnel from a region with linear dispersion to a region with a band-gap. In the latter case, contrary to tunneling through a potential barrier, the SKT is no longer observed. Finally, we find specific cases where transmission is allowed due to a symmetry breaking of sublattice equivalence.

I. INTRODUCTION

The probability for a particle to cross potential barriers even through a classically forbidden region with a and quantum field theory, resulting in the probing of interesting relativistic predictions, such as KT[8–11,14,15] and Zittebewegung[17–20].

The KT observed in graphene is strongly related to

Bibliography

[1] N David Mermin. Crystalline order in two dimensions. *Physical Review*, 176(1):250, 1968.

[2] LD Landau and EM Lifshitz. Chapter i–the fundamental principles of statistical physics. *Course of Theoretical Physics*, pages 1–33, 1980.

[3] Kostya S Novoselov, Andre K Geim, Sergei V Morozov, De-eng Jiang, Yanshui Zhang, Sergey V Dubonos, Irina V Grigorieva, and Alexandr A Firsov. Electric field effect in atomically thin carbon films. *Science*, 306(5696):666–669, 2004.

[4] Claire Berger, Zhimin Song, Tianbo Li, Xuebin Li, Asmerom Y Ogbazghi, Rui Feng, Zhenting Dai, Alexei N Marchenkov, Edward H Conrad, Phillip N First, et al. Ultrathin epitaxial graphite: 2D electron gas properties and a route toward graphene-based nanoelectronics. *The Journal of Physical Chemistry B*, 108(52):19912–19916, 2004.

[5] G Dresselhaus, Mildred S Dresselhaus, and Riichiro Saito. *Physical properties of carbon nanotubes*. World scientific, 1998.

[6] MO Goerbig. Electronic properties of graphene in a strong magnetic field. *Reviews of Modern Physics*, 83(4):1193, 2011.

[7] J.J. Sakurai and S.J. J. *Advanced Quantum Mechanics*. A-W series in advanced physics. Addison-Wesley Publishing Company, 1967.

[8] MI Katsnelson, KS Novoselov, and AK Geim. Chiral tunnelling and the klein paradox in graphene. *Nature Physics*, 2(9):620–625, 2006.

[9] Bernd Thaller. Visualizing the kinematics of relativistic wave packets. *arXiv preprint quant-ph/0409079*, 2004.

[10] Wlodek Zawadzki and Tomasz M Rusin. Nature of electron zitterbewegung in crystalline solids. *Physics Letters A*, 374(34):3533–3537, 2010.

[11] Gyula David and József Cserti. General theory of zitterbewegung. *Physical Review B*, 81(12):121417, 2010.

[12] Erwin. Schrödinger. *Über die kräftefreie bewegung in der relativistischen quanten-mechanik*. Akademie der wissenschaften in kommission bei W. de Gruyter u. Company, 1930.

[13] John Schliemann, Daniel Loss, and RM Westervelt. Zitterbewegung of electronic wave packets in III-V zinc-blende semiconductor quantum wells. *Physical Review Letters*, 94(20):206801, 2005.

[14] Tomasz M Rusin and Wlodek Zawadzki. Theory of electron zitterbewegung in graphene probed by femtosecond laser pulses. *Physical Review B*, 80(4):045416, 2009.

[15] Yi-Xiang Wang, Zhi Yang, and Shi-Jie Xiong. Study of zitterbewegung in graphene bilayer with perpendicular magnetic field. *EPL (Europhysics Letters)*, 89(1):17007, 2010.

[16] Rene Gerritsma, Gerhard Kirchmair, Florian Zähringer, E Solano, R Blatt, and CF Roos. Quantum simulation of the dirac equation. *Nature*, 463(7277):68–71, 2010.

[17] JW Braun, Q Su, and R Grobe. Numerical approach to solve the time-dependent dirac equation. *Physical Review A*, 59(1):604, 1999.

[18] A Rycerz, J Tworzydło, and CWJ Beenakker. Valley filter and valley valve in graphene. *Nature Physics*, 3(3):172–175, 2007.

[19] Han Liu, Adam T Neal, Zhen Zhu, Zhe Luo, Xianfan Xu, David Tománek, and Peide D Ye. Phosphorene: an unexplored 2D semiconductor with a high hole mobility. *ACS Nano*, 8(4):4033–4041, 2014.

[20] Fengnian Xia, Han Wang, and Yichen Jia. Rediscovering black phosphorus as an anisotropic layered material for optoelectronics and electronics. *Nature Communications*, 5(1):1–6, 2014.

[21] Jingsi Qiao, Xianghua Kong, Zhi-Xin Hu, Feng Yang, and Wei Ji. High-mobility transport anisotropy and linear dichroism in few-layer black phosphorus. *Nature Communications*, 5(1):1–7, 2014.

[22] PW Bridgman. Two new modifications of phosphorus. *Journal of the American Chemical Society*, 36(7):1344–1363, 1914.

[23] Robert W Keyes. The electrical properties of black phosphorus. *Physical Review*, 92(3):580, 1953.

[24] A Morita. Semiconducting black phosphorus. *Applied Physics A*, 39(4):227–242, 1986.

[25] Douglas Warschauer. Electrical and optical properties of crystalline black phosphorus. *Journal of Applied Physics*, 34(7):1853–1860, 1963.

[26] Y Maruyama, S Suzuki, K Kobayashi, and S Tanuma. Synthesis and some properties of black phosphorus single crystals. *Physica B+ C*, 105(1-3):99–102, 1981.

[27] John C Jamieson. Crystal structures adopted by black phosphorus at high pressures. *Science*, 139(3561):1291–1292, 1963.

[28] Haruki Kawamura, Ichimin Shirotani, and Kyoji Tachikawa. Anomalous superconductivity in black phosphorus under high pressures. *Solid State Communications*, 49(9):879–881, 1984.

[29] CA Vanderborgh and D Schiferl. Raman studies of black phosphorus from 0.25 to 7.7 GPa at 15 k. *Physical Review B*, 40(14):9595, 1989.

[30] Yu Chen, Guobao Jiang, Shuqing Chen, Zhinan Guo, Xuefeng Yu, Chujun Zhao, Han Zhang, Qiaoliang Bao, Shuangchun Wen, Dingyuan Tang, et al. Mechanically exfoliated black phosphorus as a new saturable absorber for both Q-switching and mode-locking laser operation. *Optics Express*, 23(10):12823–12833, 2015.

[31] Andres Castellanos-Gomez, Leonardo Vicarelli, Elsa Prada, Joshua O Island, KL Narasimha-Acharya, Sofya I Blanter, Dirk J Groenendijk, Michele Buscema, Gary A Steele, JV Alvarez, et al. Isolation and characterization of few-layer black phosphorus. *2D Materials*, 1(2):025001, 2014.

[32] Steven P Koenig, Rostislav A Doganov, Hennrik Schmidt, AH Castro Neto, and Barbaros Özyilmaz. Electric field effect in ultrathin black phosphorus. *Applied Physics Letters*, 104(10):103106, 2014.

[33] AS Rodin, A Carvalho, and AH Castro Neto. Strain-induced gap modification in black phosphorus. *Physical Review Letters*, 112(17):176801, 2014.

[34] Hideo Asahina and Akira Morita. Band structure and optical properties of black phosphorus. *Journal of Physics C: Solid State Physics*, 17(11):1839, 1984.

[35] Yanlan Du, Chuying Ouyang, Siqi Shi, and Minsheng Lei. Ab initio studies on atomic and electronic structures of black phosphorus. *Journal of Applied Physics*, 107(9):093718, 2010.

[36] Gabriel Oliveira de Sousa. *Anéis e pontos quânticos de fósforo negro investigadas por modelo contínuo*. PhD thesis, 2016.

[37] Adam H Woomer, Tyler W Farnsworth, Jun Hu, Rebekah A Wells, Carrie L Donley, and Scott C Warren. Phosphorene: synthesis, scale-up, and quantitative optical spectroscopy. *ACS Nano*, 9(9):8869–8884, 2015.

[38] Bart Partoens and FM Peeters. From graphene to graphite: Electronic structure around the K point. *Physical Review B*, 74(7):075404, 2006.

[39] DJP De Sousa, LV De Castro, Diego Rabelo da Costa, J Milton Pereira Jr, and Tony Low. Multilayered black phosphorus: From a tight-binding to a continuum description. *Physical Review B*, 96(15):155427, 2017.

[40] Alexander N Rudenko and Mikhail I Katsnelson. Quasiparticle band structure and tight-binding model for single-and bilayer black phosphorus. *Physical Review B*, 89(20):201408, 2014.

[41] John P Perdew, Kieron Burke, and Matthias Ernzerhof. Generalized gradient approximation made simple. *Physical Review Letters*, 77(18):3865, 1996.

[42] Lars Hedin. New method for calculating the one-particle green's function with application to the electron-gas problem. *Physical Review*, 139(3A):A796, 1965.

[43] M Shishkin and G Kresse. Implementation and performance of the frequency-dependent g w method within the paw framework. *Physical Review B*, 74(3):035101, 2006.

[44] Liangzhi Kou, Changfeng Chen, and Sean C Smith. Phosphorene: fabrication, properties, and applications. *The Journal of Physical Chemistry Letters*, 6(14):2794–2805, 2015.

[45] Jie Sun, Guangyuan Zheng, Hyun-Wook Lee, Nian Liu, Haotian Wang, Hongbin Yao, Wensheng Yang, and Yi Cui. Formation of stable phosphorus–carbon bond for enhanced performance in black phosphorus nanoparticle–graphite composite battery anodes. *Nano Letters*, 14(8):4573–4580, 2014.

[46] Likai Li, Yijun Yu, Guo Jun Ye, Qingqin Ge, Xuedong Ou, Hua Wu, Donglai Feng, Xian Hui Chen, and Yuanbo Zhang. Black phosphorus field-effect transistors. *Nature Nanotechnology*, 9(5):372–377, 2014.

[47] Saptarshi Das, Wei Zhang, Marcel Demarteau, Axel Hoffmann, Madan Dubey, and Andreas Roelofs. Tunable transport gap in phosphorene. *Nano Letters*, 14(10):5733–5739, 2014.

[48] Yuchen Du, Han Liu, Yexin Deng, and Peide D Ye. Device perspective for black phosphorus field-effect transistors: contact resistance, ambipolar behavior, and scaling. *ACS Nano*, 8(10):10035–10042, 2014.

[49] Haiwei Du, Xi Lin, Zhemi Xu, and Dewei Chu. Recent developments in black phosphorus transistors. *Journal of Materials Chemistry C*, 3(34):8760–8775, 2015.

[50] Fa Wang and Ying Ran. Nearly flat band with Chern number c= 2 on the dice lattice. *Physical Review B*, 84(24):241103, 2011.

[51] D Bercioux, DF Urban, Hermann Grabert, and Wolfgang Häusler. Massless Dirac-Weyl fermions in $\alpha - T_3$ optical lattice. *Physical Review A*, 80(6):063603, 2009.

[52] Balázs Dóra, Janik Kailasvuori, and Roderich Moessner. Lattice generalization of the dirac equation to general spin and the role of the flat band. *Physical Review B*, 84(19):195422, 2011.

[53] John D Malcolm and Elisabeth J Nicol. Magneto-optics of general pseudospin-s two-dimensional Dirac-Weyl fermions. *Physical Review B*, 90(3):035405, 2014.

[54] Zhihao Lan, Nathan Goldman, Alejandro Bermudez, Wenshu Lu, and P Öhberg. Dirac-weyl fermions with arbitrary spin in two-dimensional optical superlattices. *Physical Review B*, 84(16):165115, 2011.

[55] Emilia Illes. *Properties of the $\alpha - T_3$ Model*. PhD thesis, University of Guelph, 2017.

[56] A Raoux, M Morigi, J-N Fuchs, F Piéchon, and G Montambaux. From dia-to paramagnetic orbital susceptibility of massless fermions. *Physical review letters*, 112(2):026402, 2014.

[57] JW McClure. Diamagnetism of graphite. *Physical Review*, 104(3):666, 1956.

[58] Bill Sutherland. Localization of electronic wave functions due to local topology. *Physical Review B*, 34(8):5208, 1986.

[59] Julien Vidal, Rémy Mosseri, and Benoit Douçot. Aharonov-bohm cages in two-dimensional structures. *Physical Review Letters*, 81(26):5888, 1998.

[60] John D Malcolm and Elisabeth J Nicol. Magneto-optics of massless kane fermions: Role of the flat band and unusual berry phase. *Physical Review B*, 92(3):035118, 2015.

[61] F Piéchon, JN Fuchs, A Raoux, and G Montambaux. Tunable orbital susceptibility in α-t 3 tight-binding models. In *Journal of Physics: Conference Series*, volume 603, page 012001. IOP Publishing, 2015.

[62] AH Castro Neto, Francisco Guinea, Nuno MR Peres, Kostya S Novoselov, and Andre K Geim. The electronic properties of graphene. *Reviews of Modern Physics*, 81(1):109, 2009.

[63] Philip Richard Wallace. The band theory of graphite. *Physical Review*, 71(9):622, 1947.

[64] D.A. Bromley and W. Greiner. *Relativistic Quantum Mechanics. Wave Equations*. Springer, Berlin, Heidelberg, 2013.

[65] George Gamow. Zur quantentheorie des atomkernes. *Zeitschrift für Physik*, 51(3):204–212, 1928.

[66] Ronald W Gurney and Edw U Condon. Wave mechanics and radioactive disintegration. *Nature*, 122(3073):439–439, 1928.

[67] Paul Adrien Maurice Dirac. The quantum theory of the electron. *Proceedings of the Royal Society of London. Series A, Containing Papers of a Mathematical and Physical Character*, 117(778):610–624, 1928.

[68] Oskar Klein. Die reflexion von elektronen an einem potentialsprung nach der relativistischen dynamik von Dirac. *Zeitschrift für Physik*, 53(3-4):157–165, 1929.

[69] Norman Dombey and A Calogeracos. Seventy years of the Klein paradox. *Physics Reports*, 315(1-3):41–58, 1999.

[70] Kostya S Novoselov, Andre K Geim, Sergei Vladimirovich Morozov, Dingde Jiang, Michail I Katsnelson, IVa Grigorieva, SVb Dubonos, Firsov, and AA. Two-dimensional gas of massless dirac fermions in graphene. *Nature*, 438(7065):197–200, 2005.

[71] Yuanbo Zhang, Yan-Wen Tan, Horst L Stormer, and Philip Kim. Experimental observation of the quantum hall effect and berry's phase in graphene. *Nature*, 438(7065):201–204, 2005.

[72] Vadim V Cheianov and Vladimir I Fal'ko. Selective transmission of dirac electrons and ballistic magnetoresistance of n- p junctions in graphene. *Physical Review B*, 74(4):041403, 2006.

[73] J Milton Pereira Jr, V Mlinar, FM Peeters, and P Vasilopoulos. Confined states and direction-dependent transmission in graphene quantum wells. *Physical Review B*, 74(4):045424, 2006.

[74] B Huard, JA Sulpizio, N Stander, K Todd, B Yang, and D Goldhaber-Gordon. Transport measurements across a tunable potential barrier in graphene. *Physical Review Letters*, 98(23):236803, 2007.

[75] Roman V Gorbachev, Alexander S Mayorov, Alexander K Savchenko, David W Horsell, and Francisco Guinea. Conductance of pnp graphene structures with "air-bridge" top gates. *Nano Letters*, 8(7):1995–1999, 2008.

[76] N Stander, B Huard, and D Goldhaber-Gordon. Evidence for Klein tunneling in graphene p- n junctions. *Physical Review Letters*, 102(2):026807, 2009.

[77] Andrea F Young and Philip Kim. Quantum interference and Klein tunnelling in graphene heterojunctions. *Nature Physics*, 5(3):222–226, 2009.

[78] Pierre E Allain and Jean-Noel Fuchs. Klein tunneling in graphene: optics with massless electrons. *The European Physical Journal B*, 83(3):301–317, 2011.

[79] J Milton Pereira, FM Peeters, A Chaves, and GA Farias. Klein tunneling in single and multiple barriers in graphene. *Semiconductor Science and Technology*, 25(3):033002, 2010.

[80] M Barbier, P Vasilopoulos, and FM Peeters. Extra Dirac points in the energy spectrum for superlattices on single-layer graphene. *Physical Review B*, 81(7):075438, 2010.

[81] JH Ho, Yu-Huang Chiu, SJ Tsai, and Min-Fa Lin. Semimetallic graphene in a modulated electric potential. *Physical Review B*, 79(11):115427, 2009.

[82] Cheol-Hwan Park, Young-Woo Son, Li Yang, Marvin L Cohen, and Steven G Louie. Landau levels and quantum Hall effect in graphene superlattices. *Physical Review Letters*, 103(4):046808, 2009.

[83] L Brey and HA Fertig. Emerging zero modes for graphene in a periodic potential. *Physical Review Letters*, 103(4):046809, 2009.

[84] Li-Gang Wang and Shi-Yao Zhu. Electronic band gaps and transport properties in graphene superlattices with one-dimensional periodic potentials of square barriers. *Physical Review B*, 81(20):205444, 2010.

[85] Bruce HJ McKellar and GJ Stephenson Jr. Relativistic quarks in one-dimensional periodic structures. *Physical Review C*, 35(6):2262, 1987.

[86] Cheol-Hwan Park, Li Yang, Young-Woo Son, Marvin L Cohen, and Steven G Louie. Anisotropic behaviours of massless Dirac fermions in graphene under periodic potentials. *Nature Physics*, 4(3):213–217, 2008.

[87] Cheol-Hwan Park, Young-Woo Son, Li Yang, Marvin L Cohen, and Steven G Louie. Electron beam supercollimation in graphene superlattices. *Nano Letters*, 8(9):2920–2924, 2008.

[88] Yury P Bliokh, Valentin Freilikher, Sergey Savel'ev, and Franco Nori. Transport and localization in periodic and disordered graphene superlattices. *Physical Review B*, 79(7):075123, 2009.

[89] Cheol-Hwan Park, Li Yang, Young-Woo Son, Marvin L Cohen, and Steven G Louie. New generation of massless Dirac fermions in graphene under external periodic potentials. *Physical Review Letters*, 101(12):126804, 2008.

[90] Carlos Forsythe, Xiaodong Zhou, Kenji Watanabe, Takashi Taniguchi, Abhay Pasupathy, Pilkyung Moon, Mikito Koshino, Philip Kim, and Cory R Dean. Band structure engineering of 2d materials using patterned dielectric superlattices. *Nature nanotechnology*, 13(7):566–571, 2018.

[91] Yutao Li, Scott Dietrich, Carlos Forsythe, Takashi Taniguchi, Kenji Watanabe, Pilkyung Moon, and Cory R Dean. Anisotropic band flattening in graphene with one-dimensional superlattices. *Nature Nanotechnology*, 16(5):525–530, 2021.

[92] Esmaeil Taghizadeh Sisakht, Mohammad H Zare, and Farhad Fazileh. Scaling laws of band gaps of phosphorene nanoribbons: A tight-binding calculation. *Physical Review B*, 91(8):085409, 2015.

[93] JM Pereira Jr and MI Katsnelson. Landau levels of single-layer and bilayer phosphorene. *Physical Review B*, 92(7):075437, 2015.

[94] S.M. Rezende. *Materiais e Dispositivos Eletrônicos*. Editora Livraria da Física, 2004.

[95] Timur Tudorovskiy, KJA Reijnders, and Mikhail I Katsnelson. Chiral tunneling in single-layer and bilayer graphene. *Physica Scripta*, 2012(T146):014010, 2012.

[96] Daniel F Urban, Dario Bercioux, Michael Wimmer, and Wolfgang Häusler. Barrier transmission of Dirac-like pseudospin-one particles. *Physical Review B*, 84(11):115136, 2011.

[97] R Shen, LB Shao, Baigeng Wang, and DY Xing. Single dirac cone with a flat band touching on line-centered-square optical lattices. *Physical Review B*, 81(4):041410, 2010.

[98] E Illes and EJ Nicol. Klein tunneling in the $\alpha - T_3$ model. *Physical Review B*, 95(23):235432, 2017.

[99] Marcos H Degani and Marcelo Z Maialle. Numerical calculations of the quantum states in semiconductor nanostructures. *Journal of Computational and Theoretical Nanoscience*, 7(2):454–473, 2010.

[100] Shengjun Yuan, Hans De Raedt, and Mikhail I Katsnelson. Modeling electronic structure and transport properties of graphene with resonant scattering centers. *Physical Review B*, 82(11):115448, 2010.

[101] G Dattoli, PL Ottaviani, A Segreto, and A Torre. Symmetric-split-operator techniques and finite-difference methods for the solution of classical and quantum evolution problems. *Il Nuovo Cimento B (1971-1996)*, 111(7):825–839, 1996.

[102] MD Feit, JA Fleck, and A Steiger. Solution of the schrödinger equation by a spectral method. *Journal of Computational Physics*, 47(3):412–433, 1982.

[103] MD Feit and JA Fleck Jr. Solution of the schrödinger equation by a spectral method ii: Vibrational energy levels of triatomic molecules. *The Journal of Chemical Physics*, 78(1):301–308, 1983.

[104] B Szafran and FM Peeters. Lorentz-force–induced asymmetry in the aharonov-bohm effect in a three-terminal semiconductor quantum ring. *EPL (Europhysics Letters)*, 70(6):810, 2005.

[105] Christoph Kreisbeck, Tobias Kramer, Sven S Buchholz, Saskia F Fischer, Ulrich Kunze, Dirk Reuter, and Andreas D Wieck. Phase shifts and phase π jumps in four-terminal waveguide Aharonov-Bohm interferometers. *Physical Review B*, 82(16):165329, 2010.

[106] R Kalina, B Szafran, S Bednarek, and FM Peeters. Magnetic-field asymmetry of electron wave packet transmission in bent channels capacitively coupled to a metal gate. *Physical Review Letters*, 102(6):066807, 2009.

[107] Masuo Suzuki. Fractal decomposition of exponential operators with applications to many-body theories and monte carlo simulations. *Physics Letters A*, 146(6):319–323, 1990.

[108] João Philipe Macedo Braga. *Técnica Split Operator em Coordenadas Generalizadas*. PhD thesis, 2010.

[109] William H Press, Saul A Teukolsky, Brian P Flannery, and William T Vetterling. *Numerical recipes in Fortran 77: volume 1 of Fortran numerical recipes: the art of scientific computing*. Cambridge university press, 1992.

[110] Andrey Chaves, Lucian Covaci, Kh Yu Rakhimov, GA Farias, and FM Peeters. Wave-packet dynamics and valley filter in strained graphene. *Physical Review B*, 82(20):205430, 2010.

[111] Wlodek Zawadzki and Tomasz M Rusin. Zitterbewegung (trembling motion) of electrons in semiconductors: a review. *Journal of Physics: Condensed Matter*, 23(14):143201, 2011.

[112] Wlodek Zawadzki. Semirelativity in semiconductors: a review. *Journal of Physics: Condensed Matter*, 29(37):373004, 2017.

[113] AO Barut and AJ Bracken. Zitterbewegung and the internal geometry of the electron. *Physical Review D*, 23(10):2454, 1981.

[114] Herman Feshbach and Felix Villars. Elementary relativistic wave mechanics of spin 0 and spin 1/2 particles. *Reviews of Modern Physics*, 30(1):24, 1958.

[115] AO Barut and W Thacker. Covariant generalization of the zitterbewegung of the electron and its SO(4, 2) and SO(3, 2) internal algebras. *Physical Review D*, 31(6):1386, 1985.

[116] Kerson Huang. On the zitterbewegung of the Dirac electron. *American Journal of Physics*, 20(8):479–484, 1952.

[117] James A Lock. The Zitterbewegung of a free localized Dirac particle. *American Journal of Physics*, 47(9):797–802, 1979.

[118] F Cannata, L Ferrari, and G Russo. Dirac-like behaviour of a non-relativistic tight binding Hamiltonian in one dimension. *Solid State Communications*, 74(4):309–312, 1990.

[119] L Ferrari and G Russo. Nonrelativistic zitterbewegung in two-band systems. *Physical Review B*, 42(12):7454, 1990.

[120] F Cannata and L Ferrari. Effects of the nonrelativistic Zitterbewegung on the electron-phonon interaction in two-band systems. *Physical Review B*, 44(16):8599, 1991.

[121] D Lurié and S Cremer. Zitterbewegung of quasiparticles in superconductors. *Physica*, 50(2):224–240, 1970.

[122] József Cserti and Gyula Dávid. Unified description of zitterbewegung for spintronic, graphene, and superconducting systems. *Physical Review B*, 74(17):172305, 2006.

[123] John Schliemann, Daniel Loss, and RM Westervelt. Zitterbewegung of electrons and holes in iii–v semiconductor quantum wells. *Physical Review B*, 73(8):085323, 2006.

[124] Shun-Qing Shen. Spin transverse force on spin current in an electric field. *Physical Review Letters*, 95(18):187203, 2005.

[125] ZF Jiang, RD Li, Shou-Cheng Zhang, and WM Liu. Semiclassical time evolution of the holes from luttinger hamiltonian. *Physical Review B*, 72(4):045201, 2005.

[126] Patrik Brusheim and HQ Xu. Spin hall effect and zitterbewegung in an electron waveguide. *Physical Review B*, 74(20):205307, 2006.

[127] V Ya Demikhovskii, GM Maksimova, and EV Frolova. Wave packet dynamics in a two-dimensional electron gas with spin orbit coupling: Splitting and zitterbewegung. *Physical Review B*, 78(11):115401, 2008.

[128] Tutul Biswas and Tarun Kanti Ghosh. Wave packet dynamics and zitterbewegung of heavy holes in a quantizing magnetic field. *Journal of Applied Physics*, 115(21):213701, 2014.

[129] Wlodek Zawadzki. Zitterbewegung and its effects on electrons in semiconductors. *Physical Review B*, 72(8):085217, 2005.

[130] Xiangdong Zhang. Observing Zitterbewegung for photons near the Dirac point of a two-dimensional photonic crystal. *Physical Review Letters*, 100(11):113903, 2008.

[131] Felix Dreisow, Matthias Heinrich, Robert Keil, Andreas Tünnermann, Stefan Nolte, Stefano Longhi, and Alexander Szameit. Classical simulation of relativistic Zitterbewegung in photonic lattices. *Physical Review Letters*, 105(14):143902, 2010.

[132] Xiangdong Zhang and Zhengyou Liu. Extremal transmission and beating effect of acoustic waves in two-dimensional sonic crystals. *Physical Review Letters*, 101(26):264303, 2008.

[133] Tomasz M Rusin and Wlodek Zawadzki. Zitterbewegung of relativistic electrons in a magnetic field and its simulation by trapped ions. *Physical Review D*, 82(12):125031, 2010.

[134] V Ya Demikhovskii, GM Maksimova, and EV Frolova. Wave packet dynamics in hole luttinger systems. *Physical Review B*, 81(11):115206, 2010.

[135] R Winkler, U Zülicke, and Jens Bolte. Oscillatory multiband dynamics of free particles: The ubiquity of zitterbewegung effects. *Physical Review B*, 75(20):205314, 2007.

[136] JY Vaishnav and Charles W Clark. Observing Zitterbewegung with ultracold atoms. *Physical Review Letters*, 100(15):153002, 2008.

[137] Yi-Cai Zhang, Shu-Wei Song, Chao-Fei Liu, and Wu-Ming Liu. Zitterbewegung effect in spin-orbit-coupled spin-1 ultracold atoms. *Physical Review A*, 87(2):023612, 2013.

[138] Li-kun Shi, Shou-cheng Zhang, and Kai Chang. Anomalous electron trajectory in topological insulators. *Physical Review B*, 87(16):161115, 2013.

[139] Li-Gang Wang, Zhi-Guo Wang, and Shi-Yao Zhu. Zitterbewegung of optical pulses near the Dirac point inside a negative-zero-positive index metamaterial. *EPL (Europhysics Letters)*, 86(4):47008, 2009.

[140] Lindsay J LeBlanc, MC Beeler, Karina Jimenez-Garcia, Abigail R Perry, Seiji Sugawa, RA Williams, and Ian B Spielman. Direct observation of zitterbewegung in a bose–einstein condensate. *New Journal of Physics*, 15(7):073011, 2013.

[141] Chunlei Qu, Chris Hamner, Ming Gong, Chuanwei Zhang, and Peter Engels. Observation of zitterbewegung in a spin-orbit-coupled bose-einstein condensate. *Physical Review A*, 88(2):021604, 2013.

[142] Mikhail I Katsnelson and Mikhail Iosifovich Katsnelson. *Graphene: carbon in two dimensions*. Cambridge university press, 2012.

[143] MI Katsnelson. Zitterbewegung, chirality, and minimal conductivity in graphene. *The European Physical Journal B-Condensed Matter and Complex Systems*, 51(2):157–160, 2006.

[144] GM Maksimova, V Ya Demikhovskii, and EV Frolova. Wave packet dynamics in a monolayer graphene. *Physical Review B*, 78(23):235321, 2008.

[145] JC Martinez, MBA Jalil, and SG Tan. Klein tunneling and zitterbewegung and the formation of a polarized p-n junction in graphene. *Applied Physics Letters*, 97(6):062111, 2010.

[146] R Englman and T Vertesi. Large berry phases in layered graphene. *Physical Review B*, 78(20):205311, 2008.

[147] Tomasz M Rusin and Wlodek Zawadzki. Transient zitterbewegung of charge carriers in mono-and bilayer graphene, and carbon nanotubes. *Physical Review B*, 76(19):195439, 2007.

[148] Tomasz M Rusin and Wlodek Zawadzki. Zitterbewegung of electrons in graphene in a magnetic field. *Physical Review B*, 78(12):125419, 2008.

[149] W Zawadzki and TM Rusin. Zitterbewegung (trembling motion) of electrons in narrow-gap semiconductors. *Journal of Physics: Condensed Matter*, 20(45):454208, 2008.

[150] Viktor Krueckl and Tobias Kramer. Revivals of quantum wave packets in graphene. *New Journal of Physics*, 11(9):093010, 2009.

[151] Elvira Romera and F de Los Santos. Revivals, classical periodicity, and zitterbewegung of electron currents in monolayer graphene. *Physical Review B*, 80(16):165416, 2009.

[152] John Schliemann. Cyclotron motion in graphene. *New Journal of Physics*, 10(4):043024, 2008.

[153] Phaedon Avouris, Tony F Heinz, and Tony Low. *2D Materials*. Cambridge University Press, 2017.

[154] Vy Tran, Ryan Soklaski, Yufeng Liang, and Li Yang. Layer-controlled band gap and anisotropic excitons in few-layer black phosphorus. *Physical Review B*, 89(23):235319, 2014.

[155] Andres Castellanos-Gomez. Black phosphorus: narrow gap, wide applications. *The Journal of Physical Chemistry Letters*, 6(21):4280–4291, 2015.

[156] Kapildeb Dolui and Su Ying Quek. Quantum-confinement and structural anisotropy result in electrically-tunable Dirac cone in few-layer black phosphorous. *Scientific Reports*, 5(1):1–12, 2015.

[157] Jimin Kim, Seung Su Baik, Sae Hee Ryu, Yeongsup Sohn, Soohyung Park, Byeong-Gyu Park, Jonathan Denlinger, Yeonjin Yi, Hyoung Joon Choi, and Keun Su Kim. Observation of tunable band gap and anisotropic dirac semimetal state in black phosphorus. *Science*, 349(6249):723–726, 2015.

[158] Shengjun Yuan, Edo van Veen, Mikhail I Katsnelson, and Rafael Roldán. Quantum hall effect and semiconductor-to-semimetal transition in biased black phosphorus. *Physical Review B*, 93(24):245433, 2016.

[159] Guowei Zhang, Shenyang Huang, Andrey Chaves, Chaoyu Song, V Ongun Özçelik, Tony Low, and Hugen Yan. Infrared fingerprints of few-layer black phosphorus. *Nature Communications*, 8(1):1–9, 2017.

[160] Tony Low, AS Rodin, A Carvalho, Yongjin Jiang, Han Wang, Fengnian Xia, and AH Castro Neto. Tunable optical properties of multilayer black phosphorus thin films. *Physical Review B*, 90(7):075434, 2014.

[161] Tony Low, Rafael Roldán, Han Wang, Fengnian Xia, Phaedon Avouris, Luis Martín Moreno, and Francisco Guinea. Plasmons and screening in monolayer and multilayer black phosphorus. *Physical Review Letters*, 113(10):106802, 2014.

[162] Hongtao Yuan, Xiaoge Liu, Farzaneh Afshinmanesh, Wei Li, Gang Xu, Jie Sun, Biao Lian, Alberto G Curto, Guojun Ye, Yasuyuki Hikita, et al. Polarization-sensitive broadband photodetector using a black phosphorus vertical p–n junction. *Nature Nanotechnology*, 10(8):707–713, 2015.

[163] Qihang Liu, Xiuwen Zhang, LB Abdalla, Adalberto Fazzio, and Alex Zunger. Switching a normal insulator into a topological insulator via electric field with application to phosphorene. *Nano Letters*, 15(2):1222–1228, 2015.

[164] Tony Low, Michael Engel, Mathias Steiner, and Phaedon Avouris. Origin of photoresponse in black phosphorus phototransistors. *Physical Review B*, 90(8):081408, 2014.

[165] Ruoming Peng, Kaveh Khaliji, Nathan Youngblood, Roberto Grassi, Tony Low, and Mo Li. Midinfrared electro-optic modulation in few-layer black phosphorus. *Nano Letters*, 17(10):6315–6320, 2017.

[166] Kaveh Khaliji, Arya Fallahi, Luis Martin-Moreno, and Tony Low. Tunable plasmon-enhanced birefringence in ribbon array of anisotropic two-dimensional materials. *Physical Review B*, 95(20):201401, 2017.

[167] E Romera, JB Roldán, and F de los Santos. Zitterbewegung in monolayer silicene in a magnetic field. *Physics Letters A*, 378(34):2582–2585, 2014.

[168] Ashutosh Singh, Tutul Biswas, Tarun Kanti Ghosh, and Amit Agarwal. Wave packet dynamics in monolayer MoS_2 with and without a magnetic field. *The European Physical Journal B*, 87(11):1–8, 2014.

[169] DJP De Sousa, LV De Castro, DR Da Costa, and J Milton Pereira Jr. Boundary conditions for phosphorene nanoribbons in the continuum approach. *Physical Review B*, 94(23):235415, 2016.

[170] Andrey Chaves, GA Farias, FM Peeters, and R Ferreira. The split-operator technique for the study of spinorial wavepacket dynamics. *Communications in Computational Physics*, 17(3):850–866, 2015.

[171] Kh Yu Rakhimov, Andrey Chaves, GA Farias, and FM Peeters. Wavepacket scattering of Dirac and Schrödinger particles on potential and magnetic barriers. *Journal of Physics: Condensed Matter*, 23(27):275801, 2011.

[172] AA Sousa, Andrey Chaves, TAS Pereira, GA Farias, and FM Peeters. Quantum tunneling between bent semiconductor nanowires. *Journal of Applied Physics*, 118(17):174301, 2015.

[173] Andrey Chaves, GA Farias, FM Peeters, and B Szafran. Wave packet dynamics in semiconductor quantum rings of finite width. *Physical Review B*, 80(12):125331, 2009.

[174] MD Petrović, FM Peeters, A Chaves, and GA Farias. Conductance maps of quantum rings due to a local potential perturbation. *Journal of Physics: Condensed Matter*, 25(49):495301, 2013.

[175] Ariel Adorno de Sousa, Andrey Chaves, Gil de Aquino Farias, and FM Peeters. Braess paradox at the mesoscopic scale. *Physical Review B*, 88(24):245417, 2013.

[176] DR Da Costa, Andrey Chaves, SHR Sena, GA Farias, and FM Peeters. Valley filtering using electrostatic potentials in bilayer graphene. *Physical Review B*, 92(4):045417, 2015.

[177] DR Da Costa, A Chaves, GA Farias, Lucian Covaci, and FM Peeters. Wave-packet scattering on graphene edges in the presence of a pseudomagnetic field. *Physical Review B*, 86(11):115434, 2012.

[178] LS Cavalcante, A Chaves, DR Da Costa, GA Farias, and FM Peeters. All-strain based valley filter in graphene nanoribbons using snake states. *Physical Review B*, 94(7):075432, 2016.

[179] Andrey Chaves, DR Da Costa, GO De Sousa, JM Pereira Jr, and GA Farias. Energy shift and conduction-to-valence band transition mediated by a time-dependent potential barrier in graphene. *Physical Review B*, 92(12):125441, 2015.

[180] DR Da Costa, A Chaves, GA Farias, and FM Peeters. Valley filtering in graphene due to substrate-induced mass potential. *Journal of Physics: Condensed Matter*, 29(21):215502, 2017.

[181] AN Rudenko, Shengjun Yuan, and MI Katsnelson. Toward a realistic description of multilayer black phosphorus: From GW approximation to large-scale tight-binding simulations. *Physical Review B*, 92(8):085419, 2015.

[182] Tomasz M Rusin and Wlodek Zawadzki. Zitterbewegung of electrons in carbon nanotubes created by laser pulses. *Journal of Physics: Condensed Matter*, 26(21):215301, 2014.

[183] Kostya S Novoselov, D Jiang, F Schedin, TJ Booth, VV Khotkevich, SV Morozov, and Andre K Geim. Two-dimensional atomic crystals. *Proceedings of the National Academy of Sciences*, 102(30):10451–10453, 2005.

[184] Qing Hua Wang, Kourosh Kalantar-Zadeh, Andras Kis, Jonathan N Coleman, and Michael S Strano. Electronics and optoelectronics of two-dimensional transition metal dichalcogenides. *Nature Nanotechnology*, 7(11):699–712, 2012.

[185] Mingsheng Xu, Tao Liang, Minmin Shi, and Hongzheng Chen. Graphene-like two-dimensional materials. *Chemical Reviews*, 113(5):3766–3798, 2013.

[186] Elisabeth Bianco, Sheneve Butler, Shishi Jiang, Oscar D Restrepo, Wolfgang Windl, and Joshua E Goldberger. Stability and exfoliation of germanane: a germanium graphane analogue. *ACS Nano*, 7(5):4414–4421, 2013.

[187] Patrick Vogt, Paola De Padova, Claudio Quaresima, Jose Avila, Emmanouil Frantzeskakis, Maria Carmen Asensio, Andrea Resta, Bénédicte Ealet, and Guy

Le Lay. Silicene: compelling experimental evidence for graphene-like two-dimensional silicon. *Physical Review Letters*, 108(15):155501, 2012.

[188] Manish Chhowalla, Hyeon Suk Shin, Goki Eda, Lain-Jong Li, Kian Ping Loh, and Hua Zhang. The chemistry of two-dimensional layered transition metal dichalco-genide nanosheets. *Nature Chemistry*, 5(4):263–275, 2013.

[189] Mohammad Zarenia, Andrey Chaves, GA Farias, and FM Peeters. Energy levels of triangular and hexagonal graphene quantum dots: a comparative study between the tight-binding and Dirac equation approach. *Physical Review B*, 84(24):245403, 2011.

[190] Zhenhua Wu, ZZ Zhang, Kai Chang, and FM Peeters. Quantum tunneling through graphene nanorings. *Nanotechnology*, 21(18):185201, 2010.

[191] M Grujić, M Zarenia, A Chaves, M Tadić, GA Farias, and FM Peeters. Electronic and optical properties of a circular graphene quantum dot in a magnetic field: influence of the boundary conditions. *Physical Review B*, 84(20):205441, 2011.

[192] Prabath Hewageegana and Vadym Apalkov. Electron localization in graphene quantum dots. *Physical Review B*, 77(24):245426, 2008.

[193] CA Downing, DA Stone, and ME Portnoi. Zero-energy states in graphene quantum dots and rings. *Physical Review B*, 84(15):155437, 2011.

[194] Jörg Schelter, Björn Trauzettel, and Patrik Recher. How to distinguish between specular and retroconfigurations for Andreev reflection in graphene rings. *Physical Review Letters*, 108(10):106603, 2012.

[195] Shengli Zhang, Huawei Chen, Erhu Zhang, and Daqing Liu. The Aharonov-Anandan current induced by a time-dependent magnetic flux in graphene rings. *EPL (Europhysics Letters)*, 103(5):58005, 2013.

[196] C Kamal and Motohiko Ezawa. Arsenene: Two-dimensional buckled and puckered honeycomb arsenic systems. *Physical Review B*, 91(8):085423, 2015.

[197] Martin Pumera and Zdeněk Sofer. 2D monoelemental arsenene, antimonene, and bismuthene: beyond black phosphorus. *Advanced Materials*, 29(21):1605299, 2017.

[198] Hsu-Sheng Tsai, Sheng-Wen Wang, Ching-Hung Hsiao, Chia-Wei Chen, Hao Ouyang, Yu-Lun Chueh, Hao-Chung Kuo, and Jenq-Horng Liang. Direct synthesis and practical bandgap estimation of multilayer arsenene nanoribbons. *Chemistry of Materials*, 28(2):425–429, 2016.

[199] Zhiya Zhang, Jiafeng Xie, Dezheng Yang, Yuhua Wang, Mingsu Si, and Desheng Xue. Manifestation of unexpected semiconducting properties in few-layer orthorhombic arsenene. *Applied Physics Express*, 8(5):055201, 2015.

[200] Yanli Wang and Yi Ding. Electronic structure and carrier mobilities of arsenene and antimonene nanoribbons: a first-principle study. *Nanoscale Research Letters*, 10(1):1–10, 2015.

[201] Majid Zeraati, S Mehdi Vaez Allaei, I Abdolhosseini Sarsari, Mahdi Pourfath, and Davide Donadio. Highly anisotropic thermal conductivity of arsenene: An ab initio study. *Physical Review B*, 93(8):085424, 2016.

[202] Hasan M Abdullah, DR da Costa, H Bahlouli, A Chaves, FM Peeters, and Ben Van Duppen. Electron collimation at van der Waals domain walls in bilayer graphene. *Physical Review B*, 100(4):045137, 2019.

[203] SM Cunha, DR da Costa, GO de Sousa, Andrey Chaves, J Milton Pereira Jr, and GA Farias. Wave-packet dynamics in multilayer phosphorene. *Physical Review B*, 99(23):235424, 2019.

[204] FF Batista Jr, Andrey Chaves, DR da Costa, and GA Farias. Curvature effects on the electronic and transport properties of semiconductor films. *Physica E: Low-dimensional Systems and Nanostructures*, 99:304–309, 2018.

[205] Hong-Xia Zhong, Shiyuan Gao, Jun-Jie Shi, and Li Yang. Quasiparticle band gaps, excitonic effects, and anisotropic optical properties of the monolayer distorted 1T diamond-chain structures ReS_2 and $ReSe_2$. *Physical Review B*, 92(11):115438, 2015.

[206] Andrey Chaves, Tony Low, P Avouris, D Çakır, and FM Peeters. Anisotropic exciton stark shift in black phosphorus. *Physical Review B*, 91(15):155311, 2015.

[207] GO De Sousa, DR Da Costa, Andrey Chaves, GA Farias, and FM Peeters. Unusual quantum confined stark effect and aharonov-bohm oscillations in semiconductor quantum rings with anisotropic effective masses. *Physical Review B*, 95(20):205414, 2017.

[208] H Van Houten, CWJ Beenakker, JG Williamson, MEI Broekaart, PHM Van Loosdrecht, BJ Van Wees, JE Mooij, CT Foxon, and JJ Harris. Coherent electron focusing with quantum point contacts in a two-dimensional electron gas. *Physical Review B*, 39(12):8556, 1989.

[209] Gilles Montambaux. Semiclassical quantization of skipping orbits. *The European Physical Journal B*, 79(2):215–224, 2011.

[210] AH MacDonald. Edge states in the fractional-quantum-Hall-effect regime. *Physical Review Letters*, 64(2):220, 1990.

[211] N Aoki, CR Da Cunha, R Akis, DK Ferry, and Y Ochiai. Imaging of integer quantum hall edge state in a quantum point contact via scanning gate microscopy. *Physical Review B*, 72(15):155327, 2005.

[212] Markus Büttiker. Absence of backscattering in the quantum Hall effect in multi-probe conductors. *Physical Review B*, 38(14):9375, 1988.

[213] David E Manolopoulos. Derivation and reflection properties of a transmission-free absorbing potential. *The Journal of Chemical Physics*, 117(21):9552–9559, 2002.

[214] Yonatan Betancur-Ocampo, François Leyvraz, and Thomas Stegmann. Electron optics in phosphorene pn junctions: negative reflection and anti-super-Klein tunneling. *Nano Letters*, 19(11):7760–7769, 2019.

[215] RS Deacon, K-C Chuang, RJ Nicholas, KS Novoselov, and AK Geim. Cyclotron resonance study of the electron and hole velocity in graphene monolayers. *Physical Review B*, 76(8):081406, 2007.

[216] M Ramezani Masir, P Vasilopoulos, A Matulis, and FM Peeters. Direction-dependent tunneling through nanostructured magnetic barriers in graphene. *Physical Review B*, 77(23):235443, 2008.

[217] Long-Jing Yin, Ke-Ke Bai, Wen-Xiao Wang, Si-Yu Li, Yu Zhang, and Lin He. Landau quantization of Dirac fermions in graphene and its multilayers. *Frontiers of Physics*, 12(4):127208, 2017.

[218] Sándor Benczik, Lay Nam Chang, Djordje Minic, and Tatsu Takeuchi. Hydrogen-atom spectrum under a minimal-length hypothesis. *Physical Review A*, 72(1):012104, 2005.

[219] Pouria Pedram. New approach to nonperturbative quantum mechanics with minimal length uncertainty. *Physical Review D*, 85(2):024016, 2012.

[220] Pasquale Bosso. Rigorous hamiltonian and lagrangian analysis of classical and quantum theories with minimal length. *Physical Review D*, 97(12):126010, 2018.

[221] Musongela Lubo. Quantum minimal length and trans-planckian photons. *Physical Review D*, 61(12):124009, 2000.

[222] Fabio Scardigli and Roberto Casadio. Gravitational tests of the generalized uncertainty principle. *The European Physical Journal C*, 75(9):1–12, 2015.

[223] Matteo AC Rossi, Tommaso Giani, and Matteo GA Paris. Probing deformed quantum commutators. *Physical Review D*, 94(2):024014, 2016.

[224] Qin Zhao, Mir Faizal, and Zaid Zaz. Short distance modification of the quantum virial theorem. *Physics Letters B*, 770:564–568, 2017.

[225] Luis B Castro and Angel E Obispo. Generalized relativistic harmonic oscillator in minimal length quantum mechanics. *Journal of Physics A: Mathematical and Theoretical*, 50(28):285202, 2017.

[226] M Moniruzzaman and SB Faruque. Estimation of minimal length using binding energy of deuteron. *Journal of Scientific Research*, 10(2):99–103, 2018.

[227] Brett Bolen and Marco Cavaglia. (anti-) de Sitter black hole thermodynamics and the generalized uncertainty principle. *General Relativity and Gravitation*, 37(7):1255–1262, 2005.

[228] Salvatore Mignemi. Extended uncertainty principle and the geometry of (anti)-de Sitter space. *Modern Physics Letters A*, 25(20):1697–1703, 2010.

[229] Achim Kempf. Uncertainty relation in quantum mechanics with quantum group symmetry. *Journal of Mathematical Physics*, 35(9):4483–4496, 1994.

[230] M Asghari, P Pedram, and K Nozari. Harmonic oscillator with minimal length, minimal momentum, and maximal momentum uncertainties in SUSYQM framework. *Physics Letters B*, 725(4-5):451–455, 2013.

[231] RN Costa Filho, MP Almeida, GA Farias, and JS Andrade Jr. Displacement operator for quantum systems with position-dependent mass. *Physical Review A*, 84(5):050102, 2011.

[232] Raimundo N Costa Filho, João PM Braga, Jorge HS Lira, and José S Andrade Jr. Extended uncertainty from first principles. *Physics Letters B*, 755:367–370, 2016.

[233] João PM Braga and Raimundo N Costa Filho. Nonadditive quantum mechanics as a sturm–liouville problem. *International Journal of Modern Physics C*, 27(04):1650047, 2016.

[234] Raimundo N Costa Filho, Geová Alencar, Bo-Sture Skagerstam, and Jose S Andrade Jr. Morse potential derived from first principles. *EPL (Europhysics Letters)*, 101(1):10009, 2013.

[235] FSA Cavalcante, RN Costa Filho, J Ribeiro Filho, CAS De Almeida, and VN Freire. Form of the quantum kinetic-energy operator with spatially varying effective mass. *Physical Review B*, 55(3):1326, 1997.

[236] MA Rego-Monteiro and FD Nobre. Classical field theory for a non-hermitian schrödinger equation with position-dependent masses. *Physical Review A*, 88(3):032105, 2013.

[237] M Vubangsi, M Tchoffo, and LC Fai. Position-dependent effective mass system in a variable potential: displacement operator method. *Physica Scripta*, 89(2):025101, 2014.

[238] EG Barbagiovanni, DJ Lockwood, NL Rowell, RN Costa Filho, Isabelle Berbezier, Guillaume Amiard, Luc Favre, A Ronda, M Faustini, and D Grosso. Role of quantum confinement in luminescence efficiency of group IV nanostructures. *Journal of Applied Physics*, 115(4):044311, 2014.

[239] EG Barbagiovanni and RN Costa Filho. Quantum confinement in nonadditive space with a spatially dependent effective mass for Si and Ge quantum wells. *Physica E: Low-dimensional Systems and Nanostructures*, 63:14–20, 2014.

[240] Bruno G da Costa and Ernesto P Borges. Generalized space and linear momentum operators in quantum mechanics. *Journal of Mathematical Physics*, 55(6):062105, 2014.

[241] DR Da Costa, Andrey Chaves, M Zarenia, JM Pereira Jr, GA Farias, and FM Peeters. Geometry and edge effects on the energy levels of graphene quantum rings: A comparison between tight-binding and simplified dirac models. *Physical Review B*, 89(7):075418, 2014.

[242] LJP Xavier, DR Da Costa, A Chaves, JM Pereira, and GA Farias. Electronic confinement in graphene quantum rings due to substrate-induced mass radial kink. *Journal of Physics: Condensed Matter*, 28(50):505501, 2016.

[243] Yakir Aharonov and Aharon Casher. Ground state of a spin-1/2 charged particle in a two-dimensional magnetic field. *Physical Review A*, 19(6):2461, 1979.

[244] Y Betancur-Ocampo, ME Cifuentes-Quintal, G Cordourier-Maruri, and R de Coss. Landau levels in uniaxially strained graphene: A geometrical approach. *Annals of Physics*, 359:243–251, 2015.

[245] FMD Pellegrino, GGN Angilella, and R Pucci. Transport properties of graphene across strain-induced nonuniform velocity profiles. *Physical Review B*, 84(19):195404, 2011.

[246] Fernando de Juan, Mauricio Sturla, and Maria AH Vozmediano. Space dependent fermi velocity in strained graphene. *Physical Review Letters*, 108(22):227205, 2012.

[247] MO Goerbig, J-N Fuchs, G Montambaux, and F Piéchon. Tilted anisotropic dirac cones in quinoid-type graphene and $\alpha - (BEDT - TTF)_2 I_3$. *Physical Review B*, 78(4):045415, 2008.

[248] Gerardo G Naumis, Salvador Barraza-Lopez, Maurice Oliva-Leyva, and Humberto Terrones. Electronic and optical properties of strained graphene and other strained 2D materials: a review. *Reports on Progress in Physics*, 80(9):096501, 2017.

[249] P Nigge, AC Qu, É Lantagne-Hurtubise, Erik Mårsell, S Link, G Tom, M Zonno, M Michiardi, M Schneider, S Zhdanovich, et al. Room temperature strain-induced Landau levels in graphene on a wafer-scale platform. *Science Advances*, 5(11):eaaw5593, 2019.

[250] Ş Kuru, J Negro, and LM Nieto. Exact analytic solutions for a Dirac electron moving in graphene under magnetic fields. *Journal of Physics: Condensed Matter*, 21(45):455305, 2009.

[251] Tarun Kanti Ghosh. Exact solutions for a Dirac electron in an exponentially decaying magnetic field. *Journal of Physics: Condensed Matter*, 21(4):045505, 2008.

[252] IR Lavor, DR da Costa, Andrey Chaves, SHR Sena, GA Farias, B Van Duppen, and FM Peeters. Effect of zitterbewegung on the propagation of wave packets in ABC-stacked multilayer graphene: an analytical and computational approach. *Journal of Physics: Condensed Matter*, 33(9):095503, 2020.

[253] SM Cunha, DR da Costa, LC Felix, Andrey Chaves, and J Milton Pereira Jr. Electronic and transport properties of anisotropic semiconductor quantum wires. *Physical Review B*, 102(4):045427, 2020.

[254] SV Morozov, KS Novoselov, MI Katsnelson, F Schedin, DC Elias, John A Jaszczak, and AK Geim. Giant intrinsic carrier mobilities in graphene and its bilayer. *Physical Review Letters*, 100(1):016602, 2008.

[255] EB Sonin. Effect of Klein tunneling on conductance and shot noise in ballistic graphene. *Physical Review B*, 79(19):195438, 2009.

[256] Cheng-Cheng Liu, Hua Jiang, and Yugui Yao. Low-energy effective Hamiltonian involving spin-orbit coupling in silicene and two-dimensional germanium and tin. *Physical Review B*, 84(19):195430, 2011.

[257] ME Dávila, Lede Xian, Seymur Cahangirov, Angel Rubio, and Guy Le Lay. Germanene: a novel two-dimensional germanium allotrope akin to graphene and silicene. *New Journal of Physics*, 16(9):095002, 2014.

[258] DP DiVincenzo and EJ Mele. Self-consistent effective-mass theory for intralayer screening in graphite intercalation compounds. *Physical Review B*, 29(4):1685, 1984.

[259] NMR Peres. Scattering in one-dimensional heterostructures described by the Dirac equation. *Journal of Physics: Condensed Matter*, 21(9):095501, 2009.

[260] Raphael Tsu. *Superlattice to nanoelectronics*. Elsevier, 2010.

[261] Chunxu Bai and Xiangdong Zhang. Klein paradox and resonant tunneling in a graphene superlattice. *Physical Review B*, 76(7):075430, 2007.

[262] Michaël Barbier, FM Peeters, P Vasilopoulos, and J Milton Pereira Jr. Dirac and Klein-Gordon particles in one-dimensional periodic potentials. *Physical Review B*, 77(11):115446, 2008.

[263] Jianmin Sun, HA Fertig, and L Brey. Effective magnetic fields in graphene super-lattices. *Physical Review Letters*, 105(15):156801, 2010.

[264] Liang Zheng Tan, Cheol-Hwan Park, and Steven G Louie. Graphene Dirac fermions in one-dimensional inhomogeneous field profiles: Transforming magnetic to electric field. *Physical Review B*, 81(19):195426, 2010.

[265] Michaël Barbier, Panagiotis Vasilopoulos, and François M Peeters. Single-layer and bilayer graphene superlattices: collimation, additional Dirac points and Dirac lines. *Philosophical Transactions of the Royal Society A: Mathematical, Physical and Engineering Sciences*, 368(1932):5499–5524, 2010.

[266] Sergey Borisenko, Quinn Gibson, Danil Evtushinsky, Volodymyr Zabolotnyy, Bernd Büchner, and Robert J Cava. Experimental realization of a three-dimensional Dirac semimetal. *Physical Review Letters*, 113(2):027603, 2014.

[267] Marlou R Slot, Thomas S Gardenier, Peter H Jacobse, Guido CP van Miert, Sander N Kempkes, Stephan JM Zevenhuizen, Cristiane Morais Smith, Daniel Van-maekelbergh, and Ingmar Swart. Experimental realization and characterization of an electronic Lieb lattice. *Nature Physics*, 13(7):672–676, 2017.

[268] Zhi Li, Jincheng Zhuang, Li Wang, Haifeng Feng, Qian Gao, Xun Xu, Weichang Hao, Xiaolin Wang, Chao Zhang, Kehui Wu, et al. Realization of flat band with possible nontrivial topology in electronic Kagome lattice. *Science Advances*, 4(11):eaau4511, 2018.

[269] ZK Liu, Bo Zhou, Yong Zhang, ZJ Wang, HM Weng, Dharmalingam Prabhakaran, S-K Mo, ZX Shen, Zhong Fang, Xi Dai, et al. Discovery of a three-dimensional topological Dirac semimetal, Na_3Bi. *Science*, 343(6173):864–867, 2014.

[270] Elliott H Lieb. Two theorems on the Hubbard model. *Physical Review Letters*, 62(10):1201, 1989.

[271] Luyang Wang and Dao-Xin Yao. Coexistence of spin-1 fermion and Dirac fermion on the triangular Kagome lattice. *Physical Review B*, 98(16):161403, 2018.

[272] Andrii Iurov, Godfrey Gumbs, and Danhong Huang. Peculiar electronic states, symmetries, and Berry phases in irradiated $\alpha - T_3$ materials. *Physical Review B*, 99(20):205135, 2019.

[273] Yunkun Xie, Yaohua Tan, and Avik W Ghosh. Spintronic signatures of Klein tunneling in topological insulators. *Physical Review B*, 96(20):205151, 2017.

[274] Yafang Xu and Guojun Jin. Omnidirectional transmission and reflection of pseudospin-1 Dirac fermions in a Lieb superlattice. *Physics Letters A*, 378(47):3554–3560, 2014.

[275] Chao-Yang Tan, Chang-Xu Yan, Yong-Hong Zhao, Hong Guo, Hao-Ran Chang, et al. Anisotropic longitudinal optical conductivities of tilted dirac bands in $1T - MoS_2$. *Physical Review B*, 103(12):125425, 2021.

[276] Nicholas Weekes, Andrii Iurov, Liubov Zhemchuzhna, Godfrey Gumbs, and Danhong Huang. Generalized WKB theory for electron tunneling in gapped $\alpha - T_3$ lattices. *Physical Review B*, 103(16):165429, 2021.

[277] Sebastiano Peotta and Päivi Törmä. Superfluidity in topologically nontrivial flat bands. *Nature Communications*, 6(1):1–9, 2015.

[278] Aleksi Julku, Sebastiano Peotta, Tuomas I Vanhala, Dong-Hee Kim, and Päivi Törmä. Geometric origin of superfluidity in the Lieb-lattice flat band. *Physical Review Letters*, 117(4):045303, 2016.

[279] L Mandhour and F Bouhadida. Klein tunneling in deformed $\alpha - T_3$ lattice. *arXiv preprint arXiv:2004.10144*, 2020.

[280] Bashab Dey and Tarun Kanti Ghosh. Floquet topological phase transition in the $\alpha - T_3$ lattice. *Physical Review B*, 99(20):205429, 2019.

[281] DD Edwall, JS Chen, J Bajaj, and ER Gertner. $MOCVD Hg_{1-x}Cd_xTe/GaAs$ for IR detectors. *Semiconductor Science and Technology*, 5(3S):S221, 1990.

[282] Y Betancur-Ocampo and V Gupta. Perfect transmission of 3D massive Kane fermions in $HgCdTe$ veselago lenses. *Journal of Physics: Condensed Matter*, 30(3):035501, 2017.

[283] CH Yang, R Wieser, and L Wang. The effect of a variable coupling parameter on the tunneling properties from graphene to $\alpha - T_3$ model. *Journal of Applied Physics*, 128(9):094301, 2020.

[284] Changqing Xu, Gang Wang, Zhi Hong Hang, Jie Luo, Che Ting Chan, and Yun Lai. Design of full-k-space flat bands in photonic crystals beyond the tight-binding picture. *Scientific Reports*, 5(1):1–8, 2015.

[285] Judit Romhányi, Karlo Penc, and Ramachandran Ganesh. Hall effect of triplons in a dimerized quantum magnet. *Nature Communications*, 6(1):1–6, 2015.

[286] EV Gorbar, VP Gusynin, and DO Oriekhov. Electron states for gapped pseudospin-1 fermions in the field of a charged impurity. *Physical Review B*, 99(15):155124, 2019.

[287] Dmitry Green, Luiz Santos, and Claudio Chamon. Isolated flat bands and spin-1 conical bands in two-dimensional lattices. *Physical Review B*, 82(7):075104, 2010.

[288] Seungchul Kim, Jisoon Ihm, Hyoung Joon Choi, and Young-Woo Son. Origin of anomalous electronic structures of epitaxial graphene on silicon carbide. *Physical Review Letters*, 100(17):176802, 2008.

[289] MS Nevius, M Conrad, F Wang, A Celis, MN Nair, A Taleb-Ibrahimi, A Tejeda, and EH Conrad. Semiconducting graphene from highly ordered substrate interactions. *Physical Review Letters*, 115(13):136802, 2015.

[290] S Yi Zhou, G-H Gweon, AV Fedorov, de First, PN, WA De Heer, D-H Lee, F Guinea, AH Castro Neto, and A Lanzara. Substrate-induced bandgap opening in epitaxial graphene. *Nature Materials*, 6(10):770–775, 2007.

[291] Peter Markos and Costas M Soukoulis. *Wave propagation*. Princeton University Press, 2008.

[292] LP Miranda, SP Milovanović, RN Costa Filho, and FM Peeters. Hall and bend resistance of a phosphorene Hall bar. *Physical Review B*, 104(3):035401, 2021.

[293] Viktor G Veselago. Electrodynamics of substances with simultaneously negative values of ϵ and μ. *Usp. Fiz. Nauk*, 92:517, 1967.

[294] Vadim V Cheianov, Vladimir Fal'ko, and BL Altshuler. The focusing of electron flow and a Veselago lens in graphene pn junctions. *Science*, 315(5816):1252–1255, 2007.

[295] SM Cunha, DR da Costa, J Milton Pereira Jr, RN Costa Filho, B Van Duppen, and FM Peeters. Band-gap formation and morphing in $\alpha - T_3$ superlattices. *Physical Review B*, 104(11):115409, 2021.

[296] J Viana Gomes and NMR Peres. Tunneling of Dirac electrons through spatial regions of finite mass. *Journal of Physics: Condensed Matter*, 20(32):325221, 2008.

[297] M Zarenia, O Leenaerts, B Partoens, and FM Peeters. Substrate-induced chiral states in graphene. *Physical Review B*, 86(8):085451, 2012.

[298] M Zarenia, JM Pereira Jr, GA Farias, and FM Peeters. Chiral states in bilayer graphene: Magnetic field dependence and gap opening. *Physical Review B*, 84(12):125451, 2011.